

Study of Cold Cracking during DC-casting of High Strength Aluminum Alloys

PhD thesis

Mehdi Lalpoor

This research was carried out under the project number MC4.05237 in the framework of the strategic research program of the Materials innovation institute (M2i) (www.m2i.nl);



in the department of Materials Science and Engineering at the Delft University of Technology in the Netherlands (www.tudelft.nl).



Delft University of Technology

Study of Cold Cracking during DC-casting of High Strength Aluminum Alloys

Proefschrift

ter verkrijging van de graad van doctor
aan de Technische Universiteit Delft,
op gezag van de Rector Magnificus Prof. ir. K.C.A.M. Luyben
voorzitter van het College voor Promoties,
in het openbaar te verdedigen op dinsdag 30 november 2010 om 15.00 uur

door

Mehdi LALPOOR

Master of Science in Advanced Materials
University of Ulm, Germany
geboren te Teheran, Iran

Dit proefschrift is goedgekeurd door de promotor:

Prof. ir. L. Katgerman

Samenstelling promotiecommissie:

Rector Magnificus,	voorzitter
Prof. ir. L. Katgerman,	Technische Universiteit Delft, promotor
Dr. D.G. Eskin,	Technische Universiteit Delft, copromotor
Prof. dr. R. Boom,	Technische Universiteit Delft & Corus RD&T
Prof. dr. I.M. Richardson,	Technische Universiteit Delft
Prof. dr. ir. R. Benedictus,	Technische Universiteit Delft
Prof. dr. M. Rappaz,	Ecole Polytechnique fédérale de Lausanne (EPFL)
Dr. ir. H.A. Wouters,	Corus RD&T

Keywords: Aluminum alloys, DC-Casting, thermo-mechanical simulations, fracture, cold cracking.

ISBN 978-90-77172-63-6

Copyright © 2010 by M. Lalpoor

All rights reserved. No part of the material protected by this copyright notice may be reproduced or utilized in any form or by any means, electronic or mechanical, including photocopying, recording or by any information storage and retrieval system, without written permission from the author.

Printed in the Netherlands.

Cover: Electron backscattered image showing hot cracks formed during the solidification in the center of a Ø255-mm AA7050 DC-cast billet (Fig. 4.7d).

To my parents to whom I owe my existence

Table of contents

Preface	1
Chapter 1	
Introduction	3
1.1 Direct Chill casting	3
1.2 Defects caused by inhomogeneous temperature distribution in DC-cast ingots.....	4
1.3 Cold Cracking	7
1.4 Technical approaches to preventing cold cracking	9
1.5 Outline of the thesis	11
References	12
Chapter 2	
Thermomechanical behavior of 7xxx series aluminum alloys in the as-cast condition	15
2.1 As-cast mechanical properties of the AA7050 alloy cast in a copper mold	15
2.1.1 Introduction	15
2.1.2 Experimental procedure.....	16
2.1.3 Results	19
2.1.3.1 Mechanical tests.....	19
2.1.3.2 Structure examination.....	21
2.1.4 Discussion.....	23
2.1.5 Conclusions	25
2.2 Constitutive parameters and mechanical properties in DC-cast AA7050 billets ...	26
2.2.1 Introduction	26
2.2.2 Experimental procedure.....	26
2.2.3 Results	27
2.2.3.1 Samples along the radial direction.....	27
2.2.3.2 Samples along vertical billet axis	28
2.2.3.3 Constitutive parameters	29
2.2.3.4 Structure examination.....	30
2.2.4 Discussion.....	31
2.2.5 Conclusions	34
2.3 Investigation of fracture behavior of the DC-cast AA7050 and AA7475 alloys ...	35
2.3.1 Introduction	35
2.3.2 Charpy impact tests	35
2.3.2.1 Experimental procedure.....	35
2.3.2.2 Results.....	36
2.3.2.3 Discussion.....	37
2.3.3 Plane strain fracture toughness tests.....	38
2.3.3.1 Experimental procedure and discussion	38
2.4 Measurement of the Young's modulus	42
References	44

Chapter 3

Thermal properties and thermal contraction behavior in AA7050 alloy	47
3.1 Introduction	47
3.2 Differential Scanning Calorimetry	49
3.3 Thermal contraction in 7050 alloy	50
3.3.1 Introduction	50
3.3.2 Determination of the thermal contraction in the solidification range.....	51
3.3.3 Determination of the coefficient of thermal expansion/contraction.....	54
3.3.4 The thermodynamic database for thermal properties	59
3.4 Summary and conclusions.....	59
References	60

Chapter 4

Microstructural features of intergranular brittle fracture and cold cracking in high strength aluminum alloys	61
4.1 Introduction	61
4.2 Experimental procedure	63
4.3 Results and discussion.....	64
4.3.1 Conventional mechanical tests	64
4.3.2 In-situ tensile tests in ESEM	67
4.3.3 Observations from real cracked billets	68
4.4 Conclusions	71
References	71

Chapter 5

Thermomechanical simulation of the DC-casting process in AA7050 billets	73
5.1 Introduction	73
5.2 Presentation of the Model	74
5.3 Results and Discussion.....	80
5.4 Conclusions	85
References	85

Chapter 6

Evolution of residual thermal stresses in the billet after the end of casting, and cold cracking assessment	89
6.1 Introduction	89
6.2 Simulation results.....	91
6.3 Cracking assessment in the billet	96
6.4 Discussion	99
6.5 Conclusions	102
References	103

Chapter 7

Cold cracking development in AA7050 DC-cast billets under various casting conditions	105
7.1 Introduction	105
7.2 Model setup	106
7.3 Simulation results	107
7.4 Cracking assessment in the billet	109
7.5 Discussion	111
7.6 Conclusions	116
References	116

Chapter 8

Development of a cold cracking criterion for DC-casting of high strength aluminum alloys	119
8.1 Introduction	119
8.2 Cold cracking criterion for AA7050 DC-cast billets	121
8.2.1 Model setup	121
8.2.2 Simulation results and discussion	123
8.3 Cold cracking criterion for a typical 7xxx series alloy	125
8.3.1 Determination of the mechanical properties.....	125
8.3.2 Model setup for the new alloy	129
8.3.3 Simulation results and discussion.....	130
8.4 Conclusions	135
References	135
Conclusions and outlook	137
Summary	139
Samenvatting	143
List of publications	147
Acknowledgments	149
Curriculum Vitae	150

Preface

For half a century the aluminum industry has been facing a challenge in DC-casting of high strength aluminum alloys that has seriously affected the efficiency of the casting and has increased the product loss in terms of scraping. This problem which is the result of poor ductility of such alloys (especially 2xxx and 7xxx series alloys) in the semi-solid and as-cast conditions may be facilitated by thermal stresses developed in the ingots during the casting and eventually manifests as hot or cold-cracking. The tearing of the interdendritic liquid films above the solidus is called hot cracking while cold cracking is the catastrophic failure of the entire ingot at temperatures below solidus. On the one hand the wide solidification temperature range of high-strength aluminum alloys makes them prone to hot cracking and on the other hand their extreme brittleness assists the brittle fracture at certain temperatures in the completely solid state. Cold cracking not only results in scarping the ingots but it may also be hazardous to the personnel due to its unpredictable and explosive nature. Although a lot of research is conducted on hot tearing, the cold cracking has been rarely studied in the past. This is mainly the result of the unpredictable nature of the cold cracking that does not occur in each casting trial. Therefore the main study on this field has been confined to case studies rather than fundamental investigations. In fact, the industry preferred to solve the problem technically for the sake of production rather than performing a systematic research with the aim to understand the phenomenon. Besides being an unpredictable phenomenon, other problems have prevented the researchers from more detailed studies. Lack of knowledge on the mechanical properties, constitutive parameters and plane strain fracture toughness in the “*as-cast*” condition was the most important restricting factor. Instead, to get an overall idea about the materials resistance to cracking, the mechanical properties and the constitutive parameters of the material in homogenized or stress relieved states were applied in analysis. This was mainly due to the fact that high strength aluminum alloys have been known for their admirable properties in the fully heat treated and precipitation hardened state and not in the as-cast condition. Therefore very little research has been performed on their mechanical properties in the as-cast condition. The risk of explosive break of the billet and sudden ejection of the broken part are the main reasons why such billets are always delivered after stress relieving or homogenization treatment. But how close these properties are to the genuine as-cast materials is another issue that should be studied. Determination of the thermomechanical properties of the material in the as-cast condition was therefore the first objective of the current research. The next objective was to simulate the state of the residual thermal stresses that develop during the casting using the parameters determined in the previous step. Investigation of the contour maps of the ingot may reveal the critical stages during the casting at which thermal stresses reach their

maximum. The coincidence of these stages with the temperature range over which the material is extremely brittle may reveal the critical locations where the material is prone to cold cracking. Another important point to study is the fracture mode and the crack propagation path which has been rarely studied in the past. This may help us to understand the mechanisms of cold cracking and its probable link to hot tearing and other casting defects.

The final objective of this work was to apply the fracture mechanics to determine the critical crack/void size that may lead to the catastrophic failure of the billets. This may not only provide us with the failure probability during DC-casting process but it also gives us an idea what void/crack sizes may trigger the failure. The comparison of such crack/void sizes with the actual void size in DC-cast billets may reveal what kind of voids are the most critical.

Based on what was mentioned above, we decided to study the cold cracking phenomenon in high strength aluminum alloys by applying both experimental and computer simulation approaches. In the first step, the mechanical properties and constitutive parameters of the AA7050 alloy were determined over the post solidification temperature range. The fracture behavior and plane strain fracture toughness of the alloy were also studied over the similar temperature range. Fractographic techniques were used to check the fracture mode and the crack propagation path. In-situ tensile tests were also performed to follow the crack propagation path not only at room temperature but also at elevated temperatures. Later on, some critical thermal properties of the alloy were studied using the experimental techniques and the necessary data were extracted for the computer simulations. At the end of this phase, data-bases were prepared for both thermal and mechanical properties of the alloy using the experimentally determined data and the data obtained from thermodynamics data-bases. In the next step, the thermomechanical simulations were run to investigate the evolution of residual thermal stresses in the billet during the casting. By application of fracture mechanics, the critical crack size and the failure probability were assessed in the billet during the casting under steady state conditions and after the end of solidification when the billet is completely solid. Having learned the evolution of residual thermal stresses in the billet, the next job was to check how casting variables may affect the magnitude and distribution of thermal stresses in the billet. The effects of water flow rate, water temperature, melt temperature, casting speed and billet diameter were studied using the computer simulations with the aim to find the most influential parameters. Finally, the established criterion was validated on pilot scale DC-casting trials with a newly developed 7xxx series alloy under various casting conditions. The criterion is able to predict the critical void/crack size with a reasonable accuracy. The results of our research indicate that for cold cracking to occur the presence of some voids of critical size is required. The formation of such voids/cracks and their relationship with hot tearing is another interesting topic that needs to be further studied in the future. The connection of hot and cold cracking may be the last lost chain of the failure phenomenon in DC-casting of high strength aluminum alloys.

Chapter 1

Introduction

1.1 Direct Chill casting

Vertical Direct Chill (DC) casting is a semi-continuous casting process of aluminum alloys and has been the mainstream of the aluminum industry mainly due to its robust nature and relative simplicity [1-4]. In the DC-casting process, molten metal flows into a short, rectangular or round water-cooled mold, which is initially closed by a plug (starter or bottom block) on a movable ram. Solidification and cooling occurs at two steps namely primary or mold cooling and secondary or water cooling [3]. In primary cooling, the metal freezes against the mold and the bottom block, and forms a solidified shell. The ram is then steadily withdrawn, pulling the solidified shell with it. As the shell exits the bottom of the mold, water is sprayed directly on it for the secondary cooling. In this manner, a cast ingot of a desired cross-section and length is produced (Fig. 1.1). Apart from technical features of the setup, casting process parameters such as casting speed, cast temperature, billet geometry and size, water flow rate, and water temperature may affect the quality of the casting [3].

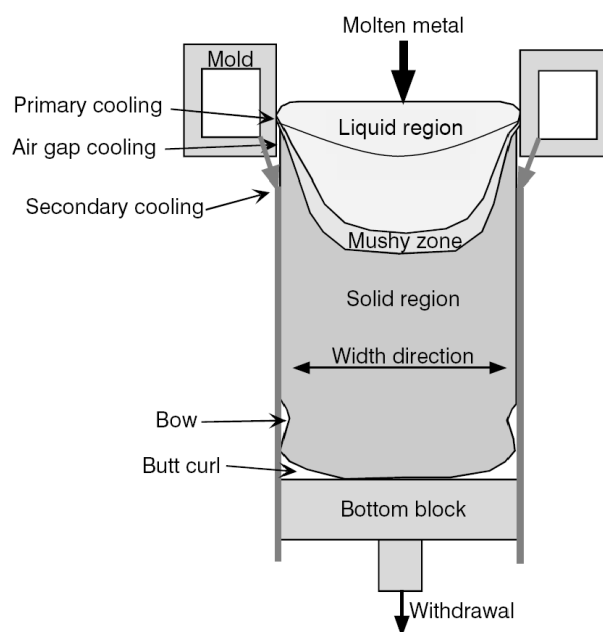


Fig. 1.1 Schematic illustration of DC-casting [5].

1.2 Defects caused by inhomogeneous temperature distribution in DC-cast ingots

Nonuniform rapid heat removal from the partially solidified ingot imparted by the mold and the bottom block results in high thermal gradients (Fig. 1.2). As materials physical properties are temperature dependent, high temperature gradients lead to high variation in materials properties including the density. At the same time, thermal contraction occurs on cooling due to the increase of the materials density [3]. This differential in contraction produces stresses, as one part of the casting restrains another [6-10]. The level of these stresses defines the final shape of the casting and determines whether a crack free product is made. Depending on the geometry of the ingot and the casting regime (start up, steady state, or the cooling down) thermal stresses may gain different magnitudes and signs at various locations of the ingot. In round billets, normal stresses are mainly compressive at the surface and tensile in the center [6]. In ingots with a rectangular cross section (slabs) however, the stress state might be slightly more complicated depending on the width to thickness ratio (multiplicity). General speaking, normal stresses appear to be compressive on the rolling face and tensile in the interior [10]. Tensile stresses may appear on the narrow side of the ingot and their magnitude increases with an increase in the multiplicity (width to thickness ratio) and cross-section area [11].

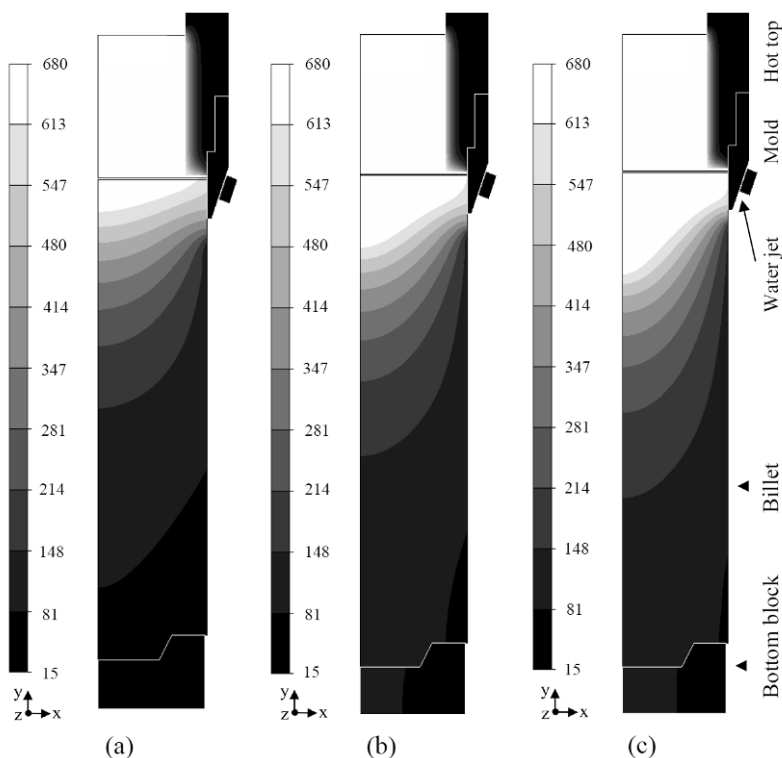


Fig. 1.2 Computer simulation results showing the temperature contours in DC-cast billets with 200 mm diameter cast at various speeds: (a) 1 mm/s, (b) 1.5 mm/s, and (c) 2 mm/s. ALSIM5* is used for simulations and temperatures are in °C.

* ALSIM is a casting-simulation software developed by the Norwegian Institute for Energy Technology (IFE), Kjeller, Norway.

Figs. 1.3a and b show the contour maps of the maximum principal stress in both billets and slabs in the steady state regime of casting.

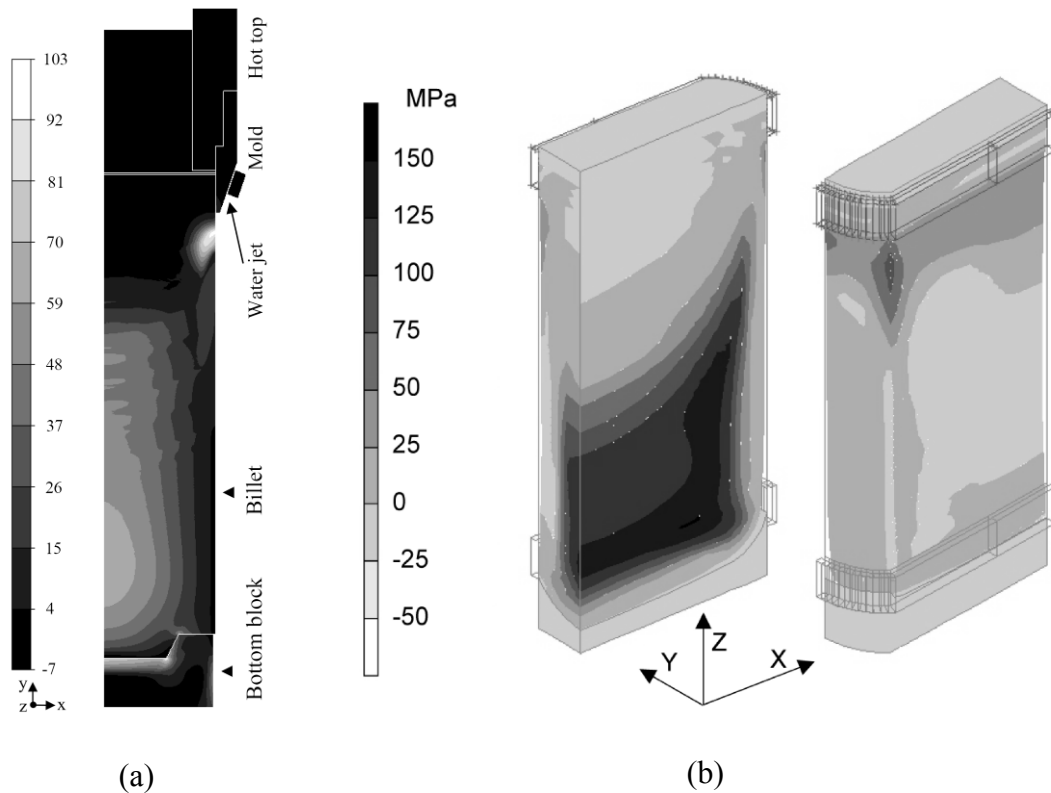


Fig. 1.3 Maximum principal stress component (MPa) in: (a) an AA7050 billet with a 200 mm diameter (computer simulations with ALSIM5) and final length of 400 mm, and (b) an Al-4.5 wt% Cu slab with the cross section $2000 \times 510 \text{ mm}^2$ and final length of 2000 mm [10]. Both ingots were cast at 60 mm/min (1 mm/s).

Thermal stresses may lead to various defects at different stages of casting and locations of the billet. They can cause distortions in the ingot and lead to butt curling or butt swelling (Fig. 1.4) [12]. Such deformations occur mainly in rolling ingots and during the non-steady-state solidification. Butt curling is caused by rapid thermal contraction of the bottom of the ingot and occurs after immersion of the bottom of the ingot and the bottom block in the direct cooling water [13]. Butt swelling occurs in connection with an excessive molten pool depth at the start of casting [12]. Another consequence of the appearance of thermal stresses in ingots is the cracking of the material at different locations and stages of casting. Such cracks may be hot cracks or cold cracks.

Before defining hot cracks, a definition of some critical temperatures is required. The *coherency temperature* is defined as the temperature (or solid fraction) at which the solid grains start to feel each other by interacting and tangling. This temperature divides the transition region into the upper slurry zone and the lower mushy zone. Closer to the solidus, inside the mushy zone, there is another important temperature marking the formation of the continuous network of solid grains that are able to transfer stress; as a result, the mush acquires strength. This temperature is called the *rigidity temperature* [14]. Slightly above solidus (below rigidity) when the solid networks coalesce and material starts holding thermal strains, hot tears may appear [15]. Hot tearing is in fact a fracture in the liquid film surrounding the solid grains and occurs when the transient stress at a point during cooling exceeds the tensile strength

of the material at the instantaneous temperature [16]. Hot tears are more frequently observed in the center of the ingots/billets where high tensile stresses rise up (Fig. 1.5) [17], but they can also appear at the surface. In fact, surface cracks are also hot cracks that form during the temperature rise at the surface due to air gap formation [4,18,19]. Fig. 1.6 shows a flowchart explaining factors that affect the mechanical behavior of metal at different stages of solidification.

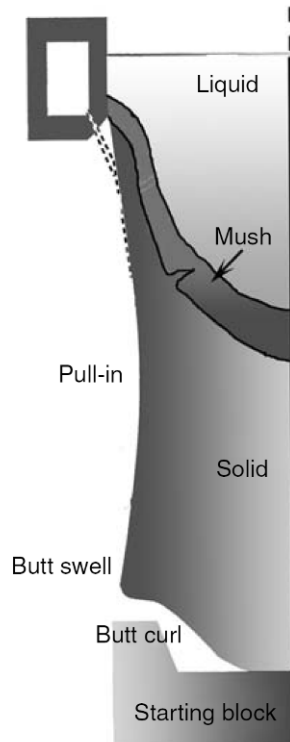


Fig. 1.4 A view from the short side of the ingot showing distortions typical of DC-cast ingots [20].

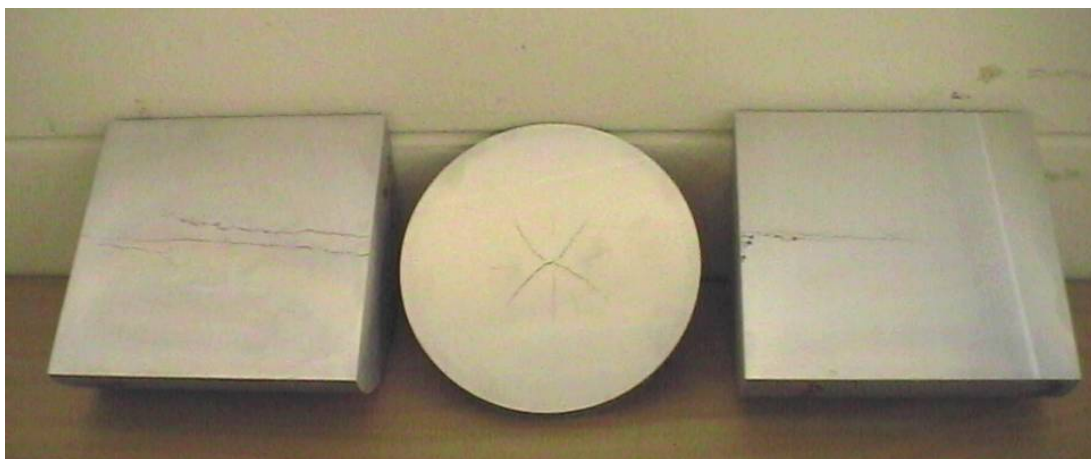


Fig. 1.5 A photograph showing hot tears in the center of 200-mm radius Al-Cu billets [21].

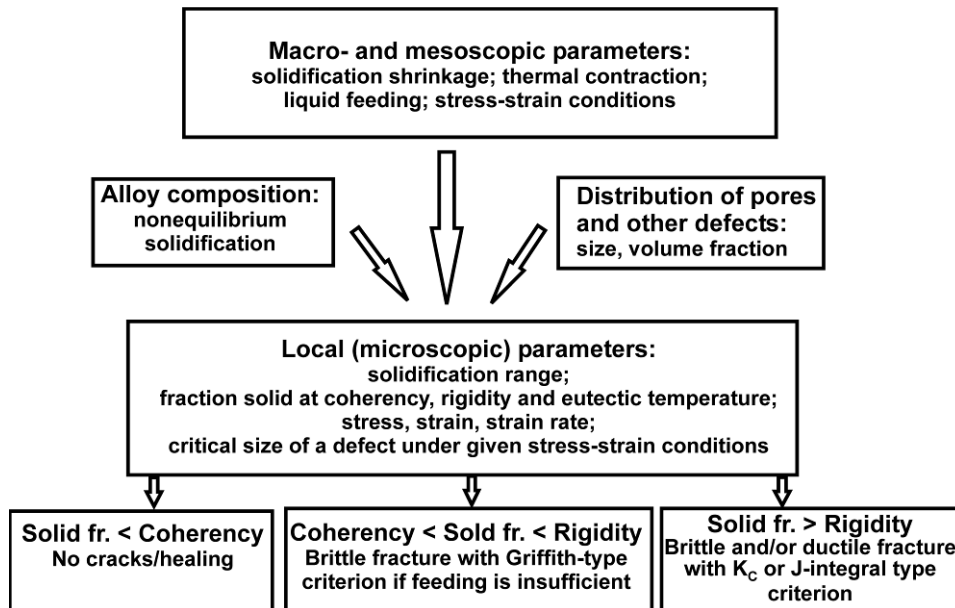


Fig. 1.6 A flowchart showing how the material is prone to cracking at different stages of solidification [14].

1.3 Cold Cracking

The most serious casting defect arisen in DC-casting of high strength aluminum alloys is cold cracking resulting in considerable scraping in aluminum industry (Fig. 1.7). Based on the shape of the crack and the location at which they appear, cold cracks may be classified as either trouser or J-cracks (Fig. 1.8).

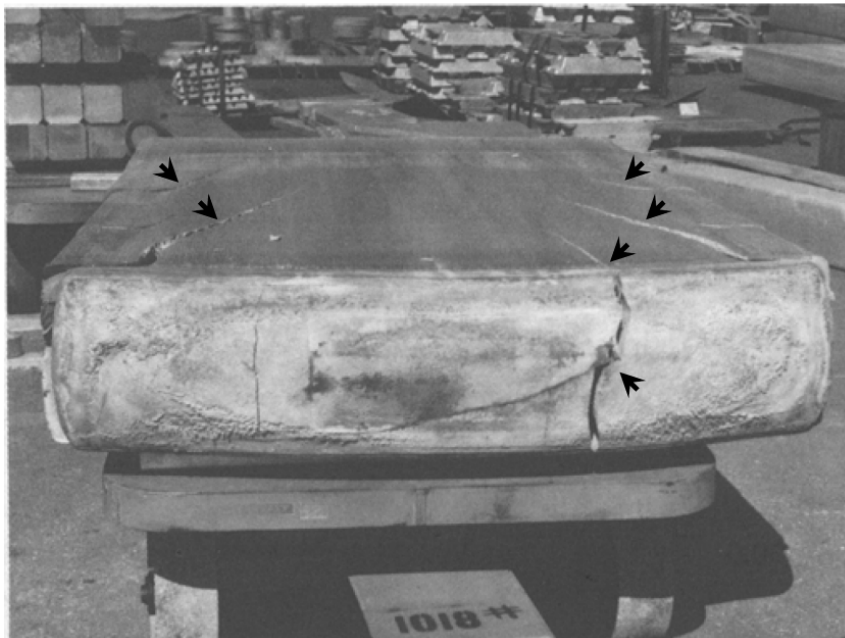


Fig. 1.7 A 0.4 m × 1.5 m DC-cast ingot of a typical 7xxx alloy that cold-cracked after completion of casting [22].

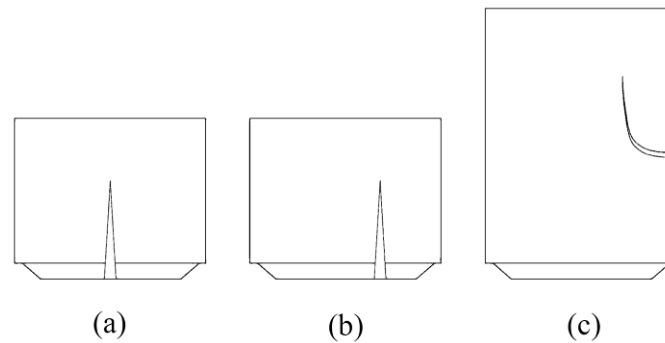


Fig. 1.8 various types of cold cracks: (a) and (b) trouser cracks, and (c) J-crack [10].

In the earliest literature [11] cold cracks were identified as being the result of high thermal stresses in the solid metal that initiate on a defect such as an inclusion or a microcavity. Later investigations revealed that the brittleness of the high strength heat treatable alloys (2xxx and 7xxx series) in the as-cast condition facilitates the cracking and failure of the material [22]. Microsegregation that occurs in the course of freezing results in the individual grains being substantially enveloped by divorced eutectics of brittle intermetallic phases. The low strength of these grain boundary networks compared to the grain bodies, can cause them to fracture under the thermal stresses [22]. A lot of research has been performed on hot cracking [23] and some criteria have been proposed in this regard [24-27]. Less work has been performed on cold cracking, although some criteria have been proposed [11, 28-31]. Some of these criteria are based on experimental results [11, 28, 31] while others apply the thermomechanical simulation results to the fracture mechanics concepts [29,30]. Experimentally derived criteria have been based on the results of numerous cast trials under various casting conditions and ingot geometries. Livanov [11] e.g., learned from numerous experiments that to prevent hot cracks in slabs the cast speed should be lowered while he advised higher cast speeds to avoid cold cracks (Figs. 1.9a and b). Experimentally derived equations and graphs could eventually indicate the proper casting speed for the corresponding slab thickness, although casting of slabs thicker than a certain value appeared not to be feasible (b_2 in Fig. 1.9a). As seen in Fig. 1.9a, above curve 1 hot cracks and below curve 2 cold cracks are formed. Fig. 1.9b shows similar curves for various width to thickness ratios (multiplicity). In another criterion, Livanov *et al.* proposed that cold cracking does not occur when the tensile elongation of the material exceeds 1.5% [31]. As performing so many experiments costs a lot of time, energy and money, they have been preferably replaced by thermomechanical simulations. Thermomechanical simulations can reveal the state of residual thermal stresses in billets/ingots during and after the DC-casting process. According to the fracture mechanics, catastrophic failure occurs when a crack or flaw (Fig. 1.10) reaches a critical length in the presence of a tensile stress field. With right selection of the crack geometry, the critical crack size leading to catastrophic failure can be calculated. The constitutive parameters as well as mechanical properties used for such thermomechanical simulations were obtained from stress relieved [32] or homogenized DC-cast billets [33]. Further studies on mechanical properties of the high strength aluminum alloys in the genuine as-cast condition have revealed however that such properties are considerably different from the stress relieved or homogenized states [34]. Application of the as-cast constitutive parameters, mechanical properties and plane strain fracture toughness (K_{Ic}) values can lead to

more realistic simulation results and eventually more reliable critical crack sizes may be assessed.

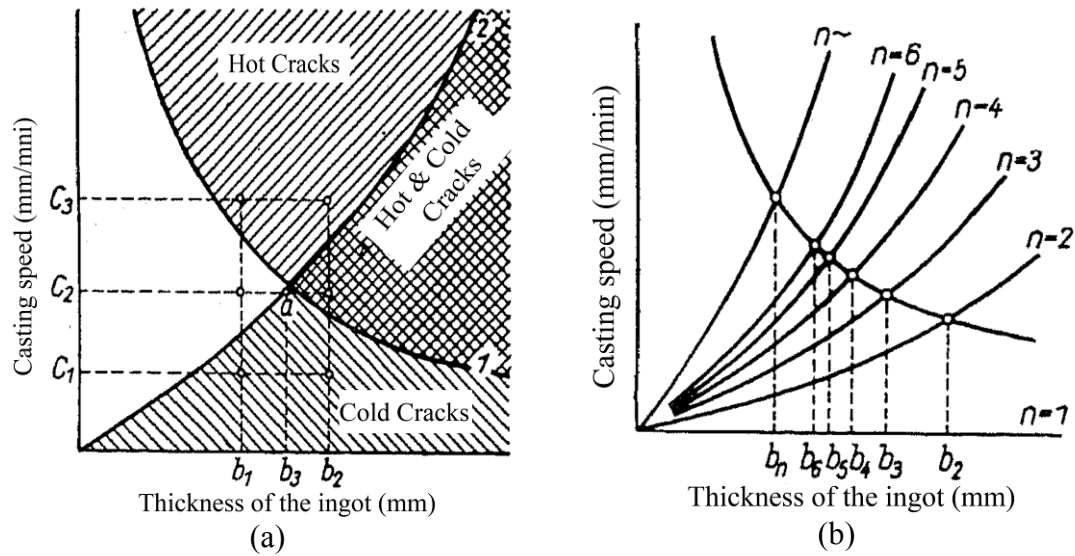


Fig. 1.9 The diagram of correlation between the thickness of an ingot and the casting speed and susceptibility to crack formation: (a) constant multiplicity, (b) different multiplicities [11].

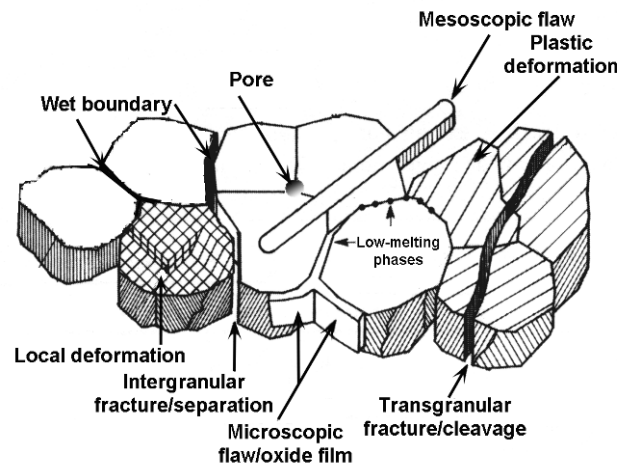


Fig. 1.10 Possible initiators and propagation paths for cracking [20, 35].

1.4 Technical approaches to preventing cold cracking

Along with trials for establishment of a criterion for cold cracking, some technical approaches have been also exercised to prevent cold cracking and catastrophic failure of high strength aluminum alloys. As non-homogenous distribution of thermal stresses in the ingot is assumed to be responsible for cold cracking and failure of the DC-cast ingots, the most practical approach to reduce their harmful effect is to anneal the ingots at temperatures around 400°C for couple of hours immediately after casting. Although such an approach can not suppress cracking during the DC casting process, it can prevent the catastrophic failure of the ingots during the sawing attempt [30]. The more efficient way of reducing thermal stresses in the ingots is to milden the temperature gradients during the DC-casting process [36-38]. Ingot wipers were

designed to control cold cracking by removing coolant from the ingot surface and reducing the temperature gradients below the wiper plane [37] (Fig.1.11).

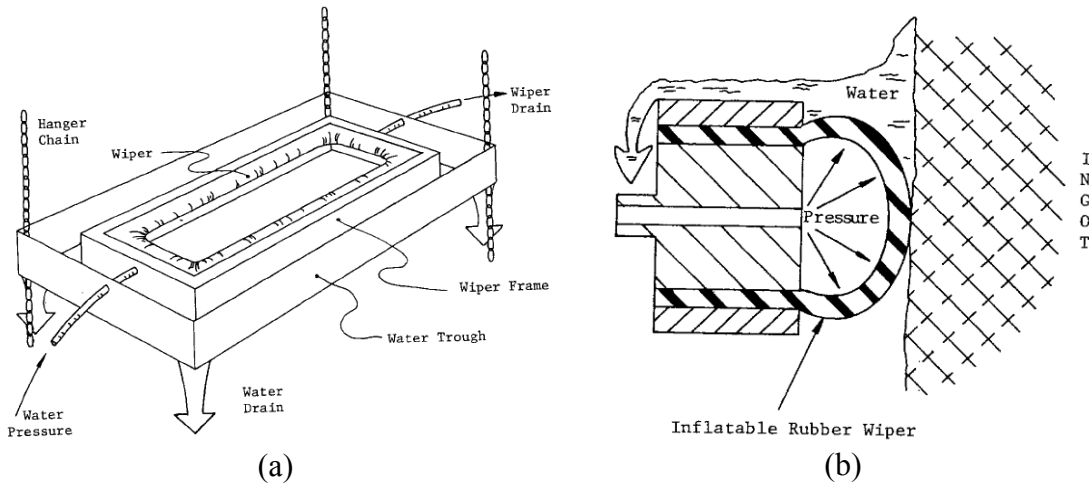


Fig. 1.11 Schematic view of the wiping process: a) the inflatable wiping system, b) cross section of the inflatable ingot wiper. The inflatable portion of the wiper is made of tough heat and wear resistant rubber which can survive molten metal spills [37].

Although wipers are believed to have no benefit for controlling hot tearing, they can eliminate cold cracking by relieving the stresses built up after solidification, thus large ingots of crack sensitive 2xxx and 7xxx series alloys become castable.

Another approach to reduce the thermal stresses in the ingots is to use electromagnetic casting (EMC) [31,39,40]. The EMC process is a method through which DC ingots are cast without any mechanical contact between the metal and the mold. The liquid metal is confined only by an electromagnetic field generated by an inductor which is a part of the mold [39]. Yubo *et al.* showed that under low frequency electromagnetic field, the temperature gradients in the melt are more uniform and the sump depth is lower which results in lower internal stresses compared to conventional DC-cast ingots [40]. More uniform macro-distribution of elements in EMC casting leads to more uniform microstructure, decreases the grain as well as constituent size, and area fraction of grain boundary eutectics, which is helpful in thinning the liquid film and improving high temperature plasticity and strength.

In spite of all scattered works and criteria, cold cracking still remains a challenge in aluminum industry; and ingots of newly developed high strength aluminum alloys crack during the DC-casting process or afterwards during the sawing attempt. The failure of the ingots not only results in their scrapping but it is also a danger to the personnel of the cast house. Hence, detailed study of the cold cracking phenomenon sounds necessary and experimental techniques as well as computer simulations may assist such a research. However, the mechanical properties, constitutive parameters and plane strain fracture toughness values in the genuine as-cast state that are essential for computation of residual thermal stresses and assessment of critical crack size are seldom available. The crack initiation and propagation mechanism as well as crack propagation paths are not well understood. The effect of casting variables such as casting speed and billet size on the magnitude, distribution and orientation of residual thermal stresses is not well understood yet. Finally, it is not known how the as-cast microstructure of the material may assist the brittle fracture of the ingot. The current thesis is written with the aim to scrutinize the cold cracking phenomenon and answer the questions arisen above as much as possible.

1.5 Outline of the thesis

As mentioned previously, this research is performed to fill the gap in understanding cold cracking in solidification processing of aluminum industry that has been existing for decades. An AA7050 alloy with wide industrial applications was selected for this purpose. Mechanical behavior of the AA7050 alloy cast under various casting conditions were studied in the genuine as-cast condition through mechanical tests. From the true stress-strain curves constitutive parameters and mechanical properties were determined afterwards. Databases were made for mechanical properties gained from tensile tests and physical properties gained from thermodynamic database JMat-Pro (provided by Corus IJmuiden) for the as-cast material to be applied in computer simulations. Thermomechanical behavior of the material was then simulated using the finite element package ALSIM5. By application of the maximum principal stress component obtained from simulations to fracture mechanics criteria the critical crack size leading to catastrophic failure of the billets was assessed. The outline of the thesis is as follows:

In Chapter 2, thermomechanical properties of the AA7050 alloy cast under various conditions in a copper mold were studied. The objective was to understand the effect of grain refinement and cooling rate on mechanical properties. AA7050 samples were also gained from a DC-cast billet for determination of the constitutive parameters and mechanical properties of the material cast under industrial conditions. Mechanical properties and constitutive parameters of the material were determined in the solid state from room temperature to 400 °C at strain rates corresponding to those arisen in DC-casting process. Young's modulus of the material was measured over a similar temperature range. Plane strain fracture toughness tests were performed to measure the K_{Ic} values from room temperature to 200 °C.

In Chapter 3, the nonequilibrium solidus and liquidus were determined through Differential Scanning Calorimetry (DSC) tests. Thermal contraction behavior of the AA7050 alloy was studied. Linear solidification contraction tests were performed to determine the onset of thermal contraction and rigidity temperature of the alloy. Eventually, the dilatometry tests were done to measure the coefficient of thermal expansion/contraction of the alloy under discussion.

In Chapter 4, microstructural features of intergranular brittle fracture and cold cracking in AA7050 alloy were studied. In-situ tensile tests were performed to follow the crack propagation path at room as well as an elevated temperature. Results were compared to the fractographs of a real cold crack AA7475 billed for further discussions.

In Chapter 5, Finite Element Simulations (FEM) were run using ALSIM5 and the state of residual thermal stresses were determined for the AA7050 alloy under the steady state casting conditions. The contour maps of the residual stresses and strains were interpreted to be able to understand the conditions leading to materials failure.

In Chapter 6, evolution of the residual thermal stresses in a AA7050 DC-cast billet was studied after the end of casting when the billet cools down to room temperature. Critical crack sizes leading to catastrophic failure were assessed for the temperatures and locations where the maximum principal stress reaches its highest value.

In Chapter 7, the effect of casting variables on the magnitude, distribution and orientation of residual thermal stresses was studied. Casting speed, billet size, water flow rate, water temperature, cast temperature, and casting time were the selected variables. For each case, FEM simulations were run for sufficient time to reach steady state and the thermal stresses were recorded. Cold cracking propensity of the billets under various casting conditions was determined and the most affecting variables are shown.

In Chapter 8, the procedure mentioned in chapters 2 and 7 was followed for a newly developed 7xxx series alloy that is highly prone to cold cracking. Constitutive parameters, mechanical properties, and K_{Ic} values were determined through experiments. FEM simulations were performed then to reveal the state of residual thermal stresses in the billets during the DC-casting. DC-casting trials were performed under similar conditions as in simulations and the effects of casting speed, billet size and water flow rate were determined. Eventually, the calculated critical crack sizes were compared to the actual ones that resulted in catastrophic failure during the DC-casting trials.

References

- [1] W. Roth, *Zeitschrift für Metallkunde* 40 (1949) 445-460.
- [2] E. F. Emley, *Int. Met. Rev.* 21 (1976) 75-115.
- [3] J.F. Grandfield, P.T. McGlade, *Mater. Forum* 20 (1996) 29-51.
- [4] Q. Han, S. Viswanathan, D.L. Spainhower, S.K. Das, *Metall. Mater. Trans. A* 32 (2001) 2908-2910.
- [5] N. Ishikawa, *Furukawa Review* 28 (2005) 46-52.
- [6] H. G. Fjær, A. Mo, *Metall. Trans. B* 21 (1990) 1049-1061.
- [7] B. Hannart, F. Cialti, R. van Schalkwijk, in: U. Mannweiler (Ed.), *Light Metals*, TMS, 1994, pp. 879-887.
- [8] J.-M. Drezet, M. Rappaz, *Metall. Mater. Trans. A* 27 (1996) 3214-3225.
- [9] K.-M. Chang, B. Kang, *J. Chin. Inst. Eng.* 22 (1999) 27-42.
- [10] W. Boender, A. Burghardt, E.P. van Klaveren, J. Rabenberg, in: A.T. Tabereaux (Ed.), *Light Metals 2004*, TMS, Warrendale (PA), 2004, pp. 679-684.
- [11] V.A. Livanov, in: A.F. Belov, G.D. Agarkov (Eds.), *Aluminum Alloys*, Oborongiz, Moscow, 1955, pp.128-168.
- [12] W. Schneider, *Aluminium* 82 (2006) 682-687.
- [13] W. Schneider, W. Droste, in: E.L. Rooy (Ed.), *Light Metals*, TMS, 1991, pp. 945-952.
- [14] D.G. Eskin, L. Katgerman, *Metall. Mater. Trans. A* 38 (2007) 1511-1519.
- [15] J. Campbell, *Castings*, Butterworth-Heinemann, Oxford, United Kingdom, 2003.
- [16] U. Chandra, A. Ahmed, in: Kuang-O Yu (Ed.), *Modeling for Casting and Solidification Processing*, Marcel Dekker Inc., New York, 2002, pp. 55-93.
- [17] I. Farup, *Thermally Induced Deformations and Hot Tearing During Direct Chill Casting of Aluminum*, PhD thesis, University of Oslo, Norway, 2000.
- [18] C. S. Wu, *J. Mater. Sci.* 23 (1988) 606-610.
- [19] S. Benum, D. Mortensen, H. Fjær, H.-G. Øverlie, O. Reiso, in: W. Schneider (Ed.), *Light Metals*, TMS, 2002, pp. 967-974.
- [20] D.G. Eskin, *Physical Metallurgy of Direct Chill Casting of Aluminum Alloys*, CRC Press, New York, 2008.

- [21] Suyitno, Hot Tearing and Deformation in Direct Chill Casting of Aluminum Alloys, PhD thesis, Delft University of Technology, The Netherlands, 2005.
- [22] J. B. Hess, *Metall. Trans. A* 14 (1983) 323-327.
- [23] D. G. Eskin, Suyitno, L. Katgerman, *Prog. Mater. Sci.* 49 (2004) 629-711.
- [24] T.W. Clyne, G.J. Davies, *Br. Foundryman*, 74 (1981) 65-73; *Br. Foundryman*, 68 (1975) 238-244.
- [25] M. Rappaz, J.-M. Drezet, M. Gremaud, *Metall. Mater. Trans. A* 30 (1999) 449-455.
- [26] D.J. Lahaie, M. Bouchard, *Metall. Mater. Trans. B*, 32 (2001) 697-705.
- [27] M. M'Hamdi, A. Mo, H.G. Fjær, *Metall. Mater. Trans. A* 37 (2006) 3069-3083.
- [28] K. Matsuda, S. Nagai, Y. Miyate, H. Maehara, I. Tsukuda, in: 6th International Aluminum Extrusion Technology Seminar, Aluminium Association and Aluminium Extruder's Council, vol. I, Chicago, Illinois, USA, 1996, pp. 525-528.
- [29] W. Boender, A. Burghardt, in: H. Jones (Ed.), 5th Decennial Int. Conf. on Solidification Processing, University of Sheffield, Sheffield (UK), 2007, pp. 714-718.
- [30] O. Ludwig, J.-M. Drezet, B. Commet, B. Heinrich, in: C-A. Gandin, M. Bellet (Eds.), *Modeling of Casting, Welding and Advanced Solidification Processes XI*, TMS, Warrendale (PA), 2006, pp. 185-192.
- [31] V.A. Livanov, R.M. Gabidullin, V.S. Shipilov, *Continuous Casting of Aluminum Alloys*, Metallurgiya, Moscow, 1977, p. 90.
- [32] K.-M. Chang, H.-M. Lu, J. Wan, J.F. Harris, in: *Second Intern. Conf. on Quenching and the Control of Distortion*, ASM International, Ohio, 1996, pp. 341-345.
- [33] J. Wan, H.-M. Lu, K.-M. Chang, J. Harris, in: B. Welch (Ed.), *Light Metals 1998*, TMS, Warrendale, 1998, pp. 1065-1070.
- [34] M. Lalpoor, D.G. Eskin, L. Katgerman, *Proc. 12th Intern. Conf. on Fracture*, Ottawa, National Research Council of Canada, 2009 (CD).
- [35] M. Janssen, J. Zuidema, R.J.H. Wanhill, *Fracture Mechanics*, 2nd ed., Delft University Press, Delft, The Netherlands, 2002.
- [36] A.T. Taylor, D.H. Thompson, J.J. Wegner, *Met. Prog.* 72 (1957) (5) 70-74.
- [37] J.L. Dassel and T.C. Zinniger, in: *Light Metals*, Dallas, 1982, pp. 793-801.
- [38] US Patent. No. US2007/0102136 A1, United States, 2007.
- [39] K. Buxmann, in: K. Hirano, H. Oikawa, K. Ikeda (Eds.), *Science and Engineering of Light Metals*, Japan Institute of light Metals, Tokyo, 1991, pp. 1015-1022.
- [40] Z. Yubo, C. Jianzhong, Z. Zhihao, Z. Haitao, Q. Ke, *Mater. Sci. Eng. A* 406 (2005) 286-292.

Chapter 2

Thermomechanical behavior of 7xxx series aluminum alloys in the as-cast condition

Finding a criterion for cold cracking during direct-chill (DC) casting of high-strength aluminum alloys sounds quite necessary for aluminum industry. The first step in achieving such a goal is determination of the mechanical behavior of material in the genuine as-cast condition through mechanical tests and thermomechanical simulations. However, lack of experimental information on the fracture mode and temperature dependence of mechanical properties as well as constitutive parameters of such alloys in the as-cast condition (without any homogenization or stress relieving) makes computer-simulation results unreliable. Mechanical tests on AA7050 alloy (a typical high strength aluminum alloy) cast under various conditions revealed that such alloys lose their ductility sharply as the temperature falls and fail in inter/transdendritic mode. Formation of pores and micro-cracks especially at the matrix–intermetallics interfaces apparently results in brittleness of the material in the as-cast condition. DC-cast AA7050 samples gained from various locations of a DC-cast billet were also used to study the mechanical behavior and to determine the constitutive parameters of the alloy in the as-cast condition. Charpy impact toughness and plane strain fracture toughness tests were performed to understand the fracture behavior of the material below solidus. Eventually, K_{Ic} values were measured from room temperature to 200 °C.

2.1 As-cast mechanical properties of the AA7050 alloy cast in a copper mold

2.1.1 Introduction

As mentioned in the previous chapter, non-homogenous cooling rates and solidification conditions during the DC-casting process can result in appearance and accumulation of thermal stresses [1-3]. Further increase of thermal stresses in the solid state accompanied by weaker mechanical properties of the alloy in certain temperature ranges may lead to crack propagation and catastrophic failure [4]. DC-cast ingots can fail by either of two mechanisms; i.e. cold or hot cracking. In both

cases, non-uniform contraction in the ingot sets up stresses and strains, which the ingot must accommodate to remain sound. In contrast to pre-solidification cracks (hot cracks), which form at temperatures above the solidus, post-solidification cracks (cold cracks) propagate in the fully solid material [5]. Cold cracks can damage the entire ingot by splitting it open, which results in complete scrapping of the ingot. Cold cracking is characteristic of alloys which are brittle in the as-cast condition. These alloys (mainly high strength Al-alloys) are apparently unable of withstanding high stresses generated during DC casting [6]. In order to study cold cracking phenomenon in more detail, sufficient information on mechanical properties of such alloys in the as-cast condition (without stress relieving and homogenization) is required.

The data on these properties however are seldom available in the literature. The alloys in question are wrought alloys and most of the tests are performed on wrought products after deformation and heat treatment [7]. Scattered information is available on the properties of ingots, but then only after homogenizing [8] or stress-relief anneals [9]. There are some general dependences that are adopted as well known. For example, the gradient of cooling during DC casting and the different thickness of the transition (liquid–solid) region across the ingot cross section result in the variation of structure (grain size, dendrite arm spacing, fraction and size of constitutive particles), composition (macrosegregation) and defects (porosity) [10]. These inhomogeneities produce different mechanical properties in different ingot sections [3], and may cause different susceptibility of the material to cracking. The inhomogeneous distribution of properties however, does not necessitate cracking and failure of the ingot. Livanov *et al.* suggested that cold cracking does not occur if the room-temperature tensile elongation of the as-cast material exceeds 1.5% [11]. But, this represents a rule of thumb based on vast industrial experience rather than a scientifically-based criterion. Another example of seemingly well accepted viewpoint is the negative influence of impurities such as silicon and iron on ductility. It is usually recommended to decrease the amount of impurities in high-strength alloys in order to improve their toughness [12,13]. Some experimental results at the same time show that a high-purity 7010 alloy (precipitation hardened) has poorer high-temperature ductility and is more prone to cold-cracking [14], or an increased amount of Si in a 7050 alloy produces higher room-temperature ductility and less cold cracking [15].

It is clear that there is a lack of experimental data on the mechanical properties of as-cast high-strength wrought alloys, especially in a range of temperatures and strain rates relevant to DC casting. This chapter is the first step in bridging this gap. The results are reported on mechanical properties of as-cast 7xxx series alloys in a wide range of subsolidus temperatures. The structure and fractures are examined in an attempt to interpret the results of mechanical testing.

2.1.2 Experimental procedure

One of the objectives of the study was to evaluate the effect of different metallurgical and structural factors on mechanical properties of the as-cast alloy. The metallurgical factors were metal purity in terms of chemical composition and inclusions, and porosity. The structural factors were grain size and dendrite arm spacing. As the properties are determined on samples with the quantified structure, the technological route of preparing the samples is not significant. Therefore, we used samples from alloys produced using different casting techniques in order to extend the variation

range of metallurgical and structural parameters. Two groups of samples used in this research work are as follows (see Table 2.1):

- 1) AA7050 alloy cast in a copper mold with 6 cylindrical cavities 20 mm in diameter and 320 mm in length. Four groups of samples were prepared as listed in Table 2.1. Aluminum of different initial purity was taken as a starting material (Low Purity (LP): 99.7% Al; High Purity (HP): 99.95% Al), further Al–47.7% Cu, Al–25.1% Mg, Al–5.8% Zr master alloys and pure Zn were used for preparing two groups of alloys designated as LP and HP. As one can see from Table 2.1, the concentrations of impurities, i.e. Fe and Si, in LP and HP alloys are very close to each other (they must have been provided by master alloys). The molten alloys were cast at 720 °C without degassing treatment in the said mold that was either preheating (HM) or cooled (CM), or kept at a room temperature (GR, NG). The cylindrical mold cavities were filled manually and successively. One alloy modification was grain refined (GR) with an Al–3% Ti–1% B master alloy.
- 2) AA7050 billet (Ø 255 mm) produced through DC casting with a conventional mold from the melt that was degassed in the furnace and supplied by Corus-Netherlands (IJmuiden) (7050 (DC cast) in Table 2.1).
- 3) AA7475 billet (Ø 200 mm) produced by a third party and cold cracked at the sawing attempt.

Table 2.1 Chemical composition of the tested alloys [16].

Alloy [†]	Alloying elements (wt %)								
	Zn	Mg	Cu	Zr	Cr	Mn	Ti	Fe	Si
7050-HP-NG	6.1	2.0	2.5	0.091	<0.01	<0.01	<0.01	0.19	0.06
7050-HP-GR	6.1	2.0	2.6	0.089	<0.01	<0.01	0.03	0.20	0.07
7050-LP-HM	6.0	1.9	2.4	0.1	<0.01	<0.01	<0.01	0.16	0.04
7050-LP-CM	6.0	2.0	2.4	0.1	<0.01	<0.01	<0.01	0.16	0.04
7050 (DC cast)	6.3	2.42	2.49	0.098	<0.01	0.04	0.03	0.07	0.04
7475 (DC cast)	5.46	2.52	1.74	–	0.20	0.025	0.057	0.09	0.06

Tensile mechanical properties of the as-cast 7050 samples cast in the copper mold were measured using a Gleeble-1500 thermomechanical simulator. Samples with the design shown in Fig. 2.1 were heated through the Joule effect at a rate of 10 °C/s, kept for 10 seconds and then uniaxially deformed at three strain rates of 10^{-2} , 10^{-3} and 10^{-4} s⁻¹. The range of strain rates was chosen to resemble those typical of DC casting [17]. A K-type (Chromel–Alumel) thermocouple was used to monitor the temperature in the middle of the gage length, while the changes in diameter were monitored simultaneously using an extensometer. Mechanical properties were measured from room temperature to 400 °C at 100 °C steps. Three to five samples were tested for each specific temperature and strain rate combination, and the average values are reported. Fig. 2.2 shows schematically how the sample is mounted in the machine and the location of the extensometer and the thermocouple.

[†] HP-NG: non-grain refined; HP-GR: grain refined; LP-HM: cast in hot mold; LP-CM: cast in cold mold.

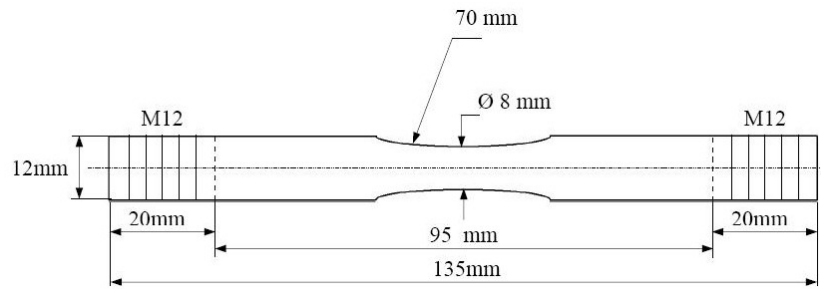


Fig. 2.1 Geometry of a tensile specimen used in Gleeble tests [16].

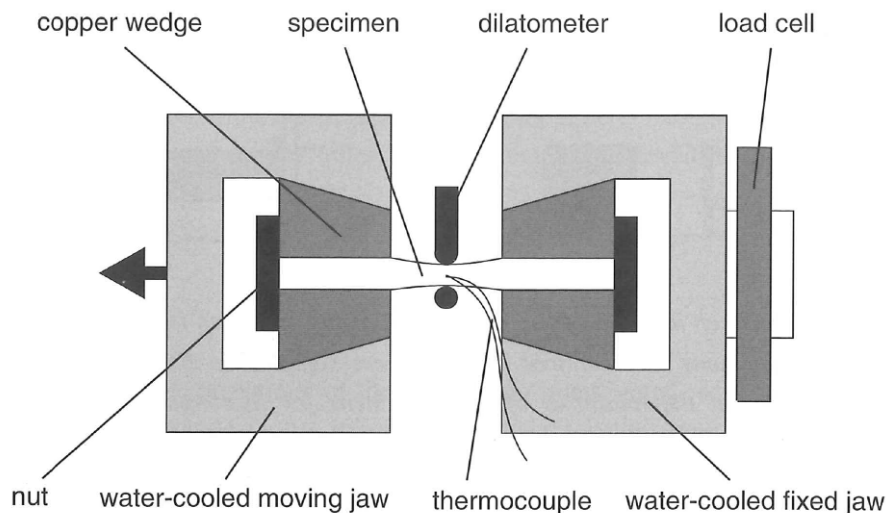


Fig. 2.2 Schematic view of the experimental setup [17].

Grain size and dendrite arm spacing were measured based on ASTM-E112 [18]. For this purpose samples were polished using diamond suspensions (up to 1 μm) and then anodized in a diluted solution of HBF_4 acid (3%) in distilled water. Grains were then revealed using polarized light in an optical microscope Neophot 30. A scanning electron microscope Jeol JSM-6500F (SEM) and the optical microscope (OM) were used for fractographical observations. Qualitative and quantitative chemical compositions of the phases present in the microstructure and those on the fracture surfaces were estimated using backscattered electron detector (BSE) and energy-dispersive X-ray spectroscopy (EDX) in the SEM.

To study the effect of porosity on mechanical properties, specific gravity measurements were performed based on Archimedes' principle. Weighing in air and distilled water was used. The reference sample was cut from the 7050 DC cast billet at half-radius position where the porosity due to the cooling conditions and melt degassing was negligible. With this reference, the porosity percentage in other samples was then calculated. Another factor affecting the mechanical properties could be the volume fraction of the non-equilibrium phases. To measure this quantity, electron backscattered images of the samples were analyzed by the image analysis software Image J.

2.1.3 Results

2.1.3.1 Mechanical tests

The true stress-strain curves of 7050-LP-CM samples deformed at five temperatures under a strain rate of 10^{-4} s^{-1} are shown in Fig. 2.3. As temperature falls below 400 °C, the material starts to behave more brittle and shows less ductility. The alloy loses its ductility below 200 °C and fails in a brittle manner, which is accompanied by a higher fracture strength. The yield (fracture) strength reaches 245 MPa at room temperature (in agreement with the results of Miklyaev [19]) and falls to 15 MPa as the temperature increases to 400 °C.

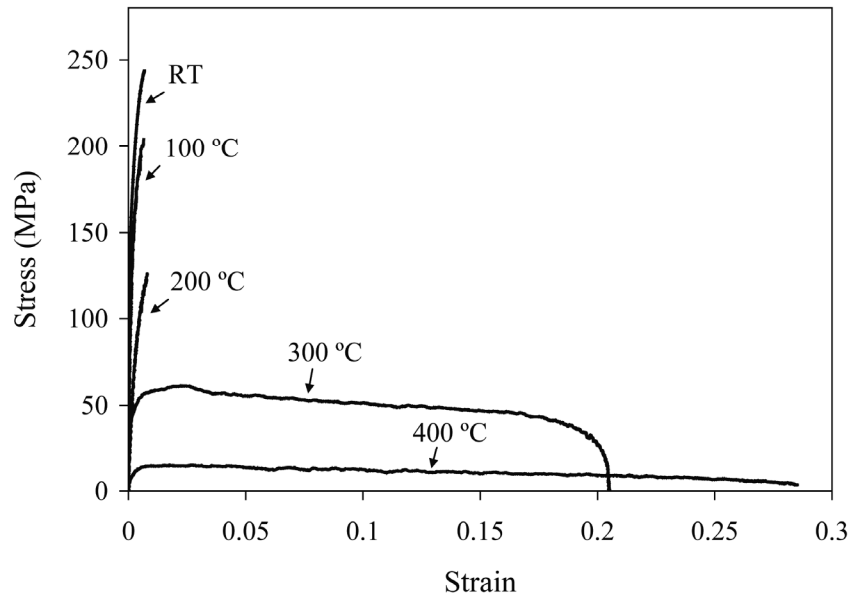


Fig. 2.3 Examples of true stress–strain curves for 7050-LP-CM samples tested at different temperatures at a strain rate of 10^{-4} s^{-1} . Similar trends were observed for the other groups of tested alloys [16].

Figs. 2.4a and 2.4b show the effect of temperature on yield strength and ductility (% reduction of area) of 7050 samples cast in the copper mold, respectively. Similar behavior is observed, with the material becoming quite brittle at temperatures below 200 °C. The yield strength increases as the temperature decreases in either linear manner or passes through a maximum at 100 °C. It can also be derived that structure differences induced by composition or solidification conditions become more important for strength and high-temperature ductility at lower temperatures, where the difference in the results between different alloys arises. It can be also concluded that the alloys cast in the cold mold (LP-CM) and grain refined (HP-GR) possess better mechanical features than other tested alloys from this group.

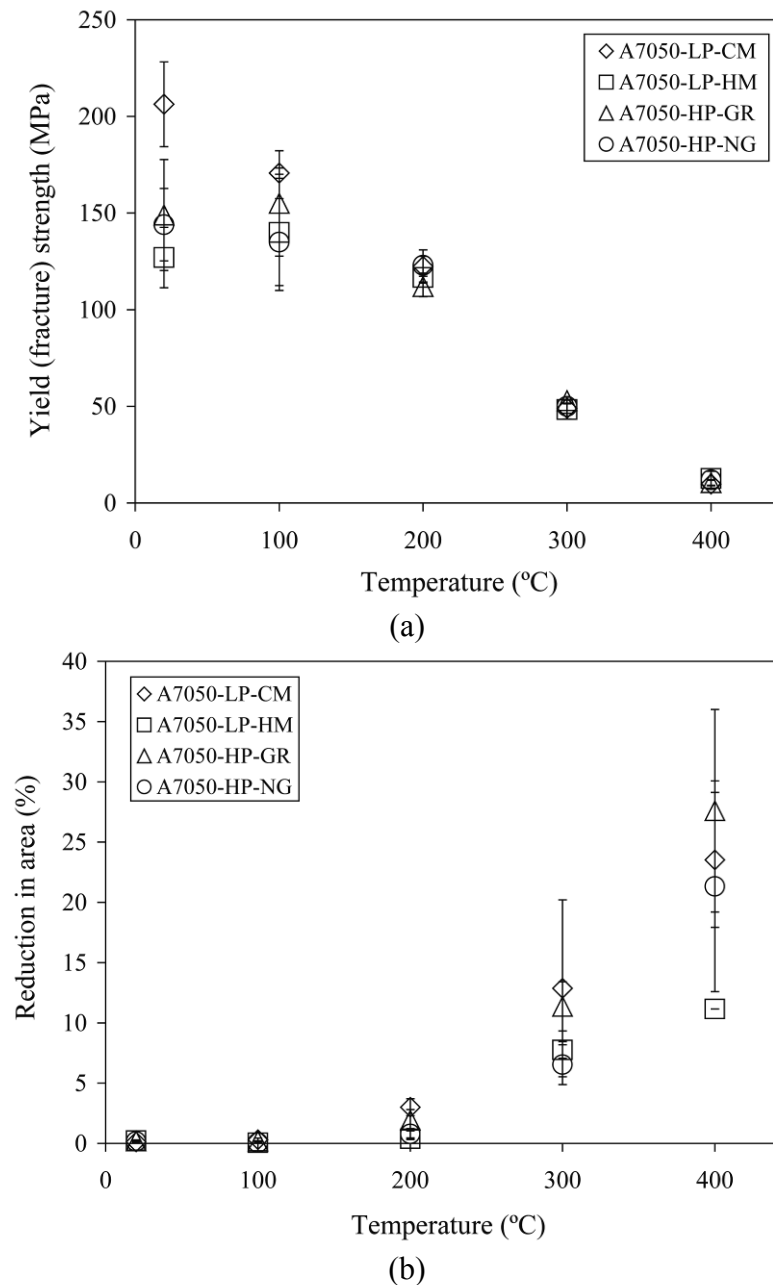


Fig. 2.4 Mechanical tests results for the 7050 samples cast in the copper mold (see Table 2.1): (a) average yield (fracture) strength at different temperatures and at a strain rate of 10^{-4} s^{-1} . (b) Average reduction in area at different temperatures at a strain rate of 10^{-2} s^{-1} [16].

Figure 2.5a shows the effect of strain rate on the shape of the true stress-strain curves at 400 °C. As can be seen from this figure, with decreasing strain rate the material behaves more ductile and has a lower yield strength. The effect of strain rate on yield (fracture) strength of the 7050-LP-CM alloy is shown in Fig. 2.5b. At high temperatures (300 and 400 °C) the yield strength increases as the deformation rate increases, but at lower temperatures (beginning at 200 °C) the material behavior becomes either strain-rate independent or with increasing the strain rate the material fails at lower stresses, before reaching the yield point.

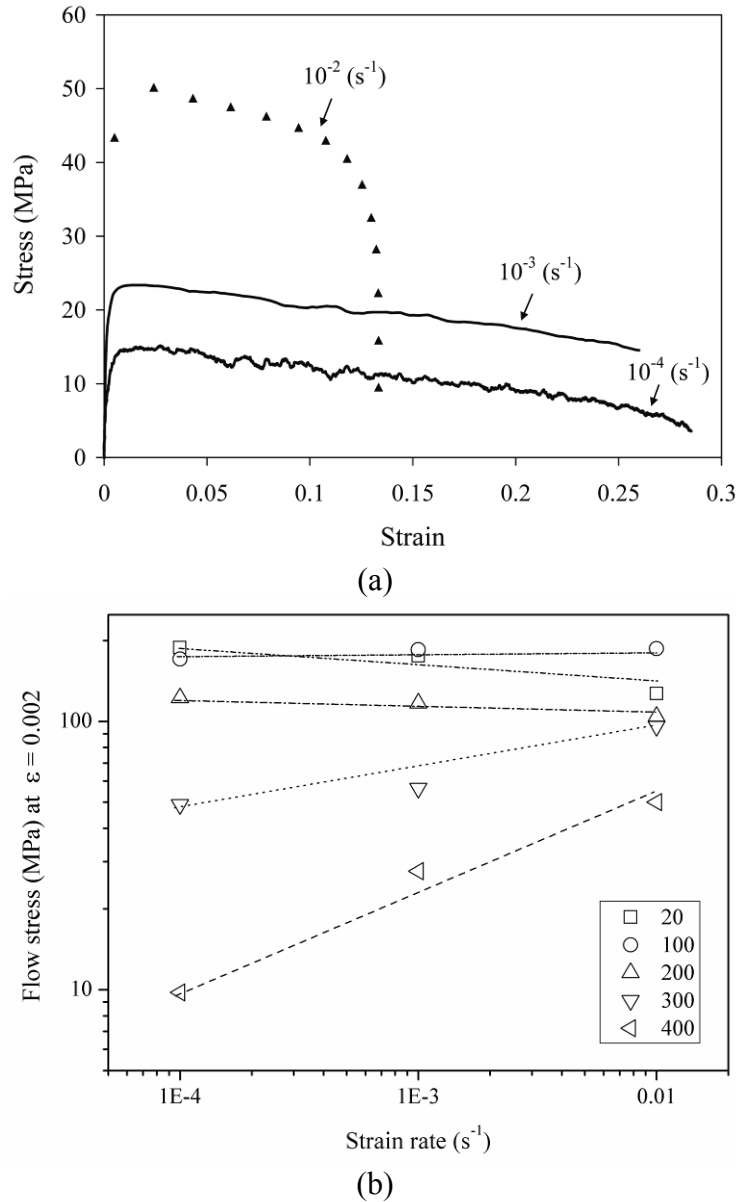


Fig. 2.5 (a) Examples of true stress–strain curves for 7050-LP-CM samples tested at different strain rates at 400 °C. Similar trends were observed for the other groups of tested alloys, (b) Effect of strain rate on the yield (fracture) strength for 7050-LP-CM samples tested at different temperatures [16].

2.1.3.2 Structure examination

The microstructure of the AA7050 alloy consists of the α -aluminum phase (a solid solution of Zn, Cu, and Mg in Al) as the matrix and non-equilibrium eutectics represented by a mixture of T (Al_6CuMg_4 and $\text{Al}_2\text{Mg}_3\text{Zn}_3$), M (AlCuMg and MgZn_2) and S (Al_2CuMg) phases [20] (Fig. 2.6a). Such phases are non-equilibrium phases that form as a result of relatively high solidification rates present under practical casting conditions. Constituent phases ($\text{Al}_7\text{Cu}_2\text{Fe}$ and Mg_2Si) formed during solidification as a result of presence of impurities can also be found, but they can hardly be detected in the as-cast microstructure. Figs. 2.6b, c show SEM micrographs of such phases, and their estimated chemical compositions are given in Table 2.2. EDX analysis revealed

that under non-equilibrium casting conditions up to 2 wt% Mg, 1.2 wt% Cu, 3 wt% Zn and 0.03 wt% Fe can be dissolved in the matrix. Microcracks and flaws can be observed inside some of intermetallic particles as well as at the matrix–eutectic interface (Fig. 2.6d).

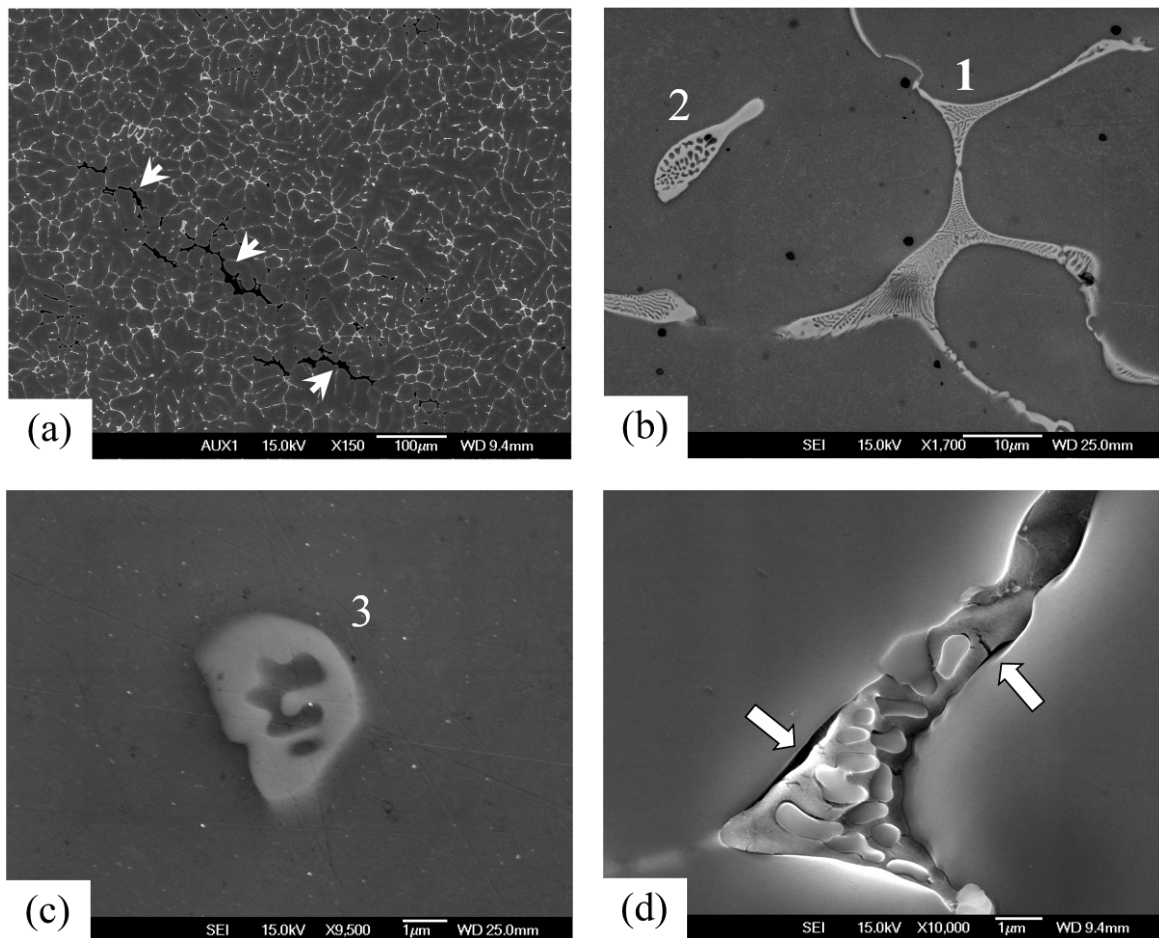


Fig. 2.6 (a) Electron backscattered image showing the microstructure of the 7050-LP-CM which is typical of all alloys cast in copper mold (see Table 2.1), arrows show the shrinkage porosities formed during solidification; (b and c) non-equilibrium phases found in the as-cast microstructure of 7050 alloys (DC-cast), estimated chemical composition of the phases marked by numbers on the images are shown in Table 2.2, and (d) microcracks/flaws at the interface of the α -aluminum matrix and non-equilibrium eutectics, and inside a eutectic constituent in a 7050-LP-CM sample. SEM images [16].

Quantitative metallographic results are shown in Table 2.3. As can be seen the samples cast in the hot mold have the largest grain size and dendrite arm spacing due to slower cooling rate. A greater dendrite arm spacing in grain refined samples can be the result of poorly developed dendritic structure where the grain size is four times refined.

Porosity and density values for all 7050 alloys cast in the copper mold are listed in Table 2.3 (with the 7050 (DC cast) alloy taken as reference). As it can be seen, the scattering in the results is high which is the result of the uncertainty of the tests on the one hand and the random size and distribution of the pores on the other hand. In spite of this, samples cast in the cold mold appear to have less porosity and the deviation from the mean value is also smaller.

Table 2.2 Measured chemical composition of non-equilibrium structure constituents present in a 7050 alloy [16].

Phase (see number in Fig. 2.6)	Element, wt %				
	Mg	Cu	Zn	Fe	Al
1	12	19	19.5	0.01	Balance
2	18	26.5	26	0.01	Balance
3	14	22	22	0.1	Balance

Table 2.3 Structure parameters of the tested alloys [16].

Alloy	Grain size (μm)	Dendrite arm spacing (μm)	Density (g/cm^3)	Porosity (%)	Fraction of eutectics (%)
7050-HP-NG	160 ± 8	15 ± 0.4	2.85 ± 0.02	3.6 ± 0.5	5.40 ± 0.14
7050-HP-GR	40 ± 5	19 ± 0.7	2.87 ± 0.03	3.2 ± 0.9	5.35 ± 0.11
7050-LP-HM	240 ± 9	18 ± 0.5	2.86 ± 0.02	3.3 ± 0.5	4.90 ± 0.10
7050-LP-CM	170 ± 9	17 ± 0.5	2.89 ± 0.01	2.4 ± 0.5	5.80 ± 0.08
7050 (DC cast)	–	–	2.95 ± 0.03	–	–
7475 (DC cast)	171 ± 7	20 ± 1	–	–	–

The amount of non-equilibrium constituents was measured based on image analysis of the BSE images and the results are also shown in Table 2.3. The alloy cast in the cold mold has the highest amount of non-equilibrium phases, whereas the one cast in a hot mold shows the lowest amount. Grain refinement does not appear to have a strong effect on the amount of non-equilibrium phases, and grain-refined samples possess just a little smaller amount of intermetallic particles compared to non-grain refined ones.

2.1.4 Discussion

As can be seen in Figs. 2.3 and 2.4b, from room temperature to 200 °C the fracture mode is quite brittle and no sign of plastic deformation is observed. This is where the cold cracking is likely to occur. Intergranular fracture mode with secondary cracks, pores and cleaved eutectic patches is characteristic of low-temperature mechanical behavior of tested alloys. Deviation from the equilibrium solidification path results in the formation of non-equilibrium eutectics at grain boundaries and interdendritic spaces as shown in Fig. 2.6 and Table 2.3. The non-equilibrium eutectics and brittle intermetallics may affect mechanical properties in several ways that will be discussed in detail in Chapter 4.

As mentioned in Introduction, lack of information on mechanical properties of high strength aluminum alloys in the genuine as-cast condition is a major problem in

studying cold cracking as data are available only on heat treated material. The importance of this could be understood by comparing the results gained in this research with those performed on homogenized and stress relieved samples from DC-cast billets. In samples extracted from a *homogenized and naturally aged* 7050 DC-cast billet yield strength, tensile strength and elongation followed similar temperature dependence as those observed in this study but the magnitudes of yield and tensile strength were higher at elevated temperatures and the ductility was higher at low temperatures [8]. For *stress relieved* samples extracted from another 7050 DC-cast billet [9], the yield and tensile strengths changed only slightly from room temperature up to 315 °C. The strength fell noticeably on further increasing the temperature. At the same time the ductility at temperatures below 200 °C remained rather high, which is quite different from the results gained in our study. For the ease of comparison the results derived by other researchers are shown in Table 2.4 along side the mechanical properties gained in this work.

Table 2.4 Mechanical properties of the as-cast 7050 alloy used in this study (7050-LP-CM) compared with those tested under naturally aged [8] and stress relieved [9] conditions.

Temp. (°C)	Yield (fracture) strength (MPa)					Ductility (%)				
	20	100	200	300	400	20	100	200	300	400
This study (10^{-2} s^{-1})	127 ±7	187 ±11.5	104 ±5	96 ±4.5	50 ±4	0.12* ±0.05	0.3* ±0.15	3* ±0.5	12.8* ±7.5	23.5* ±5.5
As-cast, stress relieved [9]	72	92	80	78	55	12.5**	11.5**	8**	31.5**	113.5**
As-cast, homogenised and naturally aged [8]	140	138	115	100	85	1.5**	2**	10**	12**	12**

* Reduction in area, ** Tensile elongation

These data demonstrate that stress relief results in a greater ductility and a lower yield strength. Homogenization and natural aging further deviates the properties from those of the as-cast material, making the material stronger at all temperatures and more ductile below 200 °C.

Porosity apparently may play a role at low temperatures. Porosity, which can be either due to reduced solubility of hydrogen in the metal at lower temperatures or shrinkage during solidification (Fig. 2.6a), results in scattering of mechanical properties and may cause fracture of the material before reaching the yield point. Reduced porosity in samples solidified in the cold mold can be a result of hydrogen quenching into the solid solution during solidification.

2.1.5 Conclusions

Tensile tests at room and elevated temperatures were performed on samples of the 7050 alloy cast in the copper mold with the aim to investigate the influence of the strain rate and temperature on the mechanical properties. Within the entire tested temperature range, all tested alloys appear to be essentially brittle, especially below 200 °C. The material shows some ductility at 400 °C and at low strain rates at temperatures as low as 300°C. The lower the temperature, the more brittle is the material, the less strain-rate dependent are the mechanical properties, and the higher is the probability of the failure before reaching the yield point. Porosity and micro-cracks (especially at the matrix-secondary phase interface) are the apparent microstructural features that may trigger the fracture and provide easy paths for crack propagation. Porosity is also a factor causing scattering in the results.

2.2 Constitutive parameters and mechanical properties in DC-cast AA7050 billets

2.2.1 Introduction

In the previous section mechanical properties of the AA7050 alloy cast under laboratory conditions were discussed. Although that research revealed the mechanical behavior and fracture mode of the alloy in the as-cast condition, it was not exactly representing the behavior of the material cast under industrial DC-cast conditions. Porosity appeared to be the dominant factor affecting the mechanical properties, and intensified the brittleness of the material in the genuine as-cast state. The constitutive parameters of the alloy on the other hand could not be determined due to the extreme brittleness and high scattering in the results. In this section, mechanical properties of a cylindrical DC-cast AA7050 billet (255-mm diameter) were examined along its axial and radial directions at different temperatures and strain rates. Tensile tests over the post-solidification temperature range (20–400 °C) revealed that the sudden fall in the material ductility (from 23% to 2.5%) below 300 °C was typical of all examined billet sections. Constitutive parameters derived from the true stress–strain curves, supported the earlier findings (see section 2.1) that below 200 °C material behavior becomes strain-rate independent.

2.2.2 Experimental procedure

The material used in this research was an AA7050 billet produced at Corus-Netherlands (IJmuiden) through DC casting with a conventional mold (without hot top) from the melt that was degassed in the furnace. Chemical composition of the alloy is shown in Table 2.1. Tensile mechanical properties of the as-cast 7050 samples were measured using the Gleeble-1500 thermomechanical simulator. Samples were cut from the cylindrical billet with a diameter of 255 mm along its radial and axial (vertical) direction (Fig. 2.7). Axial samples were cut 10 mm off the surface, at the mid-radius and center of the billet to investigate the mechanical properties of the material at different distances from the center. Radial samples were extracted from the middle of the radius to determine the constitutive parameters. Tensile specimens were heated through the Joule effect at a rate of 10 °C/s, kept for 10 s at the desired temperature and then uniaxially deformed at three strain rates of 10^{-2} , 10^{-3} and 10^{-4} s⁻¹ (only 10^{-2} s⁻¹ for the axial samples). The range of strain rates was chosen to resemble those typical of DC casting [17]. Mechanical properties were measured from room temperature to 400 °C at 100 °C steps for radial samples and at 200 °C steps for axial ones. Four samples were tested for each specific temperature and strain rate combination, and the average values are reported.

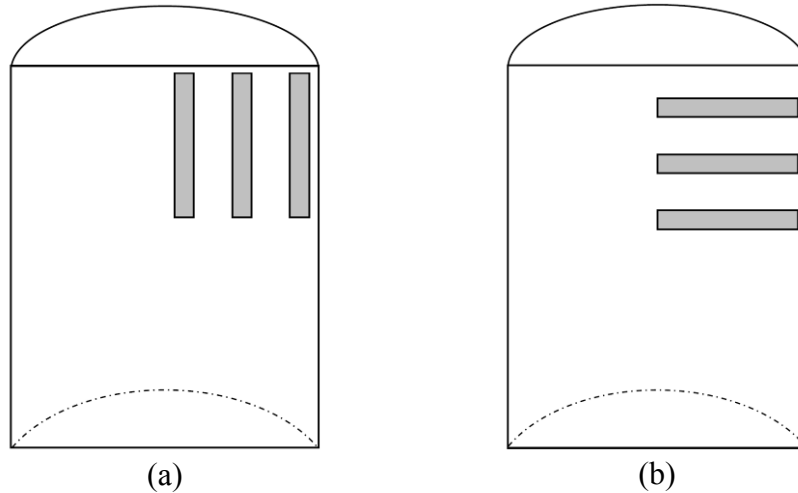


Fig. 2.7 Schematic view of the billet and the orientation of the samples cut out of it: (a) axial and (b) radial direction.

As in previous section, grain size and dendrite arm spacing were measured based on ASTM-E112 [18]. For this purpose samples were polished using diamond suspensions (up to 1 μm) and then anodized in a diluted solution of HBF_4 acid (3%) in distilled water, grains were then revealed using polarized light in an optical microscope Neophot 30. A scanning electron microscope Jeol JSM-6500F (SEM) and the optical microscope (OM) were used for structure and fracture observations. Qualitative and quantitative chemical compositions of the phases present on the fracture surfaces were estimated using backscattered electron detector (BSE) and energy-dispersive X-ray spectroscopy (EDX) in the SEM. Electron backscattered images of the samples were also analyzed using the image analysis software Image J to measure the volume fraction of the non-equilibrium phases.

2.2.3 Results

2.2.3.1 Samples along the radial direction

The true stress-strain curves of the radial samples at five temperatures under a strain rate of 10^{-4} s^{-1} are shown in Fig. 2.8. As temperature falls below 400 $^{\circ}\text{C}$, the material starts to behave more brittle and shows less ductility. The alloy loses its ductility below 200 $^{\circ}\text{C}$ and fails in a brittle manner, which is accompanied by a higher fracture strength. The yield (fracture) strength reaches 279 MPa at room temperature and falls to 30 MPa as the temperature increases to 400 $^{\circ}\text{C}$. Figures 2.9a and 2.9b show the effect of temperature on ductility (% elongation, and % reduction in area). Obviously, the material becomes quite brittle below 200 $^{\circ}\text{C}$.

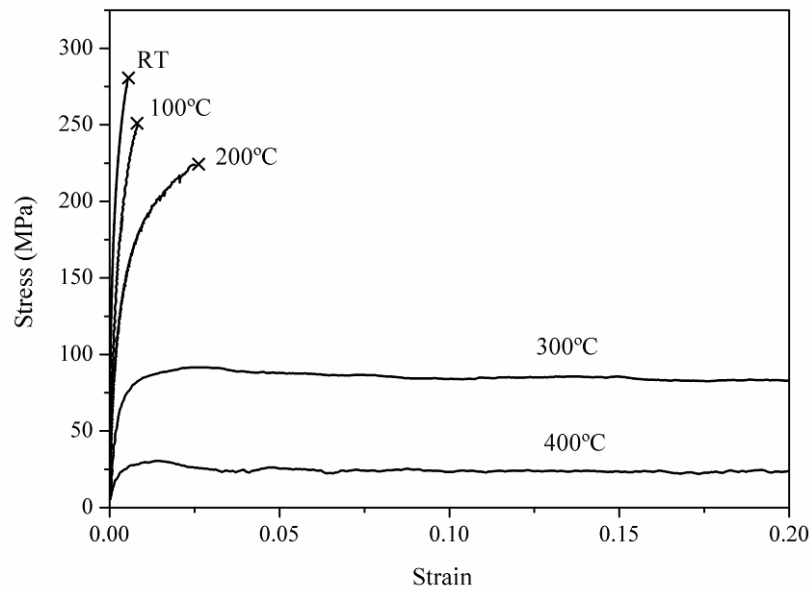


Fig. 2.8 (a) Examples of true stress–strain curves for 7050 samples (cut along the radial direction) tested at different temperatures at a strain rate of 10^{-4} s^{-1} . Similar trends were observed for the other strain rates [21].

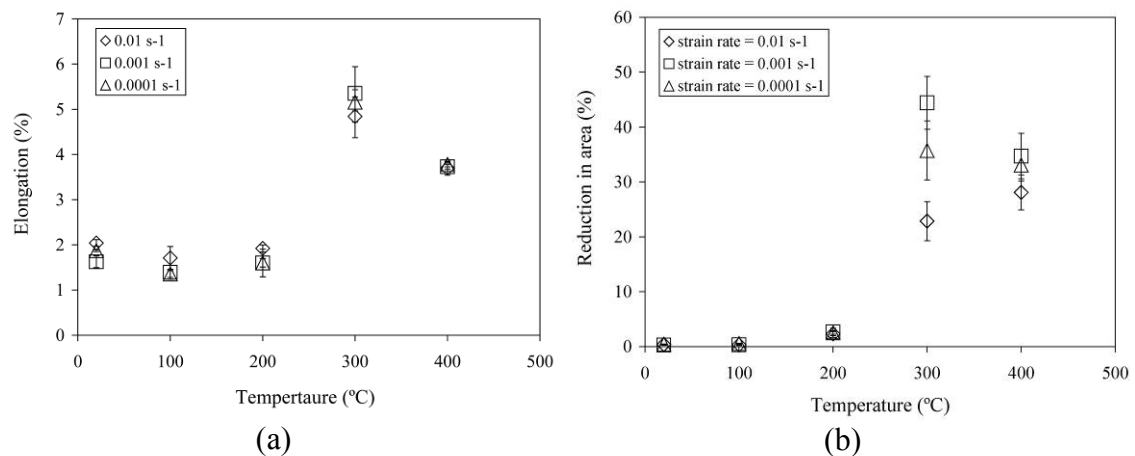


Fig. 2.9 Ductility of the 7050 samples cut along the radial direction of the billet at different temperatures and strain rates: (a) average elongation, (b) average reduction in area [21].

Fig. 2.10a shows the changes in the yield strength of the material with temperature. The yield strength increases as the temperature decreases in a linear manner. The effect of strain rate on the flow stress of the 7050 alloy at the true strain 0.002 is shown in Fig. 2.10b. At high temperatures (300 and 400 °C) the flow stress increases as the deformation rate increases, but at lower temperatures (beginning at 200 °C) the material behavior becomes strain-rate independent.

2.2.3.2 Samples along vertical billet axis

Fig. 2.11a shows the yield strength of the alloy versus distance from the center of the billet. As can be seen at 200 and 400 °C the yield strength is almost independent of the location in the billet. At room temperature however, the highest yield strength appears in the middle of the billet radius. The scattering in the results is highest for the samples near to the surface of the billet. Fig. 2.11b shows the elongation profile along

the radius of the billet. One notices that below 200 °C the material becomes brittle with elongation values around 2%. At 400 °C the curvature of the changes reverses, with the highest and lowest ductility in the center and surface of the billet, respectively. The scattering in the results are also higher at these two locations.

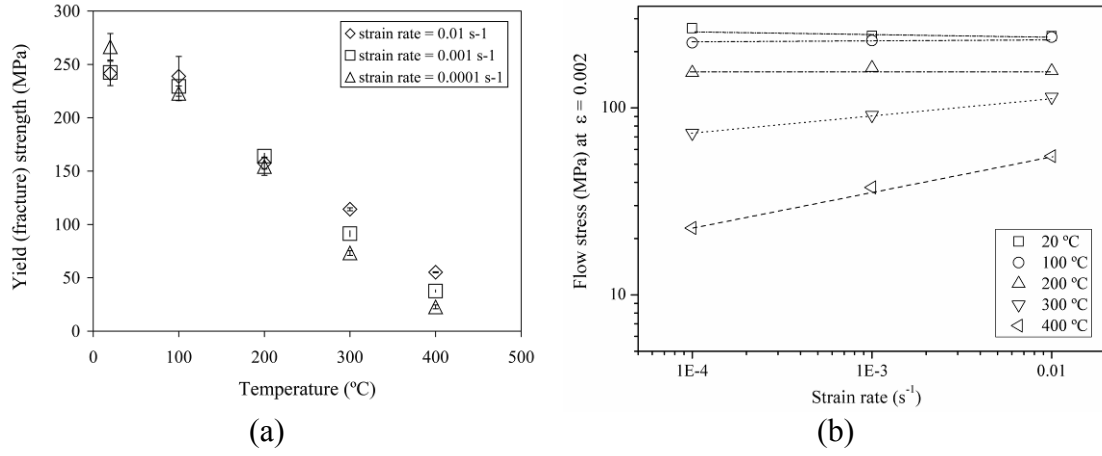


Fig. 2.10 Mechanical properties of the 7050 samples cut along the radial direction: (a) average yield (fracture) strength at different temperatures and strain rates, (b) effect of strain rate on the flow stress at $\epsilon = 0.002$ at different temperatures [21].

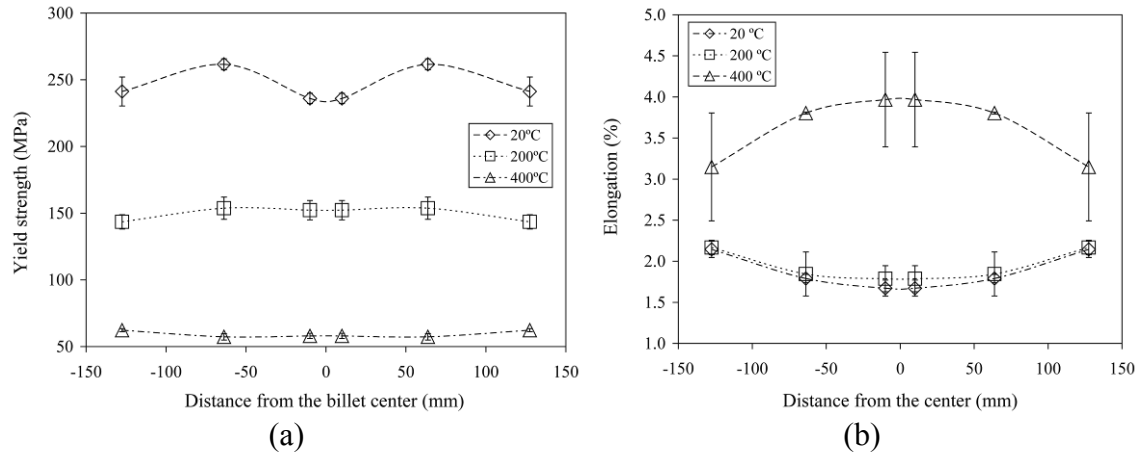


Fig. 2.11 Mechanical properties of the samples cut along the axial direction of the billet at three different locations (center, mid-radius and surface): (a) yield (fracture) strength, (b) elongation (%). Results are shown for three different temperatures and strain rate of 10^{-2} s^{-1} [21].

2.2.3.3 Constitutive parameters

In order to simulate the DC-casting process from solidus temperature to room temperature suitable equations describing the material's mechanical behavior are required. One approach is the extended Ludwik equation [22]:

$$\sigma = K(T)(\epsilon_p + \epsilon_p^0)^{n(T)} (\dot{\epsilon}_p)^{m(T)} \quad (2.1)$$

$K(T)$ is the consistency of the alloy (stress at $\epsilon = 1$ and $\dot{\epsilon} = 1 \text{ s}^{-1}$), $n(T)$ is the strain hardening coefficient, $m(T)$ is the strain rate sensitivity, and ϵ_p^0 is the constant equal to

0.001 [23]. The equation predicts a zero initial stress and an infinite initial slope, except for $n = 0$ which represents a nonhardening rigid/plastic material [24]. The higher the value of n , the more pronounced is the strain-hardening characteristic of the material. The strain rate sensitivity (m) determines how sensitive the stress-strain curve is to the changes in the strain rate. It generally increases with temperature, particularly when it is above the recrystallization temperature [24]. The true stress-strain curves of the material were fitted to Eq. 2.1 to determine $K(T)$, $n(T)$ and $m(T)$, whose values are shown in Table 2.5. As can be seen the values of K and n decrease as the temperature falls, whereas the m values increase with temperature. m values appear to be negative below 200 °C.

Table 2.5 Constitutive parameters of the 7050 alloy determined from the extended Ludwik equation [21].

Temperature (°C)	K (MPa)	n	m
20	774 ± 32	0.42 ± 0.02	-0.2 ± 0.02
100	626 ± 13	0.38 ± 0.01	-0.16 ± 0.03
200	392 ± 11	0.21 ± 0.006	-0.03 ± 0.005
300	199 ± 4.5	0.11 ± 0.007	0.03 ± 0.007
400	174 ± 5	0.09 ± 0.01	0.15 ± 0.009

Table 2.6 Microstructural features of the 7050 alloy [21].

Location in the billet	Grain size (μm)	DAS (μm)	Fraction of eutectics (%)
Centre	229 ± 6	34 ± 1.4	4.5 ± 0.2
Middle radius	179 ± 4	28 ± 0.9	4.6 ± 0.1
Surface	130 ± 2	28 ± 1.0	4.9 ± 0.1

2.2.3.4 Structure examination

Quantitative metallographic results are shown in Table 2.6. As can be seen, the grain size increases from the surface to the center of the billet. Same trend is observed for dendrite arm spacing (DAS), but it does not vary between the mid-radius and center of the billet. Volume fraction of non-equilibrium eutectics remains more or less the same in the center of the billet and at the mid-radius, but there is a slight increase as we move from the mid-radius to the surface. Fig. 2.12 shows the microstructure of the samples at various locations of the billet.

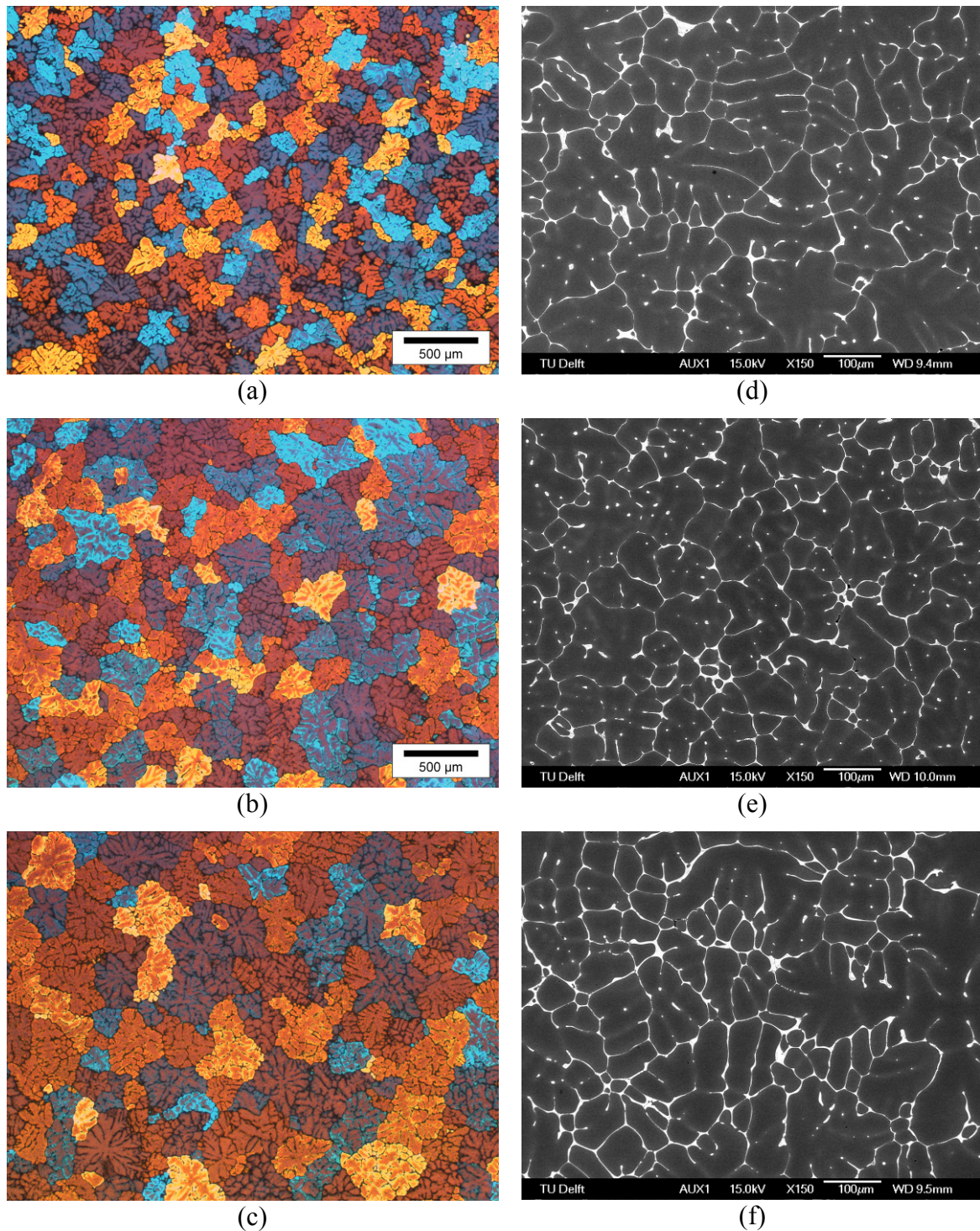


Fig. 2.12 Microstructure of the DC-cast 7050 samples gained from the surface (a,d), mid-radius (b,e), and center (c,f) of a \varnothing 255-mm billet. Figs. a, b and c are captured after anodizing the samples, and Figs. d, e and f are the electron backscattered images.

2.2.4 Discussion

Comparison of the results gained for yield strength and ductility with those gained for stress relieved [9] and homogenized [8] billets shows that the material is more brittle in the pure as-cast condition, i.e. without any stress-relieving treatment. Material's

low ductility below 200 °C ($\leq 2\%$) appears to be the main reason for the high susceptibility to cold cracking, the fact which is in agreement with the conclusions of Livanov *et. al* [11] that cold cracking does not occur when the tensile elongation of the material exceeds 1.5%. Another consequence of brittleness which makes the as-cast material more prone to cracking is that below 200 °C material behavior becomes strain rate independent (Fig. 2.10b). As discussed before, the strain rates induced during the DC-casting process by non-homogenous contractions are quiet low in the order of 10^{-5} - 10^{-2} s $^{-1}$ [17]. The strain rate independent behavior of the as-cast material may facilitate the fracture even at such low strain rates especially when the material becomes extremely brittle below 200°C. Figs. 2.13 to 2.15 compare the constitutive parameters of the DC-cast AA7050 alloy in the genuine as-cast condition to the stress relieved [9] and homogenized [25] samples.

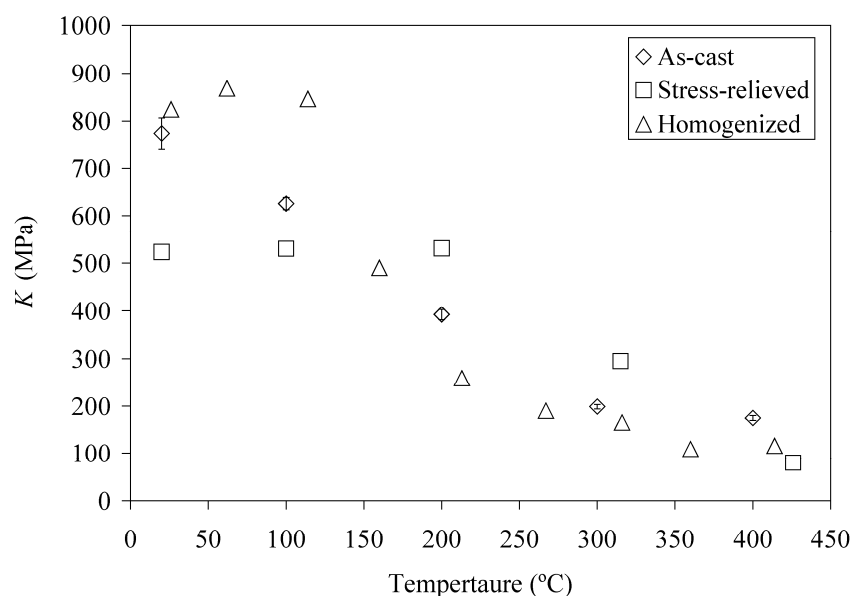


Fig. 2.13 Consistency of the 7050 alloy gained from various samples: as-cast (this study), stress relieved [9], and homogenized [25].

As can be seen in Fig. 2.13, the consistency of the genuine as-cast material falls in a continuous manner with temperature. In homogenized and stress relieved samples however, it passes through a plateau and then falls with increasing the temperature. It is noticeable that the main difference occurs at lower temperatures where the material is more prone to cracking due to its extreme brittleness. The same trend is observed for strain hardening coefficient of the alloy (Fig. 2.14), although the difference in the results appears to be higher at elevated temperatures especially in the stress relieved material. Strain rate sensitivity values are in a relatively good agreement at lower temperatures, but the difference becomes larger at higher temperatures (Fig. 2.15). The negative values of the strain rate sensitivity were disregarded as they emerged due to the extreme brittleness of the material at temperatures below 200°C. As the performance of strain rate sensitivity tests sounds challenging on such a brittle material, zero value was assigned to m at/below 200 °C. Nearly zero strain rate sensitivity values at lower temperatures are in a good agreement with the brittleness of the material and the fact that the material behavior is indeed strain rate independent (Fig. 2.15).

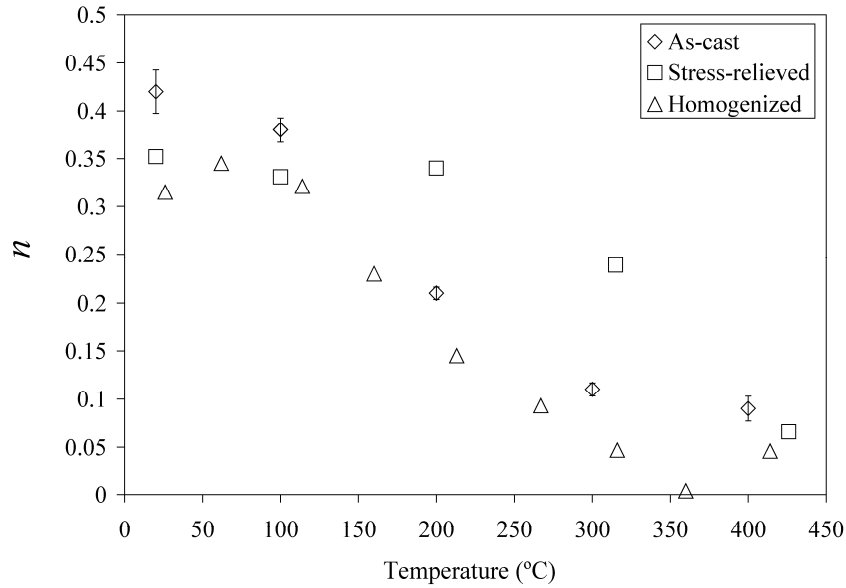


Fig. 2.14 Strain hardening coefficient of the 7050 alloy gained from various samples: as-cast (this study), stress relieved [9], and homogenized [25].

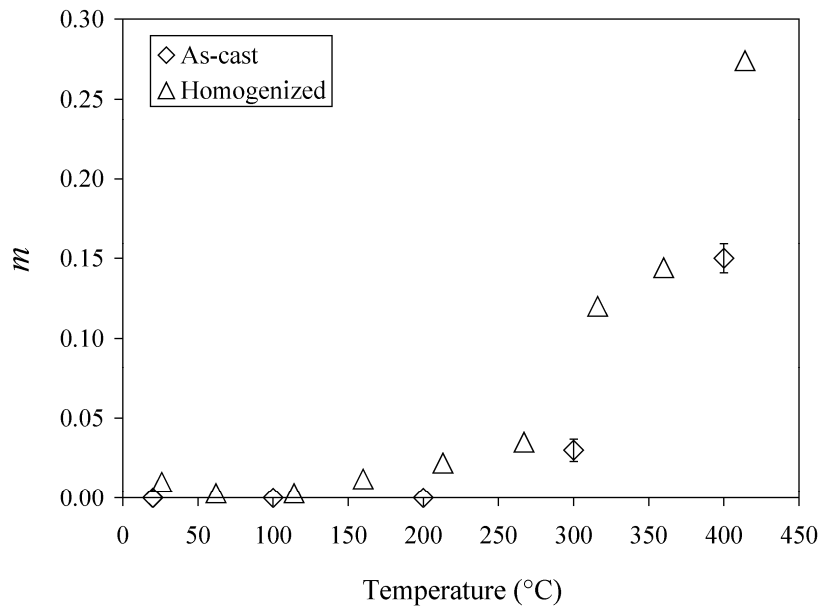


Fig. 2.15 Strain rate sensitivity of the 7050 alloy gained from various samples: as-cast (this study), and homogenized [25].

Relatively uniform grain size and DAS in the cross-section of the billet has resulted in similarities in the mechanical properties (taking the scattering of the results into account) regardless of the location on the radial axis. Hence, presence of continuous non-equilibrium phases on the boundaries and inter-dendritic spaces appears to be the main failure reason in this study (Fig. 2.12d, e, f). Existence or instantaneous formation of any defect with a critical size in one of these regions can result in catastrophic failure in the presence of residual stresses. In larger billets, however the grain size, DAS and the intermetallics size change more distinctly across the cross section which may affect the mechanical properties of the material. There, accumulation of thermal stresses during solidification accompanied by critical low

mechanical properties (e.g. ductility) at some critical positions of the billet (with critical grain size or DAS) might lead to failure.

Investigation of the fracture surfaces revealed that the grain boundary embrittlement leads to the brittleness of the material and eventually results in decohesive rupture. Detrimental effect of non-equilibrium eutectic phases on the mechanical properties arises from their continuous presence along grain boundaries and inter-dendritic spaces. More details of this will be discussed in Chapter 4.

2.2.5 Conclusions

Room and high temperature tensile tests were performed on the DC-cast AA7050 alloy to reveal the materials behavior in the as-cast condition over the post solidification temperature range. Within this range, the lower the temperature, the more brittle is the material, the less strain-rate dependent are the mechanical properties, and the higher is the probability of the failure before reaching the yield point. Constitutive parameters of the material were also derived in this temperature range using the extended Ludwik equation. The constitutive parameters gained from the genuine as-cast material were considerably different from the stress relieved and homogenized materials. Using such parameters for numerical thermal stress/strain analysis would result in a more realistic description of material's thermomechanical behavior during DC-casting.

2.3 Investigation of fracture behavior of the DC-cast AA7050 and AA7475 alloys

2.3.1 Introduction

Up to this moment the mechanical properties such as yield strength, ductility, and constitutive parameters were determined through appropriate tensile tests at room as well as elevated temperatures. The next step would be to determine the fracture behavior of the material at temperatures where the material is prone to cold cracking (from solidus down to room temperature). Plane strain fracture toughness tests may be applied for this purpose. But before performing such sophisticated tests, a more general and simple test would facilitate understanding the fracture behavior of the material over the post solidification temperature range. This can be achieved by performing Charpy impact tests. Principal advantage of the Charpy V-notch impact test is that it is a relatively simple test that utilizes a relatively cheap, small test specimen. Tests can readily be carried out over a range of desired temperatures. The chief difficulty however, is that the results of the Charpy test are difficult to use in design. Since there is no measurement in terms of stress level, it is hard to correlate C_v (energy required for fracture of a Charpy specimen) data to service performance [26]. Moreover, there is no correlation of Charpy data with flaw/crack size. To overcome such shortages, plane strain fracture toughness tests were performed to determine the K_{Ic} —an engineering property of the material that can be correlated to the flaw/crack size.

2.3.2 Charpy impact tests

2.3.2.1 Experimental procedure

Charpy impact toughness tests were conducted on 7050 samples cast in the copper mold and DC-cast 7475 samples over a temperature range from room temperature to 500 °C (at 100 °C steps). Chemical compositions of the samples are shown in Table 2.1. ASTM-E23 [27] notched samples (Fig. 2.16) were first heated up to the desired temperatures in a small chamber oven for a few minutes and then immediately transported to the machine for tests. Fig. 2.17 shows the Charpy impact test apparatus used in this study. The maximum capacity of the machine was 50 J.

To investigate the fracture mode and determine the probable crack propagation paths, fracture surfaces gained from Charpy tests were preserved. Lateral cross sections of

the fracture surfaces were mounted in epoxy resin to reveal two-dimensional features of the fracture when examining in the OM.

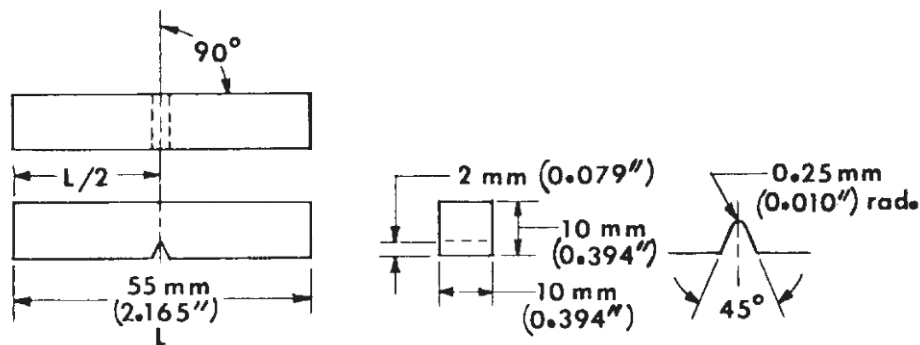


Fig. 2.16 Geometry of the samples gained from ASTM-E23 [27].

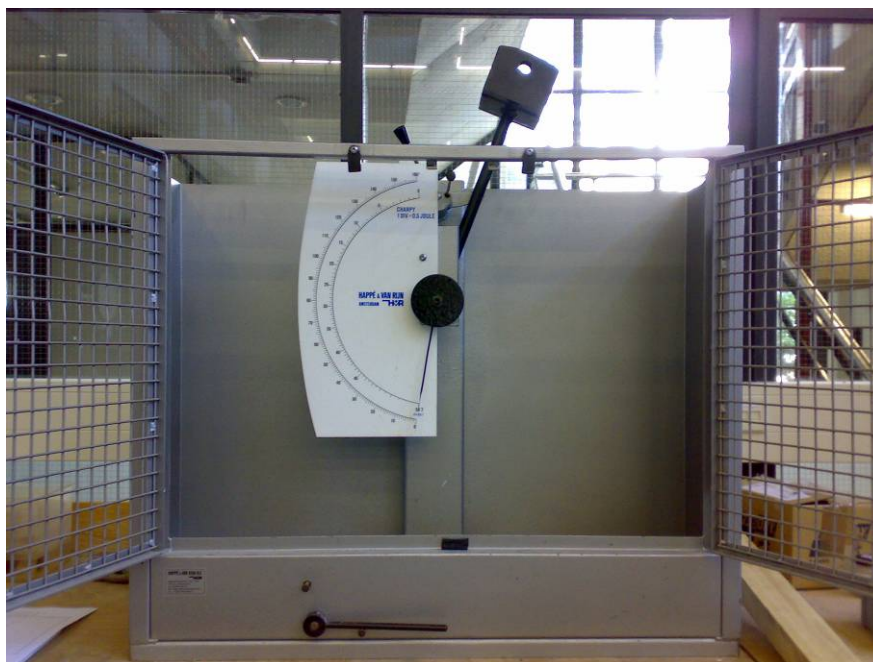


Fig. 2.17 A photograph showing the Charpy impact test apparatus used in this study.

2.3.2.2 Results

Fig. 2.18 shows the changes in the absorbed energy during the Charpy impact toughness test for 7050 (HP-NG and HP-GR) and 7475 alloys in the as-cast condition. As can be seen from the figure, there is little increase in the amount of absorbed energy up to 200 °C, hence the material is quite brittle. Then the absorbed energy increases, reaches maximum at 400 °C and afterwards falls at 500 °C. It is obvious from these results that there are two temperature ranges where material behaves more brittle, i.e. at temperatures below 200°C and above the non-equilibrium solidus (465–469 °C [20]). The 7475 DC-cast alloy appears to absorb more energy before failure at 400 °C than 7050 alloys cast in the copper mould. Below 400 °C, there is not much difference in the behavior of 7050 samples, whereas at 500 °C the grain refined alloy (7050-HP-GR) has an advantage. The behavior of 7050-LP-HM and 7050-LP-CM samples was similar to that of 7050 alloys shown in Fig. 2.18, and falls in the same range of values.

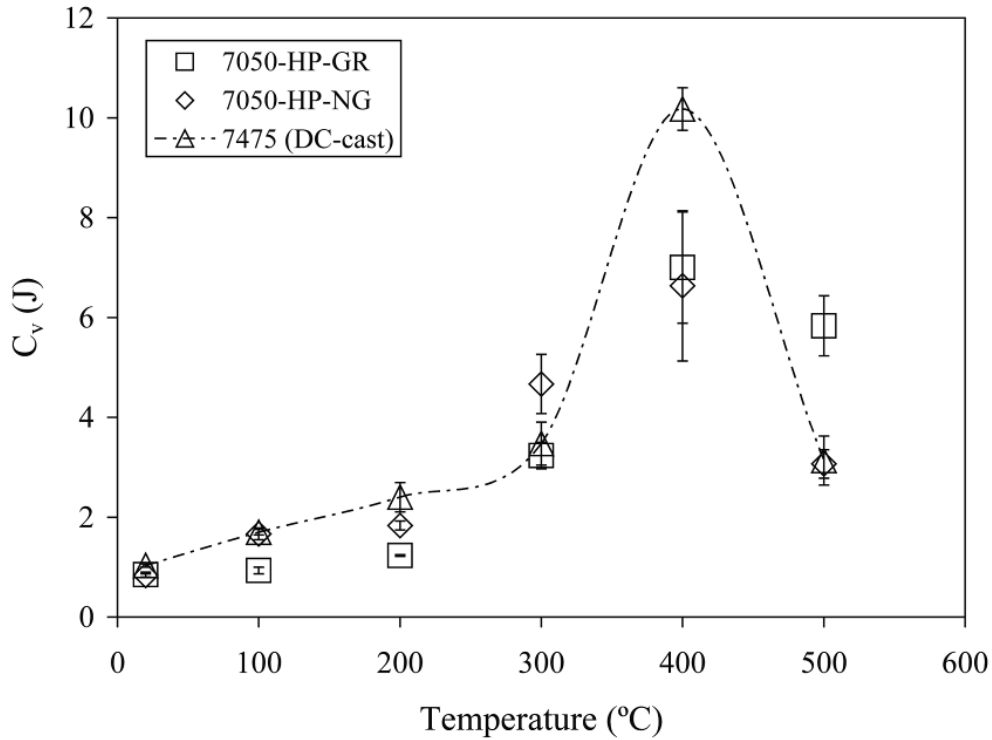


Fig. 2.18 Charpy impact toughness for two 7050 alloys cast in the copper mold (GR: grain refined; NG: non-grain refined) and DC-cast 7475 samples [16].

2.3.2.3 Discussion

Investigation of the lateral cross sections of the fracture surfaces revealed that the samples have failed in a brittle inter/transgranular manner (Fig. 2.19a). Detailed examination of fractures in SEM explained clearly why the material behaves in the way shown in Fig. 2.18. The dimples on the fracture surface of a 7475 sample failed at 400 °C are evidence for the highest energy absorption due to plastic deformation at this temperature (Fig. 2.19b). At the same time, cracked intermetallic particles can be seen inside the dimples, revealing the weak link of the structure. At 500 °C, which is above the non-equilibrium solidus temperature (465–469 °C [20]) of this alloy, the sample fails intergranularly and the magnitude of absorbed energy is smaller as a result of liquid metal embrittlement of the grain boundaries (Fig. 2.19c). Eutectic patches and secondary intergranular cracks are typical of this fracture. From room temperature to 200 °C the fracture mode is quite brittle and no sign of plastic deformation is observed (Figs. 2.19d). This is where the cold cracking is likely to occur. Intergranular fracture mode with secondary cracks, pores and cleaved eutectic patches is characteristic of low-temperature mechanical behavior of tested alloys.

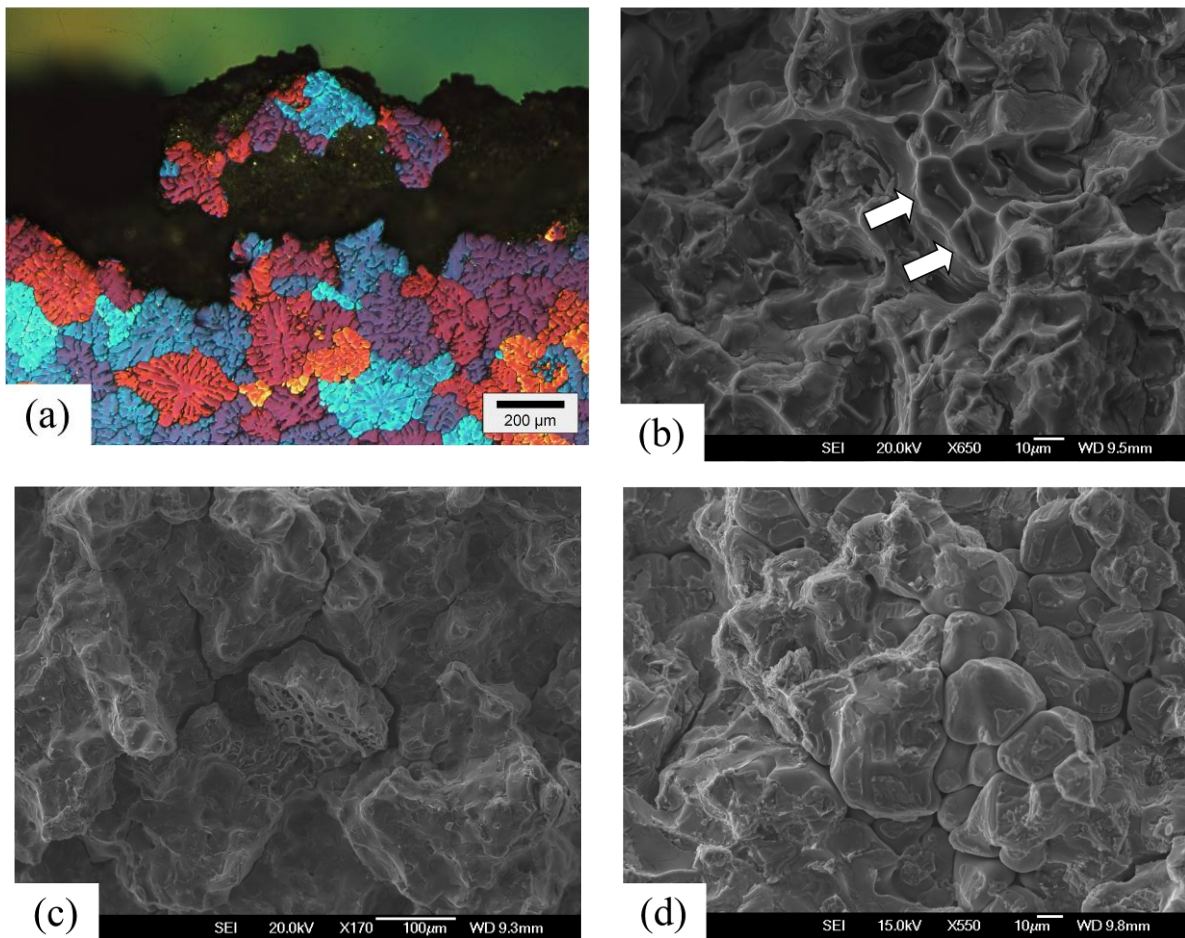


Fig. 2.19 Fracture surfaces in a DC-cast 7475 alloy failed during the Charpy tests at different temperatures: (a) lateral cross section of a sample failed at room temperature, OM, polarized light; (b) fracture surface of a sample failed at 400°C, dimples with intermetallics at the bottom are visible and indicated by arrows, SEM, and (c) fracture surface of a sample failed at 500°C, fracture is intergranular with secondary cracks. (d) 7050-HP-NG sample failed during Charpy test at room temperature. Nonequilibrium eutectic patches acting as brittle bridges between dendrite arms are visible, SEM [16].

2.3.3 Plane strain fracture toughness tests

2.3.3.1 Experimental procedure and discussion

In order to assess the critical crack size leading to catastrophic failure, plane strain fracture toughness values are required. Therefore, K_{Ic} tests were performed from room temperature to 200 °C following ASTM-E399 regulations [28]. The samples were prepared from the DC-cast 7050 alloy (Table 2.1) based on the dimensional proportions mentioned in the standard, and were locally polished around the chevron notch to be able to follow and accurately measure the fatigue crack length. Fig. 2.20 shows the geometry of the samples used for the tests. The dimensions of the samples were as follows: length 150 mm, width 30 mm and thickness 15 mm.

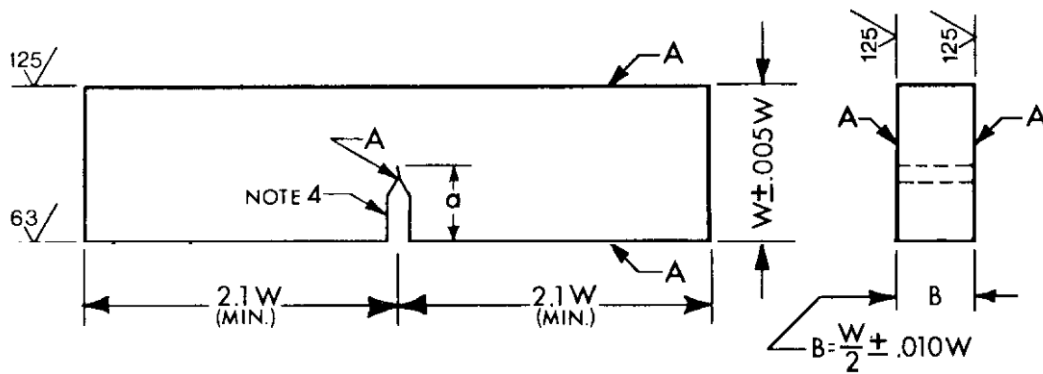


Fig. 2.20 The geometry of the three-point-bend specimen according to ASTM-E399. Standard proportions and tolerances are shown [28].

Samples were then fatigue pre-cracked at room temperature to reach the total crack length of 15 mm (including the chevron notch length of 13 mm). Loading rate was chosen in such a way to keep the stress intensity within the range of $0.55\text{-}2.75 \text{ MPa}\cdot\text{m}^{1/2}\cdot\text{s}^{-1}$. At higher temperatures, samples were first covered with a ceramic coating for insulation and preventing a sudden temperature fall (temperature tolerance was $\pm 10^\circ\text{C}$) and then kept at desired temperatures in an oven for 20 minutes. The three point bending test setup and a sample tested at room temperature are shown in Fig. 2.21.

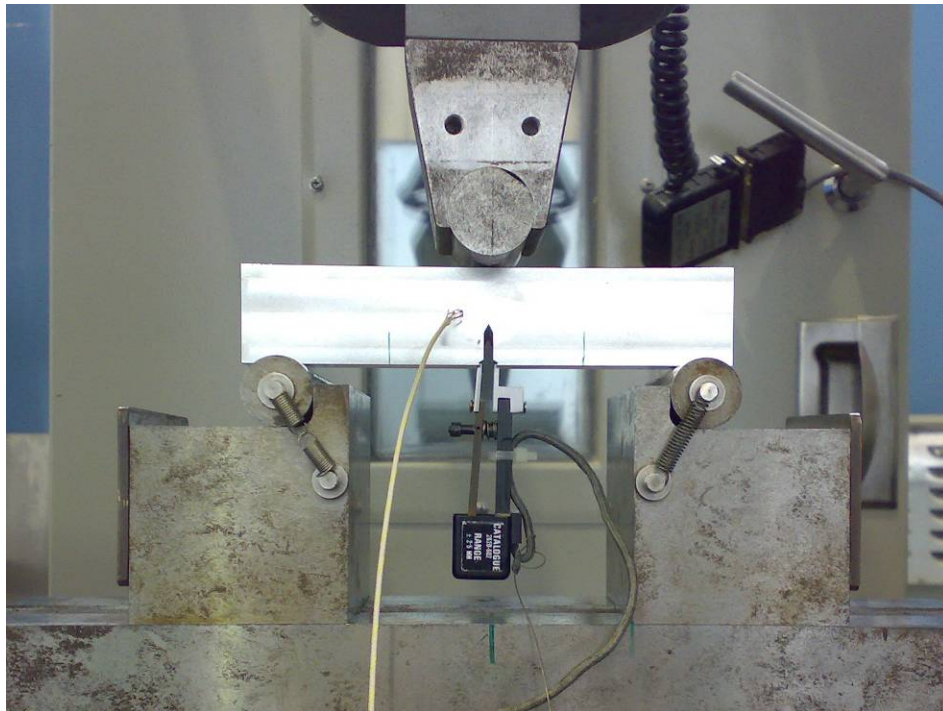


Fig. 2.21 A photograph showing the three point bending test setup, the sample, and the clip-gage used to measure the crack mouth opening displacement. A K-type thermocouple is attached to the sample to monitor the temperature.

K_{Ic} values from room temperature to 200°C were then calculated using the load-displacement curves (Fig. 2.22) and are presented in Fig. 2.23.

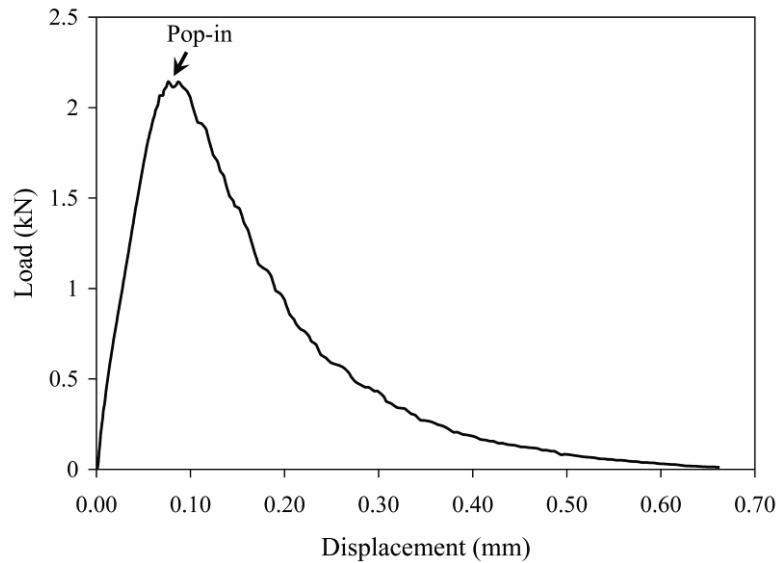


Fig. 2.22 A typical load-displacement curve obtained from the plane strain fracture toughness tests for DC-cast 7050 samples tested at room temperature. Similar curves were derived at elevated temperatures.

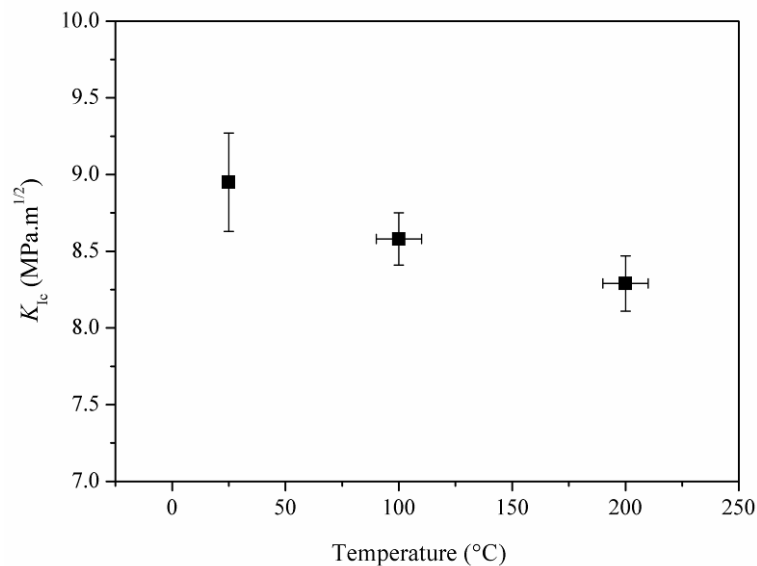


Fig. 2.23 Plane strain fracture toughness (K_{Ic}) values measured for the as-cast 7050 (DC-cast) alloy from room temperature to 200 °C [29].

As can be seen there is a slight decrease in K_{Ic} values with increasing the temperature. But taking the error values into account, the differences are insignificant. Above 200°C, plane strain conditions were not valid any more, mainly because of the sudden fall in the yield strength at that temperature (154 MPa at 200 °C to 73 MPa at 300 °C; Fig. 2.10a). Thus, the crack tip opening displacement (CTOD) values were calculated based on ASTM-E1820-01 [30] as follows: 25°C: $6.4 \pm 1 \mu\text{m}$; 100°C: $7.8 \pm 0.8 \mu\text{m}$; 200°C: $11.7 \pm 1.5 \mu\text{m}$; 300°C: $495 \pm 32 \mu\text{m}$; 400°C: $780 \pm 77 \mu\text{m}$ and are demonstrated in Fig. 2.24 on a logarithmic scale. As it is obvious, below 200°C the material is extremely brittle with CTOD values below 12 μm with a sudden increase at 300°C. Similar trends were observed for the reduction of area in tensile tests (Fig. 2.9).

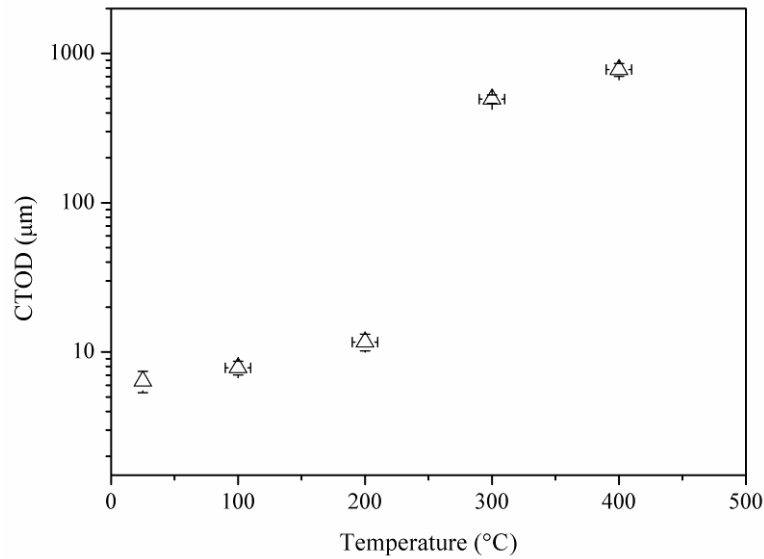


Fig. 2.24 Crack tip opening displacement values calculated for the as-cast 7050 alloy (DC-cast) from room temperature to 400 °C [29].

The comparison of the K_{Ic} results gained for the genuine as-cast material here with the minimum K_{Ic} for the material in the precipitation hardened state (20.9-27.5 MPa·m^{1/2}, at room temperature [31]) shows how brittle the material is under as-cast conditions. It is worth to mention that the plane strain fracture toughness tests were performed by Chang *et al.* [3] on 7050 samples. However, their tests did not appear to result in the official K_{Ic} values as in the load-displacement curves the P_{max}/P_Q ratio was larger than 1.10. P_{max} is the maximum load reached in the load-displacement curve and the P_Q is the interception point of the secant line (with a slope equal to 0.95 of the slope of the tangent to the initial linear part of the record.) with the curve [28]. Therefore, the values reported by Chang *et al.* are the stress intensity factors at the onset of catastrophic failure rather than official K_{Ic} values. These values measured at room temperature are 10.4 MPa·m^{1/2} (K_Q , calculated using P_Q) and 12.4 MPa·m^{1/2} (K_c , calculated using P_{max}) for the crack to width ratio (a/W) of 0.55. Comparison of these values with our result (8.9 ± 0.3 MPa·m^{1/2}) reveals that they are slightly higher, which is due to the fact that the samples used by Chang *et al.* are either from homogenized or stress relieved billets rather than genuine as-cast material which is more prone to cracking.

2.4 Measurement of the Young's modulus

Rheological torsion tests were performed on DC-cast 7050 samples in the as-cast condition using an RMS-800 setup in order to measure Young's modulus. The dimensions of the samples were as follows: length 65 ± 1 mm, width 12.5 ± 0.05 mm, and thickness 0.782 ± 0.002 mm. Fig. 2.25 shows the RMS-800 setup and the rectangular sample used for the torsion tests.

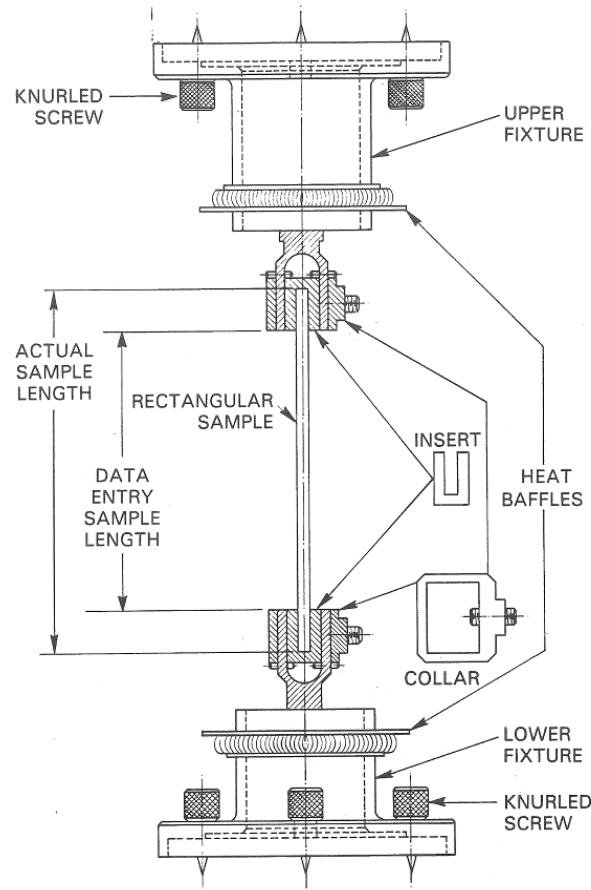


Fig. 2.25 The RMS-800 setup for the torsion tests on rectangular geometry sample [32].

Elastic stresses and strains were calculated using the following equations [32]:

$$K_{\gamma} = \frac{T}{L} \left(1 - 0.378 \left(\frac{T}{W} \right)^2 \right) \quad (2.2)$$

$$\gamma = K_{\gamma} * \theta \quad (2.3)$$

$$K_{\tau} = 1000 \left(\frac{3 + 1.8 \left(\frac{T}{W} \right)}{WT^2} \right) * G_c \quad (2.4)$$

$$\tau = M * K_{\tau} \quad (2.5),$$

where:

T = Thickness of the sample (mm)
 W = Width of the sample (mm)
 L = Length of the sample (mm)
 K_γ = Strain constant
 θ = Actuator angular displacement (radians)
 γ = Shear strain
 M = Transducer Torque (gram-centimeters)
 K_τ = Stress constant
 $G_c = 98.07$ Pascals per gram (SI)
 τ = Shear stress

Using the shear modulus values calculated from the test results (Eq. 2.3 and 2.5) and the Poisson's ratios gained from JMat-Pro (provided by Corus-Netherlands (IJmuiden)), the Young's modulus values were calculated (equation 2.6 [26]).

$$G = \frac{E}{2(1+\nu)} \quad (2.6)$$

The results are shown in Table 2.7. These results differ considerably from the ones of the tensile tests. Initial simulations showed that such differences could cause a considerable difference in the values of thermal stresses especially at high temperatures.

Table 2.7 Young's and shear moduli gained from RMS-800, tensile tests, and JMat-Pro. Poisson's ratio (JMat-Pro) is also shown.

Temp. (°C)	E (GPa) (Tensile tests)	G (GPa) (RMS-800)	Poisson's ratio (JMat-Pro)	E (GPa) (RMS-800)	E (GPa) (JMat-Pro)
20	73 ± 3.5	26	0.338	69.5	67.9
100	61 ± 4.5	24.9	0.341	67	64.9
200	34 ± 3.5	23.5	0.346	63.5	61.2
300	15 ± 2	21.9	0.352	59	57.4
400	5.8 ± 0.8	20.1	0.358	54.5	53.6

Figure 2.26 shows the Young's modulus values of the 7050 alloy obtained through different methods, i.e. tensile tests, rheological torsion tests (0.1 and 100 rad/s) and simulation results gained from JMat Pro. If we take the JMat-Pro results as reference, we notice that above 100°C, tensile tests (ASTM results for 7075 and Gleeble for 7050) underestimate the calculated values of Young's modulus mainly due to creep. Similar behavior is observed above 350 °C in rheological torsion tests at the low deformation rate of 0.1 rad/s. The high-strain rate torsion tests on the other hand are in good agreement with JMat-Pro simulation results. This assured us that the Young's moduli gained from JMat-Pro are reliable and were eventually applied in the model.

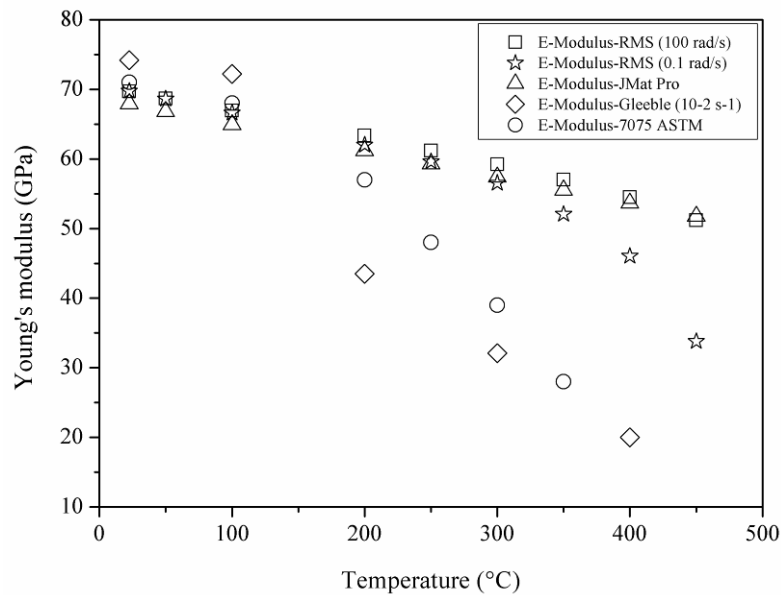


Fig. 2.26 Young's moduli measured through rheological torsion tests (RMS) and gained from JMat-Pro database for AA7050 alloy. Engineering Young's moduli measured for the AA7075 [7] and AA7050 through tensile tests are also shown for comparison [29].

References

- [1] V. A. Livanov, *Neue Hütte* 5 (1960) 535-542.
- [2] B. Hannart, F. Cialti, R. van Schalkwijk, in: U. Mannweiler (Ed.), *Light Metals*, TMS, 1994, pp. 879-887.
- [3] K.-M. Chang, B. Kang, *J. Chin. Inst. Eng.* 22 (1999) 27-42.
- [4] R.K. Paramatmuni, Keh-Minn Chang, Bruce S. Kang, X. Liu, *Mater. Sci. Eng. A* Vol. 379 (2004) 293–301.
- [5] Q. Han, S. Viswanathan, D.L. Spainhower, S.K. Das, *Metall. Mater. Trans. A* 32 (2001) 2908–2910.
- [6] J. B. Hess, *Metall. Trans. A* 14 (1983) 323-327.
- [7] J.G. Kaufman, *Properties of Aluminum Alloys; Tensile, Creep, and Fatigue Data at High and Low Temperatures*, ASM international, Materials Park, Ohio, 2002.
- [8] J. Wan, H.-M. Lu, K.-M. Chang, J. Harris, in: B. Welch (Ed.) *Light Metals 1998*, Warrendale: TMS, 1998, pp. 1065-1070.
- [9] K.-M. Chang, H.-M. Lu, J. Wan, J. F. Harris, in: *Second Intern. Conf. on Quenching and Control of Diffusion*, Ohio, ASM International, 1996, pp. 341–345.
- [10] D.A. Granger, in: A.K. Vasudevan, R.D. Doherty (Eds.) *Aluminum Alloys—Contemporary Research and Applications*, Academic Press, London, 1989, pp. 109-135.
- [11] V. A. Livanov, R.M. Gabidullin, V.S. Shipilov, *Continuous casting of aluminum alloys*, Metallurgiya, Moscow, 1977, p. 90.
- [12] E.A. Starke Jr., and J.T. Staley, *Prog. Aerosp. Sci.*, 32 (1996) 131-172.
- [13] D. Dumont, A. Deschamps, Y. Brechet, *Mater. Sci. Eng. A* 356 (2003) 326-336.
- [14] T. P. Earle, J. S. Robinson, J.J. Colvin, *J. Mater. Process. Tech.* 153/154 (2004) 330–337.
- [15] N.A. Loktionova, V. I. Kulakov, R.A. Krivenko, I.L. Teytel. *Metalloved. Termich. Obrab. Met.* 11 (1963) 46–47.

- [16] M. Lalpoor, D.G. Eskin, L. Katgerman, *Mater. Sci. Eng. A* 497 (2008) 186-194.
- [17] W.M. van Haaften, *Constitutive Behavior and Hot Tearing During Aluminum DC Casting*, PhD thesis, Delft University of Technology, The Netherlands, 2002.
- [18] ASTM Standard E112, *Standard Test Methods for Determining Average Grain Size*, ASTM Standards on Disc, Vol. 03.01, West Conshohocken, Philadelphia, 2003.
- [19] P.G. Miklyaev, *Mechanical Properties of Light alloys at Temperatures and Rates of Deformation Processing*, Metallurgiya, Moscow, 1994.
- [20] N.A. Belov, D.G. Eskin, A.A. Aksenov, *Multicomponent Phase Diagrams: Applications for Commercial Aluminum Alloys*, Elsevier, Amsterdam, 2005, pp. 199–202.
- [21] M. Lalpoor, D.G. Eskin, L. Katgerman, *Proc. 12th Intern. Conf. on Fracture*, Ottawa, National Research Council of Canada, 2009 (CD).
- [22] B. Magnin, L. Katgerman, B. Hannart, in: M. Cross and J. Campbell (Eds.), *Modeling of Casting, Welding and Advanced Solidification Processing VII*, TMS, Warrendale, 1995, pp. 303-310.
- [23] H. G. Fjær, A. Mo, *Metall. Trans. B* 21 (1990) 1049-1061.
- [24] J. Chakrabarty, *Theory of Plasticity*, third ed., Elsevier Butterworth-Heinemann, Oxford, 2006.
- [25] W. M. van Haaften, *Internal report*, Corus Ijmuiden, The Netherlands, 2002.
- [26] G.E. Dieter, D. Bacon, *Mechanical Metallurgy*, SI Metric ed., McGraw-Hill Book Company, Singapore, 1988.
- [27] ASTM Standard E23, *Standard Test Methods for Notched Bar Impact Testing of Metallic Materials*, ASTM Standards on Disc, Vol. 03.01, West Conshohocken, Philadelphia, 2003.
- [28] ASTM Standard E399, *Standard Test Method for Plane-Strain Fracture Toughness of Metallic Materials*, ASTM Standards on Disc, Vol. 03.01, West Conshohocken, Philadelphia, 2003.
- [29] M. Lalpoor, D.G. Eskin, L. Katgerman, *Metall. Mater. Trans. A* 40 (2009) 3304-3313.
- [30] ASTM Standard E1820-01, *Standard Test Method for Measurement of Fracture Toughness*, ASTM Standards on Disc, Vol. 03.01, West Conshohocken, Philadelphia, 2003.
- [31] J.R. Davis, *ASM Specialty Handbook: Aluminium and aluminium alloys*, ASM international, Materials Park, Ohio, 1994.
- [32] *RMS-800 Users' Manual*.

Chapter 3

Thermal properties and thermal contraction behavior in AA7050 alloy

In the previous chapter we discussed the mechanical properties of the 7050 alloy in the genuine as-cast condition. There, we learned that the material experiences a severe loss in ductility upon cooling and becomes brittle below 300°C. The poor ductility assists the brittle fracture of the material in the as-cast condition. The level of thermal stresses built up in the billet however is determined by thermal properties of the material. As mentioned in Chapter 1, the non-uniform thermal contraction is responsible for the rise of thermal stresses. In order to understand how thermal contraction occurs during the solidification and cooling, appropriate experiments are required. In this chapter, some thermal properties of the 7050 alloy are determined through experiments. The liquidus and nonequilibrium solidus of the alloy are measured by differential scanning calorimetry tests. Solidification contraction tests are performed to determine the onset of thermal contraction in alloys cast under various conditions. Eventually, dilatometry tests are conducted to estimate the coefficient of thermal expansion/contraction of the alloy.

3.1 Introduction

It was mentioned in Chapter 1 that 2xxx and 7xxx series aluminum alloys are the most vulnerable to cold cracking among aluminum alloys. The cold cracking susceptibility can be on the one hand addressed to the brittleness of such alloys in the as-cast state. Poor thermal properties on the other hand may eventually lead to accumulation of thermal stresses and intensify the problem. The relatively wide solidification temperature range (Table 3.1) in these alloys makes them vulnerable to *hot cracking*. In the solid state, the lower thermal conductivity (Table 3.2) and higher coefficient of thermal expansion (Table 3.3) compared to other aluminum alloys results in steeper temperature gradients and larger residual thermal stresses, respectively, which makes these alloys more susceptible to *cold cracking*.

Table 3.1 Solidification temperature range in various types of aluminum alloys [1,2]. In each series, alloys with the largest and smallest solidification temperature range are shown.

Type of alloy	Examples	T_L (°C)	T_S (°C)	$T_L - T_S$ (°C) (Solidification range)
1xxx	1350	655	645	10
	1100	655	643	12
2xxx	2219	643	543	100
	2024	638	500	138
3xxx	3003	655	643	12
	3004	655	630	25
4xxx	4343	613	577	36
	4032	570	532	38
5xxx	5657	657	638	19
	5056	638	568	70
6xxx	6063	655	615	40
	6066	645	565	80
7xxx	7072	655	640	15
	7050	630	490	140
	7075	635	475	160
8xxx	8030	655	645	10
	8176	655	645	10

Table 3.2 Thermal conductivity in various types of aluminum alloys at room temperature [1,2]. In each series, the alloys with the highest and lowest thermal conductivity are shown.

Type of alloy	Examples	Thermal conductivity at 25°C (W/m·K)
1xxx	1100	222
	1350	234
2xxx	2219	172
	2024	193
3xxx	3004	163
	3003	193
4xxx	4032	154
	4343	180
5xxx	5056	117
	5657	205
6xxx	6066	154
	6063	218
7xxx	7075	130
	7050	157
	7072	222
8xxx	8030	230
	8176	230

Table 3.3 Average coefficient of thermal expansion in various types of aluminum alloys from 20 to 100°C, the alloys with the highest and lowest coefficient of thermal expansion are shown [1,2].

Type of alloy	Example	Coefficient of thermal expansion ($10^{-6}/K$)
1xxx	1060	23.6
	1350	23.75
2xxx	2618	22.3
	2117	23.75
3xxx	3003	23.2
	3004	23.9
4xxx	4032	19.4
	4043	22.1
5xxx	5454	23.6
	5056	24.1
6xxx	6053	23
	6061	23.6
7xxx	7072	23.6
	7075	23.6
	7050	24.1
8xxx	8017	23.6
	8176	23.6

Although such qualitative comparisons may provide us with a global view of what makes 7xxx series alloys vulnerable to *hot* and *cold cracking*, the more complicated thermomechanical behavior of the material during and after solidification may be only understood through computer simulations and proper experiments. Computer simulations, however can represent the true thermomechanical behavior of the material only providing that realistic thermal properties are implemented in the model. The coefficient of thermal expansion, thermal conductivity, liquidus as well as nonequilibrium solidus temperatures, onset of thermal contraction in the mushy zone, specific heat and latent heat of fusion are required to be able to run the simulations. In this study part of such data has been gained from the thermodynamics data base JMat-Pro[‡] (provided by Corus-Netherlands (IJmuiden)). The coefficient of thermal expansion/contraction and the onset temperature of thermal contraction in the mushy zone were determined experimentally as they were neither available in the literature nor representing the properties of the as-cast material. The results gained in this chapter along with the mechanical database discussed in the previous chapter, will be implemented in ALSIM5 for computer simulations (Chapters 5, 6 and 7).

3.2 Differential Scanning Calorimetry

The knowledge of the liquidus and nonequilibrium solidus temperatures is crucial for computer simulations as they clarify the borders between liquid and solid phases. In order to determine these temperatures for the DC-cast grain refined 7050 alloy, differential scanning calorimetry (DSC) tests were performed. Sample was weighed and put in an alumina cup inside a Stanton-Redcroft DSC 1500 machine. Alumina

[‡] Sente Software Ltd., Surrey Technology Centre, 40 Occam Road, GU2 7YG, United Kingdom.

was used as the reference material in the twin's cup. Sample was heated at the rate of $10^{\circ}\text{C}/\text{min}$ up to 700°C and then cooled down to room temperature at the same rate. The entire solidification range was monitored and transformation temperatures were recorded (Fig. 3.1). As can be seen, the liquidus and solidus can be gained from the cooling curve and are equal to 632°C and 462°C respectively (630°C and 454°C calculated by Thermo-Calc).

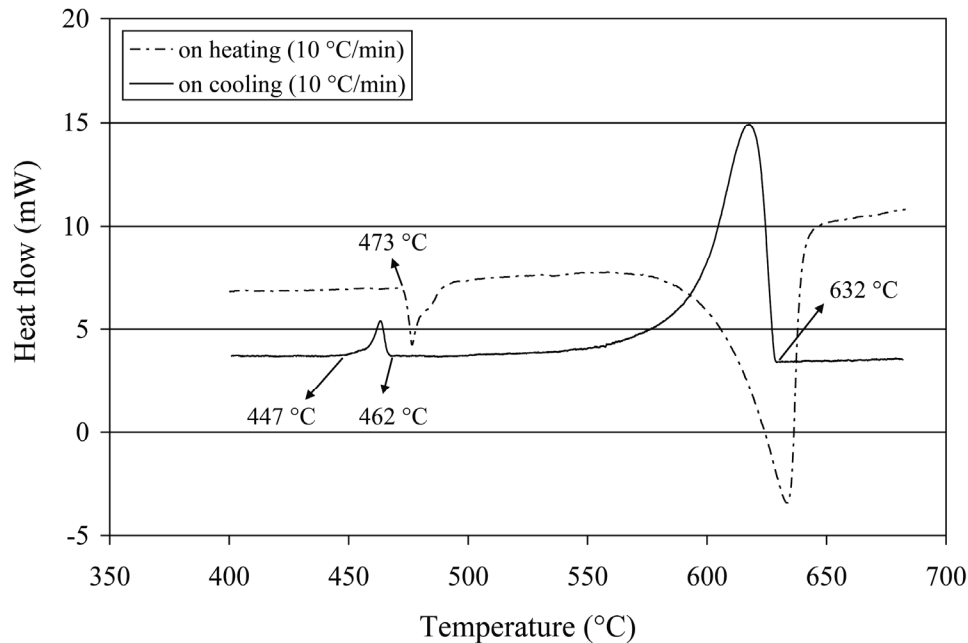


Fig. 3.1 DSC curves showing the cooling as well as heating curves gained at the heating and cooling rate of $10^{\circ}\text{C}/\text{min}$.

3.3 Thermal contraction in 7050 alloy

3.3.1 Introduction

Metals and alloys undergo dimensional changes in response to variations in temperature, a phenomenon that has critical implications for industries that process these materials at high temperatures [3]. Solidification practices, such as casting or spray-forming, and hot working procedures in the solid state, such as forging, rolling or extrusion, can be significantly influenced by thermal stresses and strains that arise from temperature variations. If not properly controlled, these effects can have an adverse influence on product quality. Residual stresses and distortion can be introduced and in the worst cases crack-type defects can be formed. Hence the optimization of such processes calls for the use of sophisticated computer models that require comprehensive data on the thermal expansion characteristics of the material. The availability of data for the thermal expansion coefficient at elevated temperatures then becomes a key issue.

In the specific case of solidification processing in DC-casting, thermal contraction occurs not only during cooling below solidus but also above solidus in the solidification range. Apparently these two phenomena have similar natures, i.e. contraction due to the fall in temperature and increase of density, but in details they

are slightly different. The solidification shrinkage is the shrinkage that occurs in the solidification range, from 100% liquid to 100% solid, as a result of density difference between the liquid and solid phases. *Solidification shrinkage* of aluminum alloys is between 6 and 8%. The *thermal contraction* is the contraction of the solid phase above and below solidus resulting from the temperature dependence of the density [4]. This contraction is in the order of 3.5% in 7050 alloy from non-equilibrium solidus to room temperature (calculated using the density values gained from JMat-Pro, see Table 3.6). It has been discussed that solidification contraction starts below an onset temperature called *rigidity temperature* [4-6]. Above this temperature, the grains are free to move with respect to each other and do not transfer any forces. Moreover, at higher than rigidity temperature, the liquid phase can easily flow between grains and therefore the melt feeding and the redistribution of solute elements occur without much difficulty [4]. Below the rigidity temperature stresses start to accumulate in the casting.

3.3.2 Determination of the thermal contraction in the solidification range

The onset of thermal contraction in the mushy zone is determined by the rigidity temperature, which can be measured experimentally using the solidification contraction setup [4]. The experimental setup used is based on the idea suggested by Novikov [5] and measures the linear contraction of the material upon solidification. It consists of the following parts: 1- a T-shaped graphite mold with a moving wall (Fig. 3.2), 2- a water cooled bronze base and 3- a linear displacement sensor (linear variable differential transformer (LVDT)) attached to the moving wall from outside and aligned with the longitudinal axis of the mold.

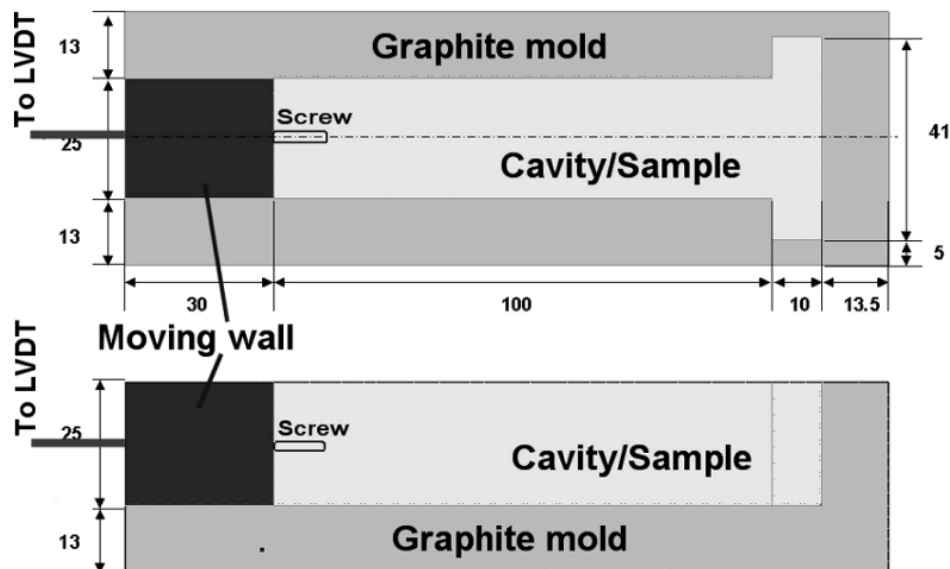


Fig. 3.2 Schematic view of the mold and the moving wall. Dimensions in mm [4].

The reason behind the T shape, which is narrower than the main cavity, is to make the melt solidify faster there than in the rest of the mold, and so the solidifying sample can be fixed on that side [4]. To attach the solidifying metal to the moving wall on the

other side of the cavity, a metallic screw was attached to the moving wall (Fig. 3.2). After filling the mold with the melt, the molten metal freezes against the metallic screw and gets attached to it. The cross section of the main cavity was 25×25 mm with a gage length of 100 mm. The linear displacement is measured by a SCHAEVITZ[§] DC-DC LVDT with accuracy up to $6 \mu\text{m}$ or 0.006 %. A low-friction mechanism of the LVDT and low friction of the moving wall/mold (graphite on graphite) contact provides minimum interference into the measured expansion/contraction. The temperature was measured by a K-type thermocouple with 0.25-mm-thick wires and an open tip that enables quick response to the changing temperature. The temperature was recorded with an accuracy of 2 K. The thermocouple was installed vertically in the center of the mold 1.5 mm above the bottom (Fig. 3.3). The position of the thermocouple was chosen based on the numerical simulation results showing that the development of solidification occurs from the opposite ends and from the corners of the mold towards the centre [7]. As a continuous solid network is required before the displacement sensor can follow the changes of the length, the bottom center of the mold was chosen for monitoring the temperature.

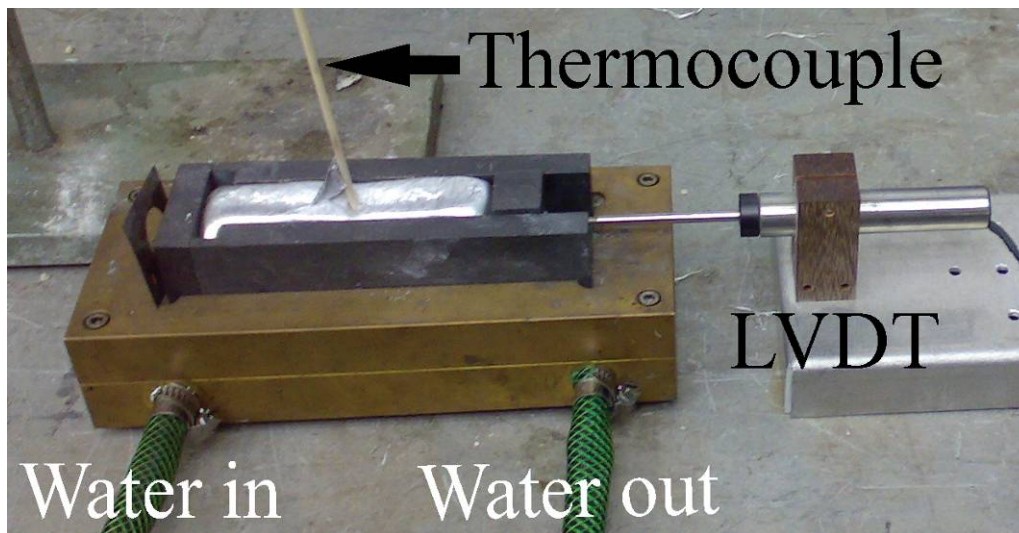


Fig. 3.3 A photograph showing the solidification contraction setup.

The samples were gained from the grain refined 7050 DC-cast billet (Ø 255-mm) mentioned in Table 2.1. The alloy was melted and poured into the mold cavity shown in Fig. 3.2. During the experiments the temperatures and displacements were recorded against time by a computer and the data was saved for further analysis. In order to obtain information on critical temperatures and cooling rates, temperature was plotted against time and cooling curves were constructed (Fig. 3.4). Afterwards, the displacement data was plotted against temperature to be able to follow the expansion/contraction behavior of the material (Fig. 3.5). The preshrinkage expansion is mainly due to the evolution of gases and the pressure drop over the mushy zone, and it depends on the alloying system, melting, and solidification conditions [5,8]. The onset temperature of thermal contraction in the mushy zone was determined for three samples using the graphs as in Fig. 3.5 with an average value of $559 \pm 5^\circ\text{C}$

[§] SCHAEVITZ is a trademark of Schaevitz Sensors, Hampton, VA.

which corresponds to the solid fraction 0.8 (calculated by JMat-Pro). The linear solidification contraction was determined as follows [4]:

$$\varepsilon_s = \frac{l_s + \Delta l_{\text{exp}} - l_f}{l_s} \times 100\%$$

Where l_s is the initial length of the cavity (100 mm); l_f is the length of the sample at the temperature of non-equilibrium solidus and Δl_{exp} is the preshrinkage expansion. For the DC-cast 7050 alloy mentioned above the linear solidification contraction was measured -0.23% at non-equilibrium solidus (462°C).

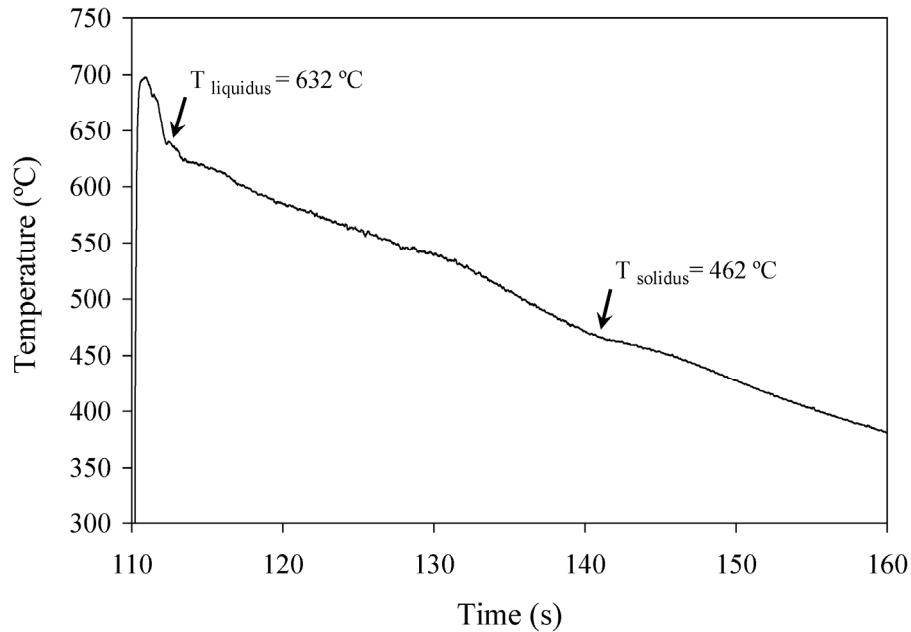


Fig. 3.4 A typical cooling curve obtained from the remolten 7050 DC-cast billet [2].

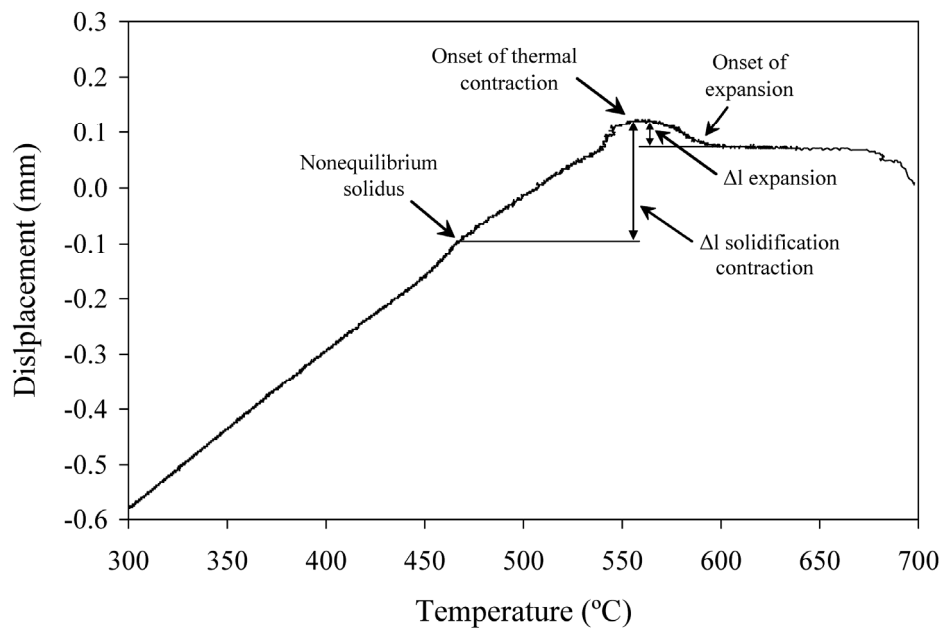


Fig. 3.5 A typical displacement-temperature curve obtained from the remolten 7050 DC-cast billet [2]. Δl expansion, Δl contraction, onset of thermal contraction, expansion and the non-equilibrium solidus are shown.

3.3.3 Determination of the coefficient of thermal expansion/contraction

Although the coefficient of thermal contraction could be determined from the solidification contraction test results, thermal gradients formed in the T-shape bar result in some deviations from the real coefficients. To investigate the thermal contraction behavior of the material in the solid state, we performed dilatometry tests in a BÄHR-805AD machine with an accuracy of 0.3 μm . Cylindrical samples 4 mm in diameter and length of 10 mm were machined out of grain refined (HP-GR) and non-grain refined (HP-NG) 7050 blocks with chemical compositions mentioned in Table 2.1. They were heated in a vacuum chamber (8.0×10^{-5} mbar) from room temperature to 450°C at the rate of 10 °C/min and then cooled down to room temperature at similar rate. The data acquisition rate was 50 points per minute. The mean coefficients of thermal contraction/expansion (α_m) were determined afterwards over the following increments using the Eq. 3.2 [9-11]: 25-100°C, 100-200°C, 200-300°C, 300-400°C, and 400-450°C.

$$\alpha_m = \frac{1}{L_0} \frac{\Delta L}{\Delta T} \quad (3.2)$$

Coefficients of thermal expansion (CTE) for both grain refined and non-grain refined alloys are shown in Fig. 3.6. As can be seen, non-grain refined alloy shows slightly higher CTE values at all temperatures, which is in agreement with Zhang *et al.* results [12]. In the same graph, the CTE values gained from the thermodynamics data base JMat-Pro (provided by Corus-Netherlands (IJmuiden)) are shown. The results gained from the JMat-Pro show a continuous increase in CTE values and they are in good agreement with our results for the non-grain refined alloy at 100°C and at ultimate high temperatures of 400°C and 450°C.

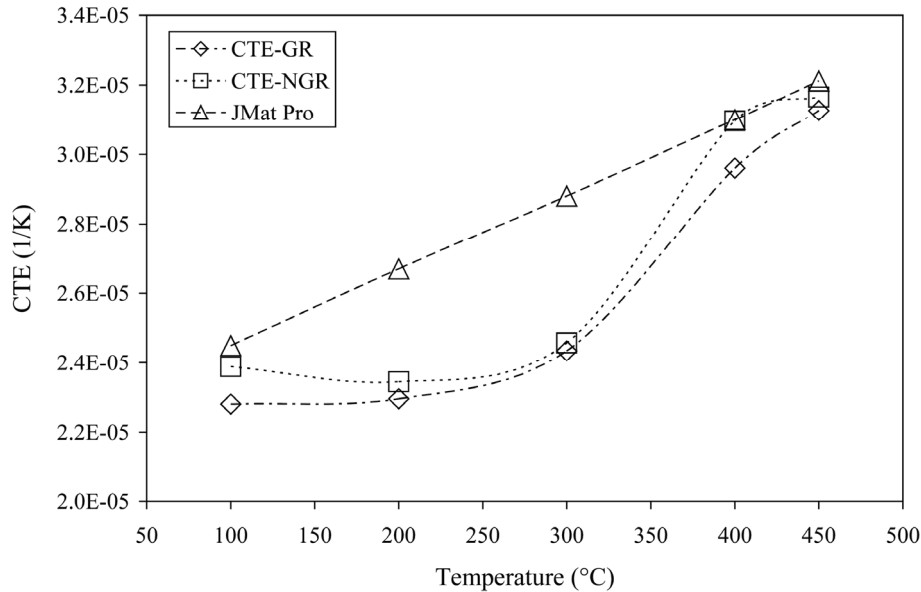


Fig.3.6 Coefficient of thermal expansion gained from dilatometry tests for grain refined and non-grain refined 7050 samples. The results from JMat-Pro database are also shown for comparison.

In contrast to the calculated data, experiments show a jump in CTE values between 300-400°C. This jump is the result of a considerable change in the slope of the thermal expansion curve against temperature at around 300°C upon heating and 255°C on cooling (Figs. 3.7 and 3.8). In Fig. 3.9 the coefficient of thermal contraction is shown against temperature. Upon cooling, our results further deviate from the JMat-Pro results. The jump in the CTC values is observable in the non-grain refined sample between 200-300°C. Although such a jump is not noticeable in the grain refined sample upon cooling, one can detect it in the thermal contraction curve (Fig. 3.8) at around 255°C. The deviation from the JMat-Pro results could be on the one hand due to the fact that our results are the average coefficients over a temperature range rather than the absolute values at expected temperatures. But on the other hand, they may express more truly the contraction behavior of the material in the as-cast state (As the sample spent only 45 minutes at temperatures below 400°C, and it was immediately cooled down after reaching this temperature, the changes in the microstructure would be insignificant and the sample may still be considered as as-cast upon cooling).

In Fig. 3.9, the CTC results gained from the T-setup are also shown. One notices that at lower temperatures they show better agreement with the JMat-Pro compared to dilatometry results. At higher temperatures, however the deviation is higher, which is due to the gas evolution in the solidified metal [12].

In order to understand why the thermal contraction/expansion curves experience such a sudden change in slope, we performed some DSC tests from room temperature to 500°C for both as-cast grain refined, non-grain refined and also DC-cast 7050 samples in the genuine as-cast condition without any heat treatment processing. Samples were heated up and cooled down in a PerkinElmer Sapphire DSC machine at the rate of 10 °C/min. Figs. 3.10 and 3.11 show the DSC results for the grain refined samples. It should be noted that the DSC curves of the grain refined, non-grain refined and DC-cast samples showed similar behavior. As can be seen, upon heating, two dissolutions occur around 127°C and 318°C. The corresponding phases might be modifications of the η' phase that form upon cooling at speeds lower than 10 °C/s [13,14]. Such phases are also detectable on the cooling curves (Fig. 3.11). The two sharp peaks on the right correspond to the T-phase (482 °C) and S-phase (500 °C) [13]. The formation of such phases might be in accordance with the strange behavior of the CTE/CTC values and the severe loss in ductility, and they may affect the mechanical properties of the material. As detailed study of solid-state transformations was not in the scope of the current project, no more research could be performed at this stage, but this interesting topic may be studied further in the future using transmission electron microscopy (TEM).

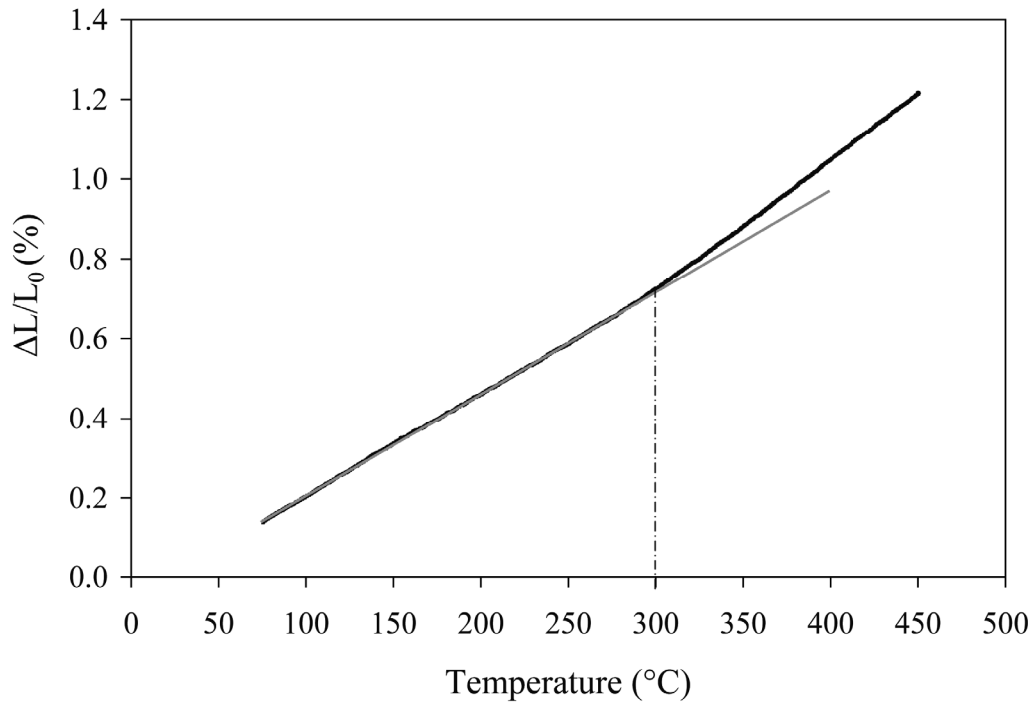


Fig. 3.7 Percentage thermal expansion as a function of temperature upon heating for the grain-refined sample.

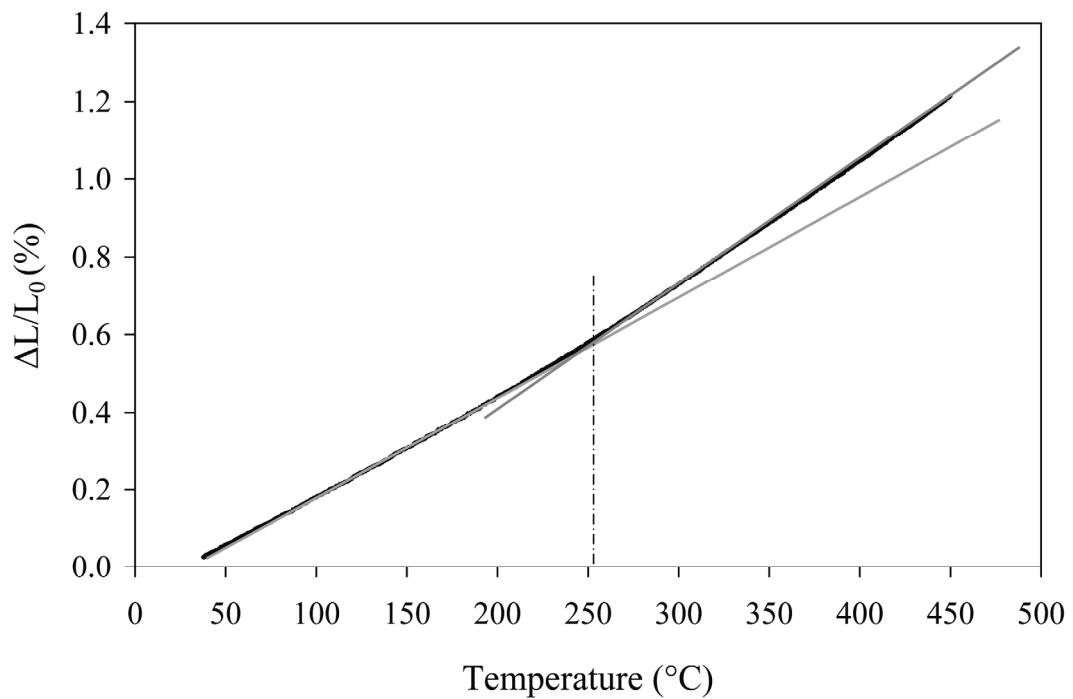


Fig. 3.8 Percentage thermal contraction as a function of temperature upon cooling for the grain-refined sample.

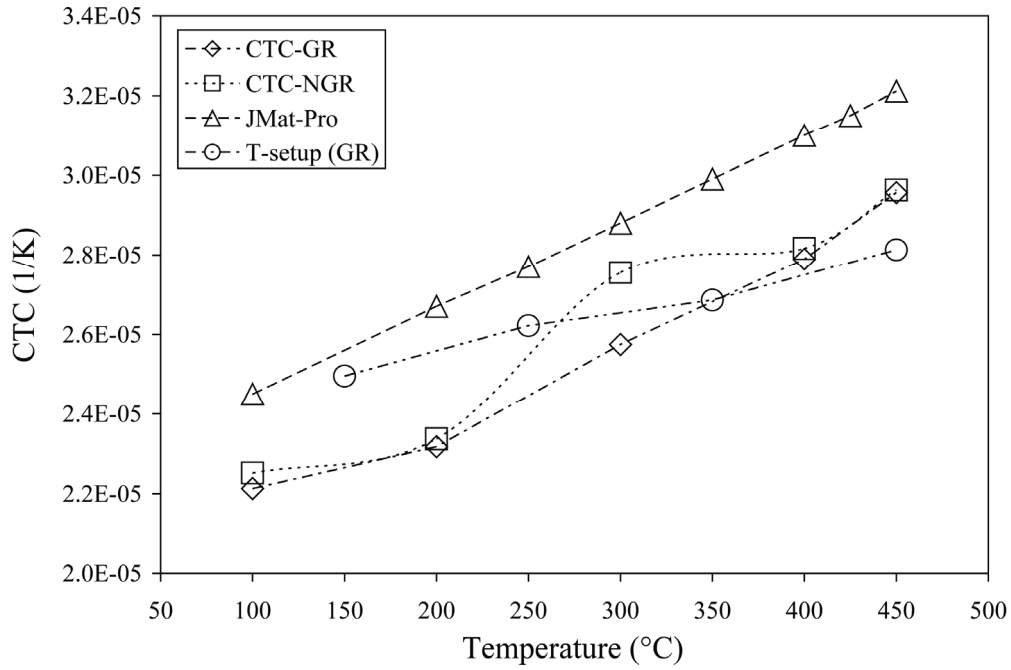


Fig.3.9 Coefficient of thermal contraction gained from dilatometry tests for grain refined and non-grain refined 7050 samples. The results from the JMat-Pro database and the T-setup are also shown for comparison.

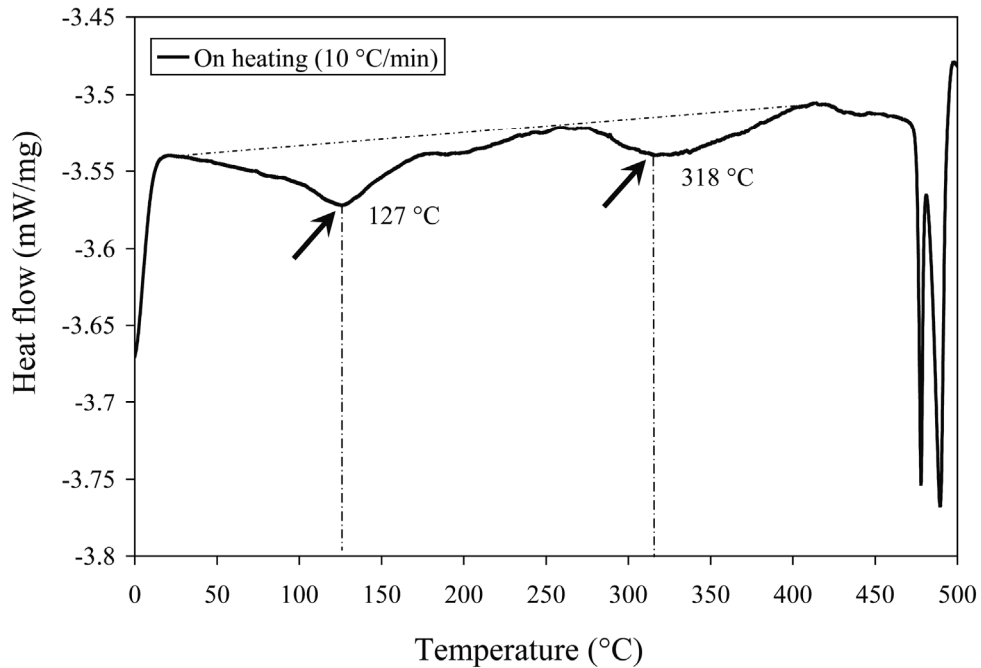


Fig. 3.10 The DSC curve of the grain refined 7050 sample from room temperature to 500°C heated at the rate of 10°C/min. Arrows show the dissolution temperatures of the precipitates formed after solidification under slow cooling conditions.

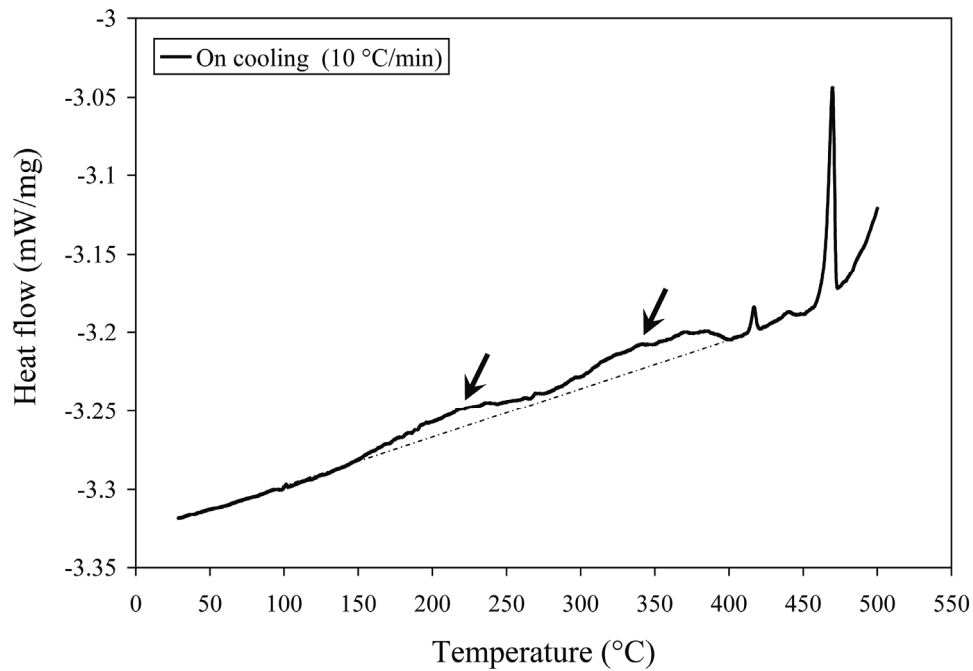


Fig. 3.11 The DSC curve of the grain refined 7050 sample from 500°C to room temperature cooled at the rate of 10°C/min. Arrows show the precipitation temperatures during solidification under slow cooling condition.

As mentioned early in this section, we measured the CTE values using different experimental techniques whose results vary from the JMat-Pro calculations. In order to check how this difference in results may affect the thermomechanical simulation results, we performed some simulations using ALSIM5, using the CTE values gained from JMat-Pro and dilatometry tests for the grain refined material (more details of the simulation process are explained in Chapters 5-7). The results are shown in Tables 3.4 and 3.5 where various components of the stress tensor are presented as follows: radial stress (σ_{rr}), circumferential stress ($\sigma_{\theta\theta}$), axial stress (σ_{zz}), mean stress (σ_m), and maximum principal stress (σ_{11}). The selected points are 65 mm above the bottom block at the center, mid-radius and surface of a billet 200 mm in diameter. As can be seen, the difference in the results is not significant although some noticeable differences appear at the surface that can be ignored as the stress level (σ_{zz}) is quite low there compared to the rest of the billet. As the contraction behavior of the material in dilatometry tests could not be well explained and due to the fact that our simulation results are not very sensitive to the variations in CTE values gained from different methods, we decided to use the thermal expansion coefficients gained from JMat-Pro.

Table. 3.4 Simulation results showing the residual stress level in Ø 200-mm billet after 500 s of casting in the steady state regime for three points: center, mid-radius, and surface of the billet 65 mm above the bottom block. CTE values from *JMat-Pro* are applied.

Distance from the center of the billet (mm)	σ_{rr} (MPa)	$\sigma_{\theta\theta}$ (MPa)	σ_{zz} (MPa)	σ_m (MPa)	σ_{11} (MPa)
0	70.8	70.9	8.4	49.9	71
50	44.4	0	-15.4	9.3	44
100	3.25	-85	3.5	-26	3.5

Table 3.5 Simulation results showing the residual stress level in Ø 200-mm billet after 500 s of casting in the steady state regime for three points: center, mid-radius, and surface of the billet 65 mm above the bottom block. CTE values from *dilatometry tests* are applied.

Distance from the center of the billet (mm)	σ_{rr} (MPa)	$\sigma_{\theta\theta}$ (MPa)	σ_{zz} (MPa)	σ_m (MPa)	σ_{11} (MPa)
0	66.8	67	8.2	47.3	67
50	43.5	1.7	-17	9.3	43.5
100	2.8	-78.4	6	-23.2	6.1

3.3.4 The thermodynamic database for thermal properties

Since experimental determination of all thermal properties of the material is time consuming and costly, the rest of thermal properties of the material was gained from the thermodynamics database JMat-Pro, provided by Corus-Netherlands (IJmuiden) for the as-cast 7050 alloy. These thermal as well as physical properties included: coefficient of thermal expansion, conductivity, specific heat, latent heat of fusion and density and are presented in Table 3.6. The fraction liquid in the mushy zone was also calculated by JMat-Pro using the Scheil equation and is presented in Table 3.7.

Table 3.6 Thermal properties of the 7050 alloy used for simulations (JMat-Pro).

Temp. (°C)	Density (kg/m ³)	Thermal conductivity (W/m.K)	Coefficient of thermal expansion (10 ⁻⁵ /K)	Specific heat (J/kg.K)
20	2825.8	149.4	2.29	857
100	2811.0	156.0	2.45	897
200	2790.1	162.7	2.67	939
300	2767.8	168.2	2.88	979
400	2744.1	173.0	3.10	1020
500	2699.8	160.9	3.45	1373
600	2629.9	124.5	4.03	4125
632	2515.0	80.8	4.88	1115
700	2491.6	83.2	5.11	1141
Latent heat of fusion (at 461°C) = 376.14*10 ³ J/kg				

Table 3.7 Fraction liquid gained from Scheil equation (JMat-Pro) for the 7050 alloy.

Temp. (°C)	632	631	630	625	620	610	600	580	540	500	460
f_l	1	0.97	0.94	0.78	0.65	0.49	0.38	0.27	0.16	0.12	0

3.4 Summary and conclusions

In this chapter, some critical thermal properties of the 7050 alloy were studied experimentally to obtain a proper knowledge and also the necessary data for the computer simulations. Liquidus as well as nonequilibrium solidus temperatures were

measured through DSC tests. Solidification contraction tests were performed to measure the onset of thermal contraction (rigidity temperature) during solidification. The rigidity temperature is crucial for computer simulations as it determines the onset of thermal stress formation. In the next step, the thermal contraction/expansion behavior of the genuine as-cast material was studied in the solid state and the CTE/CTC values were measured. These values showed some deviation from those calculated by JMat-Pro. Such a behavior might be due to the formation of some precipitates during cooling after the end of solidification. Further investigation of this phenomenon was not part of this project especially as the simulation results did not show significant difference in stress levels computed using JMat-Pro and dilatometry CTC values. The database of the thermal properties were eventually collected and prepared for implementation in ALSIM5.

References

- [1] J.R. Davis, ASM Specialty Handbook: Aluminium and aluminium alloys, ASM international, Materials Park, Ohio, 1994.
- [2] I. Alastuey, Thermo-mechanical Modelling to Predict Cold Cracking in 7xxx Aluminium Alloys During DC-casting, Master's thesis, Delft University of Technology, The Netherlands, 2009.
- [3] J.D. James, J.A. Spittle, S.G.R. Brown, R.W. Evans, Meas. Sci. Technol. 12 (2001) R1–R15.
- [4] D.G. Eskin, Suyitno, J.F. Mooney, L. Katgerman, Metall. Mater. Trans. A 35 (2004) 1325-1335.
- [5] I.I. Novikov, Goryachelomkost tsvetnykh metallov i splavov (Hot Shortness of Nonferrous Metals and Alloys), Nauka, Moscow, 1966.
- [6] L. Arnberg, L. Bäckerud, Solidification Characteristics of Aluminum Alloys, vol. 3, Dendritic Coherency, AFS, Des Plaines, IL, 1996.
- [7] M. M'Hamdi, A. Pilipenko, D.G. Eskin, in: Transactions of the American Foundry Society and the 107th Annual Castings Congress, Milwaukee, USA, 2003, pp. 333-340.
- [8] G.A. Korol'kov, G.M. Kuznetsov, Sov. Castings Technol., No. 6 (1990) 1-3.
- [9] American Society for Testing and Materials 1995 ASTM E228-295.
- [10] American Society for Testing and Materials 1999 ASTM E289-299.
- [11] R.K. Kirby, in: K.D. Maglic, A. Cezairliyan, V.E. Peletsky (Eds.), Compendium of Thermophysical Property Measurement Methods, vol 2, Plenum Press, New York, 1992, pp. 549–567.
- [12] L. Zhang, D.G. Eskin, M. Lalpoor, L. Katgerman, Mater. Sci. Eng. A 527 (2010) 3264–3270.
- [13] S.-T. Lim, Y.-Y. Lee, H.-S. Eun, Mater. Sci. Forum 475-479 (2005) 369-372.
- [14] F.X. Gang, J.D. Ming, M.Q. Chang, Z. B. You, W. Tao, Trans. Nonferrous Met. Soc. China 16 (2006) 577-581.

Chapter 4

Microstructural features of intergranular brittle fracture and cold cracking in high strength aluminum alloys

Intergranular brittle fracture in the solid state has been mainly observed and reported in steel alloys and precipitation hardened Al-alloys where intergranular precipitates cover a major fraction of the grain boundary area. 7xxx series aluminum alloys suffer from this problem in the as-cast condition when brittle intermetallics cover almost all the inter-dendritic spaces and grain boundaries. Brittle intermetallics formed during the non-equilibrium solidification upon direct chill (DC) casting provide favorable sites for crack initiation and propagation at different stages of solidification and cooling. Such micro-cracks may propagate rapidly in the presence of residual thermal stress fields and lead to catastrophic failure of DC-cast ingots; cold cracking. In this Chapter fractographic investigations are performed on as-cast AA7050 specimens failed during tensile tests described in Chapter 2. In-situ tensile tests were also performed using an environmental scanning electron microscope (ESEM) to follow the propagation path of cracks at critical temperatures corresponding to cold cracking. They revealed how catastrophic failure of the material occurs by crack propagation through the brittle intermetallics. Comparison of the fracture surfaces of tensile specimens with real cracked billets helped us to understand the mechanisms of crack formation and catastrophic failure.

4.1 Introduction

Cold cracking in DC-cast billets of high strength aluminum alloys occurs in the as-cast condition when the accumulated thermal stresses reach some critical value at the tip of the cracks [1-3] (Fig. 4.1). Ingots of such strong heat treatable alloys are normally difficult to cast because of their susceptibility to cold cracking [4]. The segregation that occurs during the non-equilibrium solidification results in the individual grains being substantially enveloped by divorced eutectics of brittle intermetallic phases. The low ductility and strength of these grain boundary networks, compared to the grain bodies, can cause them to fracture under thermal stresses generated in the ingot by the freezing process and the subsequent cooling contraction. Formation of micro-cracks above the solidus temperature and their propagation in the interdendritic liquid film, *hot cracking*, [5] can make the material even more susceptible to cold cracking. Such micro-cracks can reach a critical size and further

propagate in the presence of thermal stresses at subsolidus temperatures. The fracture mode can be classified as intergranular mainly, although the cracks fast propagating through the intermetallics may also leave some features of transgranular fracture behind when they cross the interdendritic bridges [6,7].



Fig. 4.1 A photograph showing a high-strength aluminum alloy slab failed spontaneously after casting through cold cracking. The 500 kg part broke apart and was projected several meters away [1].

It has been argued that the segregation of impurities at grain boundaries and the concomitant reduction in surface energy plays central role in most or at least many types of intergranular brittle fracture [8]. Perhaps the best known example is temper embrittlement in alloy steels, the most important impurities in this case being P, Sn and Sb [9]. At or near room temperature however, where diffusion is not involved in the actual fracture process, three types of intergranular brittle fracture has been reported as: *brittle fracture*, *intergranular chemical dissolution*, and *intergranular rupture* [10]. Brittle fracture is caused by reduced cohesion between crystals so that inter-atomic bond separation can be achieved through the action of stresses normal to the boundary before these stresses can be relieved by local plastic flow. This may be assisted by environmental factors such as hydrogen (absorbed by the solid) [11,12] or surface adsorption phenomena (e.g. liquid metal embrittlement [13]). Intergranular chemical dissolution is a form of stress corrosion cracking that appears to result from compositional differences between grain boundaries and the matrix, solute segregation or second phase particles. Intergranular rupture occurs due to void formation at hard or weakly bonded inclusions lying along grain boundaries, and coalescence of these voids due to plastic flow [10].

One of the extreme forms of the intergranular rupture is associated with the formation of intergranular precipitates that cover a major fraction of the grain boundary area. Although the phase particles would not be deleterious when more homogeneously dispersed, under some conditions they may concentrate almost entirely along the grain boundaries, often in a dendritic morphology [10]. Examples of this phenomenon can be found in different types of alloys. For example, the formation of AlN on grain boundaries of forgings of Al-killed steels containing nitrogen due to incomplete

degassing during solidification [14] and the formation of Cr_{23}C_6 in stainless steels under special conditions of heat treatment [15]. The other extreme form is associated with an intergranular precipitate which occupies a minor fraction of the grain boundary area but which is weakly bonded to the matrix so that cavities form with very little overall strain. An example of this is the overheating phenomenon in steels in which either MnS or CrS particles form in austenite upon cooling and produce intergranular rupture. A classical example of intergranular rupture in Al alloys is found with precipitation-strengthened alloys which often contain intermetallic compounds lying primarily along grain boundaries [16]. The combination of the stiff grains and the precipitate-free zone (PFZ) adjacent to the grain boundaries tends to force most of the plastic flow to be localized at the grain boundaries and the fracture strain is accordingly further reduced.

Although intergranular brittle fracture has been reported for steels and precipitation hardened Al-alloys, only few references are available on behavior of high strength aluminum alloys in the as-cast condition [17,18]. This might be due to the fact that they experience such poor mechanical properties early in the production chain. In the as-cast condition the microstructure is different from that of age hardened alloys, with intermetallics and non-equilibrium eutectics segregated at grain boundaries and interdendritic spaces. In this Chapter we try to fill the mentioned gap in the field of solidification processing of aluminum alloys. Investigation of microstructural features of crack propagation and cold cracking may help in better understanding the conditions leading to failure and in revealing the probable relations to hot cracking. To achieve this, fracture mode and failure mechanism of the high strength AA7050 were examined using in-situ tensile tests and fractography techniques. In-situ tensile tests performed in an ESEM assisted further investigation of crack propagation at elevated temperatures.

4.2 Experimental procedure

The 7050 samples used for fractographic investigations were cut from the specimens failed during the tensile and Charpy impact tests mentioned in Chapter 2 [6,19]. These samples were either cast in the copper mold or made through DC-casting at Corus-Netherlands (IJmuiden). A DC-cast AA7475 billet produced by a third party and cold-cracked at the sawing attempt was also used for fractography investigations. This gave us a rare opportunity to study the real cold crack. The chemical composition of the alloys studied in this Chapter is listed in Table 2.1.

To investigate the fracture mode and determine the probable crack propagation paths, fracture surfaces were preserved. A Jeol JSM-6500F scanning electron microscope (SEM) was used for fractographic observations.

In order to follow the crack propagation path at temperatures corresponding to cold cracking (room temperature-200°C), in-situ tensile tests were performed on DC-cast 7050 flat tensile specimens (Fig. 4.2) using a Fei/Philips XL30FEG ESEM equipped with a tensile stage and hot stage both from Kammrath & Weiss^{**}. A V-notch was introduced in the center of the specimen to be able to track and follow the crack propagation path. Specimens were all polished before tests using diamond suspensions (up to 1 μm). Room temperature tests were performed using a secondary

^{**} In-situ observations were made by Mr. G. ten Brink at Zernike Institute for Advanced Materials, University of Groningen.

electron detector (SED) mode at a scanning rate of 25 Hz (tv rate). As the SED detector could not be applied at higher temperatures, the gaseous secondary electron detector (GSED) in the ESEM mode was used. The SEM was placed in wet mode conditions at 3 torr water vapor pressure. All samples were deformed at the velocity of $0.5 \mu\text{m/s}$ corresponding to the strain rate of 10^{-5} s^{-1} , which resembles those typical of DC casting [20].

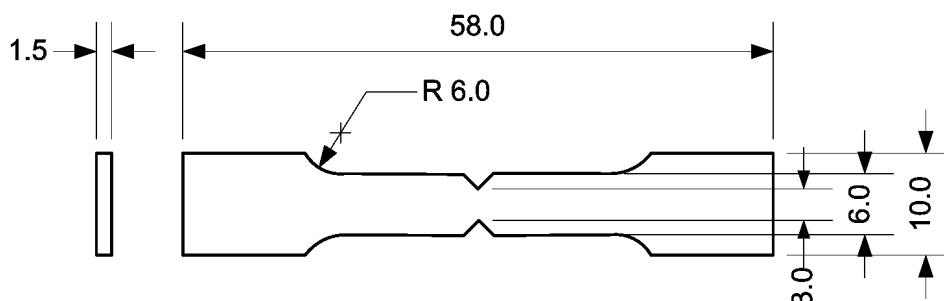


Fig. 4.2 Geometry of the tensile specimen used for in-situ tensile tests in ESEM (dimensions in mm) [21].

4.3 Results and discussion

4.3.1 Conventional mechanical tests

In Chapter 2 it was shown how the 7050 alloy experiences a severe loss in ductility at temperatures below 300°C at all strain rates (Fig. 2.9b). As our focus in this Chapter is the brittle fracture which occurs due to the lack of ductility at certain temperatures, it is worthwhile to show the corresponding graph here. Fig. 4.3 shows the changes in the ductility of the DC-cast 7050 samples failed during the tensile tests at the strain rate of 10^{-2} s^{-1} from room temperature to 400°C . As can be seen the ductility falls about 90% as the temperature decreases below 300°C and the material becomes extremely brittle at temperature close to room temperature.

Fig. 4.4a shows the fracture surface of the tensile specimen taken from the mid-radius of the 7050 DC-cast billet and failed at room temperature. As can be seen the material has failed in an interdendritic manner and the dendrites failed through decohesion have left valleys behind or are projecting outwards. Detailed examination of the fracture surfaces at higher magnifications revealed why the material fails in such a manner.

As discussed in Chapter 2, the microstructure of the 7050 alloy in the as-cast condition consists of the α -aluminum phase (a solid solution of Zn, Cu, and Mg in Al) as the matrix and non-equilibrium eutectics represented by a mixture of T (Al_6CuMg_4 and $\text{Al}_2\text{Mg}_3\text{Zn}_3$), M (AlCuMg and MgZn_2) and S (Al_2CuMg) phases [22,23]. Such phases are non-equilibrium phases that form as a result of relatively high solidification rates present under practical casting conditions. Constituent phases ($\text{Al}_7\text{Cu}_2\text{Fe}$ and Mg_2Si) formed by impurities during solidification can also be found, which are detrimental to the mechanical properties as they act as stress-raisers [4,24]. Presence of such phases at grain boundaries and interdendritic spaces can lead to fracture in two ways: either by cleavage (Figs. 4.4b and 4.5) in the presence of

resolved normal stresses on them, or decohesion from the matrix (Fig.4.4c) as a result of their weak bonding to it.

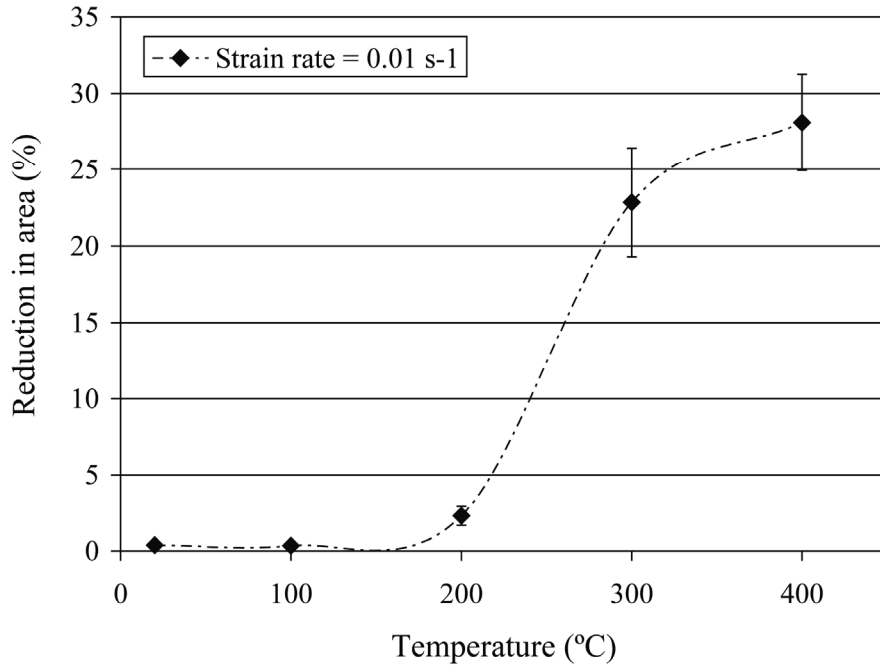


Fig. 4.3 Reduction in area in 7050 DC-cast samples in the as-cast condition at the strain rate of 10^{-2} s^{-1} [21]. Similar trend was observed for lower strain rates as shown in Fig. 2.9.

Fig. 4.4b shows the root of a dendrite failed as a result of cleavage in the intermetallics covering its surface. From fractographic point of view they resemble “terraced” fracture surfaces that found to be characteristic of Ti-6Al-4V specimens with microstructures consisting of β -phase and acicular α -phase [25]. Fig. 4.4b also shows how constituent phases such as $\text{Al}_7\text{Cu}_2\text{Fe}$ and Mg_2Si formed by impurities Fe and Si, can act as stress raisers and crack initiators (white arrow) [26]. This was proven by energy-dispersive X-ray spectroscopy (EDX) analysis of the tip of the dendrites (projecting outwards) indicating traces of Fe and Si. Electron backscattered image of the fracture surfaces can easily reveal how the intermetallics sitting at the interdendritic spaces can facilitate the materials failure through cleavage (Fig. 4.5). Decohesion of non-equilibrium phases from the matrix on the other hand occurs as a result of difference of thermal expansion coefficients (TEC) of intermetallic particles (low TEC) and aluminum matrix (high TEC). Rise and build up of thermal stresses at the particle–matrix interface may eventually lead to crack formation and decohesion at the interface (Figs. 4.4c and 2.6d). Furthermore, solidification shrinkage may lead to the preferential formation of pores at the intermetallic/matrix interfaces, which may facilitate decohesion and crack initiation in these locations upon further cooling.

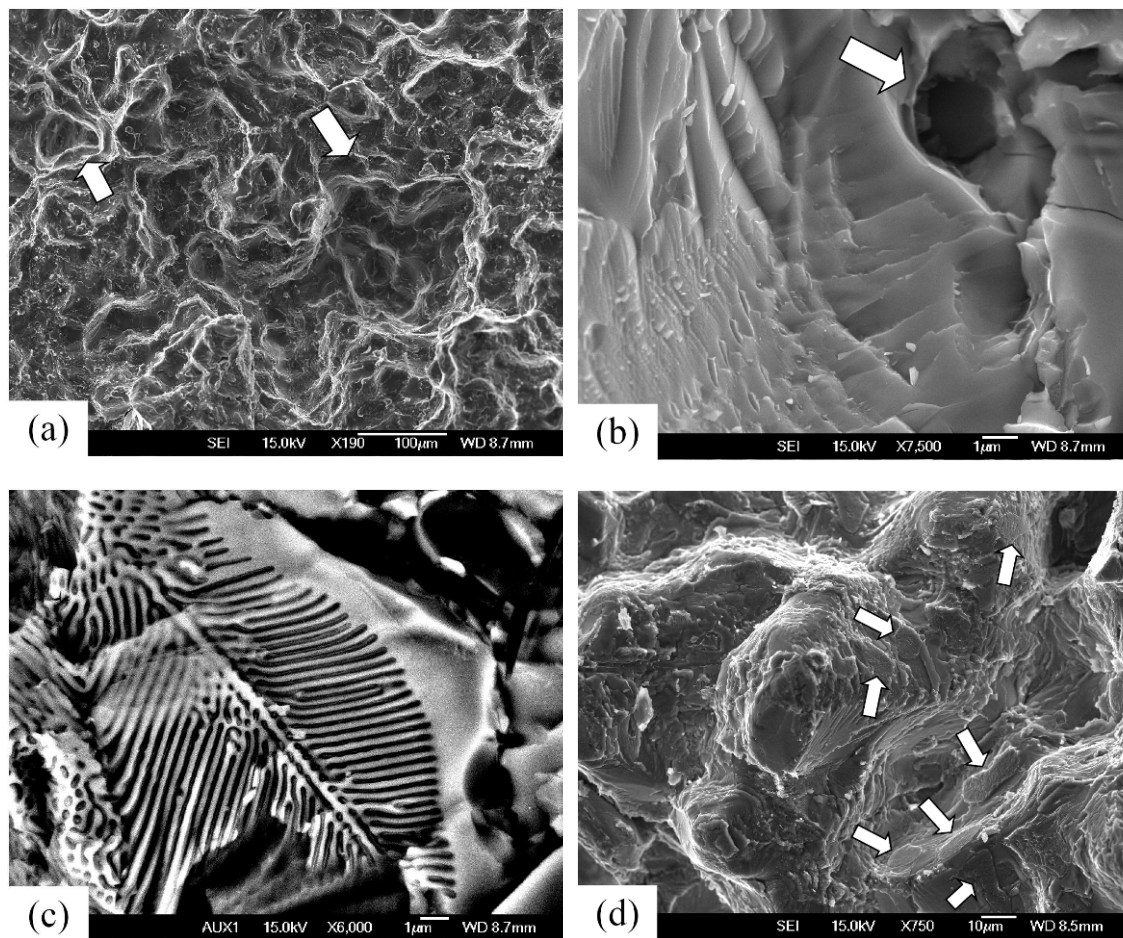


Fig. 4.4 Fracture surfaces in a 7050 alloy: (a) sample taken from the middle radius of the billet failed at room temperature at the strain rate of 10^{-2} during the tensile tests. Arrows show the dendrites failed through decohesion; (b) the same sample as (a) but at higher magnification showing the terraced cleavage on side walls of a dendrite arm. Arrow shows the probable crack initiation site, which appeared to be a Fe rich particle; (c) electron backscattered image of the sample taken from the surface of the billet failed at 200 °C at the strain rate of 10^{-2} during tensile test; and (d) the same sample as (a) showing the outward projecting dendrite arms with broken side bridges on them [6]. Arrows show the broken (cleaved?) interdendritic bridges, SEM.

Another feature of fracture surfaces is the presence of fractured interdendritic bridges that fail when the cracks propagating through the intermetallics reach them (Fig. 4.4d). In the first glance they might be mistaken for intermetallics, but closer observation and EDX analysis of such points confirms that they represent the matrix.

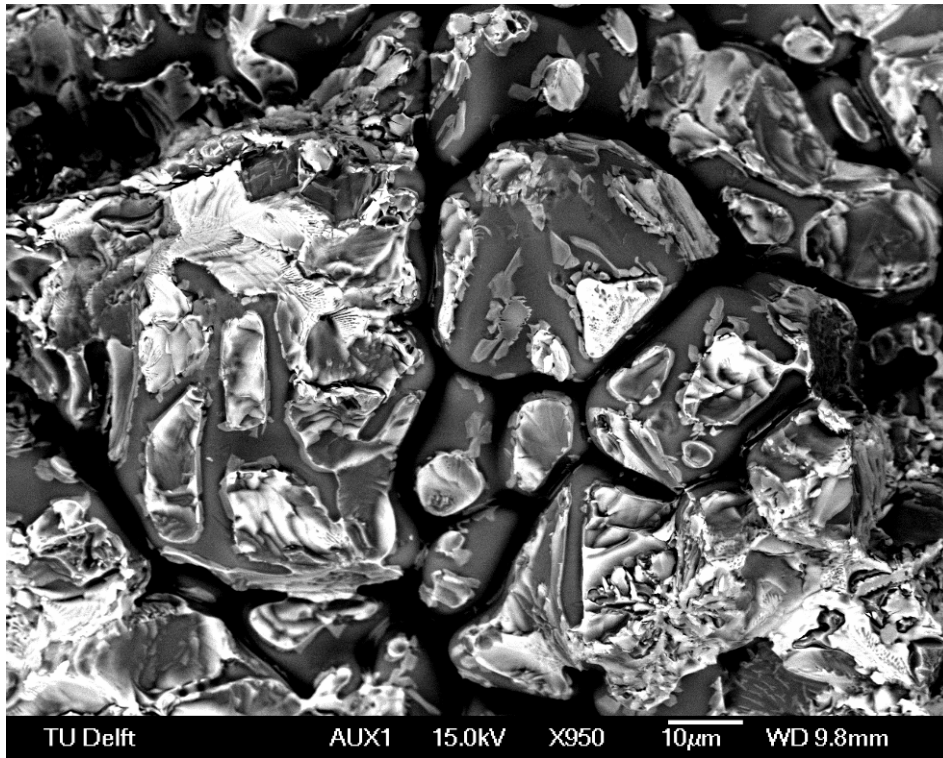


Fig. 4.5 Electron-backscattered image of the fracture surface of a 7050-HP-NG sample failed during Charpy test at room temperature; non-equilibrium eutectics and intermetallics appear brighter, signs of cleavage are visible in some of these particles [19]. The SEM image of the same sample is shown in Fig. 2.19d.

4.3.2 In-situ tensile tests in ESEM

In-situ tensile tests confirmed the results of the conventional tensile mechanical tests, although the extreme brittleness of the alloy below 300°C prohibited us from precise tracking of the crack. As mentioned before, notches were introduced in the middle of the tensile specimen to be able to confine and follow the cracks. The stress concentration at the tip of the notch however made the material even more brittle so that the samples failed catastrophically in less than 0.04 s and the scanning rate was not fast enough to be able to follow it. Comparing the images before and after failure, it turns out that the crack mainly propagates through the intermetallics (Fig. 4.6 a, b). Similar tests were performed at 200°C using the GSED and the results are presented in Fig. 4.6c, d. Although the crack propagates mainly in an intergranular manner, transgranular propagation is inevitable as the intermetallics are not covering 100% of the interdendritic spaces. Similar behavior was observed at 300°C.

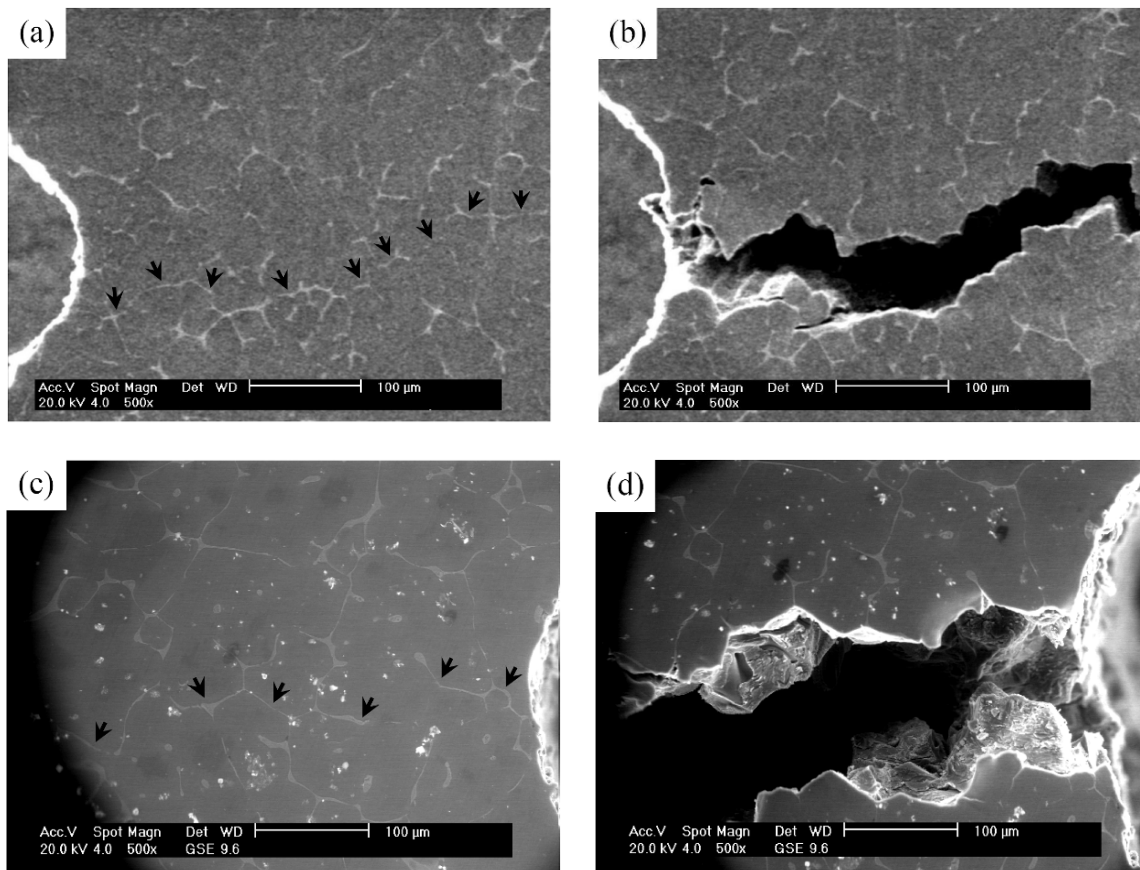


Fig. 4.6 ESEM micrographs showing the tip of the notch on the tensile specimen: a) before and b) after failure at room temperature, and c) before and d) after failure at 200°C. 500X. Stains on (c) and (d) come from the Santovac 5 grease used for thermal contact between the furnace and the sample. Arrows show the intermetallics through which the crack propagated later on [21].

4.3.3 Observations from real cracked billets

Fig. 4.7a shows a 7475 DC-cast billet failed through cold cracking at room temperature in the cast shop. As can be seen the macroscopic fracture surface consists of two parts distinguishable by a color contrast. Microscopic fracture surfaces of both parts follow the same features, i.e. decohesion of dendrite arms from each other through the mechanisms explained in the previous section. But more detailed examination suggests that they have been formed at different stages of casting under different loading conditions. Fracture surfaces of the samples gained from the darker, central part resembled Fig. 4.4a with dendrite arms failed through decohesion. At the edge of the billet, however interdendritic brittle decohesion was mixed with a transgranular brittle fracture (cleavage) of individual dendrite arms (Fig. 4.7b, c).

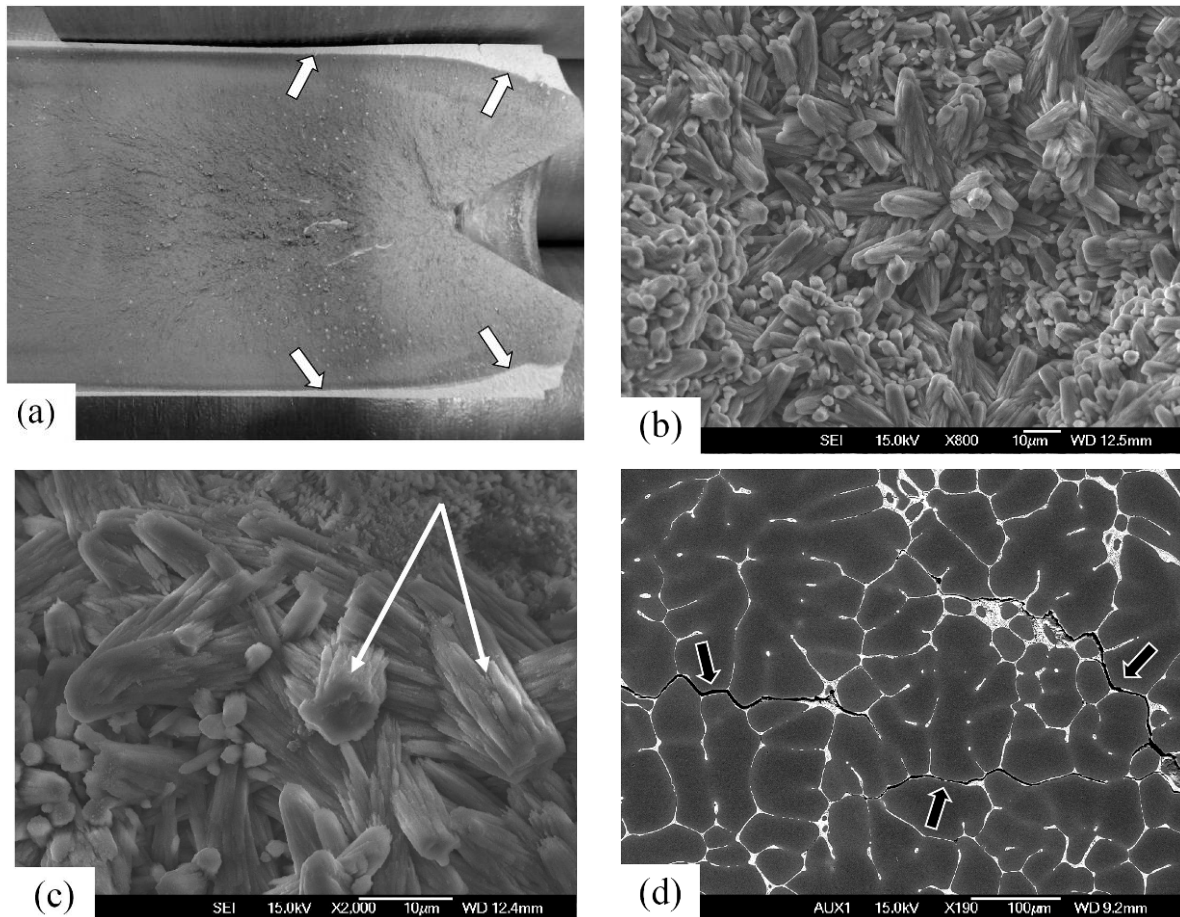


Fig. 4.7 Fracture surface of the cold-cracked Ø200-mm 7475 DC-cast billet: (a) view of the billet split open during sawing attempt, showing two parts of fracture surface separated by a color contrast, (b) fracture close to the surface of the billet, in the bright area in (a), SEM; (c) same fracture surface as (b) but at a higher magnification, arrows show broken dendrite arms [19], SEM and (d) micrograph showing hot cracks formed during the solidification in the center of the 7050 DC-cast billet with a diameter of 255 mm, these cracks did not reach the critical conditions for catastrophic failure, so the billet remained sound, electron backscattered image, SEM [21].

Similar fracture features were observed by Suyitno *et al.* [27] on DC-cast Al–1%Cu alloys, although they appeared in the center of the billets on hot crack surfaces. They were reported as bridged grain boundaries possibly failed in a transgranular manner over a temperature range close to the nonequilibrium solidus, hence in the “gray” area between hot and cold cracking. The Al–1%Cu alloy is a low-alloyed material with little eutectic liquid phase distributed in the solid network at the moment of fracture. The structure of this alloy is similar to that of the 7050 alloy, and the conditions of fracture might be close. Microcracks may be induced in the billet shell by tensile stresses formed in the water impingement zone at the surface of the DC-cast billet, as will be discussed later in Chapters 5 to 7. They may not instantly grow as the tensile stresses are immediately replaced by compressive ones [28]. Compressive stresses at the surface of the billet may relax and the microcracks can easily open and propagate during the transportation or sawing of the billet. Signs of scratching on the lateral sides of the dendrite arms (Fig 4.7c) may account for step-wise relatively slow growth of the crack under conditions of stress relieving at the surface. Catastrophic failure of the entire billet evidenced by the dark central fracture surface in Fig. 4.7a may be,

however the result of propagation of hot tears formed in the center of the billet during solidification (Fig. 4.7d). They might have not reached the critical size for the catastrophic failure in the DC-cast 7050 alloy shown in Fig. 4.7d, therefore the billet remained sound. More details on this will be discussed in Chapter 6 (section 6.4).

Conditions of crack formation and propagation at different locations of the billet may be better understood if we take the role of residual thermal stresses into account. Computer simulation results have shown that the residual thermal stresses built up during the DC-casting process of high strength aluminum alloys are highly tensile in the center of the billet and they diminish or even turn to compressive by moving towards the surface [28,29]. Fig. 4.8 shows the distribution of stresses in a AA7050 billet with a diameter of 200 mm after 300 s of DC-casting under steady state conditions.

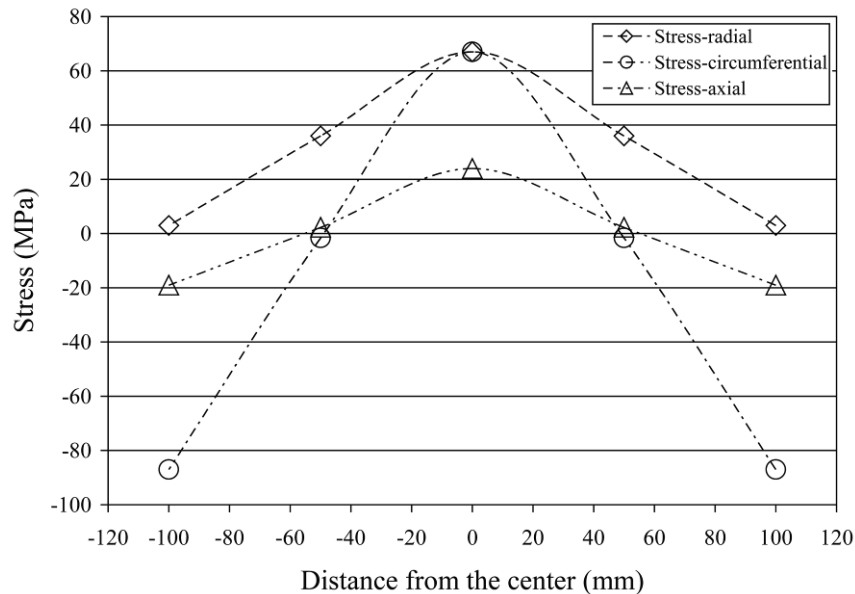


Fig. 4.8 Distribution of residual thermal stresses (normal stresses) in the lower part of a AA7050 DC-cast billet after 300 s of casting under steady state conditions. Thermal stresses are computed using ALSIM5 [21].

Tensile stresses (in all axial, circumferential and radial directions) can lead to hot cracking in the center of the billet at final stages of solidification when the dendrite arms are still surrounded by liquid films [30]. Microcracks formed at this stage may propagate further after the end of solidification in the tensile stress fields and result in cold cracking. Failure of the material can be even facilitated if we take the extreme fall (90%) in the ductility and brittleness of the material below 300 °C into account (Fig. 4.3). But not all the microcracks formed at high temperatures may lead to catastrophic failure. On macroscopic level the crack plane gets preferably oriented normal to the maximum principal stress component [31]. In microscopic scale however, microcracks may form above solidus temperature and preferably propagate through the liquid intermetallics, making a river-like pattern (Fig. 4.7d). Thus, they may not eventually get aligned normal to the maximum principal stress component; the condition, which ceases their growth and prevents the catastrophic failure.

4.4 Conclusions

Brittle intergranular fracture in high strength aluminum alloys occurs mainly due to the continuous coverage of the grain boundaries and intergranular areas by brittle intermetallics and non-equilibrium eutectics formed at final stages of solidification. Weak bonding to the matrix and cleavage are the main reasons for the abrupt fracture of the brittle intermetallics that are covering the fracture surfaces entirely. Micro-cracks formed at the interfaces between the matrix and intermetallics act as stress raisers and facilitate catastrophic failure of the DC-cast billets. What makes cold cracking rather unpredictable, however, are the microstructural complexities and the river-like pattern made by micro-cracks that are mainly *hot cracks*. Catastrophic failure may occur if they get oriented normal to the maximum principal stress and reach the critical size. In-situ tensile tests showed that any stress raiser can make the material even more brittle and result in brittle fracture even at higher temperatures where the material is expected to be more plastic. Based on the observations, cold cracking can be classified as brittle fracture, although it possesses some features of intergranular rupture, except for the fact that no plastic deformation is observed.

References

- [1] O. Ludwig, J.-M. Drezet, B. Commet, B. Heinrich, in: C-A. Gandin and M. Bellet (Eds.), *Modeling of Casting, Welding and Advanced Solidification Processes*, MCWASP XI, TMS, Warrendale (PA), 2006, pp. 185-92.
- [2] W. Boender, A. Burghardt, E. P. van Klaveren, J. Rabenberg, in: A. T. Tabereaux (Ed.), *Light Metals 2004*, TMS, Warrendale (PA), 2004, pp. 679-84.
- [3] M. Lalpoor, D.G. Eskin, L. Katgerman, *Metall. Mater. Trans. A* 40 (2009) 3304-3313.
- [4] J.B. Hess, *Metall. Trans. A* 14 (1983) 323-327.
- [5] W.M. van Haaften, W.H. Kool, L. Katgerman, *J. Mater. Eng. Perform.* 11 (2002) 537-543.
- [6] M. Lalpoor, D.G. Eskin, L. Katgerman, *Proc. 12th Intern. Conf. on Fracture*, Ottawa, National Research Council of Canada, 2009 (CD).
- [7] K.-M. Chang, B. Kang, *J. Chin. Inst. Eng.* 22 (1999) 27-42.
- [8] P. G. Shewmon, *Metall. Mater. Trans. B* 29 (1998) 509-518.
- [9] T. Ogura, C.J. McMahon, Jr., *Met. Sci.* 18 (1984) 37-43.
- [10] C. J. McMahon Jr., V. Vitek, J. Kameda, in: G.G. Chell (Ed.), *Developments in Fracture Mechanics-2; The Mechanics and Mechanism of Fracture in Metals*, Applied Science Publishers, 1981, pp. 193-246.
- [11] P.G. Shewmon, *Mater. Sci. Technol.* 1 (1985) 1-8.
- [12] J. Kameda, C.J. McMahon Jr., *Metall. Trans. A* 14 (1983) 903-911.
- [13] W. Rostoker, J.M. McCaughey, H. Markus, *Embrittlement by liquid Metals*, Reinhold Publ. Co., New York, NY, 1960, p. 22.
- [14] J. Wright, A.G. Quarrell, *J. Iron Steel Inst.* 200 (1962) 299.
- [15] J. Plateau, G. Henry, C. Crussard, *Rev. Met.* 54 (1957) 3.
- [16] D.A. Ryder, A.C. Small, *Fracture of Solids*, Interscience, New York, 1962, p. 237.
- [17] W. Roth, *Z. Metallkd.* 40 (1949) 445-460.

- [18] V.A. Livanov, in: A.F. Belov, G.D. Agarkov (Eds.), *Aluminum Alloys: Casting, Rolling Forging, Stamping and Heat Treatment*, Oborongiz, Moscow, 1955, pp. 128-168.
- [19] M. Lalpoor, D.G. Eskin, L. Katgerman, *Mater. Sci. Eng. A* 497 (2008) 186-194.
- [20] W.M. van Haaften, *Constitutive Behavior and Hot Tearing during Aluminum DC Casting*, PhD thesis, Delft University of Technology, Delft Press, The Netherlands, 2002, pp. 11–38.
- [21] M. Lalpoor, D.G. Eskin, G. ten Brink, L. Katgerman, *Mater. Sci. Eng. A* 527 (2010) 1828-1834.
- [22] N.A. Belov, D.G. Eskin, A.A. Aksenov, *Multicomponent Phase Diagrams: Applications for Commercial Aluminum Alloys*, Elsevier, Amsterdam, 2005, pp. 199–202.
- [23] J.D. Robson, *Mater. Sci. Eng. A* 382 (2004) 112-121.
- [24] Z. Yubo, C. Jianzhong, Z. Zhihao, Z. Haitao, Q. Ke, *Mater. Sci. Eng. A* 406 (2005) 286-292.
- [25] J.A. Fellows, *Fractography and Atlas of Fractographs*, *Metals Handbook*, vol. 9. 8th Ed., American Society for Metals, Metals Park, Ohio, 1974, pp. 278-279 .
- [26] D.S. Thompson, *Metall. Trans. A* 6 (1975) 671-683.
- [27] Suyitno, D.G. Eskin, L. Katgerman, *Mater. Sci. Eng. A* 420 (2006) 1–7
- [28] M. Lalpoor, D.G. Eskin, L. Katgerman, *Proc. THERMEC 2009, Adv. Mater. Res.* 89-91 (2010) 319-324
- [29] J.F. Grandfield, P.T. McGlade, *Mater. Forum* 20 (1996) 29-51.
- [30] M. M'Hamdi, A. Mo, H.G. Fjær, *Metall. Mater. Trans. A* 37 (2006) 3069-3083.
- [31] M. Schöllmann, H.A. Richard, G. Kullmer, M. Fulland, *Int. J. Fracture* 117 (2002) 129-141.

Chapter 5

Thermomechanical simulation of the DC-casting process in AA7050 billets

The experimental procedure followed in Chapters 2 and 3 revealed the thermomechanical behavior of the material over the post-solidification temperature range. We learned how the material loses its ductility upon cooling and behaves in an extremely brittle manner. However, the experiments performed were carried out under steady conditions (constant temperature) and differ from the real conditions occurring during the DC-casting process. In the latter, non-equilibrium cooling conditions govern, which leads to steep temperature gradients. To understand the thermomechanical behavior of the material under such conditions, computer simulations are required. In Chapters 2 and 3 the mechanical as well as thermal properties of the AA7050 alloy were studied with the aim to extract the constitutive parameters and establish the necessary databases for thermomechanical simulations. Numerical models can simulate the thermomechanical behavior of an ingot during casting and after solidification and reveal the critical locations and stages where the catastrophic failure of the billet is more probable to take place. Simulation of residual thermal stresses of an AA7050 alloy during DC-casting using ALSIM5 indicates that under steady-state casting conditions large compressive stresses form in the vicinity of the billet surface in the circumferential direction. Stresses change sign on moving towards the centre of the billet and become tensile with high magnitudes in radial and circumferential directions, which make the billet prone to hot and cold cracking.

5.1 Introduction

In order to optimize the DC-casting process and minimize the ingot cracking without conducting expensive trials, numerical modeling of the thermal and stress history of the ingot is required. Numerical simulation of thermal stresses during DC-casting can reveal those stages and locations at which the material susceptibility to cracking is high. The state of residual thermal stresses has been computed before for various aluminum alloys using different commercial and non-commercial finite element packages [1-8]. The simulation results have been utilized in studying and eventually prediction of hot cracks [9,10], butt curling [5,7] or cold cracks [6,8]. So far, the cold cracking criteria have been derived by applying the fracture mechanics to the normal

stresses gained from simulations [6,8]. The derived criteria, however can be more realistic providing that the mechanical properties and constitutive parameters used for determination of simulation results are extracted from the samples in the genuine as-cast condition. In the stress relieved [11] or homogenized [12] states the material shows higher plasticity and the constitutive parameters are different, which can lead to unreliable simulated stress and strain levels in the billet. The plane strain fracture toughness values that are necessary for critical crack size assessment can be hardly found in the literature. The only existing values are measured from the samples in the stress relieved or homogenized state [5] and do not represent the genuine as-cast material. The reported results are also the critical stress intensity factors rather than standard ASTM-E399 K_{Ic} values. In this Chapter, the finite element package ALSIM5 is used to compute temperatures, thermal stresses, and strains during the starting phase and the steady-state regime in an AA7050 billet with the diameter 200 mm. The constitutive parameters and mechanical properties obtained from the genuine as-cast material (Chapter 2) were embedded in the model for calculation of residual thermal stresses/strains. The contour maps of the components of the stress/strain tensor were studied afterwards in detail to understand the locations and stages over which the billet has the highest propensity to cracking. The yielding behavior of the alloy was also investigated by assessing the contour maps of the hardening parameter, the effective stress and the accumulated effective viscoplastic strain.

5.2 Presentation of the Model

ALSIM5 was used for the computation of temperature profile and stress/strain fields in a round AA7050 billet. In this chapter we discuss the mechanical models involved (with a nomenclature in Table 5.1), but a thorough description of the simulation process can be found elsewhere [13-16]. The simulated geometry consisted of the hot top, mold, water jet, bottom block and the casting domain as shown in Fig. 5.1. Rectangular bilinear iso-parametric elements with four nodes were used that become finer with moving from the center towards the surface of the billet (Fig. 5.1). As the bottom block moves downwards during casting, new elements with the size of 0.75 mm are added to the geometry at the casting speed to simulate the continuous casting conditions. Meanwhile, the mold, hot top and molten metal retain their initial position. Due to axial symmetry, only half of the billet is considered and the simulations are run in 2D. Time-dependent thermal boundary conditions are defined to account for filling time, the air gap formation between the billet and the bottom block as well as at the billet surface, and for different heat extraction in different parts of the casting system [1]. The process parameters are mentioned in Table 5.2. As explained in Chapter 3, thermophysical properties of the alloy were partly gained from the thermodynamics database JMat-Pro and partly measured experimentally. Mechanical properties of the as-cast material were also determined experimentally and details were discussed in Chapter 2. As mentioned there, the negative values of the strain rate sensitivity (m) below 200 °C were neglected and replaced by zero. The list of mechanical properties in the solid state is shown in Table 5.3.

Table. 5.1 Nomenclature.

T	temperature
g_s, g_l	volume fraction of solid, liquid
p_s, p_l	pressure in solid, liquid
σ_s	solid stress tensor
τ_s	deviatoric part of σ_s
$\hat{\sigma}_s$	effective solid stress invariants
$\bar{\sigma}_s$	von Mises stress
J_1, J_2	first and second stress invariants
$\epsilon_s, \epsilon_s^T, \epsilon_s^e, \epsilon_s^p$	total, thermal, elastic, viscoplastic strain
$\dot{\epsilon}_s^p$	effective viscoplastic strain rate
X	stress triaxiality
C	partial cohesion strain rate
E	Young's modulus
A_2, A_3	functions of g_s in closing relation
α, C^*	function of g_s and X
$p, \alpha_0, \alpha_1, \Delta g_s, X_0, \Delta X$	parameters in function α and C^*
$\sigma_0, \dot{\epsilon}_0, Q, n$	parameters in solid creep law
$F, r, m, \gamma, \gamma_0, T_0$	parameters in fully solid viscoplastic model
R	molar gas constant
g_s^{coh}	fraction of solid at coherency
t	time
I	identity tensor
$\partial a / \partial t, da / dt$	partial, material derivative of quantity a
$\text{tr}(\mathbf{a}), [\mathbf{a}]^t$	trace, transpose of tensor or vector \mathbf{a}
K, n, m	parameters in extended Ludwik equation

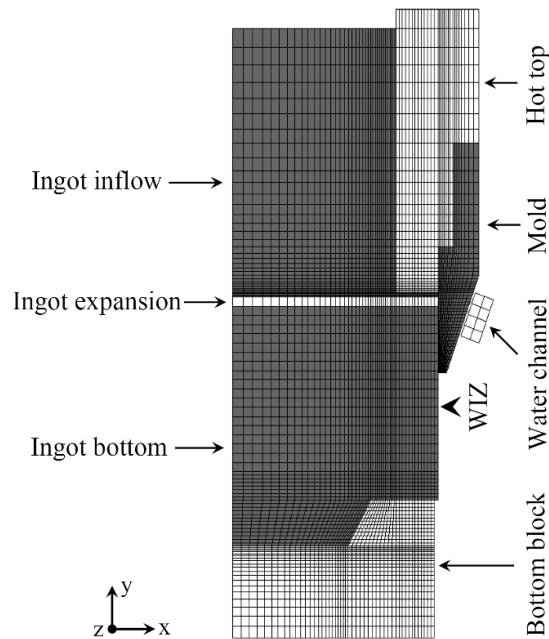


Fig. 5.1 Geometry of the DC-cast billet used for simulations showing the hot top, mold, bottom block, and the casting domain consisting of cast top (ingot inflow), cast expansion and cast bottom. Approximate position of the water impingement zone (WIZ) is also indicated on the billet surface [17].

Table 5.2 Description of casting process parameters.

Process parameter	Value
Ingot diameter (mm)	200
Final length of the billet (mm)	500
Casting speed (mm/s)	1
Melt temperature (°C)	680
Water flow rate (l/min)	80
Water temperature (°C)	15
Start temperature of bottom block (°C)	20

Table 5.3 Constitutive parameters, Young's modulus and Poisson's ratio of the 7050 alloy.

Temp. (°C)	K (MPa)	n	m	E (GPa)	Poisson's ratio
20	774 ± 32	0.42 ± 0.02	0	69.5	0.338
100	626 ± 13	0.38 ± 0.01	0	67	0.341
200	392 ± 11	0.21 ± 0.006	0	63.5	0.346
300	199 ± 4.5	0.11 ± 0.007	0.03 ± 0.007	59	0.352
400	174 ± 5	0.09 ± 0.01	0.15 ± 0.009	54.5	0.358

In ALSIM5, the metal is described as an isotropic elastic-viscoplastic material in which strain is generated during casting by thermal contraction. While the material parameters are strongly dependent on temperature, the heat generated by the viscoplastic strain is negligible [1]. A coupled thermoviscoplastic description of the material is therefore not necessary. Furthermore, the mathematical formulation is based on the classical small deformation theory, implying that the total strain may be divided into elastic, viscoplastic, and thermal parts which are noted here by superscripts e , p , and T , respectively. Hence,

$$\varepsilon = \varepsilon^e + \varepsilon^p + \varepsilon^T + \varepsilon^i, \quad (5.1)$$

where a so-called initial strain component, ε^i , is introduced. Elastic and thermal strains are calculated as follows [1]:

$$\sigma = D \cdot \varepsilon^e, \quad (5.2)$$

Where

$$D = \frac{E}{(1+\nu)(1-2\nu)} \cdot \begin{pmatrix} 1-\nu & \nu & \nu & 0 & 0 \\ \nu & 1-\nu & \nu & 0 & 0 \\ \nu & \nu & 1-\nu & 0 & 0 \\ 0 & 0 & 0 & 1-2\nu & 0 \\ 0 & 0 & 0 & 0 & 1-2\nu \end{pmatrix} \quad (5.3)$$

and

$$\varepsilon^T = - \begin{pmatrix} 1 \\ 1 \\ 1 \\ 0 \\ 0 \end{pmatrix} \int_T^{T_0} \beta(T) dT \quad (5.4)$$

where, E , ν and β are Young's modulus, Poisson's ratio and linear coefficient of thermal expansion respectively. The stress and strain calculation starts at time $t = t_0$,

which is the first time step for which the temperature field is calculated. The solution domain is then defined by all elements where one of the following two conditions is fulfilled: (1) at least three nodes are below the isotherm for the rigidity temperature T_{Rg} , or (2) two nodes are below this isotherm and the mean temperature of all four nodes is below T_{Rg} . As time proceeds, new elements are incorporated at each time step where one of the conditions given above is fulfilled [1]. All new elements are given initial values for the viscoplastic, elastic, and thermal strains in the midpoint due to the one-point integration formula of the shape functions. The initial value of the viscoplastic strain is equal to zero, and the initial value of the elastic strain, ε_0^e is generated by the hydrostatic pressure acting upon the billet by the liquid bath [1]. Since the temperature in the midpoint of new elements is generally less than the rigidity temperature, we also have an initial value of the thermal strain, ε_0^T , which is given by Eq. 5.4, while the associated stress and strain tensors in the cylindrical coordinate are given by:

$$\boldsymbol{\sigma} = \begin{pmatrix} \sigma_{rr} \\ \sigma_{\theta\theta} \\ \sigma_{zz} \\ \sigma_{rz} \\ \sigma_{zr} \end{pmatrix} \quad (5.5)$$

and

$$\boldsymbol{\varepsilon} = \begin{pmatrix} \varepsilon_{rr} \\ \varepsilon_{\theta\theta} \\ \varepsilon_{zz} \\ \varepsilon_{rz} \\ \varepsilon_{zr} \end{pmatrix}. \quad (5.6)$$

When a new element is incorporated in the mesh, the displacement in the new nodes is preset to zero, and nodes shared with “solid members” of the mesh are known from the calculation for the previous time step. Since the initial value of the total strain, ε_0 , is related to the displacement \mathbf{u} (Eq. 5.8), it is, in general, different from the sum of the (nonzero) initial values of elastic and thermal strains defined above.

$$\mathbf{u}(r, z) = \begin{bmatrix} u_r(r, z) \\ u_z(r, z) \end{bmatrix}, \quad (5.7)$$

$$\boldsymbol{\varepsilon} = \mathbf{B} \cdot \mathbf{u}, \quad (5.8)$$

where

$$\mathbf{B} = \begin{pmatrix} \frac{\partial}{\partial r} & 0 \\ \frac{1}{r} & 0 \\ 0 & \frac{\partial}{\partial z} \\ \frac{1}{2} \frac{\partial}{\partial z} & \frac{1}{2} \frac{\partial}{\partial r} \\ \frac{1}{2} \frac{\partial}{\partial z} & \frac{1}{2} \frac{\partial}{\partial r} \end{pmatrix}. \quad (5.9)$$

This problem however, is easily solved by the introduction of a so-called initial strain component defined as:

$$\boldsymbol{\varepsilon}^i = \boldsymbol{\varepsilon}_0 - \boldsymbol{\varepsilon}_0^e - \boldsymbol{\varepsilon}_0^T. \quad (5.10)$$

And its numerical value is usually much larger than the values of $\boldsymbol{\varepsilon}_0^e$ and $\boldsymbol{\varepsilon}_0^T$. The initial strain remains constant during the proceeding time steps of Eq. 5.1, and it is noted by Fjær *et al.* [1] that the $\boldsymbol{\varepsilon}^i$ in some elements has the same order of magnitude as the total strain at the end of casting.

The liquid elements are given zero stiffness, and nodes surrounded exclusively by such elements have displacements prescribed to zero. In some cases, it turns out that some regions (in the upper part) of an already solidified billet may remelt. In ALSIM, this case is modeled by resetting the strains and the stresses in the actual element(s) to zero when both conditions (1) and (2) mentioned before are no longer fulfilled and thereafter these regions are regarded as part of the liquid melt [1].

In ALSIM5, the total viscoplastic strain is treated as one quantity as it is usual in modern constitutive equations with internal variables [1]. Furthermore, a hardening parameter is introduced which accounts for the isotropic strain hardening of the material and will be discussed in section 5.3. In order to simulate the viscoplastic behavior of the material, different models are used that are valid over certain temperature ranges and some characteristic temperatures define the boundaries between them.

- 1- $\mathbf{T}_R < \mathbf{T} < \mathbf{T}_h$: the extended Ludwik equation (Eq. 2.1) and ALSPEN equations [1] (Eqs. 5.11, 5.12 and 5.13) are used to simulate the viscoplastic behavior of the material between the onset temperature of strain hardening ($T_h = 390^\circ\text{C}$) [1] and room temperature (T_R).

$$K(T) = a_c \left(1 - b_c \cdot \tanh\left(\frac{T - d_c}{c_c}\right) \right) \quad (5.11)$$

$$n(T) = a_n \left(1 - b_n \cdot \tanh\left(\frac{T - d_n}{c_n}\right) \right) \quad (5.12)$$

$$m(T) = P_0 + P_1 T + P_2 T^2 + P_3 T^3 + P_4 T^4 \quad (5.13)$$

- 2- $\mathbf{T}_h < \mathbf{T} < \mathbf{T}_m$: Between the onset of strain hardening (T_h) and the merge-properties-temperature (T_m ; few degrees below solidus (455°C) where material behavior can be described by Ludwik equation although the strain hardening is negligible), ALSPEN and cohesion model [18-22] equations are merged as follows [10]:

$$\dot{\boldsymbol{\varepsilon}}_s^p = \frac{3}{2} \frac{\dot{\boldsymbol{\varepsilon}}_s^p}{\bar{\boldsymbol{\sigma}}_s} \boldsymbol{\tau}_s, \quad (5.14)$$

with

$$\bar{\boldsymbol{\sigma}}_s = \sigma_0 \exp\left(\frac{Q}{nRT}\right) \left(\frac{\dot{\boldsymbol{\varepsilon}}_s^p}{\dot{\boldsymbol{\varepsilon}}_0}\right)^{1/n}. \quad (5.15)$$

- 3- $\mathbf{T}_m < \mathbf{T} < \mathbf{T}_{Rg}$: Between the merge-properties-temperature (T_m) and the rigidity temperature (T_{Rg} ; onset of thermal contraction in the mushy zone, 559°C , which was measured experimentally in Chapter 3) the cohesion model [18-22]

is used to simulate the thermomechanical behavior of the material in the mushy zone (all symbols are defined in Table 5.1).

$$\dot{\epsilon}_s^p = \frac{\dot{\epsilon}_0 \exp\left(-\frac{Q}{RT}\right)}{(C\sigma_0)^n} \left[-\frac{1}{9} A_2(g_s) J_1 I + \frac{3}{2} A_3(g_s) g_s \tau_s \right] \quad (5.16)$$

$$\left[\frac{1}{9} A_2(g_s) J_1^2 + 3 A_3(g_s) J_2 \right]^{\frac{n-1}{2}} ;$$

$$\dot{C} = \alpha(g_s, X) \left(1 - \frac{C}{C^*(g_s, X)} \right) \dot{\epsilon}_s^p . \quad (5.17)$$

The terms J_1 and J_2 are the first and second stress invariants defined by:

$$J_1 = -\text{tr}(\hat{\sigma}_s) = 3g_s(p_s - p_l) ; \quad (5.18)$$

$$J_2 = \frac{1}{2} \text{tr}(g_s \tau_s : g_s \tau_s) = \frac{1}{3} \bar{\sigma}_s^2 , \quad (5.19)$$

where the effective stress tensor $\hat{\sigma}_s$ is given by

$$\hat{\sigma}_s = (g_s \sigma_s - g_l p_l I) + p_l I = g_s \tau_s - g_s (p_s - p_l) I . \quad (5.20)$$

The effective strain rate is defined by

$$\dot{\epsilon}_s^p = \sqrt{\frac{2}{3} \text{tr}(\dot{\epsilon}_s^p : \dot{\epsilon}_s^p)} , \quad (5.21)$$

while the triaxiality is given by $X = J_1 / (3\sqrt{3}J_2)$. For each studied alloy, the constant parameters σ_0 , $\dot{\epsilon}_0$, Q and n can be determined from mechanical testing of the fully solid material at high temperatures. As suggested by Martin *et al.*, [20], expressions for $A_2(g_s)$ and $A_3(g_s)$ which characterize the softening effect of liquid saturated pores in the mush, can be taken from the literature [23,24]:

$$A_2(g_s) = \frac{9}{4} \left\{ n \left[(1 - g_s)^{-1/n} - 1 \right] \right\}^{-2n/(n+1)} ; \quad (5.22)$$

$$A_3(g_s) = \left[1 + \frac{2}{3} (1 - g_s) \right] g_s^{-2n/(n+1)} . \quad (5.23)$$

The functions $\alpha(g_s, X)$ and $C^*(g_s, X)$ which describe the evolution of the partial cohesion of the mush C , must be determined from careful rheology experiments at various fractions of solid and stress states. For grain refined Al-Cu alloys, Ludwig *et al.* [25] has shown that the following expressions provide a good *simplified* fit with the experimental data for the case of pure shear ($X=0$):

$$\alpha(g_s, X=0) = \alpha_0 + \alpha_1 \left(\frac{g_s^{\frac{1}{3}}}{1 - g_s^{\frac{1}{3}}} \right) ; \quad (5.24)$$

$$C^*(g_s, X=0) = 1 - (1 - g_s)^p . \quad (5.25)$$

For any stress state, the functions have been defined as [26]:

$$C^*(g_s, X) = C^*(g_s, X=0) + \frac{C^*(g_s, X=0)}{1 + \exp\left(-\frac{X - X_0}{\Delta X}\right)} ; \quad (5.26)$$

$$\alpha(g_s, X) = \alpha(g_s, X=0), \quad (5.27)$$

where the $C^*(g_s, X=0)$ and $\alpha(g_s, X=0)$ are defined as follows:

$$C^*(g_s, X=0) = \frac{1 - (1 - g_s)^p}{1 + \exp\left(-\frac{g_s - g_s^{coh}}{\Delta g_s}\right)} ; \quad (5.28)$$

$$\alpha(g_s, X=0) = \frac{\alpha_0 + \alpha_1 \left(\frac{g_s^{\frac{1}{3}}}{1 - g_s^{\frac{1}{3}}}\right)}{1 + \exp\left(-\frac{g_s - g_s^{coh}}{\Delta g_s}\right)}. \quad (5.29)$$

As the rheological parameters ($p, \alpha_0, \alpha_1, g_s^{coh}$) of the 7050 alloy are not available in the literature, the rheological parameters of the Al-2 wt% Cu were used instead [22].

- 4- $T > T_{Rg}$: At temperatures higher than rigidity temperature, the material is treated as liquid which is free to flow when forces are applied.

More details on the modeling of heat flow, fluid flow and thermal boundary conditions may be found elsewhere [27].

5.3 Results and Discussion

Casting simulation was performed for 500 s (casting length of 500 mm) to make sure that steady-state conditions are gained and stress analysis can be done. From this moment onwards the stresses remain more or less unchanged until changes in the thermal boundary conditions are applied or casting ceases. After 500 s of casting, the lower part of the billet has already reached temperatures below 80 °C (Fig. 5.4a). Figs. 5.2a through 5.2d show the contour maps of the four components of thermal stress tensor (σ_{rr} , $\sigma_{\theta\theta}$, σ_{zz} , σ_{rz}) generated under steady-state casting conditions. Other components of the stress tensor fall out due to the axial symmetry of the cylindrical coordinate. As can be seen the radial stresses displayed in the lower part of the billet (on the top of the bottom block) are compressive, which turn to tensile as we move in the positive “y” direction. Along the radial axis (x-axis) radial stresses diminish from 71 MPa to 3 MPa as we move to the surface. Similar trend is observed for the circumferential stress (along “z” axis), but the tensile stress in the center (max. 71 MPa) turns to compressive in the vicinity of the surface (–85 MPa) (Fig. 5.2b). Contour map of the axial stress (along “y” axis) follows the same trend in the lower part of the billet. This, changes in the upper part of the billet where we see compressive stresses below the high temperature zone of the billet and tensile stresses around the water impingement zone (WIZ) (Fig. 5.2c).

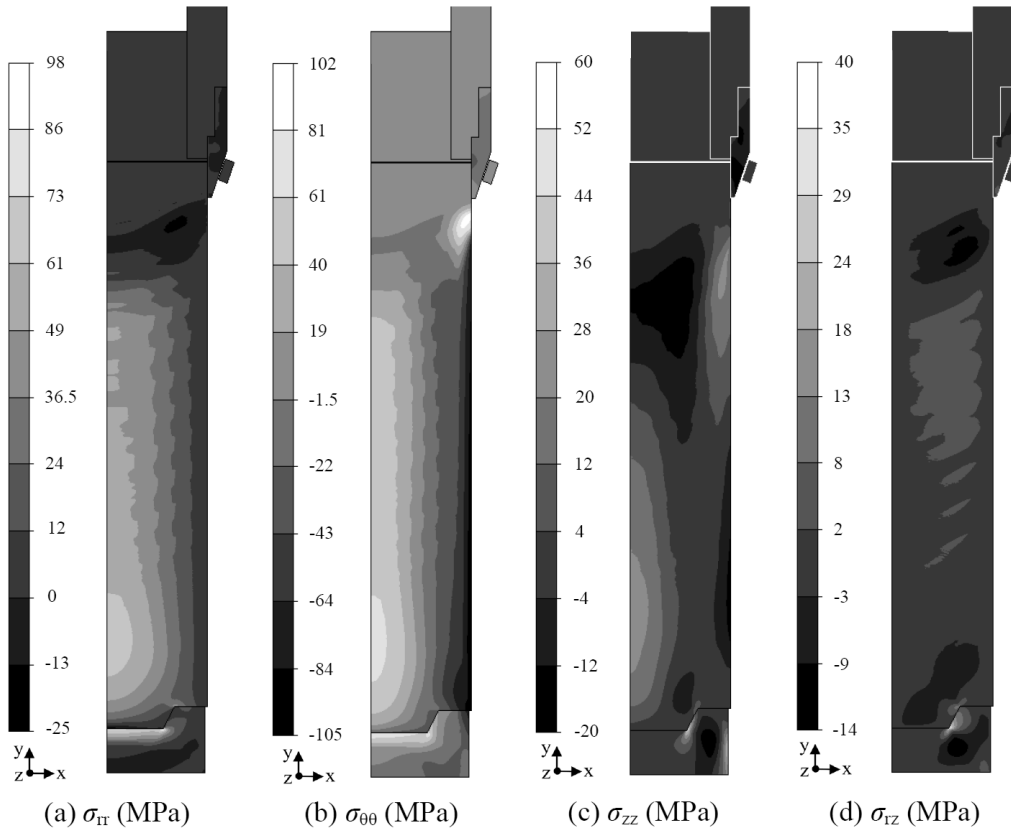


Fig. 5.2 Thermal stresses under steady-state conditions after 500 s: (a) radial, (b) circumferential, (c) axial, and (d) shear component [28]. Billet diameter 200 mm, casting speed 1 mm/s.

Shear stress component (σ_{rz}) is mainly negative with the smallest value around the water impingement area and in the lower part of the billet in the vicinity of the bottom block (Fig. 5.2d). Eventually it can be seen that the water impingement below the mold has a considerable effect on the induced stress state, especially the circumferential stress component. It appears to be highly tensile in the WIZ but turns to compressive as soon as the billet leaves the impingement zone. The reason for such a behavior is that when the billet leaves the mold, the water impinges the surface and results in rapid thermal contraction of the surface. The contraction of the surface is resisted by the central parts that are still hot and results in high tensile stresses in the WIZ. Below the WIZ, however the central parts start to contract due to the temperature fall. The surface which has now reached lower temperatures and is quite rigid counteracts the contraction of the central parts and this interaction results in the formation of tensile stresses in the center and compressive ones at the surface.

Contour maps of the viscoplastic part of the strain are shown in Fig. 5.3a through 5.3d. The radial component (Fig. 5.3a) is mostly tensile in the lower central part of the billet, decreases in mid-radius and increases again as we move to the surface of the billet. In the upper parts of the billet it remains homogenous and relatively low in value, except for the surface of the billet. The circumferential component (Fig 5.3b) appears to be tensile in the bottom center of the billet and with moving to the surface it turns to compressive in the lower corner. Unlike radial and circumferential components, the axial component shows negative (compressive) values in the center (with a minimum on top of the bottom block) and with moving to the surface (except for upper part) it converts to tensile (Fig. 5.3c). The compressive values of the axial strain in the lower part of the billet seem to be in contradiction with the aforementioned tensile axial

stresses (Fig. 5.2c). But this is mainly the consequence of negative (compressive) axial viscoplastic strain rate near the solidification front. According to the Prandtl-Reuss equations (Eq. 5.30), the sign of the viscoplastic strain rate equals the sign of the deviatoric stress component (Eq. 5.31) [29]. Similar behavior is observed in DC-casting simulation of AA6063 alloy and reported by Fjær *et al.* [1].

$$d\varepsilon^p = \frac{3}{2} \frac{d\bar{\varepsilon}^p}{\bar{\sigma}} \cdot \sigma' ; \quad (5.30)$$

$$\sigma'_z = \sigma_z - \frac{1}{3}(\sigma_r + \sigma_\theta + \sigma_z). \quad (5.31)$$

In Eq. 5.30, σ' denotes the associated deviatoric stress vector, and the effective stress $\bar{\sigma}$ and the effective viscoplastic strain increment $d\bar{\varepsilon}^p$ are defined by [29]:

$$\bar{\sigma} = \sqrt{\frac{3}{2} \sigma' \cdot \sigma'} ; \quad (5.32)$$

$$d\bar{\varepsilon}^p = \sqrt{\frac{2}{3} d\varepsilon^p \cdot d\varepsilon^p} . \quad (5.33)$$

In order to examine the occurrence of plastic yield in the billet, contour maps of the temperature, the hardening parameter α , which is defined as:

$$\alpha = \int d\alpha, \quad d\alpha = \begin{cases} d\bar{\varepsilon}_p & \text{when } T \leq T_h \\ 0 & \text{otherwise} \end{cases} [1], \quad (5.34)$$

and effective stress are used (Figs 5.4a to 5.4c). In those locations of the billet where the temperature is above T_h or no yielding is present ($\alpha = 0$) the total viscoplastic strain is generated by creep, which is the case for almost the whole billet except for the surface (Fig. 5.4b). Another clue for the strain hardening can be seen in Fig. 5.4c, where the effective stress at the surface is greater than 100 MPa, which is certainly above the 0.2% offset yield strength of the 7050 alloy above 200 °C (73 MPa at 300°C and 23 MPa at 400°C; see Fig. 2.10a). The maximum value of the accumulated (integrated) effective viscoplastic strain appears to be 2.5% and is only observed at the sharp corner on top of the bottom block (Fig. 5.4d). Another place with high accumulated effective viscoplastic strain is the surface of the billet with 1.6% deformation.

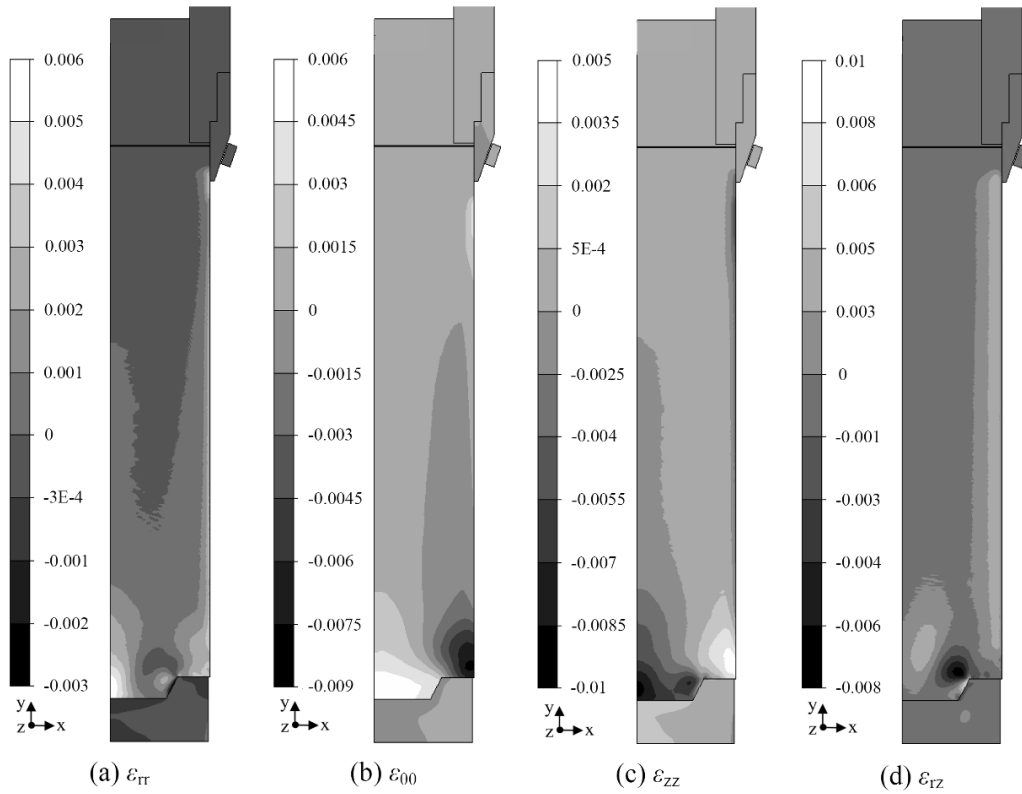


Fig. 5.3 Viscoplastic strain under steady-state conditions after 500 s: (a) radial, (b) circumferential, (c) axial, and (d) shear components [28]. Billet diameter 200 mm, casting speed 1 mm/s.

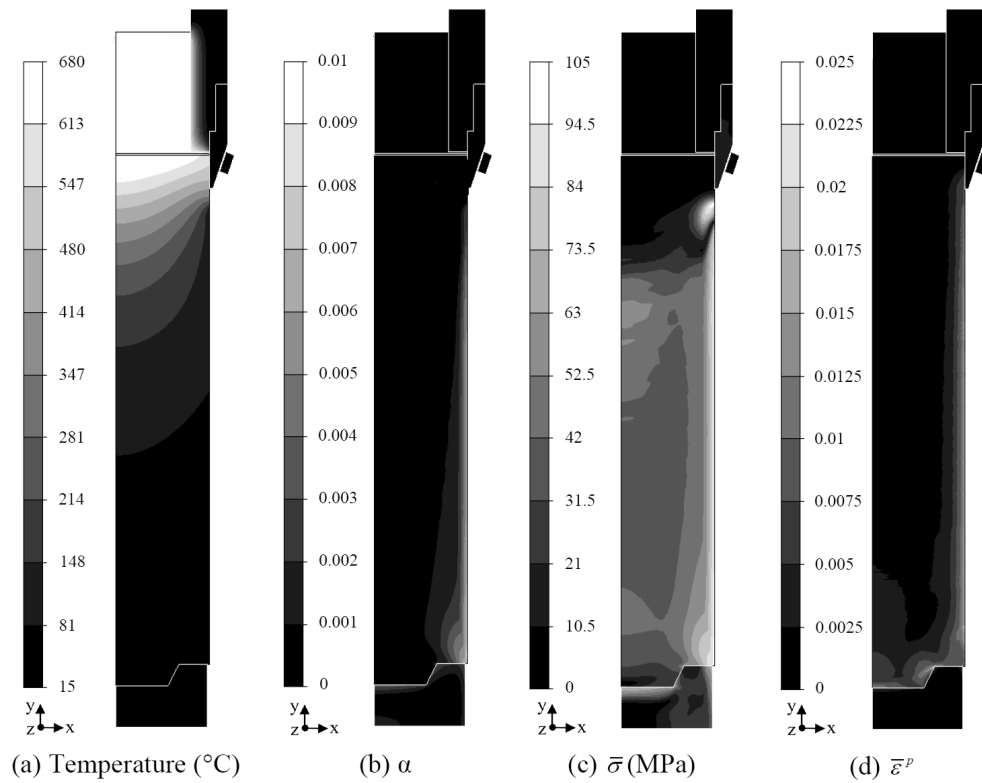


Fig. 5.4 Investigation of plastic yield and strain hardening using: (a) temperature profile, (b) hardening parameter, (c) effective stress, and (d) the accumulated effective viscoplastic strain [28]. Billet diameter 200 mm, casting speed 1 mm/s.

The contour maps of the effective stress and hardening parameter provide us with useful information on yielding of the material. In order to assess the probability of the brittle fracture however, the principal stresses ($\sigma_{11} > \sigma_{22} > \sigma_{33}$) as well as hydrostatic stress (σ_m) may be used (Figs. 5.5a to 5.5d). As can be seen the principal stress components appear to be all tensile in the center of the billet. With moving towards the surface, however they diminish or turn to compressive with σ_{33} possessing the minimum negative values (Figs. 5.5a to 5.5c). Due to the small values of the shear stress component, the principal stress axes make small angles with the normal stress axes. The σ_{33} values are in the “z” direction in the center and turn towards the “ θ ” (circumferential) axis with moving to the surface. The σ_{22} values are either in the circumferential direction (θ) or in the radial (r) as σ_{rr} and $\sigma_{\theta\theta}$ show similar values in the centre. Eventually, the σ_{11} values are mainly in the radial direction except for the WIZ where they lie in the circumferential direction. The largest component of the principal stresses can be used to assess the locations where the billet is more prone to cracking (Fig. 5.5c) [30]. More details on this issue will be discussed in Chapter 8. The maximum value of the σ_{11} stress (71 MPa) appears after 200 s of casting in the center of the billet, where the temperature is around 200°C. From this moment on, this component of stress remains roughly constant and accounts for the cracks formed in the center of the 7050 DC-cast billets cast under similar conditions. Another critical point with high tensile stresses is the WIZ, where the σ_{11} reaches its maximum (100 MPa) after 76 s. As explained before the high tensile stresses in this area are immediately replaced by compressive ones that protect the billet surface. Under specific conditions, however they may lead to the failure of the billet, but this issue will be discussed further in Chapter 8.

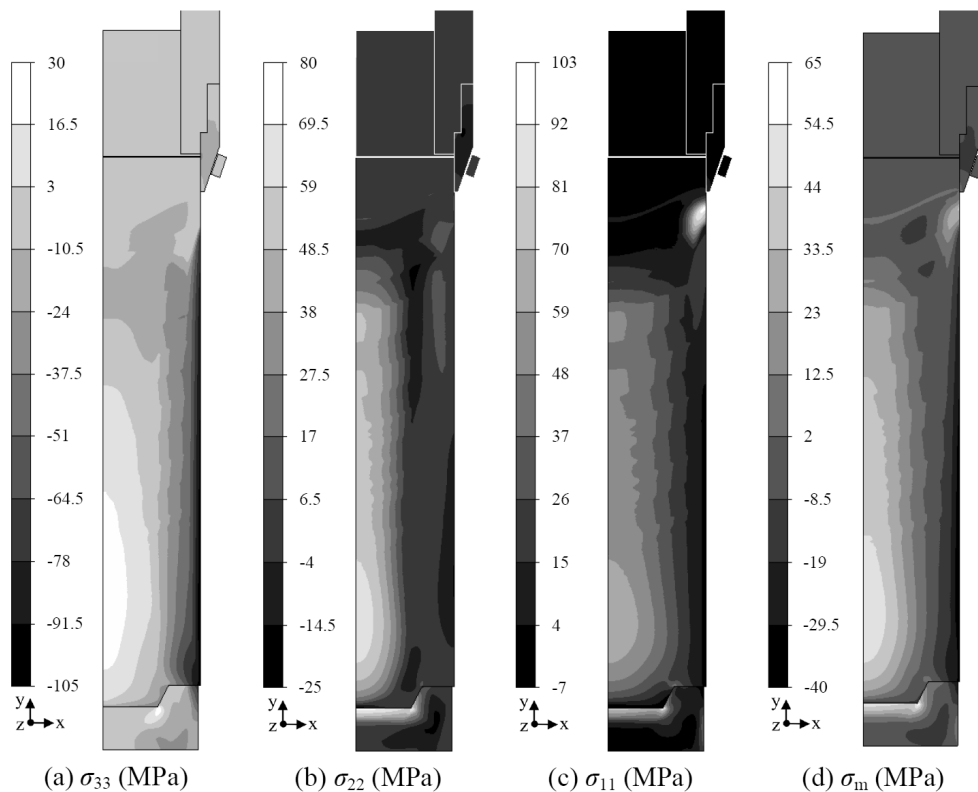


Fig. 5.5 Assessment of brittle fracture in the billet using the principal stress components and the mean stress: (a) σ_{33} , (b) σ_{22} , (c) σ_{11} , and (d) σ_m [28]. Billet diameter 200 mm, casting speed 1 mm/s.

Although the contour maps shown in Fig. 5.2 can indicate the stress state in the billet under steady state casting conditions, it is worth to bring the values of the normal stresses at those locations of the billet where they reach their maximum. Table 5.4 shows the normal stresses in the radial, circumferential and axial directions, along with the mean stress as well as maximum principal stress for the lower part of the billet 65 mm above the bottom block and in the WIZ. As explained before, the maximum stresses appear in the center and in the WIZ and it can be also easily noticed that the circumferential stress at the surface turns from 100 MPa to -85 MPa as the billet leaves the impingement zone.

Table 5.4 The values of the normal stresses, mean stress and maximum principal stress after 500 s of casting in the lower part of the billet (65 mm above the bottom block) and WIZ.

Position along the radial axis	σ_{rr} (MPa)	$\sigma_{\theta\theta}$ (MPa)	σ_{zz} (MPa)	σ_m (MPa)	σ_{11} (MPa)
Center	70.8	70.9	8.4	49.9	71
Mid-radius	44.4	0	-15.4	9.3	44
Surface	3.25	-85	3.5	-26	3.5
WIZ	-4	100	-1.5	30	100

In the theory of viscoplasticity [29], the deviatoric stresses are responsible for the yielding and plastic deformation of the material. The hydrostatic stress (σ_m), however accounts for the fracture of the material. As can be seen in Fig. 5.5d, the σ_m reaches its maximum value in the center of the billet, where the probability of brittle fracture is highest due to the plastic constraint. In Chapter 7 we will show how the mean stress is affected by casting process parameters such as casting speed or billet diameter.

5.4 Conclusions

Computation of the residual thermal stresses in a 7050 billet during DC-casting revealed that the normal stresses appear to be mainly tensile in the center of the billet and with moving to the surface of the billet they diminish or turn to compressive with high magnitude in the circumferential direction. Tensile nature of the radial, axial and circumferential components of the stress tensor in the center of the billet suggests the highest probability of crack initiation and propagation in this region. The water impingement generates locally high tensile stresses, which can also facilitate the formation of micro-cracks in this area. Shear stress components disappear due to the axial symmetry of the billet, except for the σ_{rz} component whose value is relatively small compared to the normal stress components. Therefore, the principal stress tensor may be obtained by slight rotation of the stress tensor and the principal stress axes make a small angle with the original cylindrical coordinate axes. Viscoplastic strains in the center of the billet are mainly caused by creep at high temperatures, which is proven by nearly zero hardening parameter (α) values. At the surface of the billet, however higher α value is observed that accounts for plastic deformation in this area.

References

- [1] H.G. Fjær, A. Mo, Metall. Trans. B 21 (1990) 1049-1061.

- [2] B. Hannart, F. Cialti and R. van Schalkwijk, in: U. Mannweiler (Ed.), *Light Metals*, TMS, 1994, pp. 879-887.
- [3] J.M. Drezet, M. Rappaz, Y. Krähenbühl, in: J. Evans (Ed.), *Light Metals*, TMS, 1995, pp. 941-950.
- [4] J. Du, B.S.-J. Kang, K.-M. Chang, J. Haris, in: B. Welch (Ed.), *Light Metals*, TMS, 1998, pp. 1025-1030.
- [5] K.-M. Chang, B. Kang, J. Chin. *Inst. Eng.* 22 (1999) 27-42.
- [6] W. Boender, A. Burghardt, E.P. van Klaveren, J. Rabenberg, in: A.T. Tabereaux (Ed.), *Light Metals*, TMS, 2004, pp. 679-684.
- [7] N. Ishikawa, *Furukawa Review* 28 (2005) 46-52.
- [8] O. Ludwig, J.-M. Drezet, B. Commet, B. Heinrich, in: C.-A. Gandin, M. Bellet (Eds.), *Modeling of Casting, Welding and Advanced Solidification Processes XI*, TMS, 2006, pp. 185-192.
- [9] J.-M. Drezet, M. Rappaz, in: J.L. Anjier (Ed.), *Light Metals*, TMS, 2001, pp. 887-893.
- [10] M. M'Hamdi, A. Mo, H.G. Fjær, *Metall. Mater. Trans. A* 37 (2006) 3069-3083.
- [11] K.-M. Chang, H.-M. Lu, J. Wan, J.F. Harris, in: *Second Intern. Conf. on Quenching and the Control of Distortion*, ASM International, Ohio, 1996, pp. 341-345.
- [12] J. Wan, H.-M. Lu, K.-M. Chang, J. Harris, in: B. Welch (Ed.), *Light Metals*, TMS, 1998, pp. 1065-1070.
- [13] E.E. Madsen, G.E. Fladmark, in: G.E. Fladmark and J.G. Gram (Eds.), *Numerical Solution of Partial Differential Equations*, D. Reidel Publishing Company, Dordrecht, The Netherlands, 1973, pp. 223-240.
- [14] E.E. Madsen, in: R.W. Lewis, K. Morgan (Eds.), *Numerical Methods in Thermal Problems*, Pineridge Press Limited, Swansea, United Kingdom, 1979, pp. 81-89.
- [15] H. Fossheim, E.E. Madsen, in: W.S. Peterson (Ed.), *Light Metals*, TMS-AIME, Warrendale, PA, 1979, pp. 695-720.
- [16] E.K. Jensen, W. Schneider, in: C. M. Bickert (Ed.), *Light Metals*, TMS-AIME, Warrendale, PA, 1990, pp. 937-943.
- [17] M. Lalpoor, D.G. Eskin, L. Katgerman, *Metall. Mater. Trans. A* 40 (2009) 3304-3313.
- [18] C.L. Martin, M. Braccini, M. Suéry, *Mater. Sci. Eng. A* 325 (2002) 292-301.
- [19] O. Ludwig, B. Commet, J.-M. Drezet, C. L. Martin, M. Suery: in D. M. Stefanescu, J. Warren, M. Jolly, M. Krane (Eds.), *Modeling of Casting, Welding and Advanced Solidification Processes X*, 2003, pp. 183-190.
- [20] C.L. Martin, O. Ludwig, M. Suéry, in: J. Eberhardsteiner, H.A. Mang, F.G. Rammerstorfer (Eds.), *Proc. WCCM V*, Vienna University of Technology, Austria, 2002.
- [21] O. Ludwig, C.L. Martin, M. Suéry, *Mater. Forum* 28 (2004) 357-362.
- [22] O. Ludwig, J.-M. Drezet, C.L. Martin, M. Suéry, *Metall. Mater. Trans. A* 36 (2005) 1525-1535.
- [23] J.C. Michel, P. Suquet, *J. Mech. Phys. Solids* 40 (1992) 783-812.
- [24] J.M. Duva, P.D. Crow, *Acta Metall. Mater.* 40 (1992) 31-35.
- [25] O. Ludwig, J.-M. Drezet, P. Ménéès, C.L. Martin, M. Suéry, *Mater. Sci. Eng. A* 413-414 (2005) 174-179.
- [26] O. Ludwig, PhD thesis, Institut National Polytechnique de Grenoble, Grenoble, 2004.
- [27] D. Mortensen, *Metall. Mater. Trans. B* 30 (1999) 119-133.

- [28] M. Lalpoor, D.G. Eskin, L. Katgerman, Proc. THERMEC 2009, Adv. Mater. Res. 89-91 (2010) 319-324.
- [29] I. H. Shames, F. A. Cozzarelli, Elastic and Inelastic Stress Analysis, Prentice-Hall, Inc., New Jersey, 1992.
- [30] J.H. Faupel, F.E. Fisher, Engineering Design, John Wiley & Sons Inc., New York (NY), 1981.

Chapter 6

Evolution of residual thermal stresses in the billet after the end of casting, and cold cracking assessment

In the previous Chapter, the state of residual thermal stresses was determined under steady state casting conditions in a 7050 DC-cast billet. There, we discussed the critical locations and stages where the billet is highly prone to cracking due to stress concentration. The real cold cracking, however occurs in most cases at the end of DC-casting process or during the sawing attempt. Therefore, it is important to understand how stresses evolve in the billets when the casting ceases and thermal boundary conditions alter. Thermally induced strains and stresses developed during DC-casting of high strength aluminum alloys can result in formation of micro-cracks in different locations of the billet. Rapid propagation of such micro-cracks in tensile thermal stress fields can eventually lead to catastrophic failure and cold cracking. Application of fracture mechanics can help to derive the critical crack length leading to failure. In this Chapter, the state of residual thermal stresses is determined in an AA7050 billet during and after the end of DC-casting process by means of ALSIM5. In order to assess the critical crack size that leads to catastrophic failure, the locations with highest maximum principal stress component were detected. The critical crack sizes were calculated afterwards using the corresponding K_{Ic} values and the maximum principal stress component.

6.1 Introduction

In Chapter 5, the state of residual thermal stresses was determined in a 7050 DC-cast billet under steady state casting conditions. There, we learned that under such conditions, tensile stresses form in the center in all directions; while at the surface compressive stresses develop (except for the water impingement zone). The small hardening parameter (α) values in the center explained that the viscoplastic deformation in that area is mainly caused by creep at elevated temperatures. At the surface of the billet however, higher α values appeared which accounted for the strain hardening generation. Higher effective stress (Eq. 6.1 [1]) values at the surface were a consequence of this strain hardening generation.

$$\bar{\sigma} = \frac{\sqrt{2}}{2} \left[(\sigma_{11} - \sigma_{22})^2 + (\sigma_{22} - \sigma_{33})^2 + (\sigma_{33} - \sigma_{11})^2 \right]^{1/2} \quad (6.1)$$

The low effective stress in the center does not necessarily imply that this region is not prone to cracking and failure. The plastic constraint brought about by the triaxial tensile state of stress in that area makes the alloy prone to brittle fracture [1]. What makes the situation even worse is that during the DC-casting process, the material passes through a transition from liquid to solid, and stresses develop gradually depending on the degree of thermal contraction constraint. Hence, thermal stresses appear below the rigidity temperature and increase in value as the temperature falls [2]. Thermal stresses developed due to the non-uniform thermal contraction can lead to crack formation above [3-5] and below the solidus [6,7]. Above solidus, the grain boundaries and interdendritic spaces are mainly covered by nonequilibrium eutectics with low melting temperature [8,9]. The presence of liquid on the grain boundaries makes the material weak against the induced stresses and in many cases results in hot tearing [10]. The cracking below the solidus is also possible, especially in the center of the billets where the brittle intermetallics (non-equilibrium eutectics) are under triaxial tensile stress state and relatively high hydrostatic stress [11,12]. Although the mechanical behavior of the brittle intermetallics has not been specifically studied under such loading conditions, it is not hard to guess that due to the complicated crystallographic structure and consequently limited slip systems, they may fracture easily under triaxial tensile stress state. Regardless of how the cracks form above or below the solidus, they make the brittle as-cast 7xxx alloys even more prone to brittle fracture. The comparison of the stresses appeared during the thermomechanical simulation of the residual thermal stresses (Chapter 5) with the fracture strength of the material during the uniaxial tensile tests (Chapter 2) reveals that the computed stresses are far below the fracture strengths. During the tensile tests, the fracture strengths were recorded as follows at various temperatures: 200°C: 225 ± 4 MPa, 100°C: 226 ± 8 MPa and room temperature: 266 ± 12 MPa, which are higher compared to the effective stress or the maximum principal stress values computed by ALSIM5. This indicates that there must be some cracks, flaws or defects at the tip of which the stresses are amplified to some critical levels that approach the fracture strength of the material. In order to assess the critical size of such defects which lead to catastrophic failure, the fracture mechanics concepts may be used. They apply the nominal stress and the plane strain fracture toughness to the Griffith type equations [1,12] and derive the critical crack size. Boender *et al.* [13] and Ludwig *et al.* [14] used the simulated maximum principal stress to assess the critical crack size that results in catastrophic failure. For slabs (width: 1150 mm, thickness: 360 mm, length: 1500 mm) of Al-4.5%Cu [14] with the maximum principle stress 80 MPa the critical crack size was assessed to be 8 mm. In AA2024 slabs (width: 2000 mm, thickness: 510 mm, length: 2000 mm) [13], critical crack sizes appeared to be between 5 and 50 mm for various maximum principal stress values found in different locations. But such study has not been performed for highly prone to cold cracking 7050 or 7075 alloys over the critical temperature range of 200 °C down to room temperature, mainly due to lack of necessary data (constitutive parameters and K_{Ic} values). In the aforementioned studies [13,14], the room temperature K_{Ic} values for the AA7050 alloy and the AA2024 alloys were obtained from the literature [15,16].

In practical DC-casting trials cold cracking occurs in most cases at the end of casting or during the sawing attempt. In order to check what conditions lead to such a failure, thermomechanical simulations must be performed under similar thermal boundary conditions. In this Chapter we achieve this goal by using ALSIM5 to compute temperatures, thermal stresses, and strains after the end of casting in an AA7050 alloy billet. Afterwards, we use the experimentally measured K_{Ic} values from room

temperature to 200°C (see Chapter 2) for the genuine as-cast material to assess to critical crack size that triggers the catastrophic failure. The results reported in this Chapter will provide input for a cold cracking criterion that can be used for optimizing casting regimes in such a way that the probability of cold cracking becomes negligible.

6.2 Simulation results

Since cold cracking occurs in the completely solid state and even sometimes at room temperature during the sawing attempt, it is necessary to study the state of stresses not only when the steady state is gained but also when the casting and the water flow are stopped. The former was studied in Chapter 5 and to achieve the latter simulations were planned to run at the speed 1 mm/s for 2800 s in the following manner: casting for the first 600 s, ramping the casting speed to zero from 600 to 700 s, cooling the side walls with water flow from 700 to 1000 s, switching off the water from 1000 to 1100 s, and air cooling from 1100 to 2800 s. It is worth to mention that at this moment the temperature in the entire billet is between 30 and 60 °C. As the steady-state conditions are reached after 200 s of casting for the current billet, 600 s of casting would be long enough to investigate the evolution of residual thermal stresses built up during the casting process. Figs. 6.1a through 6.1d show the contour maps of the four components of residual thermal stress tensor remaining in the billet after 2800 s. The magnitudes and distribution of stresses remained more or less constant after ceasing the casting and the water flow, except for the upper part of the billet close to the mold and water impingement zone (WIZ). As observed in Chapter 5, the radial stress (σ_{rr} —along x-axis) is highly tensile in the center of the billet (with a max. in the lower part) and reduces in magnitude as we move towards the surface (Fig. 6.1a). The same trend holds for the axial (σ_{zz} —along y-axis) and circumferential ($\sigma_{\theta\theta}$ —along z-axis) components of the stress tensor (Fig. 6.1b and 6.1c). Values of the circumferential component of stress are compressive at the surface and tensile in the center, with a transition point in mid-radius. Shear stress component (σ_{rz}) is mainly small and its minimum value appears around the water impingement zone and in the lower part of the billet in the vicinity of the bottom block (Fig. 6.1d). Contour maps of the viscoplastic part of the plastic strain are shown in Fig. 6.2a through 6.2d. The radial component of the plastic strain is mostly tensile in the lower central part of the billet, decreases in mid-radius and increases again as we move to the surface of the billet. In the upper parts of the billet it remains homogenous and relatively low in value, except for the surface of the billet. The circumferential component (Fig 6.2b) appears to be tensile in the bottom center of the billet and by moving to the surface it turns to compressive with minimum values in the lower right corner. Unlike radial and circumferential components, the axial component shows negative (compressive) values in the center (with a min. on top of the bottom block) and by moving to the surface (except for upper part) it converts to tensile (Fig. 6.2c). The compressive values of the axial plastic strain in the lower part of the billet are due to the negative (compressive) axial viscoplastic strain rate near the solidification front as explained in Chapter 5. Shear strain component is mainly small with the most negative values in the lower part of the billet in the vicinity of the bottom block (Fig. 6.2d).

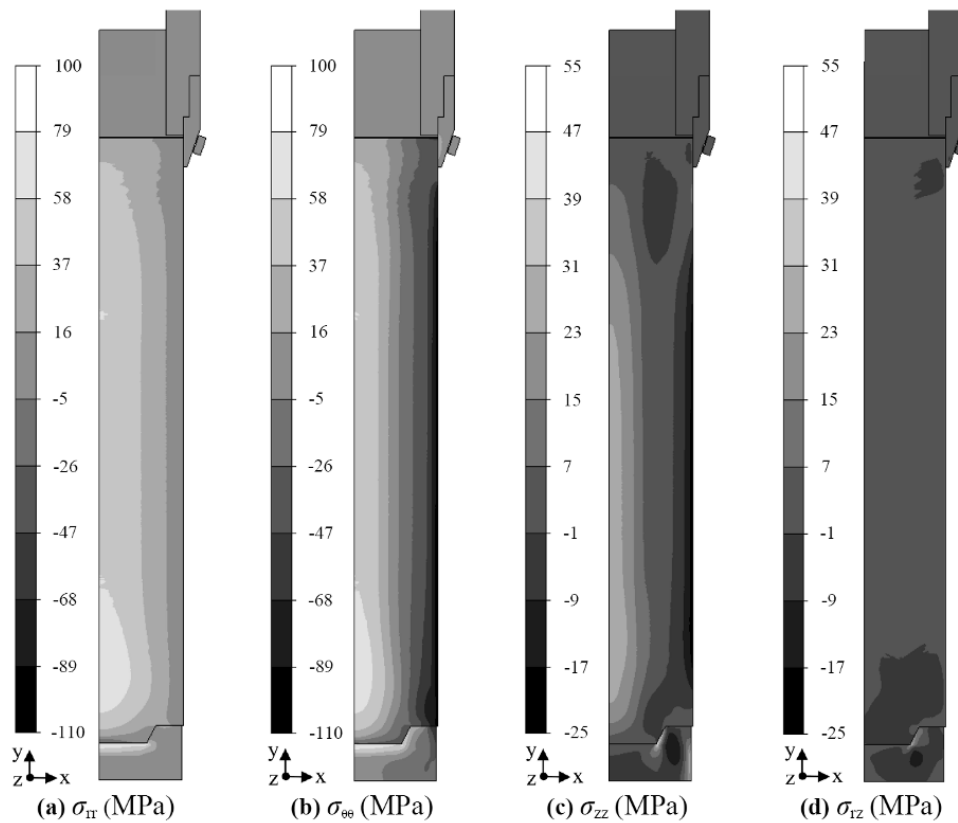


Fig. 6.1 Computer simulated residual thermal stresses after 2800 s: (a) radial, (b) circumferential, (c) axial, and (d) shear component [2].

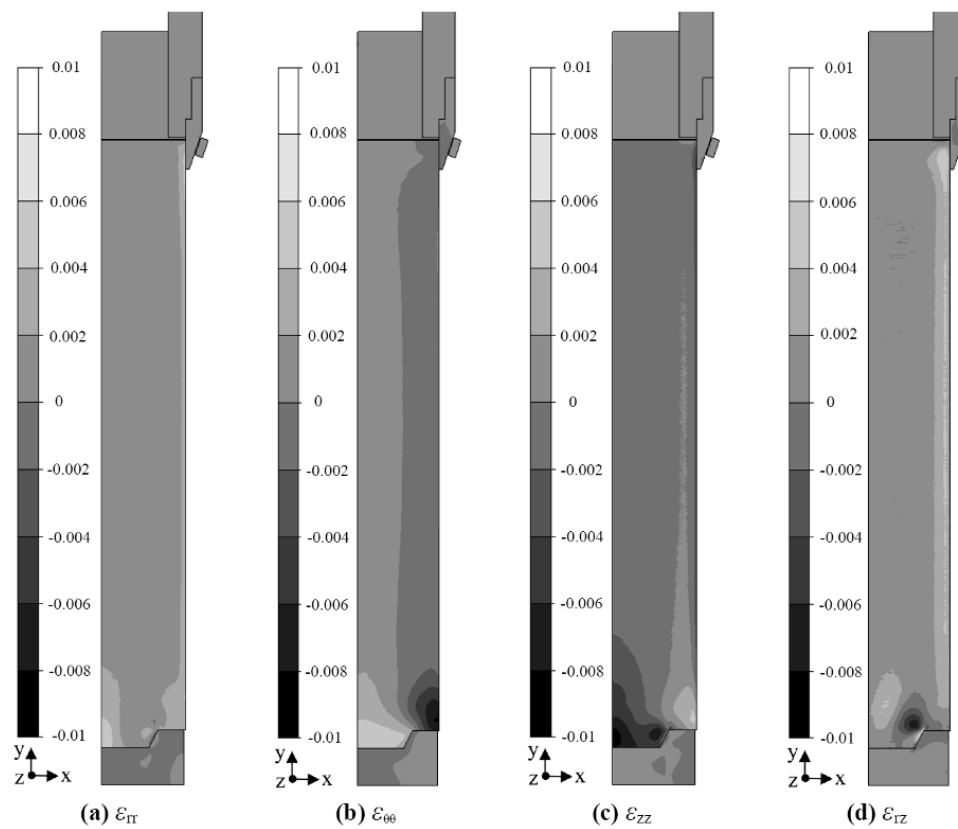


Fig. 6.2 Computer simulated residual viscoplastic strains after 2800 s: (a) radial, (b) circumferential, (c) axial, and (d) shear components [2].

In order to examine the occurrence of plastic yield in the billet, contour maps of the hardening parameter α , effective stress, and accumulated effective viscoplastic strain are used (Figs 6.3a to 6.3c). As discussed in Chapter 5, in those locations of the billet where the temperature is above the onset of strain hardening (T_h) or no yielding is present ($\alpha = 0$) the total viscoplastic strain is generated by creep, which is the case for the entire center of the billet (Fig. 6.3a). A result of strain hardening can be seen in Fig. 6.3b, where the effective stress at the surface is greater than 100 MPa, which is certainly above the 0.2% offset yield strength of the 7050 alloy above 200 °C (Table 6.1; see also Fig. 2.10a). High effective stresses at the surface are either the result of high tensile stresses in the water impingement zone or the high compressive values appearing in lower parts (both in circumferential direction; see Fig. 5.4c). After the end of casting, high tensile stresses in the water impingement zone disappear and the stress state at the surface becomes highly compressive, which although leads to some plastic deformation but is indeed not critical.

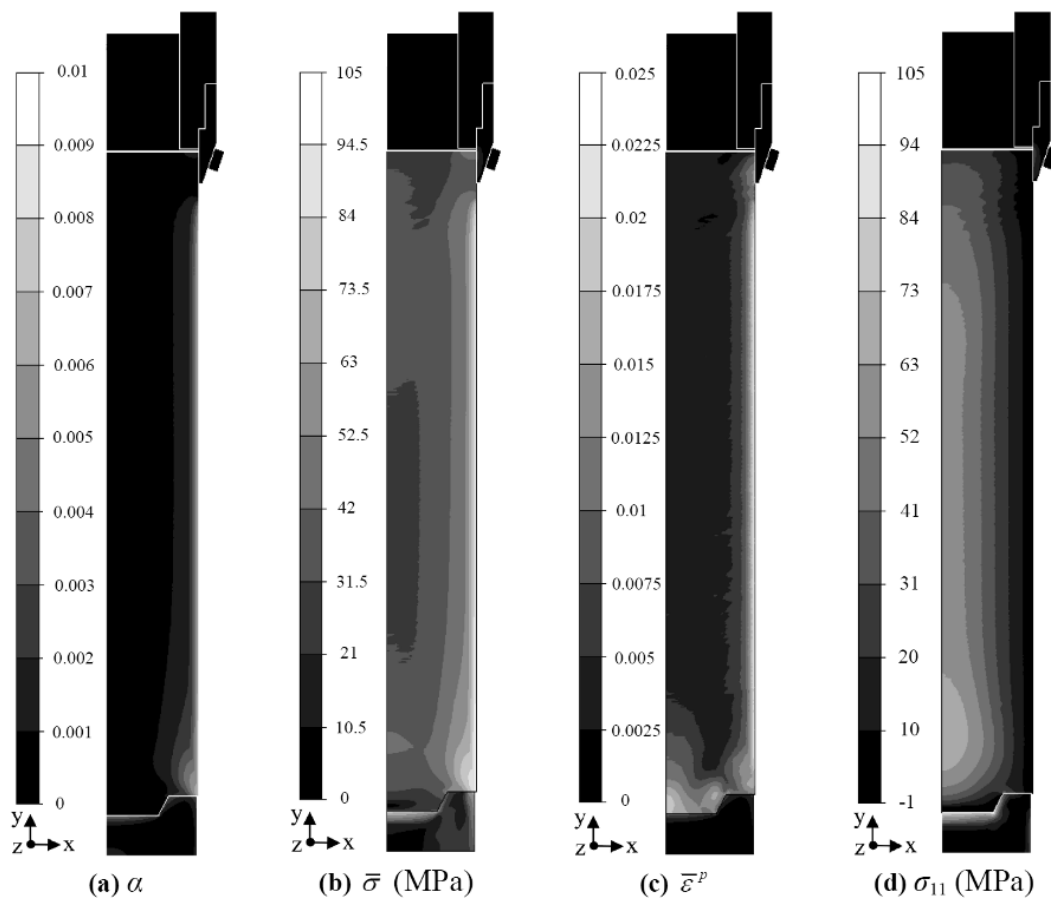


Fig. 6.3 Investigation of plastic yield and strain hardening using the computer simulated contour maps of: (a) hardening parameter, b) effective stress, c) accumulated effective viscoplastic strain, and d) the largest component of the principal stresses (σ_{11}) [2].

The maximum value of the effective viscoplastic strain appeared to be the same as observed in Fig. 5.4d (1.6 % at the surface of the billet and 2.5% in the lowest central part on top of the bottom block (Fig. 6.3c)). Contour map of the largest component of the principal stresses (σ_{11}) is shown in Fig. 6.3d. As can be seen, its maximum value appears in the lower central part of the billet (after 200 s of casting (Fig. 6.7a)). The evolution of the largest component of the principal stresses and its effect on cracking will be discussed in the following section in more detail.

Up to this moment we have just shown the contour maps of the residual thermal stress components. Such contour maps show the state of residual thermal stresses in the entire billet after some time, but the evolution of thermal stresses during the casting can not be understood from them unless one watches the movie of the entire simulation. As showing the movie is not possible here, we show the evolution of the residual stress tensor components during the casting for some points in the billet where the stresses reach the maximum level. Having chosen the origin of the coordinate system in the center of the top surface of the bottom block, the following points were taken for stress analysis: Surface (x: 95 mm, y: 34 mm), Mid-radius (x: 48 mm, y: 34 mm), Center (x: 1×10^{-5} mm, y: 24 mm), and Center+10 (x: 1×10^{-5} mm, y: 34 mm) (this point represents the lowest point in the billet with the maximum σ_{11}). Figs. 6.4 to 6.6 show the evolution of the three normal stresses (σ_{rr} , $\sigma_{\theta\theta}$ and σ_{zz}) in the billet during the casting. As can be seen in Fig. 6.4, the radial stress component increases after 100 s in the center and at mid-radius of the billet and reaches some maximum value after 200 s. At the surface of the billet however, this component passes through a minimum first and then remains low in value up to the end of casting. It is worth to mention here that the stress state does not change significantly in the lower part of the billet after the end of casting.

Table 6.1. Mechanical properties of the as-cast 7050 alloy gained using Gleeble 1500 at a strain rate of 10^{-4} s^{-1} (see Figs. 2.9 and 2.10) [2].

Temp. (°C)	Yield strength (MPa)	Reduction in area (%)	Elongation (%)
20	266 ± 12	0.4 ± 0.1	1.9
100	223 ± 7	0.5	1.4 ± 0.1
200	154 ± 8	2.5 ± 0.2	1.6 ± 0.1
300	73 ± 2	36 ± 5	5.2 ± 0.8
400	23 ± 2	33 ± 3	3.8 ± 0.1

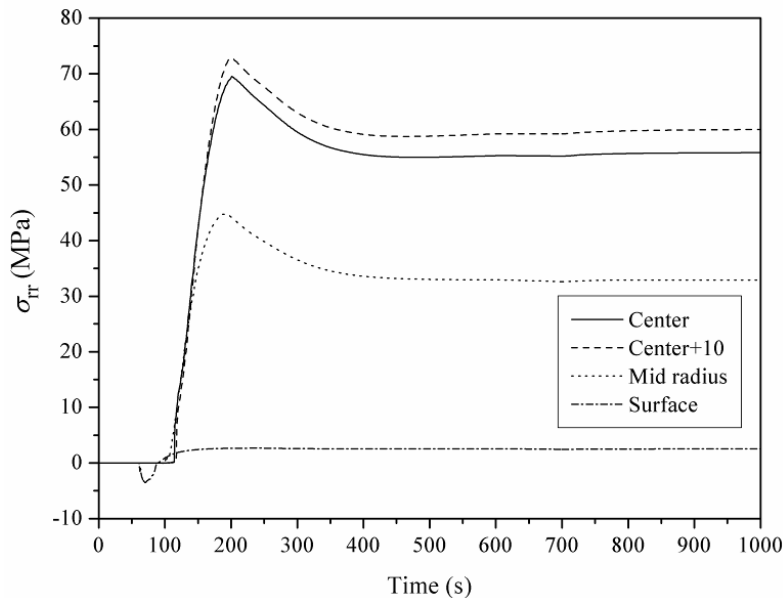


Fig. 6.4 Evolution of the radial stress (σ_{rr}) component with time in the $\text{\O} 200\text{-mm}$ billet. The stress state does not change after 1000 s.

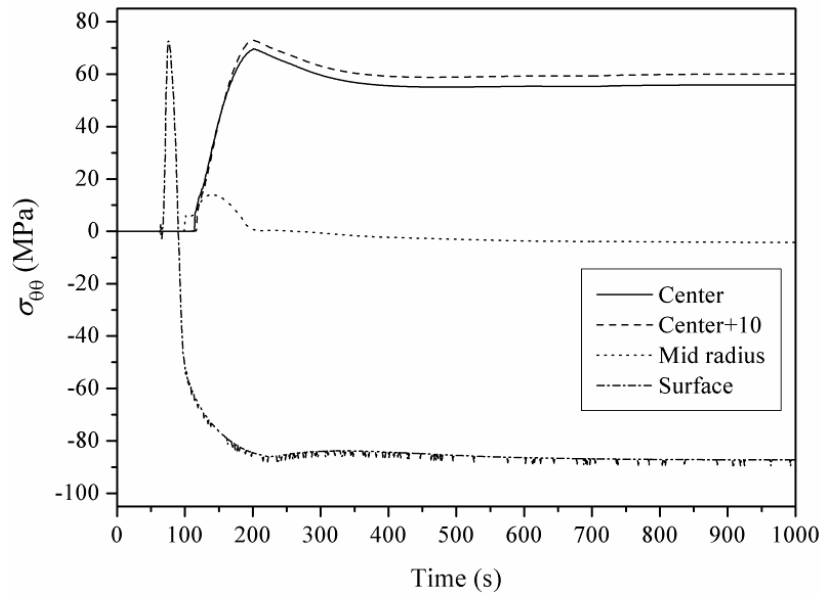


Fig. 6.5 Evolution of the circumferential stress ($\sigma_{\theta\theta}$) component with time in the \varnothing 200-mm billet. The stress state does not change after 1000 s.

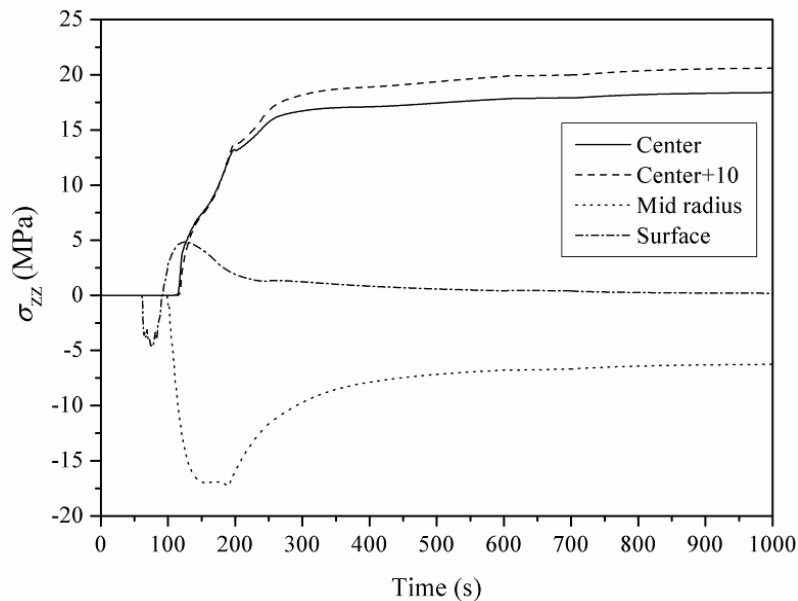


Fig. 6.6 Evolution of the axial stress (σ_{zz}) component with time in the \varnothing 200-mm billet. The stress state does not change after 1000 s.

The evolution of the circumferential stress component can be observed in Fig. 6.5. Similar to radial component, in the center and at mid-radius the circumferential stress increases to reach a maximum at 200 s and then decreases slightly and reaches a plateau. At the surface of the billet, a maximum occurs after 76 s in the WIZ, where we observe a relatively high tensile stress. This component of the stress falls immediately afterwards as the billet leaves the impingement zone and turns to compressive. This relatively high compressive stress is basically responsible for saving the billet from failure at the surface in this stage. The evolution of the axial stress component in the center of the billet (Fig. 6.6) is similar to the circumferential stress at this point i.e. an increase to reach a maximum and eventually a plateau. The

surface of the billet however, experiences a minimum first after 76 s followed by a ramp up to reach a maximum after 130 s. The axial stress at the surface falls afterwards and gains nearly zero value up to the end of casting. At mid-radius, the axial stress falls to reach a minimum and remains compressive up to the end of casting at this specific point.

6.3 Cracking assessment in the billet

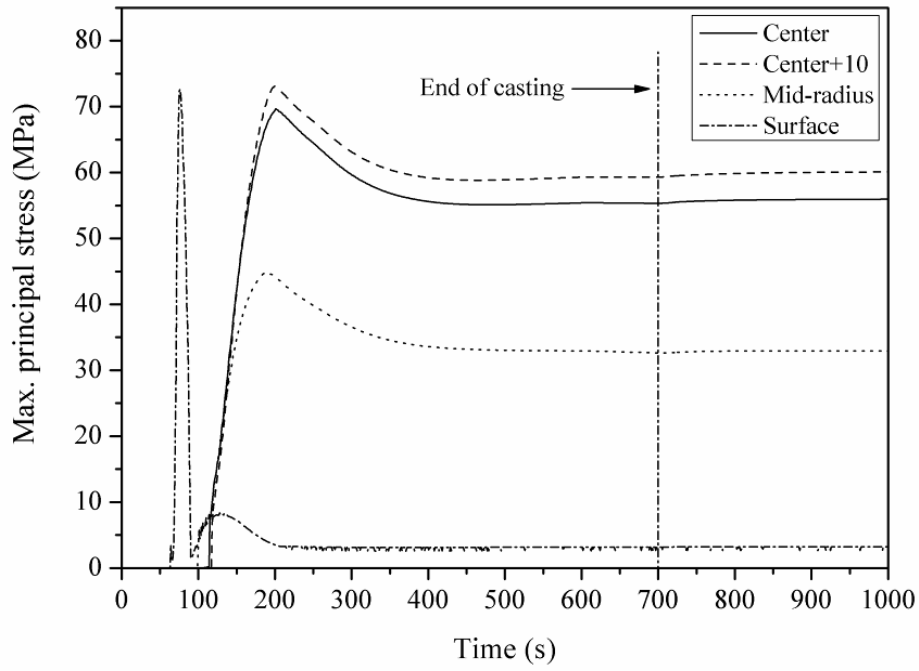
As a good approximation, the grain refined material under discussion can be assumed to be homogeneous and isotropic, i.e. in macroscopic view there is no preferred crack orientation and cracks propagate normal to the maximum principal stress component [17]. Having the plane strain fracture toughness of the material and assuming the ingot as a semi-infinite medium, one can calculate by application of fracture mechanics [13,14] the critical crack size that leads to catastrophic brittle fracture. Before turning to that point let us have a look at the evolution of the σ_{11} in the billet during the casting. Fig. 6.7a shows the changes of the σ_{11} with time for the points mentioned previously, and the correspondent computer simulated cooling curves are shown in Fig. 6.4b. The σ_{11} reaches its maximum (73 MPa) at the surface after 76 s where the temperature is around 200 °C (Fig. 6.7b). It falls afterwards mainly due to the change in the stress mode at the surface from tensile to compressive. However, this point does not represent the center of the WIZ, where the σ_{11} gains its maximum value (100 MPa) as explained in Chapter 5. This value of σ_{11} is used for the calculation of critical crack size at the surface of the billet. In the center of the billet, the σ_{11} reaches its maximum (73 MPa) after 200 s and the temperature is 200 °C (Fig. 6.7a). Having reached the steady state, this value falls and remains constant even after ceasing the casting and stopping the water flow. It is also obvious from Fig. 6.4a that the maximum in the σ_{11} occurs sooner and with a lower value as we move towards the surface (except for the initial peak occurring in the WIZ due to the initial tensile stresses). As the σ_{11} reaches its maximum in the center where the temperature is 200°C, the K_{Ic} value corresponding to this temperature can be applied to assess the critical crack size. Following the same procedure for lower temperatures down to the room temperature and using the corresponding σ_{11} , we can evaluate the critical crack size leading to catastrophic failure in the billet upon cooling. Taking into account the billet geometry, cracks with different shapes were assumed to form either at the surface or in the center.

The penny shaped crack (PSC) was chosen for the center and mid-radius of the billet with the assumption that $K_{II} = K_{III} = 0$ (Fig. 6.8a). The critical crack size (radius of the “penny”) for brittle fracture corresponding to this geometry is calculated as follows based on Griffith’s analysis [18]:

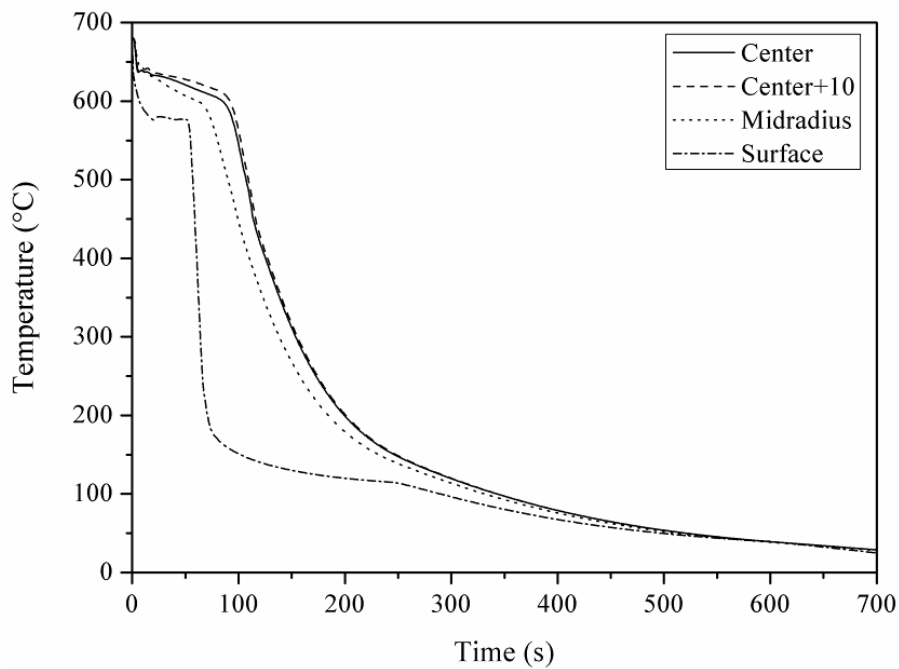
$$a_c = \frac{\pi}{4} \left(\frac{K_{Ic}}{\sigma} \right)^2. \quad (6.2)$$

At the surface of the billet, the surface breaking semi-circular (thumbnail) crack is chosen (Fig. 6.8b), for which the critical crack size is related to the K_{Ic} and nominal stress as follows [18]:

$$a_c = \frac{\pi}{(2 \times 1.13)^2} \left(\frac{K_{Ic}}{\sigma} \right)^2. \quad (6.3)$$



(a)



(b)

Fig. 6.7 (a) Evolution of the largest component of the principal stresses in the center of the billet (24 mm above the bottom block), center+10 (34 mm above the bottom block), mid-radius (34 mm above the bottom block) and at the surface with the same height as mid-radius (computer simulation results), (b) computer simulated cooling curves for the points mentioned above [2].

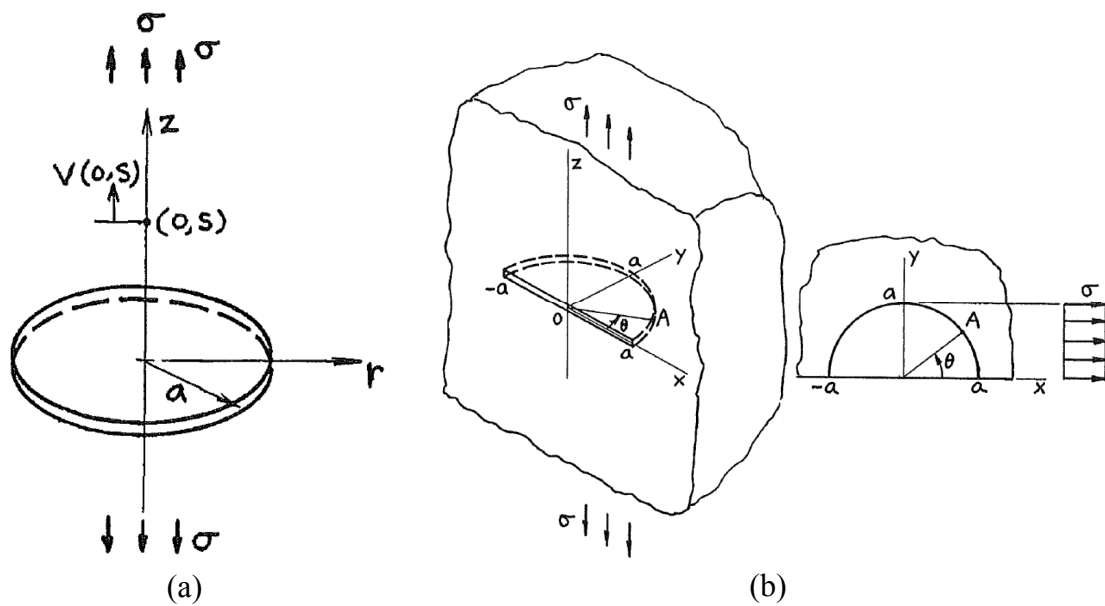


Fig. 6.8 Schematic view of the crack geometries used in this study: a) a penny shaped crack. $V(0, s)$ is the displacement at $(0, s)$ when uniform pressure σ is applied on crack surfaces, b) a thumbnail crack in a semi-infinite body ($y \geq 0$) ($y = 0$: free surface) [18].

Critical crack sizes leading to the catastrophic failure are presented in Fig. 6.9 in the center, center+10, at the mid-radius and at the surface of the billet. Since the K_{Ic} values were only measurable at and below 200 °C, the critical crack sizes have been calculated for the moments that the temperature in the billet falls below the mentioned temperature. The critical crack sizes were calculated by applying the corresponding σ_{11} value of the mentioned points in the billet (Fig. 6.7a) and the K_{Ic} values to equations 6.2 and 6.3 (Fig. 2.23).

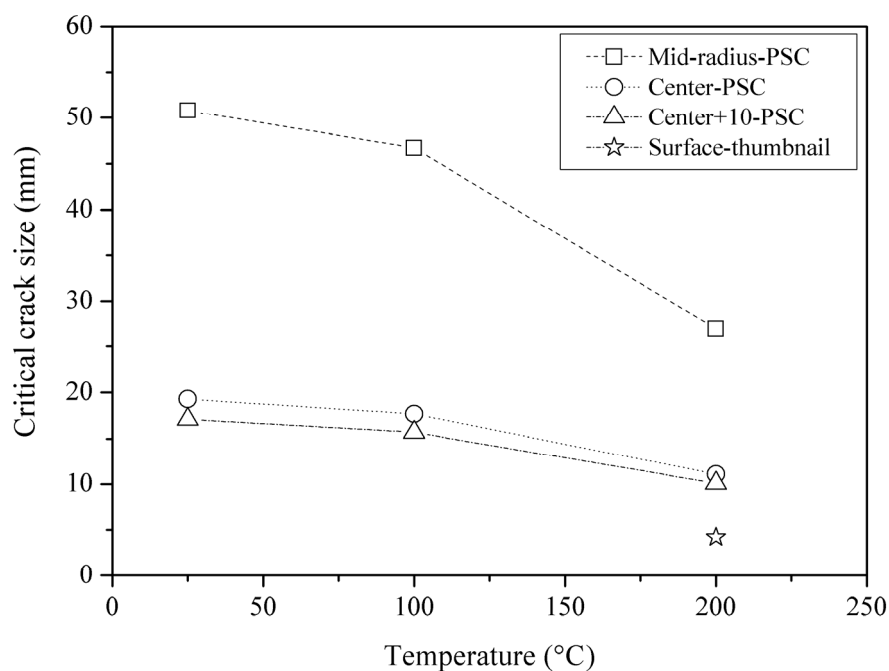


Fig. 6.9 Critical crack size for a penny shaped crack in the center, center +10, mid-radius and surface of the billet.

As can be seen in Fig. 6.9, the critical crack size leading to catastrophic failure of the penny shaped crack is minimum in the center, center+10 and mid-radius when they are at 200 °C, mainly due to the maximum σ_{11} value reached at this moment. As the temperature falls below 200°C, the σ_{11} decreases a little bit leading to larger critical crack sizes at these points i.e. lower failure probability. The cracking probability increases also as we move from the mid-radius to the center. Maximum probability zone starts from 34 mm above the bottom block in the positive “y” direction (the light-gray zone in Fig. 6.3d). The smallest critical crack size (10 mm), which appears at 200°C, is mainly due to the highest value of the largest component of the σ_{11} at this temperature.

For the surface of the billet, the maximum σ_{11} (100 MPa) appears after 76 s in the WIZ where the temperature is around 200°C. At this temperature and under described stress conditions, the critical crack size was calculated as 4.2 mm for a thumbnail crack (Fig. 6.9). On moving away from the water impingement zone during the casting, stresses at the surface either diminish or turn to compressive, thus the σ_{11} decreases dramatically (as seen in Fig. 6.7a). This results in very large and unrealistic critical crack sizes (6.7 m at 100°C and 7.3 m at 25 °C), which were not plotted here.

6.4 Discussion

Following the evolution of residual thermal stresses in the DC-cast billet mentioned above one learns that the stress state in the center of the billet remains tensile for almost the entire casting time except for the very beginning, when it is slightly under compression resulting from the contraction of the surface. At the surface of the billet, however stresses are tensile in the water impingement zone, but they turn to compressive upon further cooling. Thus, two critical stages appear during DC-casting of high strength aluminum alloys billets of the given size; first at the surface after 76 s when high tensile stresses form and second in the center after 200 s when the σ_{11} reaches its maximum value. Large initial tensile stresses at the surface can lead to crack formation in this region, although the compressive stresses formed later may save the billet from failure in this stage. According to fracture mechanics however, large thumbnail cracks with the critical length of 8 mm (where $\sigma_{11} = 73$ MPa, or 4.2 mm where $\sigma_{11} = 100$ MPa) can catastrophically propagate in the tensile stress field and result in J-cracks (Fig. 1.8) [13,14,16]. This occurs mainly in slabs where the stress state in the vicinity of the narrow side remains tensile [13,19]. Apparently such cracks rarely get the chance to reach such lengths during the short period of the tensile stress occurrence in billets, especially if we take the fact into account that the neighboring regions are all at higher temperatures with substantial plastic deformation capability.

In the center of the billet, the situation remains always critical especially after 200 s when the σ_{11} reaches its maximum value (73 MPa). What makes the situation even more critical is the fact that the material loses its ductility and becomes extremely brittle below 200 °C (Table 6.1, Figs. 2.9 and 2.24). Under these conditions cracks may initiate and/or the already initiated ones may propagate up to the critical length of 10-17 mm for penny shaped cracks. Initial cracks in the center of the billet may initiate through hot cracking above the solidus temperature and gradually grow in the tensile stress fields in radial, circumferential, or axial directions until they reach the critical length. From this moment on, the material is prone to cold cracking. An example of such cracks can be seen in Figs. 6.10a and b showing a 7475 DC-cast billet failed through cold cracking.

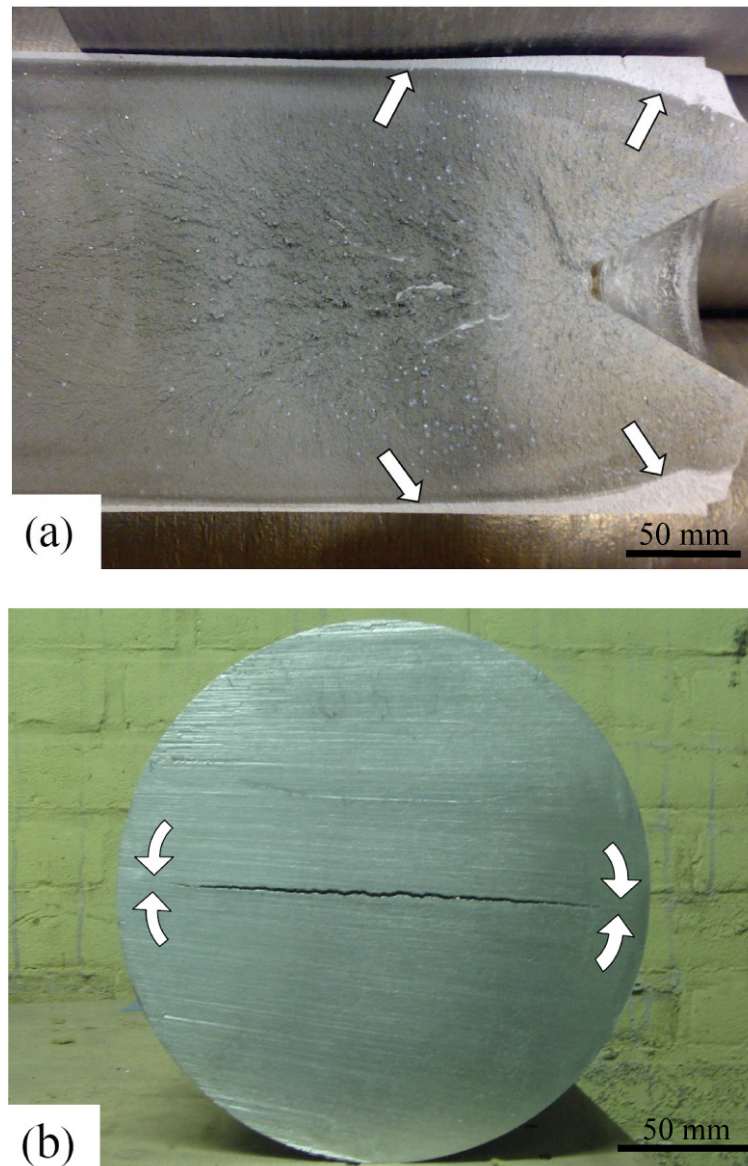


Fig. 6.10 Photos showing cold cracks in 200-mm 7475 DC-cast billet: (a) view of the billet split open during sawing attempts, showing two parts of fracture surface separated by a color contrast, and (b) cross section of the cold-cracked billet with arrows showing the direction of compressive circumferential stresses tending to cease the crack [2].

Chemical composition of this billet is mentioned in Table 2.1. Cold cracking has resulted in splitting the billet open in Fig. 6.10a, while in Fig. 6.10b the crack has stopped near the surface. As it is obvious in Fig. 6.10a the macroscopic fracture surface consists of two parts separated by color contrast from each other. The measurement of the width of the narrow bright part at the surface of billet (3.4 mm) in Fig. 6.10a shows that it is smaller than the critical crack size (4.2 mm) predicted by fracture mechanics. So the crack might be initiated at the surface in the beginning of casting but did not propagate during casting due to the compressive stresses (Fig. 6.1b). However, the wider part of this zone at the surface closer to the bottom of the billet is more than 20 mm wide (longer than the calculated critical length of 4.2 mm), which implies that the crack size in that area must have exceeded the critical size for a thumbnail crack. This wider cracked part was observable in some billets of the same batch before any cold cracking had occurred (Fig. 6.11).

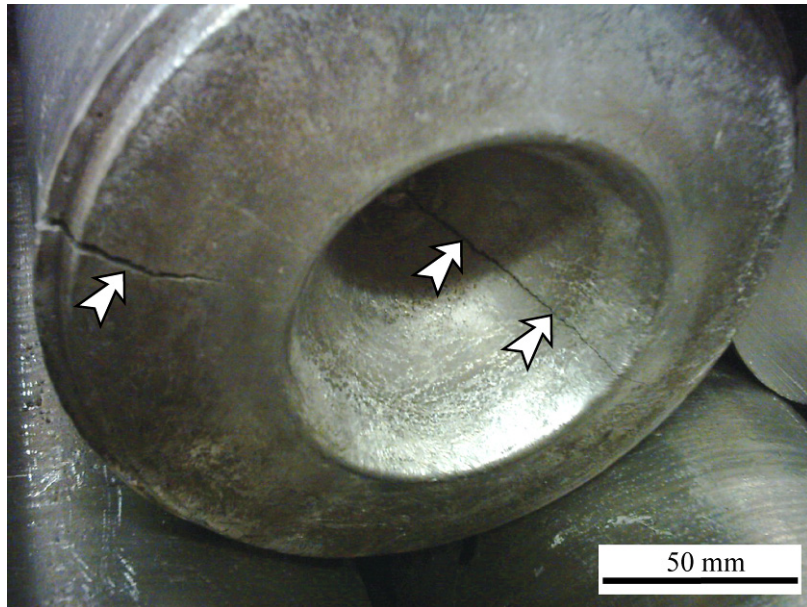


Fig. 6.11 A photo showing a 7475 DC-cast billet from the same batch as in Fig. 6.10. The arrows show the surface cracks on the bottom of the billet.

During sawing attempt however, the compressive stresses were relieved and the existing crack of critical size propagated catastrophically from the bottom and surface of the billet. Figure 6.10b shows another case when the crack has propagated along the radial direction under the influence of the tensile circumferential and radial components of the stress tensor (Figs. 6.1a and b). The crack has stopped near the surface when the elastic strain energy of the tensile stresses has been released upon crack propagation. In the mean time strong compressive circumferential component of the stress (Fig. 6.1b) at the surface protects the billet from splitting open. Removing this protective compressive stressed layer during the sawing attempt in cast halls makes the billet defenseless and provides a chance for the existing micro-cracks to propagate catastrophically.

As mentioned in Chapter 4, cracks mainly propagate along the grain boundaries and inter-dendritic spaces where the brittle intermetallics (non-equilibrium eutectic phases) are located (Figs. 6.12a, b) [6,7,20,21]. As a result of this, they follow a river like pattern and may not eventually get aligned normal to the largest component of the principle stresses. The crack may even stop at the matrix, where the plasticity is high enough to cease the brittle fracture (Fig. 6.12b). Thus, the final shape and microstructural features of the cracks are the main factors that make cold cracking an unpredictable phenomenon. In fact, the tri-axial stress state in the billet and the preferable propagation path along the grain boundaries and inter-dendritic spaces might drive the cracks in such a way that none of them get eventually exactly aligned normal to the σ_{11} nor reach the critical length for catastrophic propagation. In this case no cold cracking occurs.

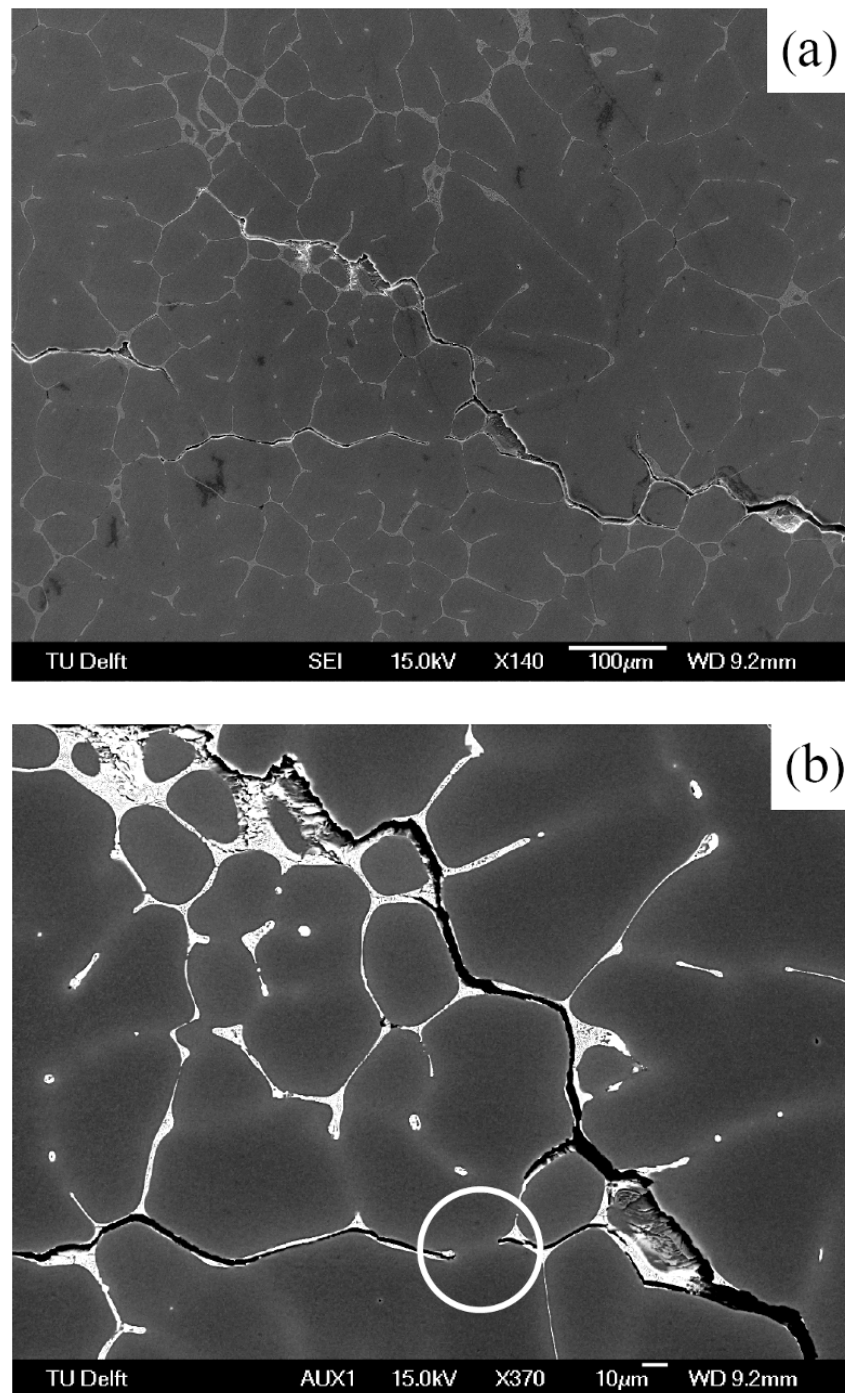


Fig. 6.12 Micrographs showing the propagation of micro-cracks: (a) a hot crack formed during the solidification in the center of a 7050 DC-cast billet with a diameter of 255 mm, this crack did not reach the critical conditions for catastrophic failure, so the billet remained sound, SEM, and (b) the same crack showing propagation through intermetallics, electron backscattered image. The circle shows how the cracks stop as they reach the matrix [2].

6.5 Conclusions

Thermo-mechanical simulation of residual thermal stresses in an AA7050 DC-cast billet revealed that large tensile stresses form in the water impingement zone at the surface and in the center of the billet. Such stresses can result in formation of micro-

cracks especially in the center of the billet, where all components of the stress tensor are tensile. After 200 s, the largest component of the principal stresses (σ_{11}) reaches its maximum in the center of the billet, where the material is extremely brittle due to the fall in the ductility at corresponding temperature. Since the magnitude and distribution of the residual thermal stresses would not change unless the billet is annealed or cut, the billet remains vulnerable to cold cracking after 200 s of casting. Any micro-crack or defect formed during or after the solidification may propagate in the tensile stress field especially in the center of the billet and reach the critical value for catastrophic failure. Large compressive circumferential stress at the surface may protect the billet from failure under steady state conditions and after the end of casting. Removing the protective outer shell (with large compressive stresses) of the billet during, e.g. sawing results in changing the distribution of the stresses in the billet and provides a chance for propagation of existing defects or micro-cracks. Our results show that cold cracking of high-strength aluminum alloys requires the presence in the structure of defects with a considerable length. Such defects can be micro-cracks at the interface of matrix with intermetallics [7, 21], chain of porosities or inclusions, or hot tears formed in the solidification range, which requires further investigation. But it is worth to mention that the complexity of the microstructure in the as-cast condition and the geometry of defects play an important role in either ceasing the crack development or leading to catastrophic failure.

References

- [1] G.E. Dieter, D. Bacon, *Mechanical Metallurgy*, SI Metric ed., McGraw-Hill Book Company, Singapore, 1988.
- [2] M. Lalpoor, D.G. Eskin, L. Katgerman, *Metall. Mater. Trans. A* 40 (2009) 3304-3313.
- [3] J. Campbell, *Castings*, Butterworth-Heinemann, Oxford, United Kingdom, 2003.
- [4] Suyitno, D.G. Eskin, L. Katgerman, *Mater. Sci. Eng., A* 420 (2006) 1–7.
- [5] A. Stangeland, A. Mo, M. M’Hamdi, D. Viano, C. Davidson, *Metall. Mater. Trans. A* 37 (2006) 705-714.
- [6] J. B. Hess, *Metall. Trans. A* 14 (1983) 323-327.
- [7] M. Lalpoor, D.G. Eskin, G. ten Brink, L. Katgerman, *Mater. Sci. Eng. A* 527 (2010) 1828-1834.
- [8] N.A. Belov, D.G. Eskin, A.A. Aksenov, *Multicomponent Phase Diagrams: Applications for Commercial Aluminum Alloys*, Elsevier, Amsterdam, 2005, pp. 199–202.
- [9] J.D. Robson, *Mater. Sci. Eng. A* 382 (2004) 112–121.
- [10] D.G. Eskin, Suyitno, L. Katgerman, *Prog. Mater. Sci.* 49 (2004) 629–711.
- [11] M. Lalpoor, D.G. Eskin, L. Katgerman, *Proc. THERMEC 2009, Adv. Mat. Res.* 89-91 (2010) 319-324
- [12] M. Janssen, J. Zuidema, R.J.H. Wanhill, *Fracture Mechanics*, 2nd ed., Delft University Press, Delft, The Netherlands, 2002.
- [13] W. Boender, A. Burghardt, in: H. Jones (Ed.), 5th Decennial Int. Conf. on Solidification Processing, University of Sheffield, Sheffield (UK), 2007, pp. 714-718.
- [14] O. Ludwig, J.-M. Drezet, B. Commet, B. Heinrich, in: C-A. Gandin, M. Bellet (Eds.), *Modeling of Casting, Welding and Advanced Solidification Processes XI*, TMS, Warrendale (PA), 2006, pp.185-192.
- [15] K.-M. Chang, B. Kang, *J. Chin. Inst. Eng.* 22 (1999) 27-42.

- [16] R.K. Paramatmuni, K.-M. Chang, B.S. Kang, X. Liu, *Mater. Sci. Eng. A* 379 (2004) 293-301.
- [17] M. Schöllmann, H.A. Richard, G. Kullmer, M. Fulland, *Int. J. Fracture* 117 (2002) 129-141.
- [18] H. Tada, P.C. Paris, G.R. Irwin, *The Stress Analysis of Cracks Handbook*, 3rd ed., The American Society of Mechanical Engineers, New York (NY), 2000, sections 24.1 and 28.1, pp. 342 and 410.
- [19] V.A. Livanov., in: A.F. Belov, G.D. Agarkov (Eds.), *Aluminum Alloys*, Oborongiz, Moscow, 1955, pp.128-168.
- [20] M. Lalpoor, D.G. Eskin, and L. Katgerman: *Mater. Sci. Eng. A* 497 (2008) 186-194.
- [21] S. Benum, D. Mortensen, H. Fjær, H.-G. Øverlie, O. Reiso, in: W. Schneider (Ed.), *Light Metals*, TMS, 2002, pp. 967-974.

Chapter 7

Cold cracking development in AA7050 DC-cast billets under various casting conditions

In Chapters 5 and 6 we discussed the stresses that develop during and after the end of DC-casting process. We also assessed the critical crack size that triggers the catastrophic failure and discussed under which conditions such voids may propagate or cease. However, we still do not know precisely how the stress state in the billet and consequently the failure probability may be affected by casting process parameters. What we know qualitatively is that the casting process parameters affect the magnitude and distribution of stresses in the billet and increase the susceptibility of the DC-cast billets to cold cracking. In order to investigate the effect of casting process parameters such as casting speed, billet size and water flow rate in more detail, thermo-mechanical simulations are applied in this chapter using ALSIM5. If a smaller critical crack size would be interpreted as higher probability of brittle fracture and catastrophic failure, we learn that among the studied casting process parameters, the increased billet size and high casting speed result in the most dramatic increase in residual stress level. In order to make this clearer in a quantitative manner, critical crack sizes that lead to catastrophic failure are also calculated and are reported against process parameters.

7.1 Introduction

During the direct chill (DC) casting process heat extraction occurs from the surface and to a lesser extent from the bottom of the ingot. As a result, high temperature gradients appear facilitated by the direct contact of water or starting block (bottom block) with the partially solidified ingot as schematically shown in Fig. 1.1. High temperature gradients lead to inhomogenous contraction and eventually thermal stresses appear as one part of the billet restrains another [1,2]. Sign, magnitude and distribution of the thermal stresses depend on the thermo-physical properties of the alloy under discussion and also on the casting process parameters. In Chapter 3, we compared the thermal properties of various groups of aluminum alloys and showed that 7xxx series (e.g. AA7050 and AA7075) have the lowest thermal conductivity, widest solidification temperature range, and relatively higher coefficient of thermal expansion [3]. Combination of such unfavorable thermal properties along with poor ductility in the as-cast condition [4,5] make such alloys vulnerable to both hot and

cold cracking [6,7]. Casting process parameters such as casting speed [8-10] and water flow rate [10] can affect the stress level in the ingot and enhance the problem. Size and geometry of the ingot influence the thermal stress level and play an important role in crack susceptibility [1,11]. Even the shape of the bottom block (Fig. 1.1) controls the state of thermal stresses in the start up phase and can result in distortion of the ingot bottom (butt curl) or formation of surface cracks [12,13]. In spite of all modifications and some technical approaches to prevent cold cracking [7,14,15], it still remains a major problem in DC-casting of high strength aluminum alloys.

Thermomechanical simulations of the DC-casting process have been used extensively for optimization of the cast production line and minimizing the occurrence of ingot cracking without conducting expensive experimental trials [16]. The cold cracking, however still remains a problem in the aluminum industry especially when newly developed alloys are tested. Ever increasing demand of the industry for higher productivity rates on the one hand and complaints on unsuccessful casting trails with newly developed high strength aluminum alloys on the other hand necessitates the systematic study of the effect of casting variables on cracking susceptibility of billets. Therefore, in the current Chapter we go one step further to study the influence of casting variables on magnitude and distribution of residual thermal stresses in DC-cast billets.

As in Chapters 5 and 6, ALSIM5 is used to investigate the effect of casting variables including casting speed, billet size, water temperature, water flow rate, melt temperature, and casting time on the magnitude and distribution of residual thermal stresses in DC-cast AA7050 billets. Having detected the most influential variables, corresponding critical crack sizes were calculated for the most critical locations of the billet using the maximum principal stress values. The results reported in this Chapter can be applied for optimization and improvement of the casting production line in aluminum industry and may lead to production of crack-free billets.

7.2 Model setup

ALSIM5 was used for the computation of temperature profile and stress/strain fields for round AA7050 billets under various casting conditions. A detailed description of the models involved was given in Chapter 5. The standard process parameters are the same as in Chapter 5 and are listed in Table 5.2. Casting speed, billet size, water temperature, water flow rate, casting time, and melt temperature were varied according to the values in Table 7.1. In case of changing water temperature, water flow rate, melt temperature or casting time conditions, other parameters were kept the same as the standard ones indicated in Table 5.2. For higher casting speeds and larger billet diameters however, water flow rates were increased accordingly to compensate for the higher heat input related to the greater mass of hot metal coming into the mold. Chemical composition of the tested alloy and its thermal as well as physical properties are the same as in Chapters 5 and 6 i.e. the grain refined 7050 DC-cast material.

Table 7.1 Selected cast variables and their values [17].

Process parameter	Value
Ingot diameter (mm)	200, 300 and 400
Final length of the billet (mm)	500, 1000
Casting speed (mm/s)	1, 1.5 and 2
Melt temperature (°C)	680 and 700
Water flow rate (l/min)	40, 80 and 120
Water temperature (°C)	15, 25 and 45

7.3 Simulation results

In Fig. 4.8 we showed the distribution of residual thermal stresses in a 7050 DC-cast billet with the diameter of 200 mm after 500 s of standard casting (Table 5.2). The selected points have the following coordinates (see Fig. 5.1): Surface: (x: 95 mm, y: 65 mm), Mid-radius: (x: 48 mm, y: 65 mm), Center: (x: 1×10^{-5} mm, y: 65 mm), with coordinate point in the center of the top surface of the bottom block. As explained in Chapter 5, in all radial (rr), circumferential ($\theta\theta$) and axial (zz) directions the stresses appear to be tensile in the center and by moving to the surface they diminish or turn to compressive. Investigation of the simulation results showed that water temperature, water flow rate and cast temperature had no noticeable effect on the state of residual thermal stresses in the billets. The threshold water flow rate of 80 l/min was found to be sufficient to prevent the remelting of the solidified shell at the surface of the billet (bleed-out) in the standard case. Although lower stresses were recorded at the lower water flow rates, the bleed-out may make the experimental casting trial impossible. Higher amounts of water flow rate did not have any impact on the results either. The casting speed and billet size, however, appeared to be the most influential variables. Fig. 7.1 shows the effect of casting speed on the magnitude of various stress components as well as the mean (hydrostatic) stress in the center of the billet.

The largest tensile stress appears in the center in radial, circumferential, and axial direction (Fig. 7.1) and at the surface in the WIZ in circumferential direction (Fig. 7.2). Stresses reported here correspond to the casting time $t = 200$ s (at casting speeds 1 and 1.5 mm/s) and $t = 275$ s (at casting speed 2 mm/s) at which the maximum principal stress (σ_{11}) gains its maximum value in the center of the billet. In the water impingement zone however, the maximum σ_{11} is reached after roughly 75 s at all given casting speeds. With increasing the casting speed, the residual stress level in the center increases in all directions (Fig. 7.1). The axial stress increases at the highest rate, and from the smallest component at a speed of 1 mm/s it turns to the maximum normal stress at the casting speed of 2 mm/s. It is worth to mention again here that as the shear stresses are much smaller compared to normal stresses, the principal stress values and axes are close to the correspondent normal stress components. Radial and circumferential stress components show similar values at all casting speeds in the center of the billet and they do not change significantly at casting speeds higher than 1.5 mm/s. The circumferential component of stress in the WIZ at the surface (Fig. 7.2) changes very slightly as the casting speed increases from 1 to 1.5 mm/s with a noticeable increase on further raising the speed.

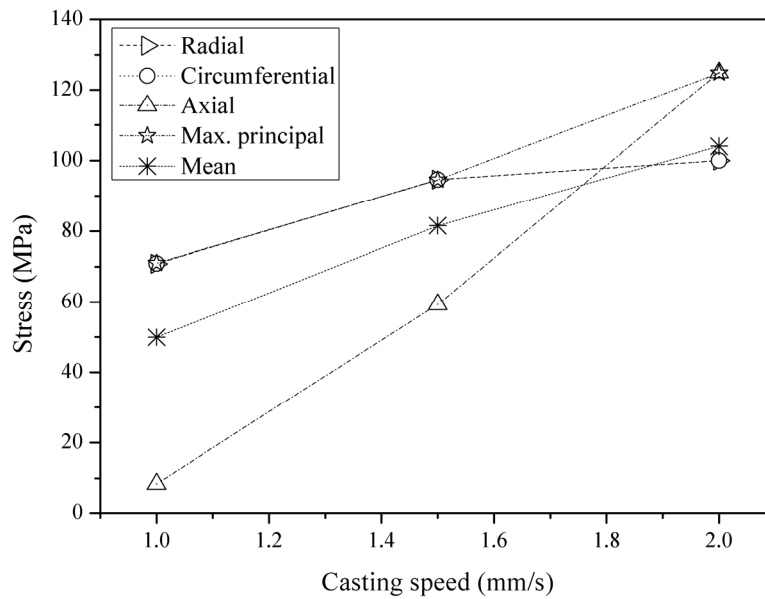


Fig. 7.1 The effect of cast speed on residual stress values formed in the center of the billet with the diameter 200 mm. Radial, circumferential, axial, maximum principal and mean stresses are reported in this figure [17].

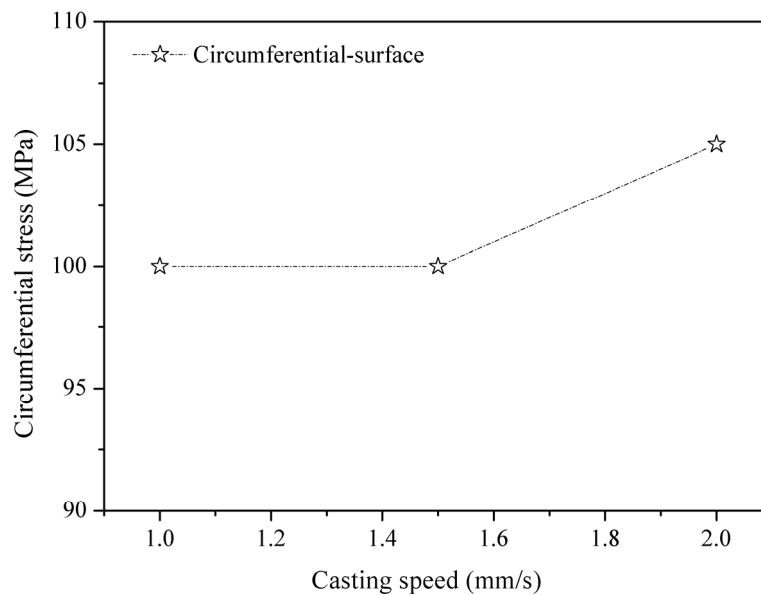


Fig. 7.2 Circumferential (maximum principal) stress values versus casting speed in the water impingement zone at the surface of the billet with the diameter 200 mm.

Effect of the billet size on the magnitude of residual thermal stresses can be observed in Fig. 7.3 and 7.4. In the billet with the diameter 300 mm the σ_{11} appears after 78 s in the WIZ and after 347 s in the center. For the 400 mm diameter billet these times read 160 and 680 s respectively. Trends are the same as those observed in Fig. 7.1 and 7.2 except for the fact that the radial and circumferential stress components increase all the way as the billet size increases. Again the axial stress component increases at the highest rate and becomes the maximum principal stress component in the 400 mm diameter billet. Similar to the effect of the casting speed (Fig. 7.2), the circumferential stress (σ_{11}) in the WIZ first passes through a plateau and then increases with increasing the billet size and reaches 105 MPa in a 400 mm diameter billet. Another

point that can be understood from Figs. 7.1 and 7.3 is that increasing either the casting speed or the billet size results in the increase of the mean stress in the center of the billets, which in turn increases the probability of brittle fracture, as discussed in Chapter 5.

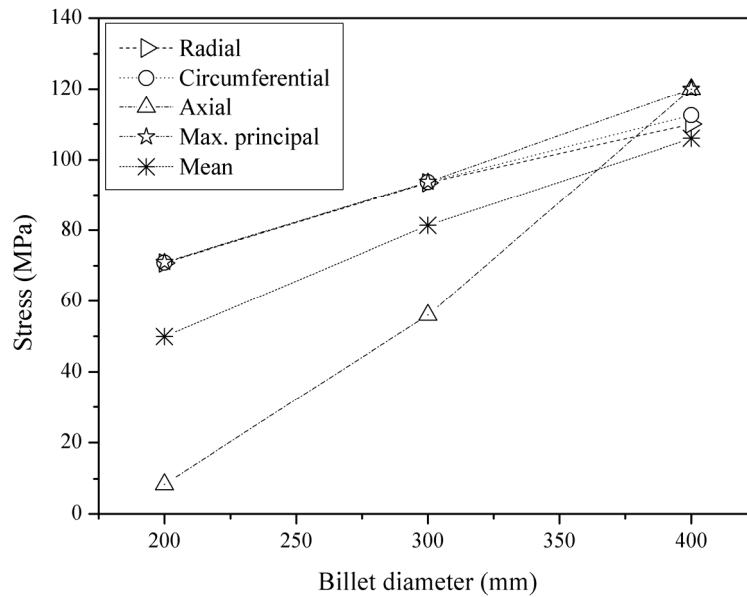


Fig. 7.3 The effect of billet size on residual stress values formed in the center of the billet at the standard casting speed of 1 mm/s. Radial, circumferential, axial, maximum principal and mean stresses are reported in this figure [17].

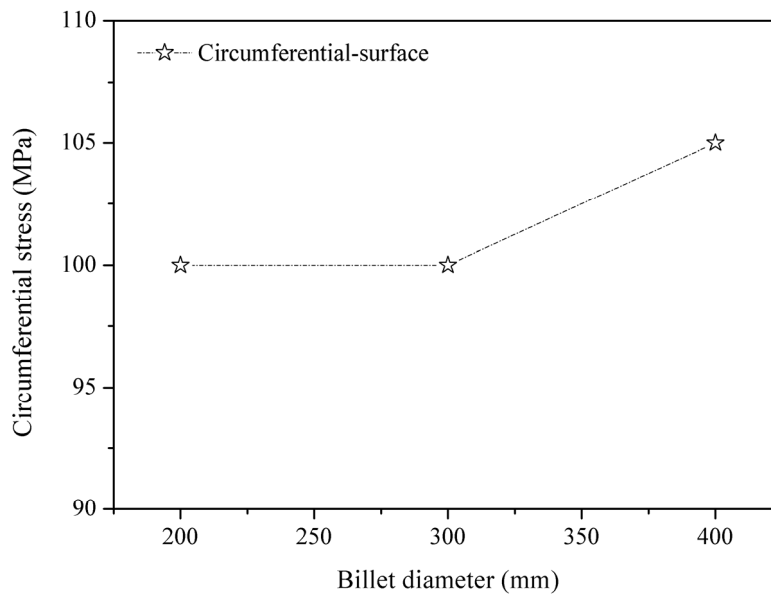
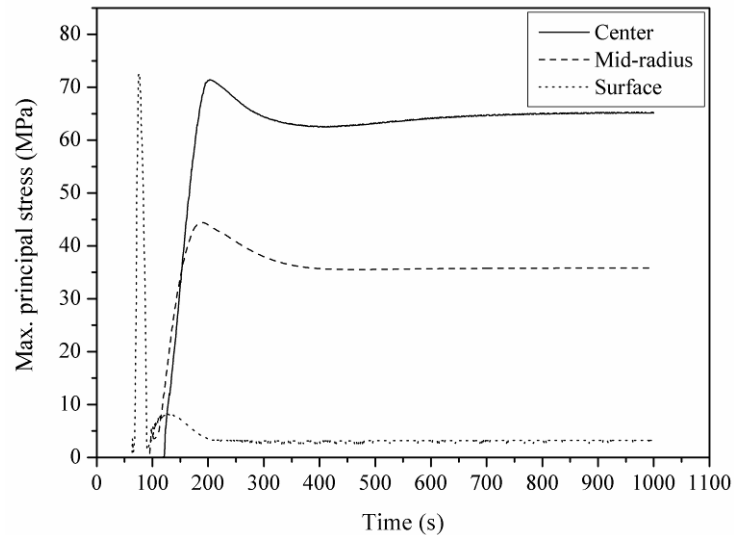


Fig. 7.4 Circumferential (maximum principal) stress values versus billet size in the water impingement zone at the surface of the billet cast at the speed of 1 mm/s.

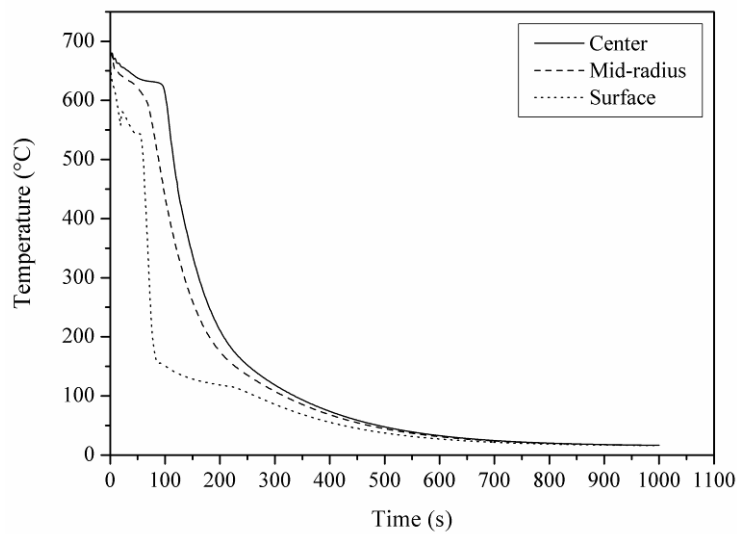
7.4 Cracking assessment in the billet

The critical crack size assessment is based on similar assumptions as in Chapter 6, i.e. there is no preferred crack orientation and cracks propagate normal to the maximum principal stress component. The additional assumption is that a higher σ_{11} level may

be interpreted as a higher failure probability due to a smaller critical crack size it causes. Having the plane strain fracture toughness of the material and assuming the ingot as a semi-infinite medium, we calculate by application of fracture mechanics the critical crack size that leads to catastrophic brittle fracture under various casting conditions.



(a)



(b)

Fig. 7.5 Computer simulation results showing: a) maximum principal stress values for the center (65 mm above the bottom block), mid-radius (35 mm above the bottom block) and surface (65 mm above the bottom block) of the billet cast under standard casting conditions mentioned in Table 5.2, b) cooling curves for the points mentioned above [17].

As in Chapter 6, the first step in such an approach is to locate the points in the billet where the σ_{11} is the highest. Fig. 7.5a shows the changes of the σ_{11} with time in the billet cast under standard conditions (\varnothing 200-mm and 1mm/s cast speed) and for similar coordinates as in Section 7.3 except for the lower mid-radius point (x: 48 mm, y: 35 mm). Corresponding computer-simulated cooling curves are shown in Fig. 7.5b. The evolution of the σ_{11} and the cooling curves shown here are similar to Figs. 6.7a and b. In the steady state regime, stresses increase in magnitude and reach a maximum.

They fall afterwards a little bit and reach a plateau, which remains constant up to the end of casting. This is also the case for the newly created elements afterwards and the stresses that reach the plateau value retain their magnitude until the billet is annealed or sawn [18,19].

From Fig. 7.5a it is obvious that the σ_{11} reaches its largest value in the center and in the WIZ, so these two points are used to calculate the critical crack sizes. The σ_{11} reaches a maximum (73 MPa) after 76 s in the WIZ where the temperature is around 200°C (Fig. 7.5b). It falls afterwards mainly due to the change in the stress mode at the surface from tensile to compressive. Similar to section 6.3, the maximum value of the σ_{11} in the center of the WIZ reads 100 MPa, which will be utilized for critical crack size assessments. In the center of the billet, the σ_{11} reaches its maximum value (71 MPa) after 200 s at the similar temperature (200 °C) (Fig. 7.5a, b). When casting reaches the steady state, this value falls and remains constant even after the end of the casting and stopping the water flow [19]. The same trend is observed for the mid-radius position with the maximum (44 MPa) after 200 s and the corresponding temperature of 175 °C.

As the σ_{11} reaches its maximum in the center and in the WIZ at the temperature around 200 °C, the experimentally measured K_{Ic} value (8.29 MPa m^{1/2} [19]) corresponding to this temperature can be applied to assess the critical crack size. Following the same procedure for higher casting speeds and bigger billet sizes, we would be able to investigate the effect of cast speed and billet size on the critical crack size and failure probability of the billets. As explained in Chapter 6, the penny shaped crack (PSC) (Fig. 6.8a) was chosen for the center of the billet while at the surface of the billet, the surface breaking semi-circular (thumbnail) crack (Fig. 6.8b) is chosen. Changes in the critical crack size with casting speed are presented in Fig. 7.6a and b for the center and the WIZ at the surface of the billet.

The critical crack sizes were calculated by applying the corresponding σ_{11} values of the mentioned points in the billet and the K_{Ic} value at 200°C to Eqs. 6.2 and 6.3. As can be seen in Fig. 7.6a, for the penny shaped crack the critical crack size leading to catastrophic failure decreases with increasing the casting speed. The same trend is observed for the thumbnail crack in the WIZ (Fig. 7.6b). The difference is that no changes are observed in the latter case between 1-1.5 mm/s casting speeds mainly because no changes occur in the maximum principal stress in this range.

Figs. 7.7a and 7.7b show the effect of billet size on the critical crack size formed in the center and in the WIZ, respectively. Like Fig. 7.6a and 7.6b, with increasing the billet size the critical crack sizes leading to catastrophic failure decrease resulting in a higher cracking susceptibility.

7.5 Discussion

As explained in the previous Chapter, the main idea behind application of fracture mechanics is that there must be some pre-existing voids, flaws or cracks at the tip of which the stress level is amplified to some critical levels. Such voids might be inclusions, chain of pores, or hot tears that reach a critical size. Cold cracking may also be the continuation of hot tearing, i.e. a hot crack that reaches a critical length and is oriented in the favorable direction might lead to catastrophic failure of the billet and cold cracking. However, there is not much information available on the exact mechanism of cold cracking, therefore the main assumption is that such defects exist at the onset of cold cracking.

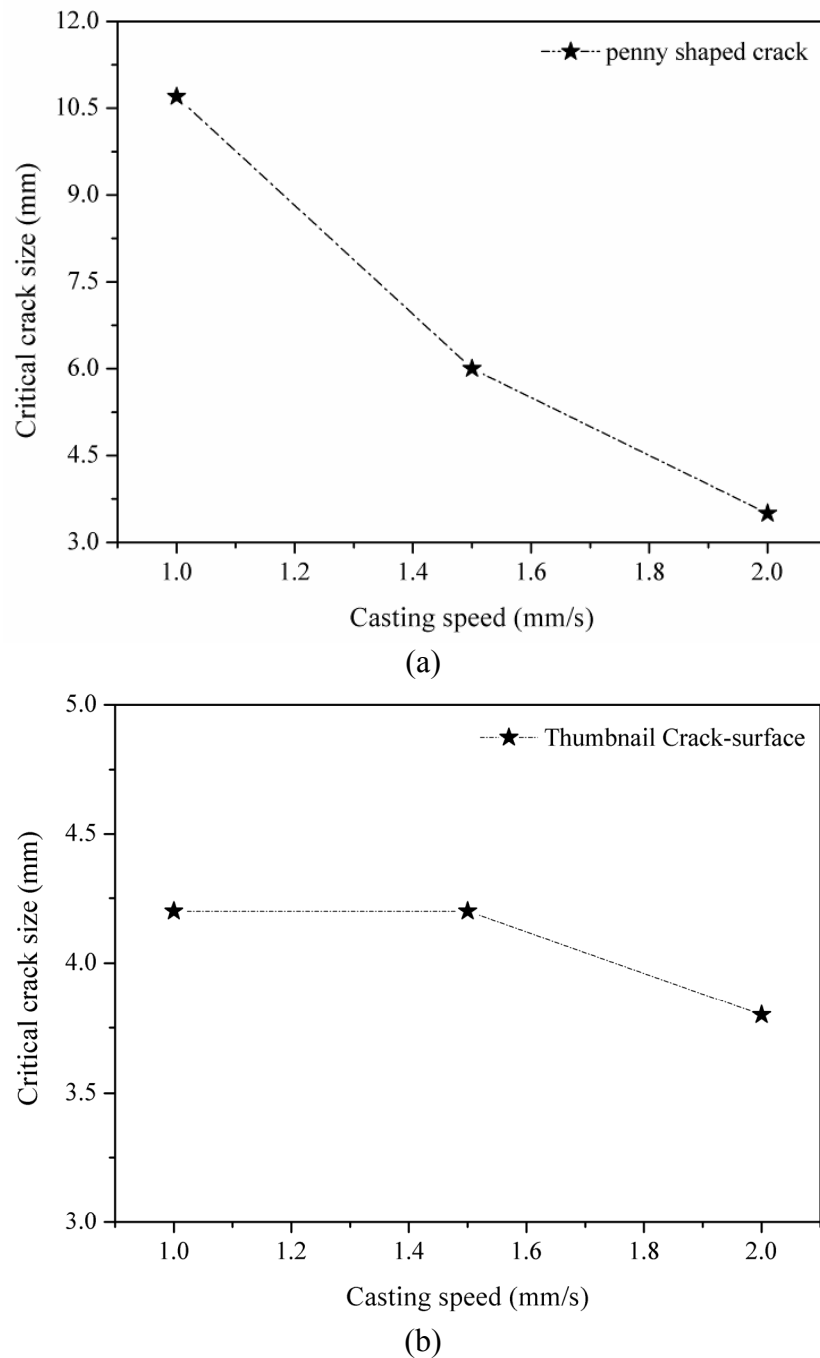


Fig. 7.6 Critical crack sizes in billets cast at various speeds: a) the penny shaped crack in the center of the billet [17], b) the thumbnail surface crack in the water impingement zone.

Distribution of residual thermal stresses in the billet (Fig. 4.8) shows that the stress state in the center of the billet is mainly tensile. As explained in Chapters 5 and 6, this holds for almost the entire casting time except for the very beginning, when it is slightly under compression due to the contraction of the surface. At the surface of the billet, the circumferential stress is tensile in the water impingement zone, while it turns to compressive upon further cooling (Fig. 7.5a).

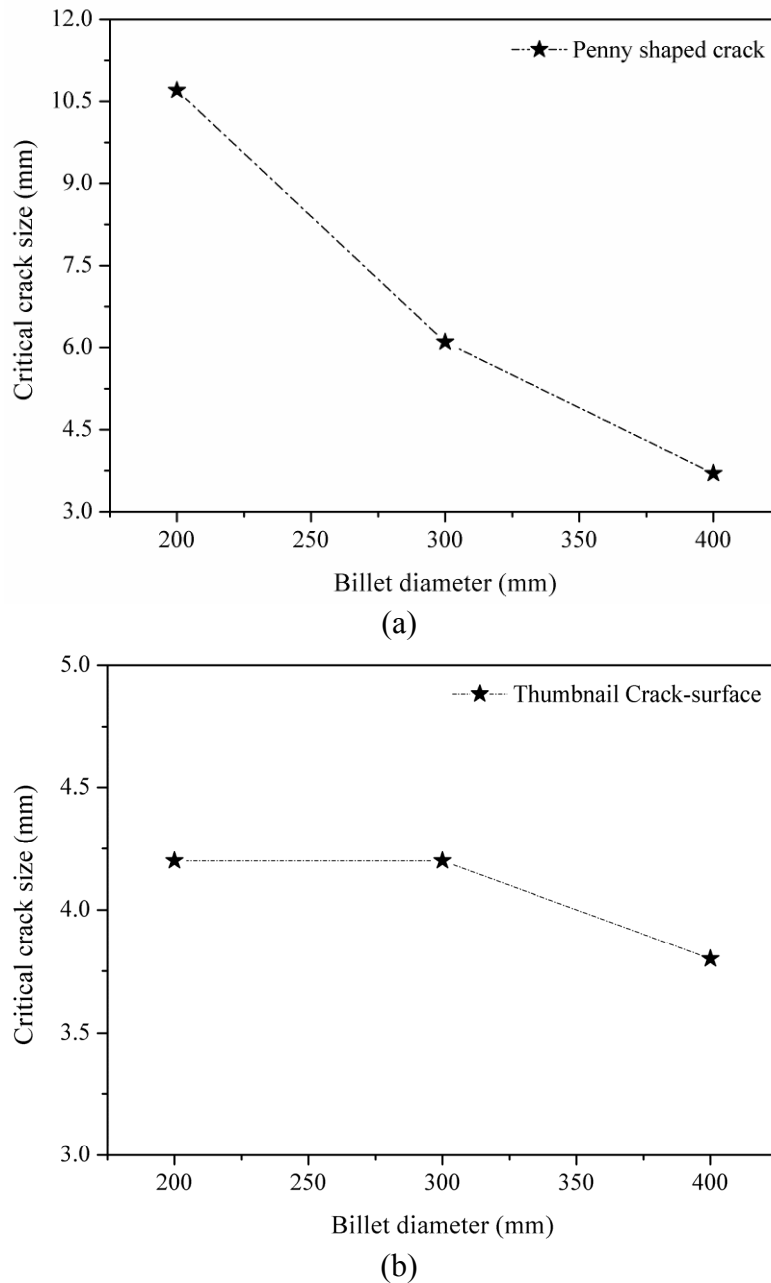


Fig. 7.7 Critical crack sizes in billets with various diameters: a) the penny shaped crack in the center of the billet [17], b) the thumbnail surface crack in the water impingement zone.

As cracks are expected to initiate and propagate under tensile stress fields, the center of the billet and the WIZ are the most vulnerable locations to cracking. In round billets compressive circumferential stress replaces the tensile one at the surface soon after the surface leaves the impingement zone. This results in an acceptable billet, although some small cracks may form at the surface of the billet in this stage. In Chapter 6 we discussed that according to fracture mechanics assessment (Fig. 7.6b) microcracks that reach the critical size of 4.2 mm may propagate catastrophically and result in failure of billets (\varnothing 200 mm, 1 mm/s). This is mainly observed in rectangular flat ingots (slabs) where the stress state in the vicinity of the narrow side remains tensile [20, 21]. In the center of the 200-mm billet, the situation becomes critical after 200 s when the σ_{11} reaches its maximum value (71 MPa for the standard case).

The increase in the magnitude of residual thermal stresses with increasing the casting speed and billet size (Figs. 7.1 to 7.4) is related to the increased thermal inhomogeneity in the billet. Heat balance in the billet is a function of the energy content of the material, i.e. the balance between the heat introduced by the molten metal in the mold, latent heat of fusion and the heat extracted by the mold and direct water cooling. The heat input depends on the casting speed and billet size. Faster casting speeds increase the heat input which in turn results in steeper temperature gradients and more inhomogeneous thermal contractions (Fig. 1.2). Similarly a larger billet size results in the increased heat input and a longer thermal conduction path. The specific heat of the liquid C_{pl} contributes to only ~5% of the total energy content of the material, hence melt temperature has low impact on the heat flow and the eventual thermal stresses [1]. According to Figs. 7.1 and 7.3, the rate of increase of residual thermal stresses is higher in the axial direction compared to the radial and circumferential directions. This can be explained by the fact that as the thermal conductivity of the material changes only slightly, the increased heat input results in a deeper sump which in turn brings about higher temperature differences in the axial direction (Fig. 1.2). It can also be mathematically shown by using the advection diffusion heat flow equation in cylindrical coordinates [1]:

$$\rho V C_p \frac{\partial T}{\partial z} = k \left(\frac{\partial^2 T}{\partial r^2} + \frac{1}{r} \frac{\partial T}{\partial r} + \frac{\partial^2 T}{\partial z^2} \right) + \rho L V \frac{\partial f_s}{\partial T} \frac{\partial T}{\partial z}, \quad (7.1)$$

where ρ is the density, V is the casting speed, C_p is the specific heat, k is the thermal conductivity, L is the latent heat of fusion, and f_s is the fraction solid (note that the term $\left(\frac{1}{r^2} \frac{\partial^2 T}{\partial \theta^2} \right)$ falls out due to the axial symmetry). The left hand side is the

convective heat flow (input), which increases by increasing the billet size or cast speed. The first compound term on the right is the diffusive heat flow and the second term the latent heat generation. Numerical solution of the above equation in the steady state condition has shown that the sump depth increases with the square of the diameter, linearly with the cast speed and is inversely proportional to the alloy thermal conductivity [22], which is in good agreement with earlier analytic approximations [23].

With increasing convective heat input, the left hand side of Eq. 7.1 increases which results in a higher rate of latent heat generation on the right hand side. As the thermal conductivity is constant, the temperature gradients should also increase to satisfy the energy conservation relationship. Higher temperature gradients cause higher thermal stresses [24] especially in the axial direction (Figs. 7.1 and 7.3). The fact that higher temperature gradients and subsequently higher stresses are formed in axial direction can be explained by the cooling conditions during DC-casting. Except for the start-up phase, where the heat is extracted through the bottom block, mold, and water jet, in the steady state regime the heat transfers more efficiently along radial and circumferential directions. Heat extraction efficiency in the z-direction decreases as the cast length increases. At this stage the bottom block acts mainly as a billet support. The higher residual thermal stresses bring about on the one hand the lower critical crack size and the higher probability of failure in the billets specifically in the center and in the water impingement zone (Fig. 7.5a). Their orientation on the other hand may affect the orientation of the crack plane with respect to the axial direction of the billet. It was explained in Chapter 5 that due to the small magnitude of the shear stress component, the principal stress axes make small angles with the original normal stress

axes. At lower casting speeds and smaller billet sizes the σ_{11} is oriented either in the radial or circumferential direction (Figs. 7.1 and 7.3) which results in cracks with planes parallel to the axial direction of the billet (Fig. 7.8) [10,19].

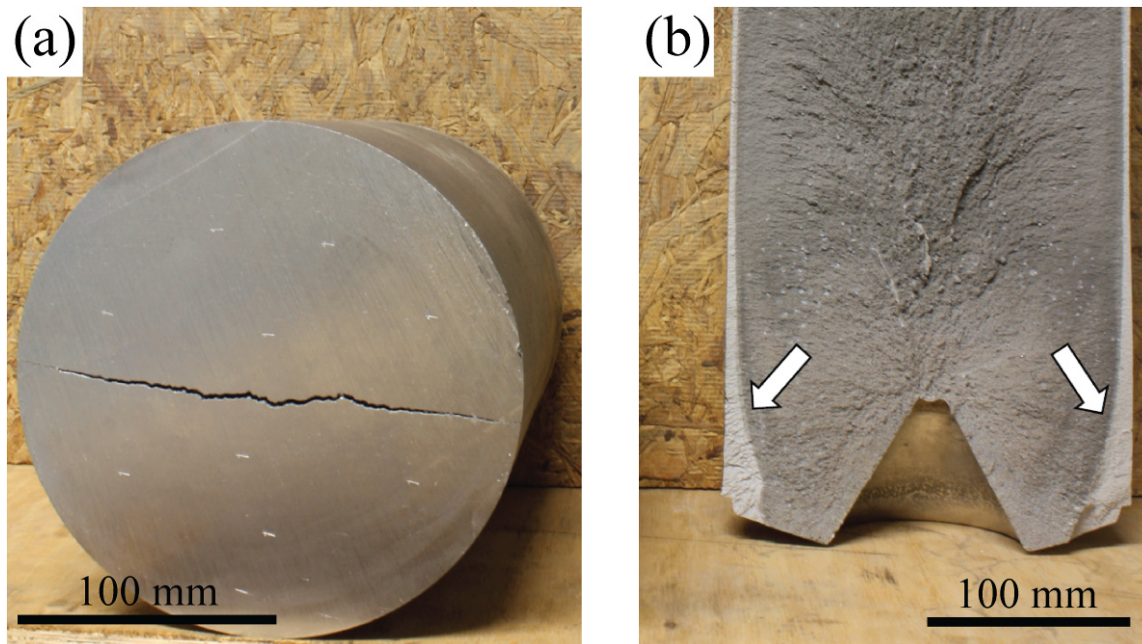


Fig. 7.8 Photos showing cold cracks in 200-mm 7475 DC-cast billets: (a) cross section of a billet with a cold crack propagated along radial direction, and (b) view of another billet split open, showing two parts of fracture surface separated by a color contrast [17]. In both billets the crack plane is parallel to the axial direction of the billet.

With increasing the casting speed or the billet size however, the σ_{11} turns towards the axial direction of the billet (Figs. 7.1 and 7.3). This means that the plane of the crack should also turn up to 90 degrees to get normal to the σ_{11} , which is now parallel to the axial direction of the billet. This results in so-called cup and cone cracks with various depths depending on the degree of inadequate cooling balance [10]. In our case when the penny shaped crack is considered, the plane of the crack would be parallel to the axial direction of the billet when the σ_{11} is oriented in the radial or circumferential direction. When the σ_{11} aligns with the axial direction of the billet however, the normal vector of the crack plane has an angle between 0 and 90° with the upward axial direction. Similar discussion may be done for the WIZ at the surface of the billet, i.e. with increasing either the casting speed or the billet diameter, temperature gradients become steeper and higher thermal stresses appear. Therefore, increasing the billet diameter or the casting speed facilitates the surface cracking and failure of the billets.

In the range of water flow rate chosen in this research, our results are in agreement with experimental results reported by Matsuda *et al.* [10], i.e. no impact on cracking susceptibility. At higher water flow rates (130-310 l/min) however, cracking occurred in practice [10]. Regarding the water temperature, the experimental results show that the heat flux decreases slightly as the water temperature increases [25]. In the water temperature range of 15-45 °C however, these changes are not considerable and may explain the negligible effect of water temperature on the simulation results.

7.6 Conclusions

The effect of various casting variables was studied in order to determine the cracking susceptibility in DC-cast billets. Thermomechanical simulations revealed that at the constant casting speed and billet size, the water temperature, water flow rate and melt temperature have negligible impact on either the magnitude or the distribution of residual thermal stresses. Casting speed and billet size however, appeared to be the most influential variables. Increasing either the casting speed or the billet size, results in increased temperature gradients and consequently higher thermal stresses not only in the center but also in the water impingement zone at the surface of the billet. The thermal stress in the axial direction of the billet increases faster than the radial and circumferential directions with the increasing casting speed and billet diameter. As a result, the principal stress axis rotates towards the billet axis with changing the process parameters. As cracks preferably align and propagate normal to the maximum principal stress component, the rotation of the axis of the principal stresses results in different crack plane orientations to be formed during DC-casting. At lower casting speeds and billet sizes, the maximum principal stress component lies either along the radial or circumferential direction, leading to cold cracks parallel to the axial direction. At higher casting speeds or larger billet diameters however, the crack plane tilts and gets aligned normal to the maximum principal stress, which is in the axial direction, and results in cup and cone cracks.

References

- [1] J.F. Grandfield, P.T. McGlade, *Mater. Forum* 20 (1996) 29-51.
- [2] U. Chandra, A. Ahmed, in: Kuang-O Yu (Ed.), *Modeling for Casting and Solidification Processing*, Marcel Dekker Inc., New York, 2002, pp. 55-93.
- [3] J.R. Davis, *Aluminium and Aluminium Alloys*, ASM Specialty Handbook, ASM International, Materials Park (OH), 1994, pp. 68-69.
- [4] M. Lalpoor, D.G. Eskin, L. Katgerman, *Mater. Sci. Eng. A* 497 (2008) 186-94.
- [5] J. B. Hess, *Metall. Trans. A* 14 (1983) 323-327.
- [6] B. Hannart, F. Cialti, R. van Schalkwijk, in: U. Mannweiler (Ed.), *Light Metals*, TMS, 1994, pp. 879-887.
- [7] Z. Yubo, C. Jianzhong, Z. Zhihao, Z. Haitao, Q. Ke, *Mater. Sci. Eng. A* 406 (2005) 286-292.
- [8] W. Roth: *Z. Metallkunde*, Vol. 40, No. 12, 1949, p. 145.
- [9] B. Commet, P. Delaire, J. Rabenberg, J. Storm, in: P. N. Crepeau (Ed.), *Light Metals*, TMS, 2003, pp. 711-717.
- [10] K. Matsuda, S. Nagai, Y. Miyate, H. Maehara, I. Tsukuda, in: *6th International Aluminum Extrusion Technology Seminar*, Aluminium Association and Aluminium Extruder's Council, Vol. I, Chicago, Illinois, USA, 1996, pp. 525-528.
- [11] A. Burghardt, B. Commet, J-M Drezet, H.G. Fjær: in P.R. Sahm, P.N. Hansen, J.G. Conley, (Eds.), *Modeling of Casting, Welding and Advanced Solidification Processes IX*, Shaker Verlag, Germany, 2000, pp. 25-32.
- [12] W. Schneider, E.K. Jensen, B. Carrupt, in: J. Evans (Ed.), *Light Metals*, TMS, 1995, pp. 961-967.
- [13] S. Benum, D. Mortensen, H. Fjær, H-G Øverlie, O. Reiso, in: W. Schneider (Ed.), *Light Metals*, TMS, 2002, pp. 967-974.

- [14] J.L. Dassel, T.C. Zinniger, in: *Light Metals*, The Metallurgical Society of AIME, Warrendale, PA, 1982, pp. 793-801.
- [15] US Patent. No. US2007/0102136 A1, United States, 2007.
- [16] K.-M. Chang, B. Kang, *J. Chin. Inst. Eng.* 22 (1999) 27-42.
- [17] M. Lalpoor, D.G. Eskin, L. Katgerman, *Metall. Mater. Trans A* 41 (2010) 2425-2434.
- [18] O. Ludwig, J.-M. Drezet, B. Commet, B. Heinrich, in: C-A. Gandin, M. Bellet (Eds.), *Modeling of Casting, Welding and Advanced Solidification Processes XI*, TMS, Warrendale (PA), 2006, pp. 185-192.
- [19] M. Lalpoor, D.G. Eskin, L. Katgerman, *Metall. Mater. Trans. A* 40 (2009) 3304-3313.
- [20] W. Boender, A. Burghardt, E.P. van Klaveren, J. Rabenberg, in: A.T. Tabereaux (Ed.), *Light Metals 2004*, TMS, Warrendale (PA), 2004, pp. 679-684.
- [21] V.A. Livanov., in: A.F. Belov, G.D. Agarkov (Eds.), *Aluminum Alloys*, Oborongiz, Moscow, 1955, pp. 128-168.
- [22] S. C. Flood, P.A. Davidson, S. Rogers, in: M. Cross, J. Campbell (Eds.), *Modeling of Casting, Welding and Advanced Solidification Processes VII*, London (UK), 1995, pp. 801-808.
- [23] V.I. Dobatkin, *Continuous Casting and Casting Properties of Alloys*, Moscow, Oborongiz, 1948.
- [24] N. Noda, R.B. Hetnarski, Y. Tanigawa, *Thermal Stresses*, 2nd Ed., Taylor & Francis, New York (US), 2003, p. 225.
- [25] J. Langlais, T. Bourgeois, Y. Caron, G. Béland, D. Bernard, in: J. Evans (Ed.), *Light Metals*, TMS, 1995, pp. 979-986.

Chapter 8

Development of a cold cracking criterion for DC-casting of high strength aluminum alloys

In Chapters 5, 6 and 7 we discussed the stress state in the DC-cast billets under steady state casting conditions and after the end of casting. We learned how stresses develop, when they reach their maximum and under which conditions they may lead to catastrophic failure of the billet. The most critical locations of the billets were also detected and the critical crack sizes were calculated for these points. However, the critical crack sizes were not calculated for the entire billet due to the fact that the crack calculation module was not embedded in the model. In this chapter, we discuss the elements required for establishment of a cold cracking criterion. A new module embedded in ALSIM5, calculates the critical crack sizes for the entire billet. Contour maps of the critical crack sizes help us understand the stages and locations where the AA7050 billet is most prone to cracking. In the next step, a typical 7xxx series aluminum alloy with high propensity to cold cracking is selected for assessment of the model. Following the procedures mentioned in Chapter 2, the mechanical properties as well as plane strain fracture toughness of this alloy were measured and embedded in the model. The estimated critical crack sizes were tested by performing DC-casting trials at Corus-Netherlands (IJmuiden). The effect of casting variables is also studied for this alloy using both computer simulations and DC-casting experiments.

8.1 Introduction

In spite of all technical improvements and developments in aluminum industry, ingots of high strength aluminum alloys still suffer from cracking and failure. The cracking may occur above solidus temperature when the major fraction of inter-dendritic spaces is covered by low melting point nonequilibrium eutectics and result in hot cracks [1]. It can also occur below solidus or at temperatures near room temperature where the material is extremely brittle, and lead to cold cracking [2]. It is not well understood whether cold cracks are the hot cracks that catastrophically propagate when reach the critical length or they just occur when the elastic strain energy of the system releases abruptly on voids or brittle intermetallics. Therefore separate criteria for hot [3-6] and cold cracking [7-10] have been established. Criteria developed on cold cracking can be classified in two groups: experiment based criteria [7,8] and computer simulation based criteria [9,10]. Experimentally derived criteria have been

based on the results of numerous cast trials under various casting conditions and ingot geometries. Livanov [7] e.g., noticed that to prevent hot cracks in slabs the cast speed should be lower than the speed predicted by Eq. 8.1, while he advised higher cast speeds than what Eq. 8.2 predicts to avoid cold cracks (Fig. 1.9).

$$V_h = \frac{K}{b^m}; \quad (8.1)$$

$$V_c = Mb^x \left(\frac{n}{n+1} - a \right)^y \quad (8.2)$$

where:

$V_{h,c}$ = casting speed (mm/min)

b = thickness of the ingot (mm)

m = exponent (larger than unity, close to 1.5)

K = a constant depending on the alloy

n = multiplicity (width to thickness ratio)

x, y = nonzero parameters

M = a constant depending on the alloy

a = a coefficient equal to 0.5.

Experimentally derived equations and graphs (Fig. 1.9) could eventually indicate the proper casting speed for the corresponding slab thickness, although casting of slabs thicker than a certain value appeared not to be feasible (probably due to the mold design available at that time). The main disadvantage of such a criterion is that numerous casting trials are required to gain the optimum casting conditions. On the contrary, computer simulation criteria are more physically based and deal with the fracture mechanics concepts. According to the fracture mechanics, catastrophic failure occurs when a crack or flaw reaches a critical length in the presence of a tensile stress field. Normal stress values can be obtained through thermomechanical simulation of the DC-casting process, and plane strain fracture toughness (K_{Ic}) values may be measured experimentally for the alloy under consideration. By application of fracture mechanics, the critical crack size leading to catastrophic failure can be calculated with right selection of the crack geometry [9,10]. W. Boender *et al.* [9] and O. Ludwig *et al.* [10] used the simulated maximum principal stress to assess the critical crack size that results in catastrophic failure. For slabs (width: 1150 mm, thickness: 360 mm, length: 1500 mm) of Al-4.5%Cu [10] with the maximum principal stress 80 MPa and the K_{Ic} equal to 15 MPa·m^{1/2} [11] the critical crack size was assessed to be 8 mm. In AA2024 slabs (width: 2000 mm, thickness: 510 mm, length: 2000 mm) [9], penny-shaped critical crack sizes (radius of the “penny”) appeared to be between 5 and 50 mm for various maximum principal stress values found in different locations (Fig. 8.1a; the same K_{Ic} value as in [10] was used). By means of computer simulations, Boender *et al.* [9] also studied the effect of wipers application [12] on the eventual critical crack size (Fig. 8.1b) and noticed that the cracking probability decreases due to the partial stress relief brought about by the wiping process. The wiping process was further developed later and is patented under the name of in-situ homogenization [13]. In this chapter, the results of thermomechanical simulations for AA7050 alloy are reported. Using the computer simulated values of the maximum principal stress and application of K_{Ic} values from room temperature to 200°C, the critical crack sizes are calculated for the billets cast at two different speeds and the contour maps are presented. Later on we follow the same procedure as mentioned in Chapter 2 to measure the mechanical

properties and the plane strain fracture toughness of another typical 7xxx series aluminum alloy in the as-cast condition. By performing DC-casting trials, the critical crack sizes calculated by ALSIM are examined and validated. The key strength of this work is that the constitutive parameters and the plane strain fracture toughness values represent the genuine as-cast material.

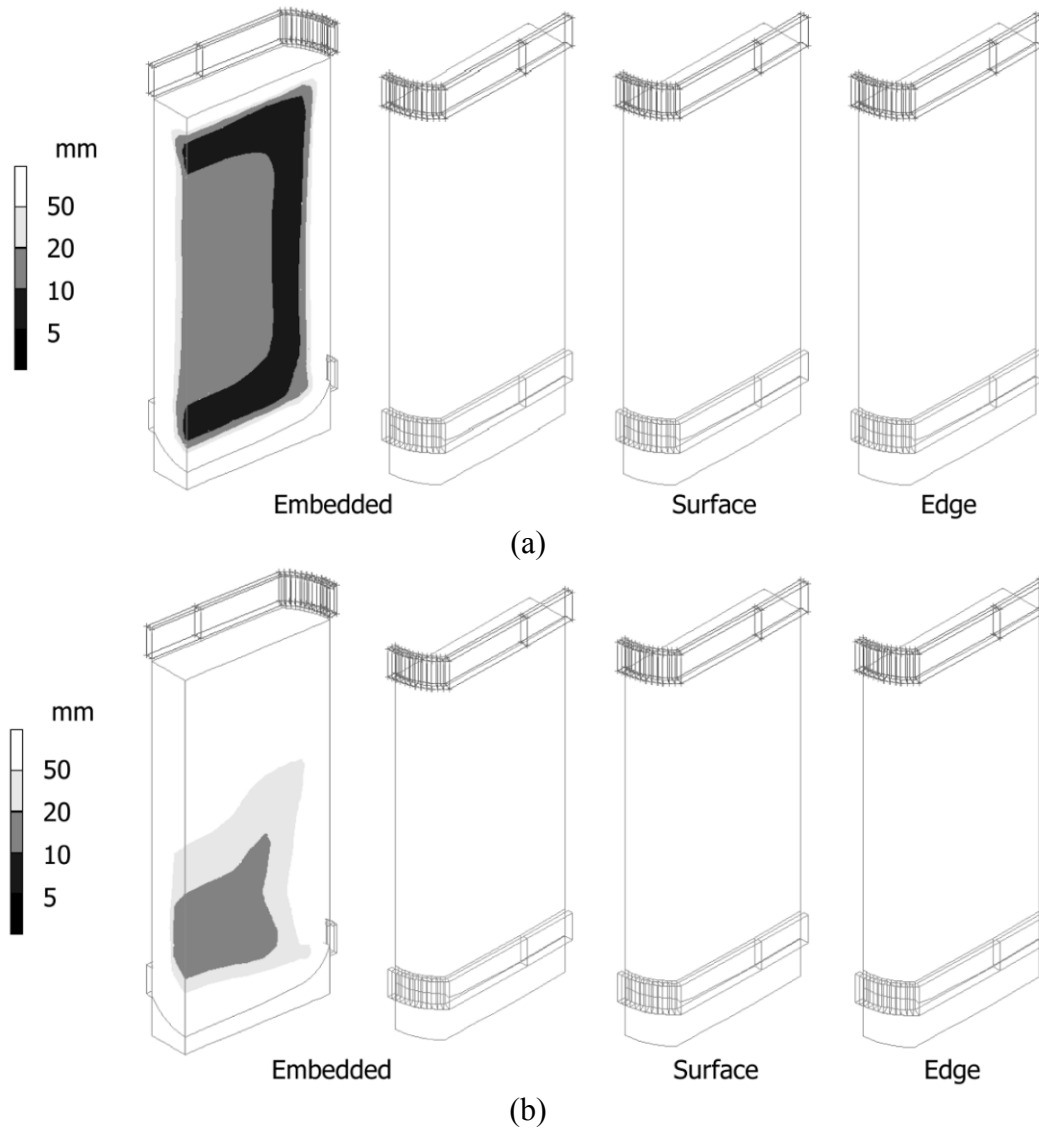


Fig. 8.1 The critical crack size at the end of cooling in the DC-cast slab modeled by Boender *et al.* [9]: (a) no wiper applied, (b) wiper applied. Embedded stands for penny shape crack, surface and edge for the semi-circular thumbnail and quarter-circular edge cracks [9].

8.2 Cold cracking criterion for AA7050 DC-cast billets

8.2.1 Model setup

As in Chapters 5 to 7, ALSIM5 was used for thermomechanical simulations. A new module was added to ALSIM5 through which critical crack sizes can be calculated using equations 6.2 and 6.3. The main assumption is that the cracks are oriented

normal to the maximum principal stress (opening mode, Fig. 8.2a) with a tensile nature. Where the σ_{11} is compressive (negative value) “-1” is assigned to the critical crack size (CCS) and is disregarded. Various shape factors can be selected to account for different crack geometries. K_{Ic} values were also listed as a function of temperature and used as input data for the model. In this chapter we confine our analysis to the penny shaped crack as shown in Fig. 6.8a. We run two sets of simulations for round AA7050 billets at casting speeds 1 and 2 mm/s under the conditions shown in Table 8.1.

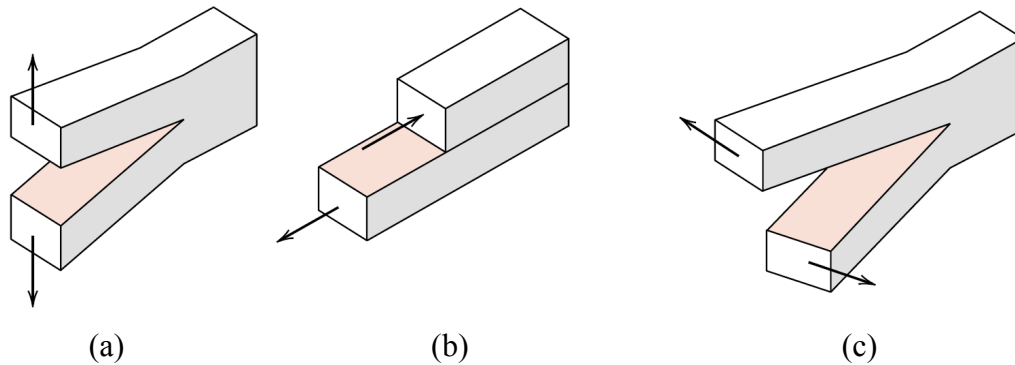


Fig. 8.2 The three modes of crack surface displacement: (a) mode I, opening or tensile mode; (b) mode II, sliding mode; and (c) mode III, tearing mode [14].

Table 8.1 Description of casting process parameters. Second values correspond to the billet cast at 2 mm/s [15].

Process parameter	Value
Ingot diameter (mm)	200
Final length of the billet (mm)	380 and 400
Casting speed (mm/s)	1 and 2
Melt temperature (°C)	680
Water flow rate (l/min)	80, 200
Water temperature (°C)	15
Start temperature of bottom block (°C)	20

8.2.2 Simulation results and discussion

From Fig. 5.2 we recall that the stress state in the center of the billet is mainly tensile. Another critical point in the billet is the WIZ, where the largest tensile stress appears in the circumferential direction. To be able to discuss the failure probability in the billet the contour maps of the three components of the principal stress tensor ($\sigma_{33} < \sigma_{22} < \sigma_{11}$) are shown in Fig. 8.3a, b, and c. The simulation is run for 380 s to make sure that the steady state conditions are reached. In agreement with the results shown in Fig. 5.2 the principal stress components appear to be tensile in the center of the billet and compressive at the surface. As discussed by Boender *et al.* [16], although having three tensile principal stress components in the center results in a nearly zero equivalent von Mises stress, it does not imply that no failure may occur. In other words, such a stress state facilitates the occurrence of a brittle fracture in the center of the billet. According to Rankine's theory which is more applicable to brittle materials, failure occurs when either the maximum principal stress reaches the tensile strength or the minimum principal component reaches the uniaxial compressive strength [17]. As the stresses computed by ALSIM are far below the fracture strength of the material (200°C: 225 ± 4 MPa, 100°C: 226 ± 8 MPa and room temperature: 266 ± 12 MPa [18]), the effect of stress raisers (cracks and flaws) should be taken into account. Similarly, in a brittle material and under a triaxial state of stress cracks mainly orient themselves normal to the largest component of the principal stresses (σ_{11}) [19]. Hence, the maximum principal stress component is selected for calculation of the critical crack sizes. Fig. 8.3d shows the distribution of the critical crack size in a billet cast at a speed of 1 mm/s. As can be seen the most dangerous location appears to be in the WIZ where the critical crack size is below 10 mm. In the center of the billet the situation is the same although the critical crack size is larger due to the smaller σ_{11} values. Another vulnerable point is the corner on top of the bottom block where the billets shown in Figs. 6.11 and 7.8 cracked. The cracking probability decreases by moving outwards from the center of the billet or the WIZ. In the remaining parts of the billet (mainly top center) stresses are either compressive or have low values resulting in unrealistic high values of critical crack size, which have been sorted out. Similar contour maps are shown in Fig. 8.4 for a billet cast at 2 mm/s. After 220 s, the stress state in the billet did not change noticeably, which indicates that the steady state conditions governed. As can be seen, three components of the principal stress tensor (Figs. 8.4a, b, and c) have increased considerably compared to the case of 1 mm/s. As discussed in Chapter 7, a higher cast speed results in a higher heat input and eventually increases the temperature gradients especially in the axial (y) direction [20,21]. Fig. 8.4d shows the distribution of the critical crack size in the billet cast at 2 mm/s. Closer observation reveals three main differences with the billet cast at 1 mm/s. First, the critical crack size has decreased to below 10 mm in the center of the billet which is the result of higher σ_{11} values there. The area with the smallest critical crack size is larger compared to the billet cast slower. Second, the area indicating the critical crack size in the WIZ has shrunk due to the shorter time the billet spends in this region. Third, the vulnerable point at the corner on top of the bottom block has disappeared mainly due to the negative corresponding σ_{11} value.

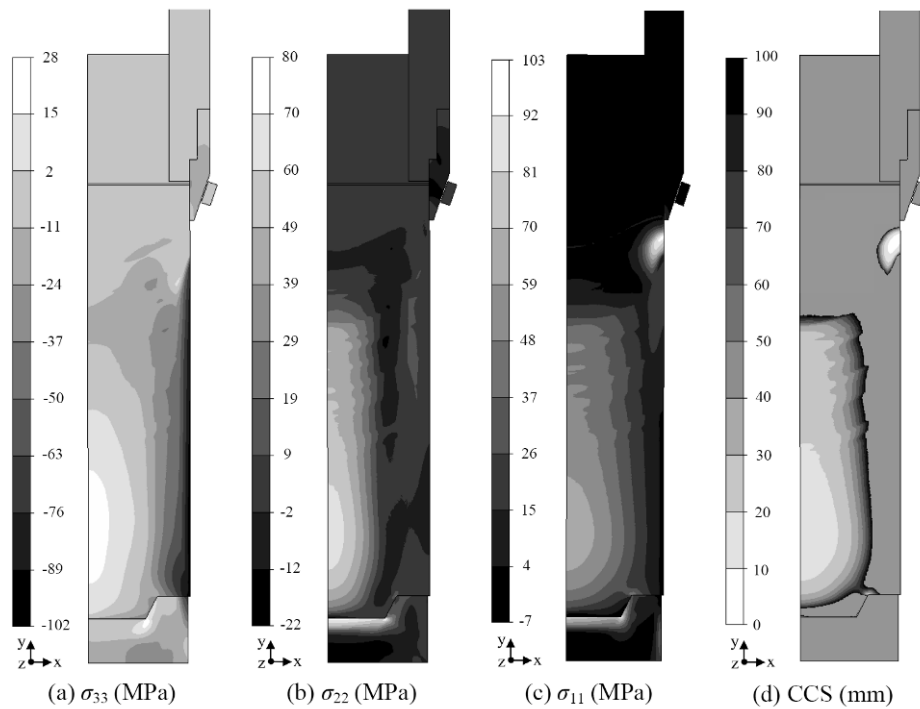


Fig. 8.3 Computer simulation results showing the components of the principal stress tensor: (a) σ_{33} , (b) σ_{22} , and (c) σ_{11} after 380 s of casting at speed 1mm/s. (d) Critical crack size distribution for a penny shaped crack calculated using σ_{11} [15].

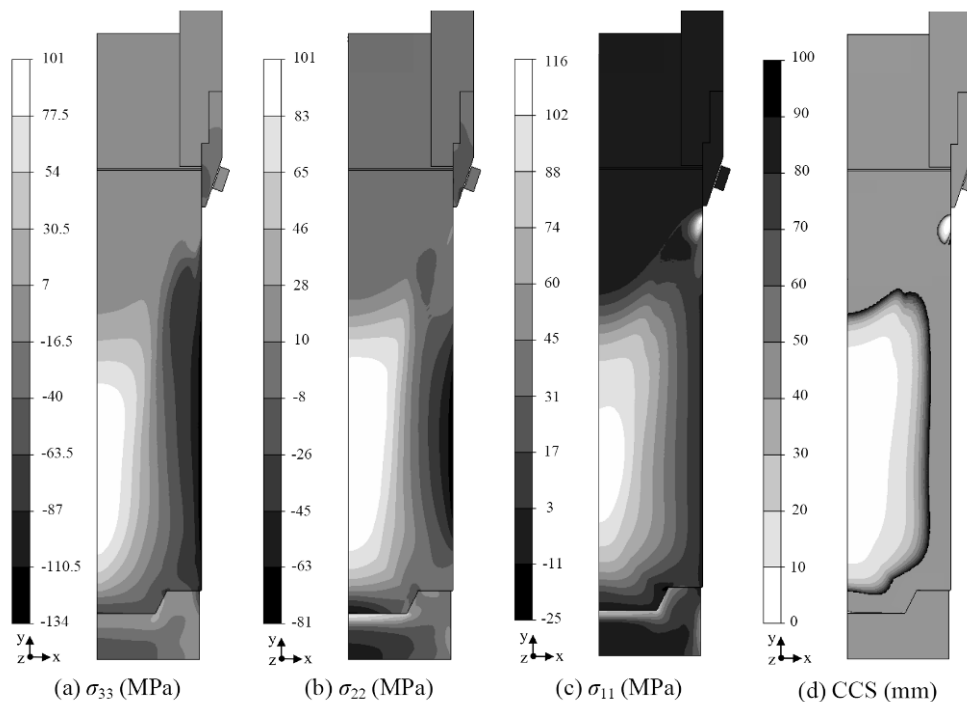


Fig. 8.4 Computer simulation results showing the components of the principal stress tensor: (a) σ_{33} , (b) σ_{22} , and (c) σ_{11} after 220 s of casting at speed 2 mm/s. (d) Critical crack size distribution for a penny shaped crack calculated using σ_{11} [15].

Although the direction of the principal stress components are not shown here, comparison of the stress tensor with the principal stress tensor revealed that the σ_{11} is either in the radial or circumferential direction at lower cast speeds (1 mm/s). As the

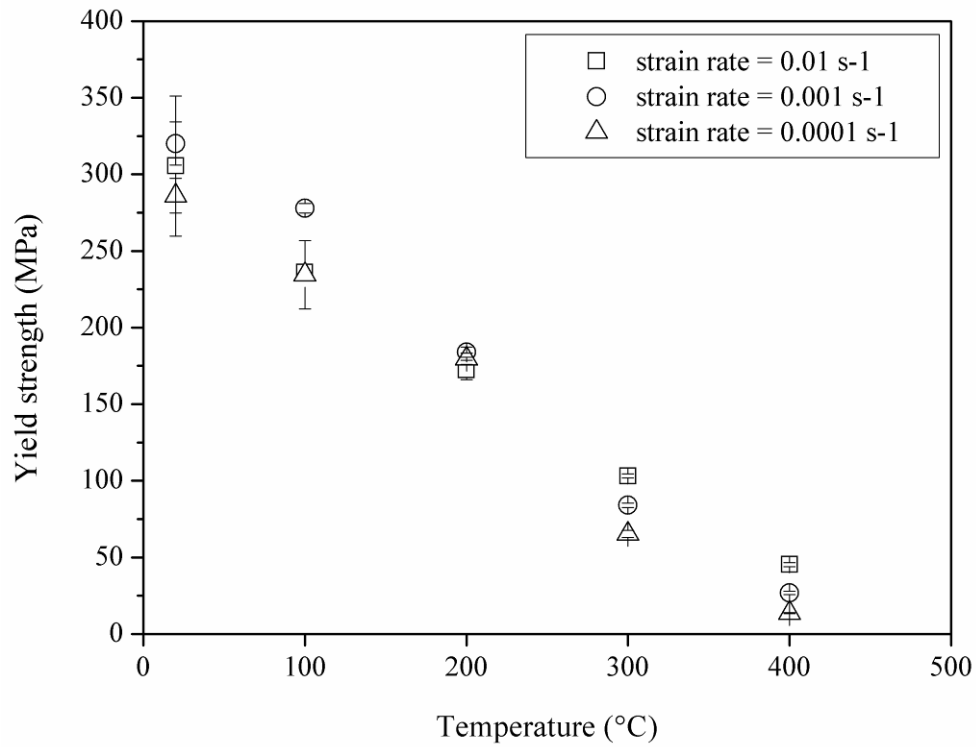
cracks propagate mainly normal to the largest component of the principal stresses, cracks with planes parallel to the axial direction of the billet result [21]. At higher cast speeds (2 mm/s) however, the σ_{11} -axis turns towards the axial direction of the billet, which in turn results in crack planes normal to that direction. This issue was discussed in detail in Chapter 7.

8.3 Cold cracking criterion for a typical 7xxx series alloy

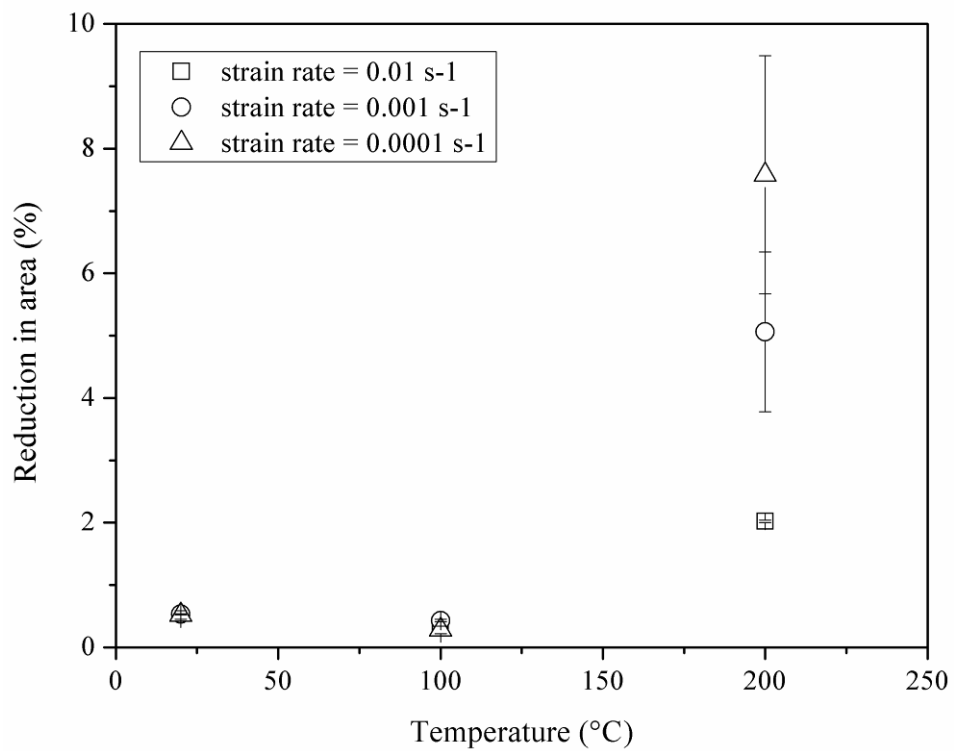
As mentioned in Chapter 1, cold cracking is a major problem in the DC-casting of high strength aluminum alloys. The efficiency of the casting process is rather low in the beginning when newly developed alloys are cast. In this section we study the thermomechanical behavior of one of new 7xxx series aluminum alloys which is highly prone to cold cracking. As in Chapter 2, we first determine its mechanical properties, constitutive parameters and plane strain fracture toughness. In the next step, we run simulations to examine the cold cracking propensity of the alloy under various casting conditions (Simulations were run at Corus-Netherlands (IJmuiden)). The results of the DC-casting trials performed at Corus-Netherlands (IJmuiden) were utilized for validation of the calculated critical crack sizes.

8.3.1 Determination of the mechanical properties

The material used in this research was gained from a 260 mm diameter billet produced at Corus-Netherlands (IJmuiden) through DC casting with a conventional mold (without hot top) from the melt that was degassed in the furnace. Tensile specimens were cut along the radial axis of the billet and machined using the geometry shown in Fig. 2.1. Tensile tests were performed at room temperature, 100, 200, 300 and 400°C at the strain rates of 10^{-2} , 10^{-3} and 10^{-4} s⁻¹. Experiment conditions were the same as in section 2.2.2. Figs. 8.5a and b show the changes in the yield strength and ductility of the alloy with temperature. The results show that although the mechanical behavior of the material is very similar to AA7050, some differences are noticeable. Compared to AA7050 (Fig. 2.10a) higher yield strength values are recorded at lower temperatures. Although the new alloy shows higher ductility at 200°C, it becomes extremely brittle below this temperature and behaves similar to 7050 alloy. Based upon our experience with AA7050 in Chapter 2, we knew that the material undergoes substantial plastic deformation above 200°C (23-44%), therefore samples were not deformed more than 10% above 200°C and no ductility values are recorded. The fact that the alloy shows more plasticity at 200°C compared to AA7050 strengthens the idea that the new alloy must be more prone to cracking below 200°C. The effect of strain rate on the flow stress of the 7050 alloy at the true strain 0.002 is shown in Fig. 8.6. Similar to AA7050, at high temperatures (300 and 400 °C) the flow stress increases as the deformation rate increases, but at lower temperatures (beginning at 200 °C) the material behavior becomes strain-rate independent.



(a)



(b)

Fig 8.5 Mechanical properties of the 7xxx samples: (a) average yield (fracture) strength at different temperatures and strain rates; (b) average reduction in area (%).

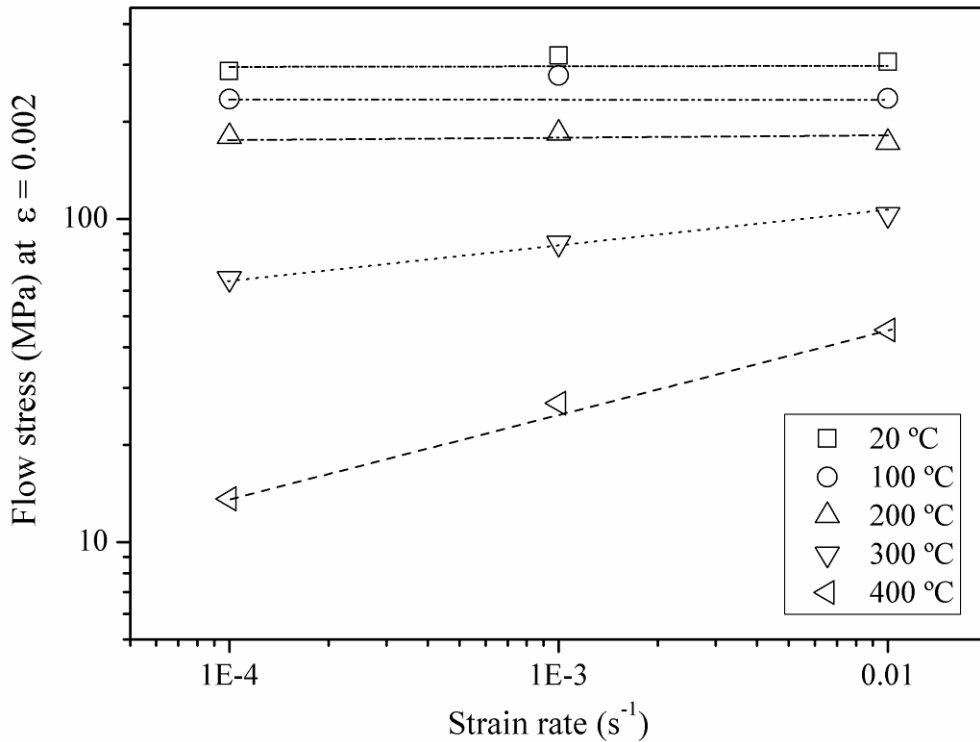


Fig. 8.6 The effect of strain rate on the flow stress at $\varepsilon = 0.002$ at different temperatures.

Table 8.2 Constitutive parameters of the newly developed 7xxx series alloy determined from the extended Ludwik equation.

Temperature (°C)	K	n	m
20	1742 ± 8	0.49 ± 0.04	0
100	1571.5 ± 120	0.46 ± 0.03	0
200	659 ± 5	0.15 ± 0.005	0.07 ± 0.01
300	242 ± 3	0.07 ± 0.01	0.1 ± 0.005
400	161 ± 22	0.07 ± 0.01	0.13 ± 0.02

The constitutive parameters of the alloy were also determined by fitting the extended Ludwik equation [22] (Eq. 2.1) to the true stress-strain curves. $K(T)$, $n(T)$ and $m(T)$ are listed in Table 8.2 and are plotted against temperature in Figs. 8.7a, b and c. As in AA7050, the negative values of m below 200°C were neglected and replaced by zero. Comparison of the Figs. 8.7a, b and c with 2.13, 2.14 and 2.15 reveals that the temperature dependence of the constitutive parameters of the newly developed alloy is similar to AA7050 although some differences are noticeable. The K values of the new alloy are much larger at lower temperatures. The strain hardening coefficient n also shows relatively higher values at lower temperatures. Regarding the strain rate sensitivity m , the results are roughly the same as AA7050, although at 200°C, a nonzero value is recorded.

The plane strain fracture toughness of the alloy was also measured from room temperature to 200°C following the same procedure as in section 2.3.3 (ASTM-E399) and the results are shown in Fig. 8.8. Compared to AA7050, higher K_{Ic} values are recorded which remain roughly the same over the temperature range examined here (20-200°C). The fracture mode was the same as AA7050, i.e. brittle intergranular.

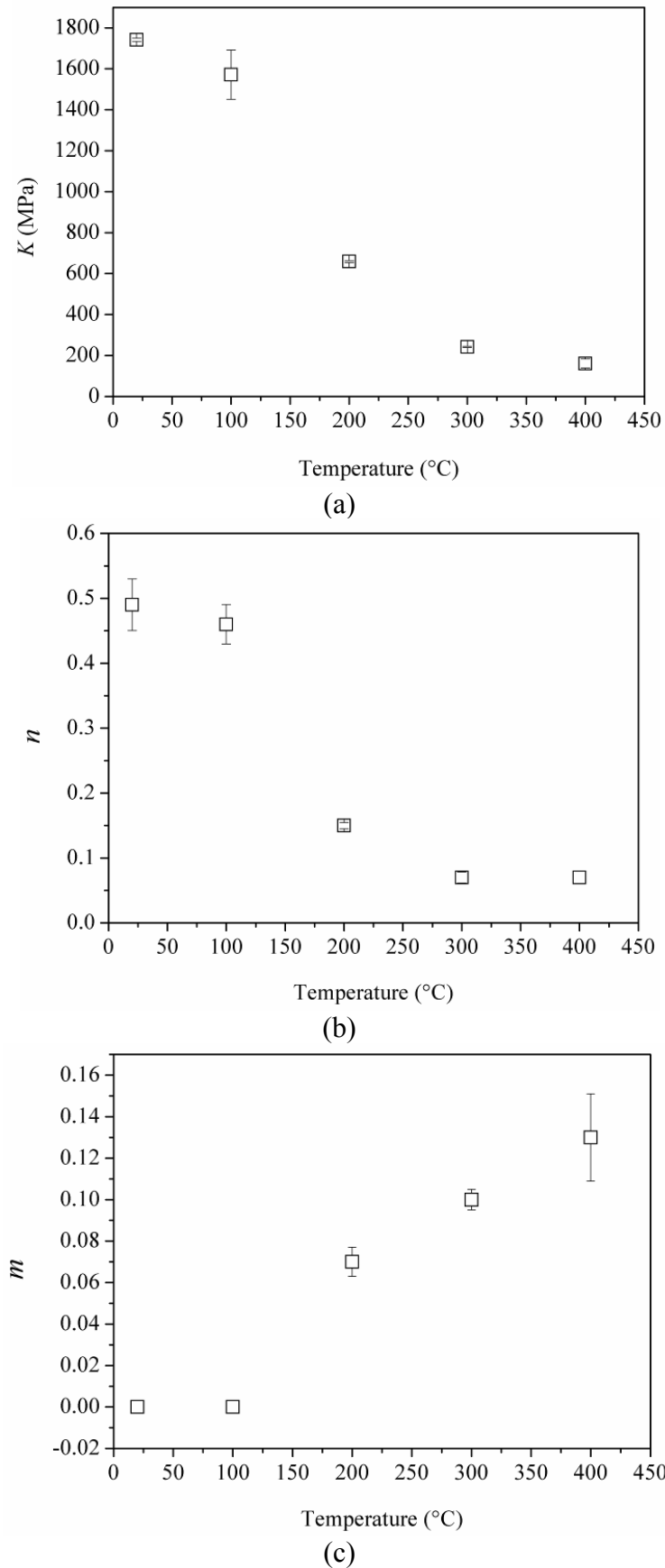


Fig. 8.7 The constitutive parameters of the newly developed 7xxx series alloy gained from the as-cast material: (a) consistency; (b) strain hardening coefficient and (c) strain rate sensitivity.

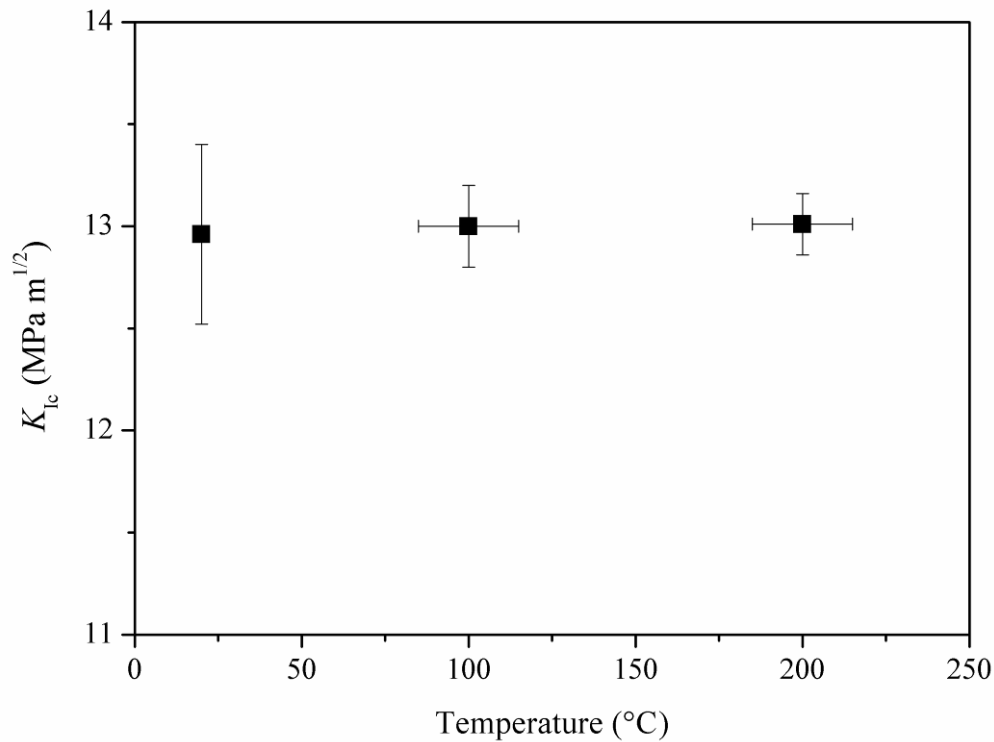


Fig. 8.8 Plane strain fracture toughness (K_{Ic}) values measured for the as-cast newly developed 7xxx alloy from room temperature to 200 °C.

8.3.2 Model setup for the new alloy

As before, ALSIM5 was used for the computation of temperature profile and stress/strain fields in round billets. Physical properties of the alloy were gained from the thermodynamics database JMat-Pro, provided by Corus-Netherlands (IJmuiden). The thermomechanical databases were made for simulations using the physical and mechanical properties collected. A 260-mm diameter billet, cast at 60 mm/min (1 mm/s) with water flow rate of 35 l/min was taken as the standard case. Casting speed and water flow rate was varied to study the effect of these variables on the cracking propensity (Table 8.3). The first 500 s of all simulations was performed under standard conditions (case 1). Changes in casting speed or water flow rate were applied afterwards by ramping up from case 1. The billet was cast then with new parameters (cases 2-4) or the same parameters (case 1) for another 500 s. Finally, the casting speed was ramped down to zero and the billet was cooled to room temperature during 200 s.

Table 8.3 Description of casting process parameters for the Ø 260 mm billets [23].

case	Casting speed (mm/min)	Water flow rate (l/min)
1	60 (1 mm/s)	35
2	80 (1.3 mm/s)	35
3	110 (1.8 mm/s)	90
4	60 (1 mm/s)	70

8.3.3 Simulation results and discussion

Contour maps of the σ_{11} are shown in Fig. 8.9 for the cases described in Table 8.3. In Figs. 8.9b,c and d, the lower part of the billet corresponds to the initial casting conditions and the upper part to the new conditions. With increasing the cast speed, the σ_{11} increases in the centre of the billet (Figs. 8.9a to 8.9c). The increase in the magnitude of the σ_{11} is due to the increased heat input mainly in the axial direction (y) resulting in higher temperature gradients in that direction [19]. As discussed in Chapter 7, investigation of the stress tensors revealed that the σ_{11} axis turns from radial or circumferential direction towards the axial direction (y) of the billet with increasing the casting speed. Water flow rate (Fig. 8.9d) has a negligible effect on the magnitude of the σ_{11} and its contour map is very similar to Fig. 8.9a.

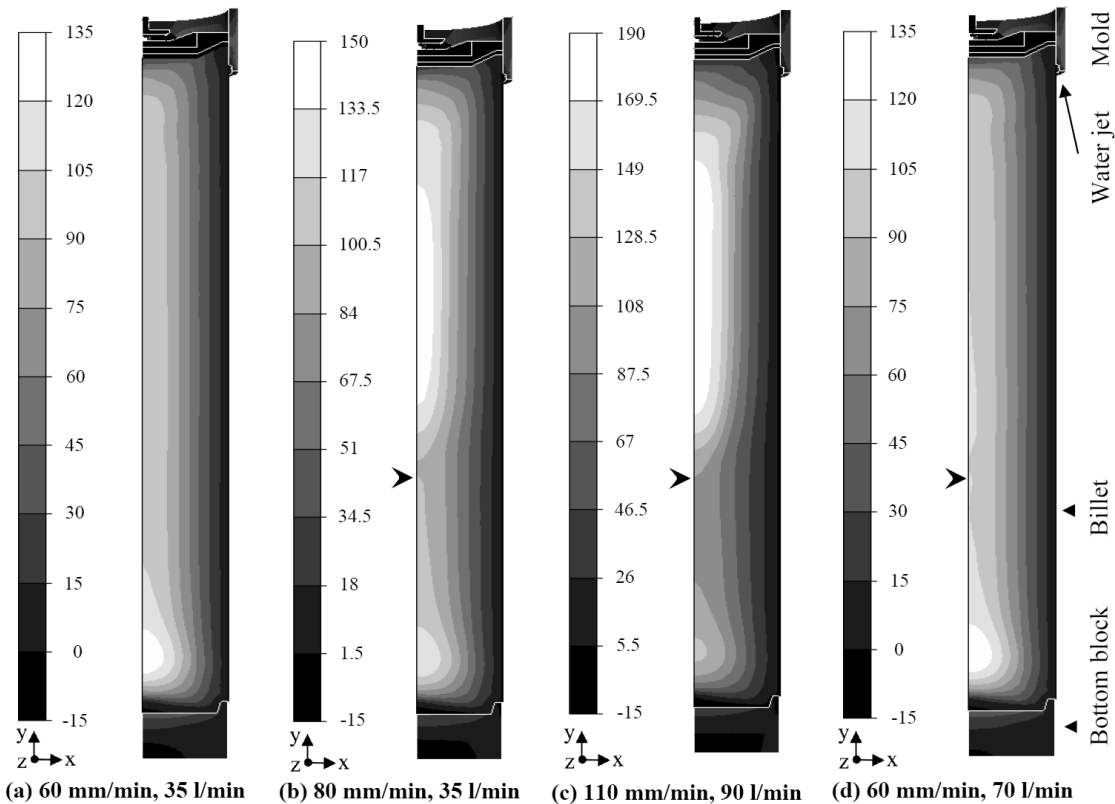


Fig. 8.9 Simulation results showing the σ_{11} (MPa) in the billets cast at various conditions mentioned in Table 8.3 [23]. Arrows show the transition between casting regimes.

Fig. 8.10 shows the contour maps of the critical crack size (CCS) distribution in billets cast under conditions described in Table 8.3. As expected, increasing the casting speed leads to smaller CCS values in the center of the billet, which means higher failure probability (Fig. 8.10a to c). The water flow rate has a negligible effect on the crack size (Fig. 8.10d) that is in agreement with our findings in Chapter 7. DC-casting trials were also performed for some cases mentioned in Table 8.3 to check the simulation results. No cracks were observed in cases 1 and 4. Case 2 was not cast practically, although another cast trial at 70 mm/min and 35 l/min went perfect without any cracking. A real cold crack, however occurred in case 3 during the casting with an audible bang resulting in the failure of the billet. According to Fig. 8.10c, in the center of the billet cracks or defects with a critical diameter between 6-12 mm (3-6 mm in radius) may lead to catastrophic failure. Further investigation of the

fracture surface in case 3 revealed an inclusion with a length of 7 mm (Fig. 8.11), which was located 20 mm away from the center of the billet and 730 mm above the bottom block. The size of the void fits well to the computed range.

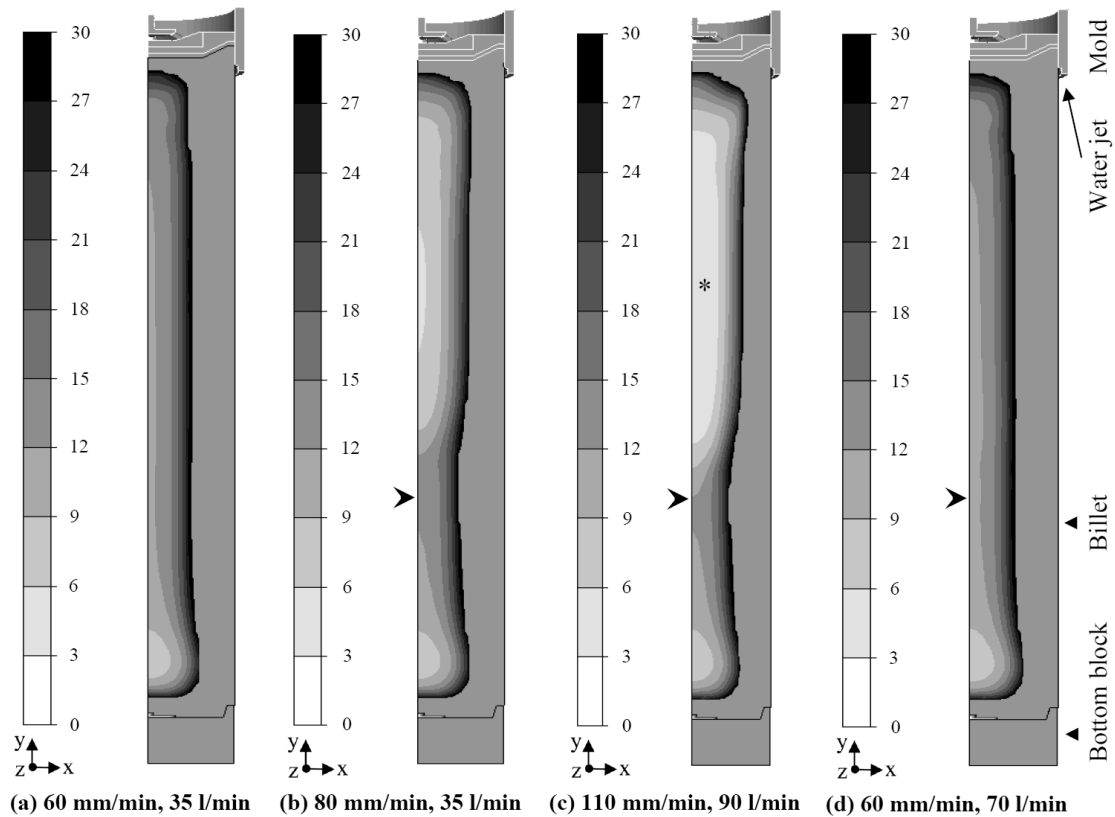


Fig. 8.10 Simulation results showing the critical crack size distribution (mm) in the billets cast at various conditions mentioned in Table 8.3. Crack sizes larger than 30 mm are neglected and appear as gray between the billet surface and the black area at mid-radius [23]. Arrows show the transition between casting regimes and the star in (c) indicates the location of the inclusion which triggered the catastrophic failure.

It is obvious from Fig. 8.11 that the 7 mm inclusion has triggered the failure as the so-called V-shaped chevron markings are all radiating from this defect. Computer simulation results showed that the temperature of the corresponding point is around 55°C at the moment of fracture, which fits in the temperature range where the material is expected to be extremely brittle. Thus, the void existed there since the beginning of the casting, but its catastrophic propagation was facilitated by the extreme brittleness of the material below 200°C and the high corresponding σ_{11} value. Another feature of the crack is that its plane is not oriented in the same way as in the AA7475-alloy billets observed in Fig. 7.8. There, the crack plane was parallel to the axial direction of the billet due to the action of σ_{11} in the radial or circumferential directions. At the higher casting speed 110 mm/min (1.8 mm/s), the σ_{11} (in the center) turns towards the axial direction of the billet and results in the rotation of the crack plane (Fig. 8.12). As can be seen in Fig. 8.12, the normal to the crack plane makes an angle θ with the axial direction of the billet (direction of casting). As the crack propagates to the surface of the billet it deviates and tends to orient parallel to the axial direction of the billet. Other billets were also examined through ultrasonic defectoscopy (with accuracy to measure voids as small as 1.5 mm) to check the presence of voids of critical size which did not lead to catastrophic failure. Although no specific defects were detected,

two suspicious locations were marked. After stress relief, the billets were cut at those locations and the cross sectional areas were polished however, no cracks were detected. In order to check in more detail, samples were randomly cut from the center, mid-radius and the surface of the billets, polished and prepared for SEM analysis (Jeol JSM-6500F scanning electron microscope). Closer observations of the samples from the center and mid-radius revealed that there are some voids such as shrinkage porosities in the microstructure with a maximum size in the order of hundred microns (Figs. 8.13 and 8.14). At the surface of the billet, no specific voids were detected. The maximum size of the detected shrinkage porosities are far below the estimated critical crack size by fracture mechanics, which explains well why they did not lead to the failure of the billets.

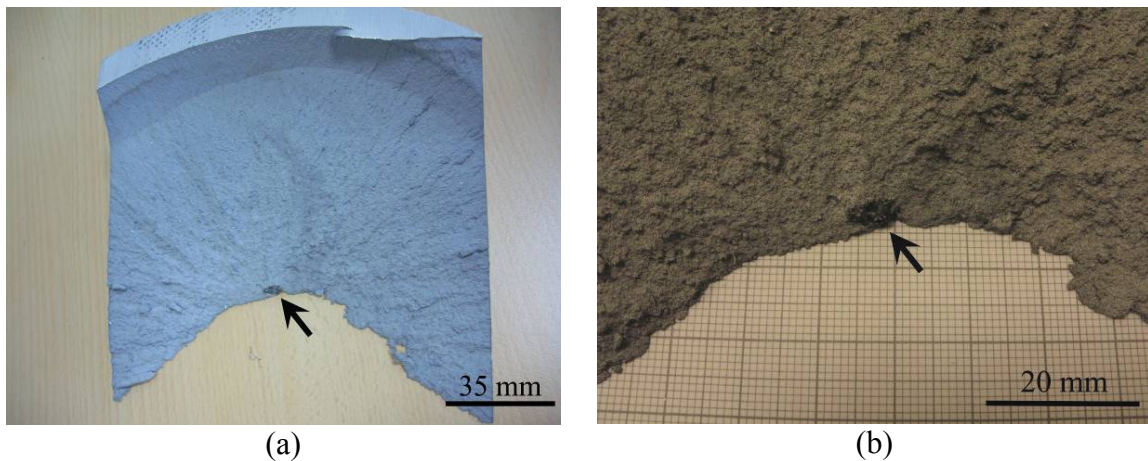


Fig. 8.11 (a) The cold crack surface in the billet cast at 110 mm/min (1.8 mm/s) and water flow rate of 90 l/min. The dark point shown by an arrow triggered the fracture. The chevron markings radiating from this Mg-oxide inclusion account for its role in the fracture. (b) The same figure at a higher magnification [23].

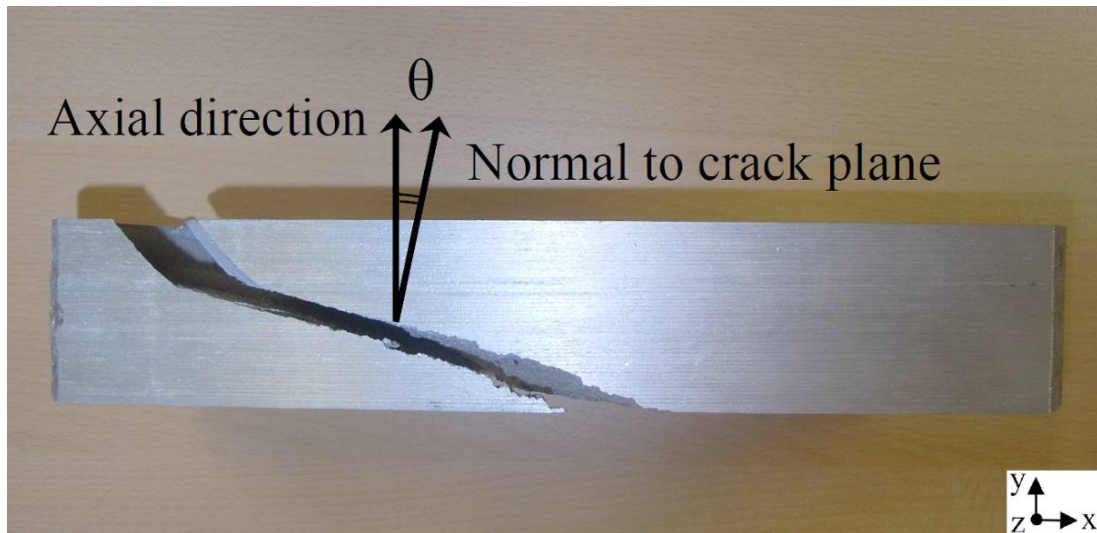


Fig. 8.12 The lateral cross section of the cracked billet shown in Fig. 8.11. The orientation of the crack plane is shown using the axial direction and a normal to the plane.

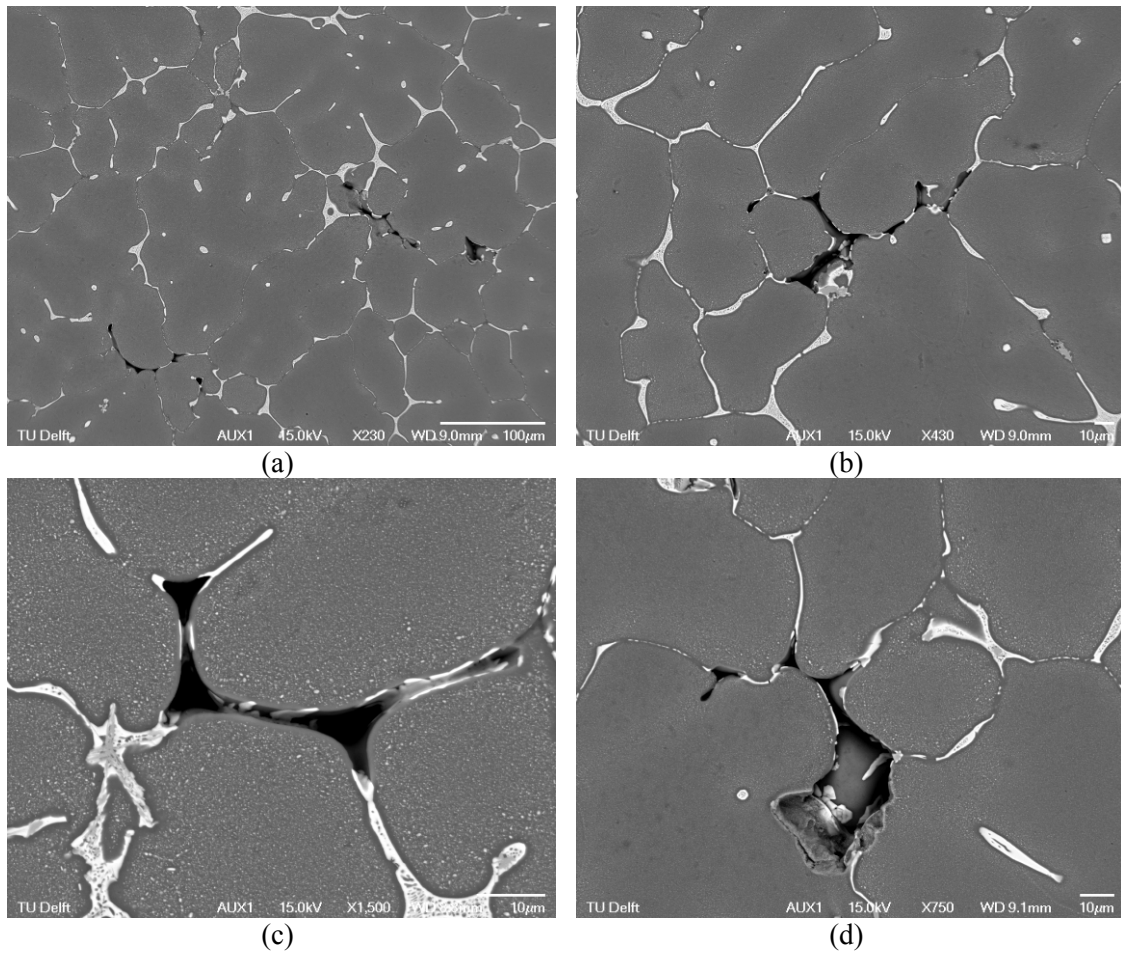


Fig. 8.13 Electron backscattered images showing various voids formed during the solidification in the mid-radius of a \varnothing 260-mm billet of the newly developed 7xxx alloy.

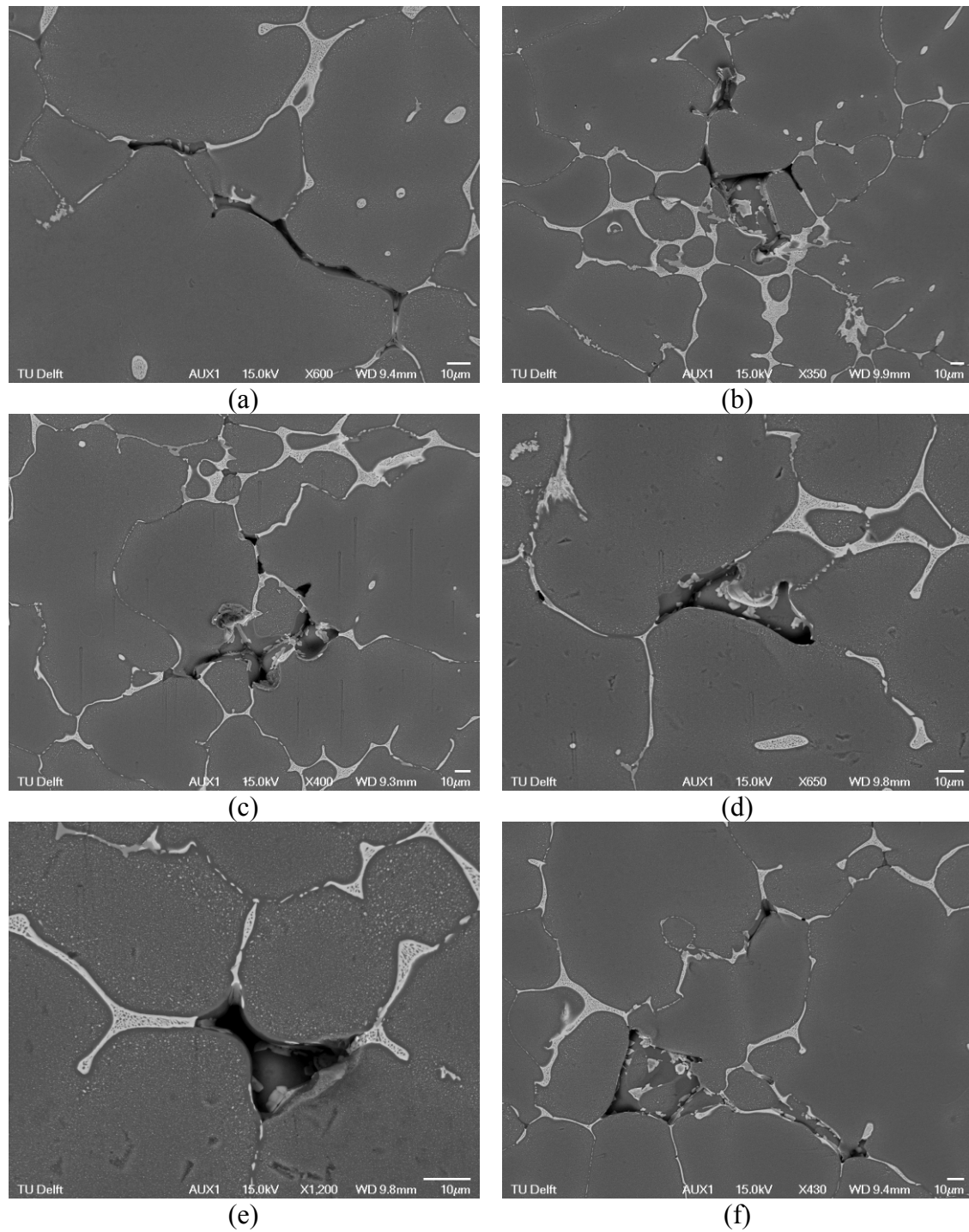


Fig. 8.14 Electron backscattered images showing various voids formed during the solidification in the center of a Ø 260-mm billet of the newly developed 7xxx alloy.

8.4 Conclusions

In this chapter cold cracking propensity of 7050 billets was studied under steady state conditions during DC-casting. The contour maps of the critical crack size calculated by ALSIM5 for the penny shaped crack admitted our former findings that the center and the water impingement zone are the most vulnerable locations of the billet. The effect of casting speed was also studied and revealed that at higher casting speeds the vulnerable area to cold cracking becomes larger in the center while it shrinks at the surface in the water impingement zone. At higher casting speeds the failure probability increases in the center mainly due to higher σ_{11} values. In order to check the cold cracking criterion, the entire procedure mentioned for AA7050 alloy was repeated for a newly developed 7xxx series alloy, which is highly prone to cold cracking. The mechanical properties of the alloy in the genuine as-cast condition resemble that of AA7050 except for the fact that the new alloy shows more plasticity at 200°C. Thermomechanical simulations were also run for the new alloy under various casting conditions. In agreement with our former findings, the simulation results showed that as the casting speed increases, the CCS decreases leading to a higher failure probability of the billets. Simulations were followed by experimental DC-casting trials to check the critical crack sizes calculated by ALSIM5. The critical crack sizes were validated upon experiments, where a 7 mm inclusion in the centre of the billet cast at 1.8 mm/s and 90 l/min triggered the catastrophic failure. Based on our former findings, increasing the casting speed not only increases the magnitude of the maximum principal stress, but it also turns its axis towards the axial direction of the billet resulting in the rotation of the crack plane. The orientation of the crack plane in the cold-cracked billet with respect to the axial direction of the billet easily proves this simulation result.

References

- [1] J. Campbell, *Castings*, Butterworth-Heinemann, Oxford, United Kingdom, 2003.
- [2] M. Lalpoor, D.G. Eskin, L. Katgerman, *Mater. Sci. Eng. A* 497 (2008) 186-194.
- [3] T.W. Clyne, G.J. Davies, *Br. Foundryman* 74 (1981) 65-73, *Br. Foundryman* 68 (1975) 238-244.
- [4] M. Rappaz, J.-M. Drezet, M. Gremaud, *Metall. Mater. Trans. A* 30 (1999) 449-455.
- [5] D.J. Lahaie, M. Bouchard, *Metall. Mater. Trans. B* 32 (2001) 697-705.
- [6] M. M'Hamdi, A. Mo, H.G. Fjær, *Metall. Mater. Trans. A* 37 (2006) 3069-3083.
- [7] V.A. Livanov., in: A.F. Belov, G.D. Agarkov (Eds.), *Aluminum Alloys*, Oborongiz, Moscow, 1955, pp. 128-168.
- [8] K. Matsuda, S. Nagai, Y. Miyate, H. Maehara, I. Tsukuda, in: *6th International Aluminum Extrusion Technology Seminar*, Aluminium Association and Aluminium Extruder's Council, Vol. I, Chicago, Illinois, USA, 1996, pp. 525-528.
- [9] W. Boender, A. Burghardt, in: H. Jones (Ed.), *5th Decennial Int. Conf. on Solidification Processing*, University of Sheffield, Sheffield (UK), 2007, pp. 714-718.
- [10] O. Ludwig, J.-M. Drezet, B. Commet, B. Heinrich, in: C-A. Gandin, M. Bellet (Eds.), *Modeling of Casting, Welding and Advanced Solidification Processes XI*, TMS, Warrendale (PA), 2006, pp. 185-192.
- [11] R.K. Paramatmuni, K.-M. Chang, B.S. Kang, X. Liu, *Mater. Sci. Eng. A* 379 (2004) 293-301.

- [12] J.L. Dassel and T.C. Zinniger, in: *Light Metals*, Dallas, 1982, pp. 793-801.
- [13] US Patent. No. US2007/0102136 A1, United States, 2007.
- [14] W. D. Callister Jr., *Fundamentals of Materials Science and Engineering*, 5th ed., John Wiley & Sons Inc., New York, 2001.
- [15] M. Lalpoor, D.G. Eskin, L. Katgerman, in: *Proc. ICAA 12*, The Japan Institute of Light Metals, Yokohama, Japan 2010, pp. 727-732.
- [16] W. Boender, A. Burghardt, E.P. van Klaveren, J. Rabenberg, in: A.T. Tabereaux (Ed.), *Light Metals*, TMS, 2004, pp. 679-684.
- [17] J.H. Faupel, F.E. Fisher, *Engineering Design*, John Wiley & Sons Inc., New York (NY), 1981.
- [18] M. Lalpoor, D.G. Eskin, L. Katgerman, *Proc. 12th Intern. Conf. on Fracture*, Ottawa, National Research Council of Canada, 2009 (CD).
- [19] M. Schöllmann, H.A. Richard, G. Kullmer, M. Fulland, *Int. J. Fracture* 117 (2002) 129-141.
- [20] J.F. Grandfield, P.T. McGlade, *Mater. Forum* 20 (1996) 29-51.
- [21] M. Lalpoor, D.G. Eskin, L. Katgerman, *Metall. Mater. Trans A* 41 (2010) 2425-2434.
- [22] B. Magnin, L. Katgerman, B. Hannart, in: M. Cross and J. Campbell (Eds.), *Modeling of Casting, Welding and Advanced Solidification Processing VII*, TMS, Warrendale, 1995, pp. 303-310.
- [23] M. Lalpoor, D.G. Eskin, H. G. Fjær, A. Ten Cate, N. Ontijt, L. Katgerman, in: *The 7th Pacific Rim International Conference on Advanced Materials and Processing*, *Mater. Sci. Forum* 654-656 (2010) 1432-1435.

Conclusions and outlook

1. Analysis of the mechanical properties in the genuine as-cast condition shows that 7xxx series aluminum alloys lose their ductility upon cooling from the solidus and become extremely brittle below 300°C. The constitutive parameters, mechanical properties and the plane strain fracture toughness of the material are considerably different from the material in the homogenized or stress relieved states. Another feature of the mechanical behavior of the material is that below 300°C it becomes either strain-rate independent or with increasing the strain rate the material fails at lower stresses, before reaching the yield point.
2. In the temperature range where the material exhibits brittle behavior, the fracture mode is brittle intergranular although some features of transgranular fracture are also visible on the fracture surfaces. Crack propagation occurs mainly through the brittle intermetallics and non-equilibrium eutectics which cover the major interdendritic and intergranular spaces.
3. Thermomechanical simulation results show that under steady state conditions the stresses appear to be mainly tensile in the center of the billet while they either diminish or turn to compressive with moving towards the surface. Three normal components of the stress tensor are all tensile in the center of the billet, which provides the maximum plastic constraint in this region. The WIZ and the center of the billet are the most vulnerable locations of the billet to cracking as the maximum principal stress is highest in these locations. When the maximum principal stress reaches its highest value the temperature is around 200 °C and the material is extremely brittle due to the loss of ductility.
4. Analysis shows that the casting speed and the billet diameter are the most influential parameters that determine the distribution and magnitude of the residual thermal stresses. The stress level elevation occurs both in the center of the billet and in the WIZ when the casting speed or the billet diameter is increased. The increased stress level at the surface of the billet facilitates the surface cracking of large round billets, although such a failure is rarely observed in small billets. In the center of the billet, the increased casting speed or billet diameter not only increases the magnitude of the maximum principal stress but it also turns its axis towards the axial direction of the billet. The rotation of the maximum principal stress axis turns the crack plane and results in so-called cup and cone cracks at higher cast speeds or larger billet diameters.

5. Our results indicate that for cold cracking to occur voids/cracks of a considerable size are required that are oriented normal to the maximum principal stress component. The difficulty of having both conditions simultaneously explains why cold cracking is such a random phenomenon.
6. Studying the initiation process of microcracks, the propagation up to the critical length and their orientation may help understand the cold cracking phenomenon more elaborately. This interesting topic needs to be studied further in more details and would be a topic for the next PhD work. Another important point to bear in mind is the fact the material under discussion is a composite with secondary brittle phases covering the grain boundaries and interdendritic spaces. For modeling the failure in micro scale the knowledge of the mechanical properties of such phases would be essential. As the material is extremely brittle below a certain temperature range, some modifications in the constitutive equations sound necessary in order to fit the model to the real case more efficiently.

Summary

The catastrophic failure of DC-cast ingots in the solid state, “*cold cracking*”, is the major problem in aluminum industry that exists since large billets started to be produced in the 1940s. High strength aluminum alloys of 2xxx and 7xxx series are particularly susceptible to *cold cracking*. The reason behind such a long persistence is the nature of the problem and the way it has been treated. On the one hand, the cold cracking is a non-predictable phenomenon which does not occur in each casting trial. On the other hand for the sake of higher productivity, most of the research performed in this area has been limited to case studies rather than deep investigations. In this study we scrutinized the cold cracking phenomenon with the aim to establish a criterion that predicts cold cracking during DC-casting.

As the genuine as-cast mechanical properties of the AA7050 alloy have been rarely studied before, we started our research with investigation of the mechanical properties in that state. The results of tensile tests at various temperatures below solidus and strain rates corresponding to DC-casting revealed that the alloy experiences a severe loss in ductility upon cooling and turns to an extremely brittle material below 300°C. Another feature of the material behavior below 300°C is that it becomes strain rate independent, which facilitates the brittle fracture even at low strain rate conditions induced during DC-casting. Similar to ceramic materials a lot of scattering exists in the results below 300°C and this problem can be intensified by potentially existing defects. The comparison of the mechanical properties and constitutive parameters of the alloy with those gained from homogenized and stress relieved samples manifests how brittle the as-cast material is at temperatures below 300°C. The plane strain fracture toughness (K_{Ic}) of the alloy was also measured for the first time under genuine as-cast conditions not only at room temperature but also at 100 and 200°C. The K_{Ic} in the genuine as-cast condition is noticeably smaller than that in the homogenized or stress relieved states and is far below the K_{Ic} of the precipitation hardened alloy. The experimentally determined K_{Ic} values were used later for calculation of the critical crack sizes.

The investigation of the fracture surfaces revealed that the grain boundaries and interdendritic spaces, where the non-equilibrium eutectics and brittle intermetallics form during solidification, are the main crack initiation sites during and after the end of solidification. Above solidus, cracks may form through hot cracking when the liquid film at the boundaries is unable to withstand the induced stresses. Below solidus, the brittle intermetallics may easily break under the tri-axial stress state and form cracks of critical size. Regardless of the crack initiation mechanism, however cracks mainly propagate through the grain boundaries and interdendritic spaces which are mostly covered by intermetallics. This results in a brittle intergranular mode of fracture. Our in-situ tensile tests at room as well as elevated temperatures proved this. The fracture

mode of the real cold-cracked billets, however, showed some interesting features of both brittle intergranular failure and transgranular fracture of individual dendrite arms. The latter was observed near the surface of the billet and demands more research.

Some of the thermal properties of the alloy were also measured experimentally in order not only better to understand the thermal behavior of the material, but also to determine the key parameters for the simulations. The onset of thermal contraction in the mushy zone was determined through linear solidification contraction tests. The thermal contraction behavior of the alloy was also studied through dilatometry and the linear solidification contraction setup. The as-cast thermal contraction behavior of the material in dilatometry and linear solidification contraction setup was slightly different than what the thermodynamics database JMat-Pro predicts. In dilatometry test results, there is a jump in the coefficient of thermal contraction at around 200°C which can be attributed to formation of some precipitates during cooling after the end of solidification. Differential scanning calorimetry test results showed this on both heating and cooling.

In order to examine the thermomechanical behavior of the alloy, computer simulations were run for round billets using ALSIM5. The simulation results showed that in a 200-mm diameter billet cast at 1 mm/s, the steady state conditions are obtained after roughly 200 s. From this moment on, the stress analysis could be performed. Investigation of the contour maps of the stress tensor components revealed that the stress is mainly tensile in the center of the billet, while it either diminishes or turns to compressive with moving towards the surface of the billet. Another critical point is the water impingement zone (WIZ) at the surface where high tensile stresses appear in the circumferential direction. The results of the viscoplastic strain analysis were in agreement with the Prandtl-Reuss equations, i.e. the sign of the viscoplastic strain rate equals the sign of the corresponding deviatoric stress component. In order to assess the occurrence of plastic deformation, contour maps of the effective stress as well as hardening parameter were used. High effective stresses at the surface bring about relatively higher hardening parameters in this region compared to the center of the billet. The viscoplastic strains in the center of the billet are mainly caused by creep at elevated temperatures.

In order to assess the cracking probability in the billet, the components of the principal stress tensor were used. $\sigma_{33} < \sigma_{22} < \sigma_{11}$ appear to be all tensile in the center while they turn to compressive or slightly tensile at the surface. Having three tensile principal stresses in the center results in the low effective stress and consequently the low plastic deformation (strain hardening). Although the effective stress is low in the center, the mean stress appears to be the highest in that region which increases the probability of plastic constraint and brittle fracture. The maximum values of the σ_{11} show up in the water impingement zone after 76 s of casting and in the center after 200 s. Our critical crack size calculations showed that these locations are the most vulnerable locations of the billet to cracking. Upon casting, the σ_{11} rises and reaches its maximum at the surface and then falls due to the change in the stress state at the surface from tensile to compressive as soon as the billet leaves the impingement zone. During the period when the σ_{11} is maximum at the surface some cracks may form and propagate. In spite of this, the cracking from the surface rarely happens in small round billets due to the high compressive stresses that immediately replace the tensile stresses. In the center of the billet however the situation remains critical during the entire casting period especially after 200 s when the σ_{11} reaches its maximum. Hot cracks formed above solidus may further propagate and result in the failure of the billet. Inclusions or other imperfections which have reached the critical size may also

facilitate the catastrophic failure of the billet. At the surface of the billet in the WIZ, a thumbnail crack with the critical size 4.2 mm may result in the failure. In the center of the billet and at 200°C where the σ_{11} exhibits its maximum, the critical crack size reads 10.1 mm.

We also performed simulations to study the thermomechanical behavior of the billets after the end of casting. We learned that the situation does not change noticeably in the lower central part of the billet where the stresses have already reached the steady state conditions. In the upper parts of the billet, however the stress state changes and the stresses that develop may reach a maximum as high as in the lower parts. Under such conditions when the entire billet is at room temperature, a penny-shaped crack with the radius 17.1 mm may trigger the catastrophic failure in the center of the billet. This value is larger compared to the 10.1 mm mentioned above due to the reduction in σ_{11} magnitude upon further cooling.

The effect of casting variables was also studied to check how casting speed, billet diameter, water temperature, water flow rate and melt temperature may affect the final stress state and failure probability in the billets. Our investigations showed that among the examined parameters, the casting speed and billet diameter have the most influential effects. With increasing the casting speed or billet diameter the stresses rise in the center and in the water impingement zone and enhance the failure probability. The increased casting speed raises the failure probability in the center of the billet by making the area corresponding to the minimum critical crack size larger. At the surface of the billet in the WIZ however, the area corresponding to the minimum critical crack size shrinks with increasing the casting speed due to the shorter time the billet spends in that zone. The increased billet diameter or casting speed not only increases the failure probability in the center, it also makes the billet more prone to fracture at the surface by an increase in the σ_{11} . Another point is that increasing the billet diameter or casting speed not only increases the magnitude of the maximum principal stress, it also changes its orientation. At higher casting speeds and billet diameters, the σ_{11} turns from the radial or circumferential directions towards the axial direction of the billet mainly due to the higher temperature gradients in that direction. The rotation of the σ_{11} -axis rotates the crack plane from parallel to the axial direction of the billet at low casting speeds or small billet diameters to normal to it at higher casting speeds or billet diameters. This may result in so-called cup and cone cracks.

Eventually the cold cracking criterion was validated using a newly developed high strength aluminum alloy that is highly prone to cold cracking. The simulation results were supported by experimental DC-casting trials. A billet cast at the high speed 1.8 mm/s cracked during the DC-casting with an audible bang. The investigation of the fracture surface revealed that a 7 mm long inclusion has triggered the catastrophic failure. The crack length fits well to the predicted crack size (6-12 mm) and its orientation admits the fact that the σ_{11} acted in the axial direction of the billet. Other billets were investigated for probable voids using the ultrasonic defectoscopy, but no voids of critical size were detected. The only present voids were the shrinkage porosities with a maximum size of 100 μm which is far below the critical crack size required for catastrophic failure.

What makes the cold cracking phenomenon rather unpredictable however, is the difficulty of having voids with the critical size that are simultaneously oriented normal to the corresponding maximum principal stress component. In our metallographic observations of a AA7050 DC-cast billet, we found hot cracks that were a few millimeters long, but they did not lead to cold cracking and the billet remained sound. The billet did not fail probably not only due to uncritical length but

also the unfavorable orientation of the cracks. Under such complicated conditions and by taking the extreme brittleness of the material into account, the following tips may help to produce sound billets: well controlled casting conditions, homogenous molten metal without inclusion particles, right selection of the bottom block which does not locally induce high stresses and careful handle of the billets after casting. For any alloy the right casting speed corresponding to the diameter should be found using the computer simulation results. If the minimum crack size predicted by the model is smaller than the typical inclusion size in the castings, lower casting speeds should be selected.

Samenvatting

Sinds de productie van grote aluminium gietblokken in de jaren 40 van de vorige eeuw, is het grootste probleem in de aluminiumindustrie het scheuren van continu gegoten (DC) gietblokken, ook wel koudscheuren genoemd. Vooral de hoge sterkte aluminiumlegeringen van de 2xxx en de 7xxx series zijn gevoelig voor koudscheuren. De reden waarom dit probleem blijft voortbestaan, is de aard en de manier waarop het benaderd wordt. Aan de ene kant is koudscheuren een onvoorspelbaar fenomeen dat niet voorkomt bij elke giettest. Aan de andere kant is het meeste onderzoek naar dit probleem, door de hoge productievraag, beperkt tot casestudies in plaats van diepgaand onderzoek. Tijdens dit onderzoek hebben we het verschijnsel koudscheuren gedetailleerd onderzocht met als doel een criterium te kunnen formuleren, dat koudscheuren tijdens DC-gieten kan voorspellen.

Omdat de echte mechanische eigenschappen van de legering AA7050 in gegoten toestand nauwelijks bestudeerd waren, begonnen we met het onderzoeken van de mechanische eigenschappen van deze legering in gegoten toestand. De resultaten van de trekproeven bij temperaturen beneden de solidus en bij verschillende reksnelheden, die overeenkomen met DC-gietcondities, lieten zien dat de legering zijn taaiheid verloor tijdens het koelen en dat het beneden de 300 °C veranderde in een extreem bros materiaal. Een andere eigenschap van het materiaal beneden de 300 °C was dat het gedrag grotendeels onafhankelijk werd van de reksnelheid. Dit kon zelfs bij een lage reksnelheid, zoals optreedt tijdens DC-gieten, leiden tot brosse breuken. De experimentele resultaten beneden de 300 °C vertoonden een grote spreiding, zoals bij keramische materialen, en dit probleem kon verslechteren door eventuele bestaande defecten. Het vergelijken van de mechanische eigenschappen en de constitutieve parameters van deze legering en die van gehomogeniseerde spanningsvrije trekstaven liet zien hoe bros het gegoten materiaal was bij temperaturen beneden de 300 °C. Tevens werd, voor de eerste keer, de breuktaaiheid (K_{Ic}) van de legering daadwerkelijk gemeten in gegoten toestand bij kamertemperatuur, 100 °C en 200 °C. Hieruit bleek dat in de giettoestand de K_{Ic} beduidend lager was dan in de gehomogeniseerde of de spanningsarme toestand en dat de waarden ver beneden de K_{Ic} lagen van de verouderde legering. De K_{Ic} -waarden verkregen uit de experimenten werden later gebruikt om de kritische scheurgrootte te berekenen.

Uit breukvlakonderzoek aan de gegoten trekstaven bleek dat de korrelgrenzen en interdendritische holtes, waar de niet-evenwicht eutectische fasen en brosse intermetallische verbindingen zich vormden tijdens het stollen, de voornaamste plekken waren voor breukinitiatie tijdens en na het stollen van het materiaal. Boven de solidus konden scheuren ontstaan door *warmscheuren*, waarbij de vloeibare fase op de grenzen van de dendrieten bezwijkt onder de aanwezige lokale spanning. Door de drie-assige spanningstoestand beneden de solidus konden de brosse intermetallische

verbindingen gemakkelijk breken en scheuren vormen met een kritische grootte. Onafhankelijk van het mechanisme dat de breuk veroorzaakte, vormden de scheuren zich vooral langs de korrelgrenzen en interdendritische holtes die voornamelijk bedekt werden door intermetallische verbindingen.

Dit resulteerde in brosse interkristallijne scheurvorming. Onze in-situ trekproeven op kamer- en hogere temperaturen bewezen dit. De scheurvorming van de echte koudgescheurde DC gietblokken lieten echter kenmerken zien van zowel brosse interkristallijne scheurvorming als transkristallijne breuk van individuele dendriten. Dit laatste werd gezien nabij het externe oppervlak van het gietblok en zal nog verder onderzocht moeten worden.

Voor een beter begrip van het thermisch gedrag van de legering en het vaststellen van de belangrijkste parameters voor de simulaties, werden een aantal van de thermische eigenschappen van het materiaal experimenteel bepaald. Het begin van de thermische contractie in het vloeibaar-vast gebied werd bepaald door middel van lineaire stolling-contractietesten. Het thermische contractiegedrag van de legering werd tevens bestudeerd door middel van dilatometrie en de lineaire stolling-contractieopstelling. Het thermische contractiegedrag van het materiaal in de giettoestand in de dilatometer en de lineaire stolling-contractieopstelling kwamen niet geheel overeen met de voorspellingen van de thermodynamische database JMat-Pro. Uit de resultaten van de dilatometertest bleek dat er een sterke toename was in de thermische uitzettingscoëfficiënt bij ongeveer 200 °C, wat toegeschreven kon worden aan de uitscheiding van precipitaten tijdens het afkoelen na afloop van de stolling. Differentiële scanning-calorimetrietesten lieten zien dat dit gebeurde bij zowel verhitte als afkoeling.

Teneinde het thermomechanische gedrag van de legering te bestuderen werden computersimulaties uitgevoerd voor ronde gietpalen met het programma ALSIM5. De simulatieresultaten lieten zien dat in een gietblok met een diameter van 200 mm, dat met 1 mm/s gegoten werd, de stationaire condities werden bereikt na ongeveer 200 s. Vanaf dit moment kon de spanningsanalyse uitgevoerd worden. De contourplots van de componenten van de spanningstensor lieten zien, dat er voornamelijk trekspanningen aanwezig zijn in het centrum van het gietblok die overgaan in drukspanningen naar het oppervlak van het gietblok toe. Een andere kritische plek was de plek waar het water in contact komt met het oppervlak van het gietblok, de *water impingement zone* (WIZ), waar een sterke trekspanning in de omtreksrichting heerste. De resultaten van de viscoplastische spanningsanalyse waren in overeenstemming met de Prandtl-Reuss vergelijkingen; het teken van de viscoplastische reksnelheid was gelijk aan het teken van de corresponderende deviatorische spanningscomponent. Om de plastische deformatie te beoordelen, werden de contourplots van zowel de effectieve spanning als de verstevigingsparameter gebruikt. In vergelijking tot het centrum van het gietblok, brachten hogere spanningen aan het oppervlak relatief hogere verstevigingsparameters teweeg. De viscoplastische krachten in het centrum van het gietblok werden voornamelijk veroorzaakt door kruip bij verhoogde temperaturen.

Om de kans op het ontstaan van scheuren in het gietblok te bepalen, werden de hoofdcomponenten van de spanningstensor gebruikt. $\sigma_{33} < \sigma_{22} < \sigma_{11}$ bleken allemaal trekspanningen te zijn in het centrum, terwijl deze overgingen in drukspanningen aan het oppervlak. De aanwezigheid van drie positieve hoofdspansingen in het centrum resulteerde in een lage effectieve spanning en als gevolg daarvan een lage plastische vervorming (versteviging). Hoewel de effectieve spanning laag was in het centrum, bleek de gemiddelde spanning het hoogste te zijn in dat gebied. Dit verhoogde de kans

op plastische vormverhinderende en brosse breuk. De maximale waarden van σ_{11} werden na 76 s in de WIZ bereikt en na 200 s in het centrum. Onze berekeningen van de kritische scheurgroottes lieten zien dat deze gebieden in het gietblok het gevoeligst voor scheurvorming waren. Tijdens het gieten nam σ_{11} toe en bereikte zijn maximum aan het oppervlak en nam daarna af. Dit werd voornamelijk veroorzaakt door veranderingen in het type spanning van trek naar druk aan het oppervlak op het moment dat het gietblok de *impingement zone* verliet. Op het moment dat σ_{11} maximaal was aan het oppervlak, konden een aantal scheuren zich vormen en verspreiden. Desondanks kwam het in kleine ronde gietpalen door de aanwezige hoge drukspanningen zelden voor dat scheuren zich vanuit het oppervlak vormden. In het centrum van het gietblok echter, blijft de situatie kritiek tijdens de gehele gietperiode, vooral na 200 s wanneer de σ_{11} component zijn maximum bereikte. Warme scheuren gevormd boven de solidus konden mogelijk verder groeien en resulteren in het bezwijken van het gietblok. Insluitsels of andere gietdefecten van een kritische grootte, hebben mogelijk het bezwijken van het gietblok bevorderd. Een breuk in de vorm van een duimnagel, met een kritische grootte van 4.2 mm aan het oppervlak van het gietblok in de WIZ, kon mogelijk resulteren in het bezwijken van het gietblok. In het centrum van het gietblok en bij 200 °C wanneer σ_{11} zijn maximum bereikte, was de kritische scheurgrootte 10.1 mm.

We hebben ook simulatietesten uitgevoerd om het thermomechanische gedrag van de gietpalen na het einde van het gieten te bestuderen. Dit leerde ons dat de situatie niet merkbaar veranderde in het lagere centrale deel van het gietblok, waar de spanningen al de stationaire toestand bereikt hadden. In de hogere gedeelten van het gietblok echter, veranderde de spanningstoestand en de spanningen die zich ontwikkelden konden mogelijk een maximum bereiken dat even hoog was als in het lagere deel van het gietblok. Onder zulke condities, wanneer het gehele gietblok op kamertemperatuur was, kon een schijfvormige breuk met een radius van 17.1 mm mogelijk de aanleiding zijn tot het bezwijken van het centrum van het gietblok. Deze waarde was hoger in vergelijking tot de 10.1 mm genoemd in de vorige alinea dankzij de vermindering in σ_{11} na verdere afkoeling.

Het effect van gietvariabelen werden tevens bestudeerd om te controleren hoe de gietsnelheid, de diameter van het gietblok, de watertemperatuur, de stroomsnelheid van het water en de smelttemperatuur de uiteindelijke spanningstoestand en de kans op het mislukken van het gietblok beïnvloedde. Ons onderzoek toonde aan dat onder de bestudeerde parameters, de gietsnelheid en de diameter van het gietblok de meeste invloed hadden. Met het verhogen van de gietsnelheid of het vergroten van de diameter van het gietblok namen de spanningen toe in het centrum en in de WIZ, wat de kans op bezwijken vergrootte. De verhoogde gietsnelheid zorgde voor een toegenomen kans op bezwijken in het centrum van het gietblok door het vergroten van het gebied dat correspondeerde met de minimale kritische scheurgrootte. Echter, aan het oppervlak van het gietblok in de WIZ kromp het gebied dat correspondeerde met de minimale kritische grootte bij toenemende gietsnelheid dankzij de kortere tijd dat het gietblok in die zone doorbracht. De toegenomen diameter van het gietblok of de gietsnelheid verhoogde niet alleen de kans op bezwijken in het centrum, het maakte het gietblok ook meer vatbaar voor scheuren aan het oppervlak door een toename in σ_{11} . Daarnaast verhoogde de toename in de diameter van het gietblok of de gietsnelheid niet alleen de omvang van de maximale hoofdspanning, het veranderde ook de richting ervan. Bij hogere gietsnelheden en gietpalen met een grotere diameter, veranderde σ_{11} van de radiale of de omtreksrichting naar de axiale richting van het gietblok, voornamelijk door de hogere temperatuurgradiënt in die richting. De

consequentie van het draaien van de σ_{11} -as was dat het breukvlak draaide van parallel naar loodrecht op de axiale richting van het gietblok. Dit resulteerde mogelijk in zogenoemde *cup* en *cone* breuken.

Uiteindelijk werd het criterium voor koudscheuren gevalideerd met behulp van een nieuw ontwikkelde, hoge sterkte aluminiumlegering die zeer gevoelig is voor koudscheuren. De simulatieresultaten werden ondersteund door experimentele DC-gietproeven. Het gieten van een gietblok bij een hoge snelheid van 1.8 mm/s resulteerde tijdens de DC-gieting in het breken van het gietblok met een luide knal. Onderzoek naar het breukvlak liet zien dat een 7 mm lang insluitsel het bezwijken veroorzaakte. Deze scheurgrootte was in overeenstemming met de voorspelde scheurgrootte van 6-12 mm en de oriëntatie ervan bevestigde dat σ_{11} in de axiale richting van het gietblok werkte. Andere gietpalen werden onderzocht op mogelijke porositeit met behulp van ultrasonische defectoscopie, maar geen enkele porositeit van kritische grootte werd gedetecteerd. De enige aanwezige porositeiten waren krimpporositeiten met een maximale grootte van 100 μm , wat ver beneden de kritische scheurgrootte voor het bezwijken van een gietblok lag.

Wat het koudscheurfenomeen nogal onvoorspelbaar maakte, was de aanwezigheid van porositeiten met een kritische grootte, die tegelijkertijd loodrecht op de corresponderende maximale hoofdspanning georiënteerd waren. Tijdens onze metallografische observaties van een AA7050 DC-gegoten gietblok, vonden we warmscheuren die een paar millimeter groot waren, maar die niet leidden tot koudscheuren en het gietblok bleef intact. Waarschijnlijk leidde niet alleen de niet-kritische lengte maar ook de ongunstige oriëntatie van de scheuren niet tot het bezwijken van het gietblok. Onder zulke gecompliceerde omstandigheden en rekening houdend met de extreme brosheid van het materiaal, zouden de volgende aanbevelingen kunnen helpen bij de productie van defectvrije gietpalen; goed gecontroleerde gietcondities, homogeen gesmolten metaal zonder opname van deeltjes, de juiste keuze van het startblok zodat lokaal geen hoge spanningen geïnduceerd worden en voorzichtige behandeling van het gietblok na het gieten. Met behulp van resultaten verkregen uit computersimulaties dient voor elke legering de juiste gietsnelheid corresponderend met de diameter bepaald te worden. Wanneer de minimale scheurgrootte die voorspeld wordt door het model kleiner is dan de typische grootte van een insluitsel tijdens het gieten, moeten lagere gietsnelheden geselecteerd worden.

List of publications

Journal papers:

1. **M. Lalpoor**, D.G. Eskin, D. Ruvalcaba, H.G. Fjær, A. Ten Cate, N. Ontijt, L. Katgerman, Cold cracking in DC-cast high strength aluminum alloy ingots; an intrinsic problem intensified by casting process parameters, submitted to Materials Science and Engineering A.
2. **M. Lalpoor**, D.G. Eskin, L. Katgerman, thermal expansion/contraction behavior of AA7050 alloy in the as-cast condition relevant to thermomechanical simulation of residual thermal stresses, submitted to the International Journal of Materials Research (Zeitschrift für Metallkunde).
3. **M. Lalpoor**, D.G. Eskin, L. Katgerman, Cold cracking development in AA7050 DC-cast billets under various casting conditions, Metallurgical and Materials Transactions A 41 (2010) 2425-2434.
4. L. Zhang, D.G. Eskin, **M. Lalpoor**, L. Katgerman, Factors affecting thermal contraction behavior of an AA7050 alloy, Materials Science and Engineering A 527 (2010) 3264-3270.
5. **M. Lalpoor**, D.G. Eskin, G. ten Brink, L. Katgerman, Microstructural features of intergranular brittle fracture and cold cracking in high strength aluminum alloys, Materials Science and Engineering A 527 (2010) 1828–1834.
6. **M. Lalpoor**, D.G. Eskin, L. Katgerman, Cold-cracking assessment in AA7050 billets during DC-casting by thermomechanical simulation of residual thermal stresses and application of fracture mechanics, Metallurgical and Materials Transactions A 40 (2009) 3304-3313.
7. **M. Lalpoor**, D.G. Eskin, L. Katgerman, Fracture behavior and mechanical properties of high strength aluminum alloys in the as-cast condition, Materials Science and Engineering A 497 (2008)186-194.

Conference papers:

1. **M. Lalpoor**, D.G. Eskin, L. Katgerman, On the development of a cold cracking criterion for DC-casting of high strength aluminum alloys, Proc. of the 12th International Conference on Aluminum Alloys (ICAA 12), The Japan Institute of Light Metals, Yokohama, Japan, 2010, pp. 727-732.
2. **M. Lalpoor**, D.G. Eskin, H. G. Fjær, A. Ten Cate, N. Ontijt, L. Katgerman, Application of a criterion for cold cracking to casting high strength aluminum alloys, PRICM7, Materials Science Forum 654-656 (2010) 1432-1435.
3. **M. Lalpoor**, D.G. Eskin, L. Katgerman, Numerical simulation of residual thermal stresses in AA7050 alloy during DC-casting using ALSIM5, THERMEC 2009, Advanced Materials Research 89-91 (2010) 319-324.
4. **M. Lalpoor**, D.G. Eskin, L. Katgerman, Constitutive parameters, mechanical properties and failure mechanism in DC-cast AA7050 billets, Proc. of the 12th

International conference on Fracture, Ottawa, National Research Council of Canada, 2009 (CD).

5. **M. Lalpoor**, D.G. Eskin, L. Katgerman, Investigation of fracture behavior of high strength aluminum alloys in the as-cast condition, ICAA11, DGM & Wiley-VCH, Aachen, Germany, 2008, pp. 1474-1479.

Curriculum Vitae

Mehdi Lalpoor

born on 17 July 1979 in Tehran, Iran

- 1993 - 1997 High school in Mathematics and Physics
Amir Kabir High School, Tehran, Iran.
- 1997 - 2002 Bachelor of Science in Metallurgy and Materials Engineering
Iran University of Science and Technology, Tehran, Iran.
BSc thesis: The Effect of Step Quenching Cycle on the
Microstructure and Mechanical properties of Dual-Phase Steels.
- 2004 - 2006 Master of Science in Advanced Materials
University of Ulm, Germany
MSc thesis: Investigation of Ostwald Ripening in Al-Cu Alloys
by X-ray Microtomography
- 2006 - 2010 Researcher at Materials Innovation Institute (M2i)
PhD in Materials Science and Engineering
Delft University of Technology, The Netherlands.
PhD thesis: Study of Cold Cracking during DC-casting of High
Strength Aluminum Alloys.